17th INTERNATIONAL CONGRESS of the Geological Society of Greece

GEOLOGICAL SOCIETY OF GREECE • 1951 •

Mytilene, Lesvos Greece
28-31 May 2025
GSG2025

Book of Abstracts

ORGANIZED BY:

UNIVERSITY OF THE AEGEAN

www.ege2025lesvos.gr

NATURAL HISTORY MUSEUM OF THE LESVOS PETRIFIED FOREST

17th INTERNATIONAL CONGRESS
of the Geological Society of Greece

MYTILENE, LESVOS GREECE
28–31 MAY 2025
GSG2025

Book of Abstracts

17th INTERNATIONAL CONGRESS of the Geological Society of Greece

BULLETIN OF THE GEOLOGICAL SOCIETY OF GREECE, SP. PUBL.

EXTENDED ABSTRACT 001

Monitoring the evolution of landslide phenomena in Pyrra, Trikala, using advanced geospatial technologies

Agrafiotis Athanasios.[1], Papathanassiou Georgios.[1], Valkaniotis Sotirios.[2]
1 Aristotle University of Thessaloniki, Thessaloniki, Greece, aagrafia@geo.auth.gr
1 Aristotle University of Thessaloniki, Thessaloniki, Greece, gpapatha@geo.auth.gr
2 Aristotle University of Thessaloniki, Thessaloniki, Greece, valkaniotis@yahoo.com

Abstract

This study utilizes Unmanned Aerial Vehicles (UAVs) and advanced 3D modeling techniques to monitor and analyze the evolution of a significant landslide in Pyrra, Trikala, following the severe weather event known as Daniel in 2023. Specifically**,** In September 2023, Greece was impacted by the severe weather event known as Daniel, which led to intense rainfall and caused widespread natural disasters in Thessaly, including extensive landslides and floods (Dimitriou et al.,2024). The village of Pyrra in Trikala was notably affected, experiencing a large-scale landslide. This study focuses on documenting and monitoring this landslide to understand its progression over time.

Objectives: The primary objectives of this study was to employ advanced geospatial technologies to capture detailed data on the landslide and to use this data to monitor its evolution. (Highland & Bobrowsky, 2008). By doing so, the study aims to contribute to a better understanding of landslide dynamics and inform future mitigation strategies.

Geological setting: The landslide in Pyrra, occurred in an area consisting mainly of Pindus flysch. The failure mechanism of the landslide is a translational slide influenced by pre – existing cracks, the geometry of the slope and dye to the continuous rainfall.

Methods: The methodology involves multiple steps. Initially, high-resolution aerial imagery of the landslide area was captured using UAVs. These images were processed using photogrammetric methods, specifically the Structure from Motion (SfM) technique, to create detailed 3D models of the terrain. CloudCompare software was employed to analyze the changes in the landscape by comparing datasets collected at two different times: October 2023 and June 2024. The software's C2C (Cloud-to-Cloud) and M3C2 (Multiscale Model-to-Model Cloud Comparison) methods were used to quantify the displacement of materials and provide a comprehensive assessment of the landslide's evolution.

Results: The analysis revealed substantial material displacement and changes in the morphology of the landslide. The generated 3D models offer a detailed visualization of the impacted region, showing significant shifts in terrain and volume changes. Quantitative analysis revealed the extent of material movement and highlighted critical areas of instability.

Figure 1 Point cloud representation of the landslide, generated from UAV imagery using SfM techniques.

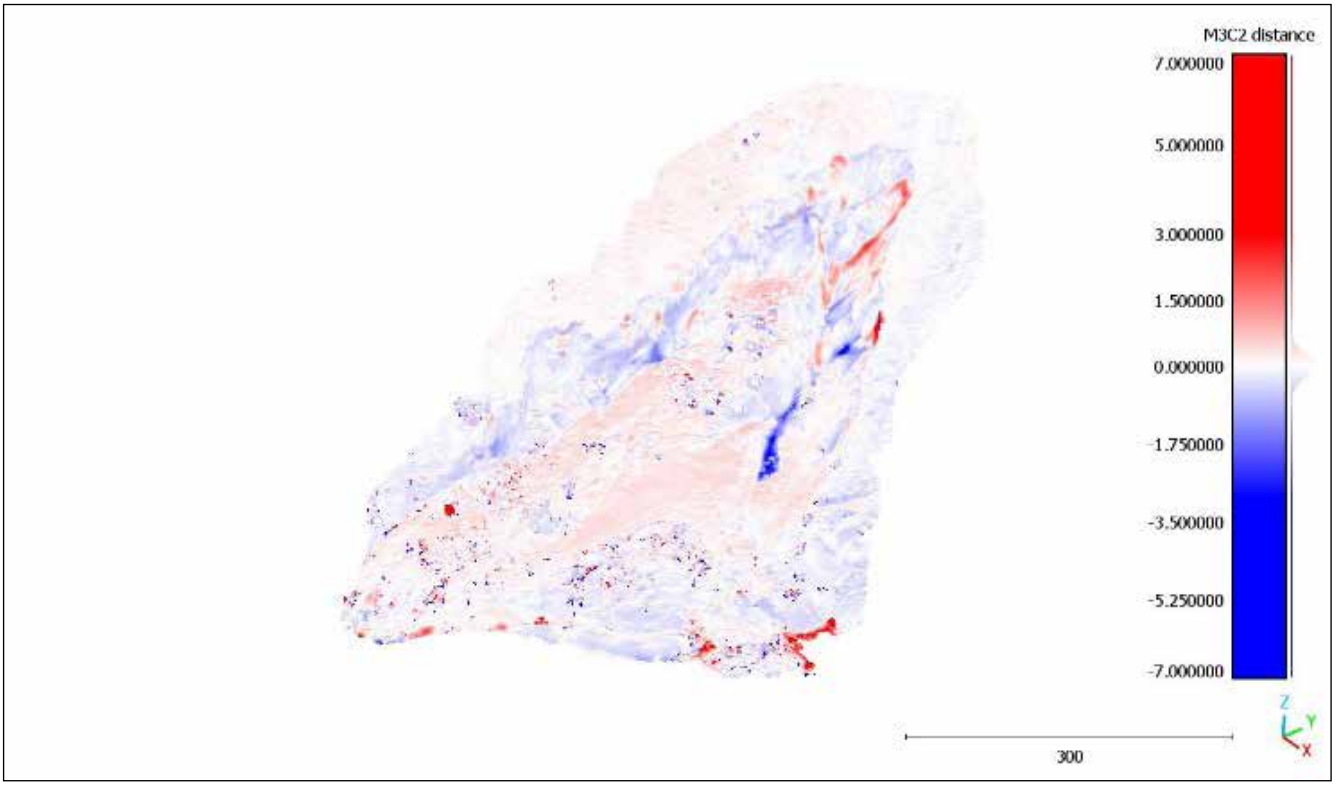

Figure 2 Detection of surficial displacement based on the M3C2 method. With red color depicts the areas where we have removal material and in blue the locations where we have deposited material.

Conclusions

The use of UAVs combined with advanced software tools like CloudCompare proved highly effective in monitoring and analyzing the landslide phenomena. This approach enables detailed observation and documentation of the landslide over time and provides valuable information for developing risk assessment and mitigation strategies. These findings of this study emphasize the potential of modern geospatial technologies in enhancing our understanding of landslide behavior and improving disaster response planning (Lacroix, 2020).

References

Dimitriou, E., et al. (2024). “Post-Analysis of Daniel Extreme Flood Event in Thessaly.” Water, 16(7): 980. **[Journal Article]**

Highland, L.M., & Bobrowsky, P. (2008). “The Landslide Handbook.” U.S. Geological Survey Circular 1325. **[Book]**

Lacroix, P. (2020) “Life and death of slow-moving landslides. “ Nat Rev Earth Environ 1, 404–419. **[Journal Article]**

17th INTERNATIONAL CONGRESS
of the Geological Society of Greece

BULLETIN OF THE GEOLOGICAL SOCIETY OF GREECE, SP. PUBL.

EXTENDED ABSTRACT 002

Structural study of the Theodorion meta-migmatitic complex (Serbomacedonian massif, northern Greece)

Amanatidou Dimitra[1], Soukis Konstantinos[1], Dimitri Klea[1], Stouraiti Christina[1]
(1) National and Kapodistrian University of Athens, dimitraam@gmail.com

Introduction

This paper presents the results of detailed mapping (1:10.000 scale) tectonostratigraphic and structural study on the high-grade metamorphic rocks of Vertiskos Unit, exposed in the Theodorion area (Northern Greece), which shows that they form an east-dipping sequence affected by at least three ductile deformation events.

Geological Setting

The high-grade SerboMacedonian Massif (SMM), exposed in northern Greece, represents the structurally highest crustal block of the Hellenides. It is bounded to the west by the low-grade Circum Rhodope metasediments and the Vardar ophiolitic rocks (Peonias Unit) and to the east by the high-grade rocks of the Rhodope Massif (Kockel et al., 1977; Kilias et al., 1999; Papanikolaou 2021). The SMM is subdivided into two main units: the overlying Vertiskos Unit and the underlying Kerdylia Unit. The contact is decorated by lenses of metamorphosed basic to ultrabasic rocks comprising the Volvi-Therma-Gomati complex, and it has been characterized as a top-SW Cenozoic detachment (Sokoutis et al., 1993). Geochronological data revealed that Vertiskos Unit includes late Proterozoic Pan-African rocks intruded by early (Silurian) and late (Carboniferous) Paleozoic granites and pegmatites and later on by Triassic A-type Arnea-Kerkini granites (Christofides et al., 1999, 2007; Himmerkus et al., 2007, 2009; Poli et al., 2009; Abbo et al., 2020). During the Mesozoic - Cenozoic period, the SMM was involved in the prolonged closing of the Neotethyan Vardar oceanic basin (Pe-Piper and Piper 2002; Papanikolaou 2021).

Tectonostratigraphy - Structural data

Detailed mapping along an NE transect revealed that the Theodorion area comprises three formations (Figure 1a-d): a lower migmatitic gneiss, an overlying biotite gneiss, and the uppermost garnet-mica schists. The overall structural thickness of the sequence reaches 1000m. The lowermost migmatitic gneiss shows a coarse-grained granitic core surrounded by typical gneissic layers with typical mineral assemblage, including feldspars + quartz ± biotite ± muscovite + opaque. It has to be noted that the granitic core is also foliated but not as strongly as the gneissic cover. At the transition zone between the two lithologies, high-grade structures such as ptygmatic folding are often observed (Figure 2a). The overlying biotite gneiss is lithologically quite heterogeneous and includes alternating biotite-rich schistose and gneissic layers, with a typical mineral assemblage of feldspars + quartz + biotite ± muscovite + opaque. Amphibolitic lenses are intercalated in places with mineral assemblage hornblende + epidote + plagioclase ± pyroxene + opaque. The uppermost garnet-mica schists include more aluminum-rich lithologies such as muscovite and garnet porphyroblasts and typical mineral assemblage muscovite + quartz + garnet ± biotite ± feldspars + opaque.

All the rocks present a roughly east-northeast-dipping gneissic layering with a coarse-grained foliation Sn and an east-north-east plunging stretching lineation Ln. In the microscopic scale, Sn is formed by alternating layers of quartz, felspar and quartz+biotite+white mica aggregates. Isoclinally folded quartz veins reveal that Sn is an axial planar foliation to Bn isoclinal folds, which have folded an older Sn-1 foliation, now observed as inclusion traces in feldspar porphyroblasts. Kinematic indicators such as S-C fabrics and garnet porphyroblasts show a consistent top-to-E or NE sense of shear. The entire sequence and the Sn are further folded by macro-to-mesoscale asymmetric SW-verging NW-SE open to tight folds, producing a fine-grained Sn+1 foliation associated with an Ln+1 intersection/stretching lineation trending NW-SE. Locally, Sn is reworked by a mylonitic Sn+1 foliation. On a microscopic scale, Sn+1 is formed by quartz+biotite aggregates (Figure 2b). The fold vergence indicates a top-SW tectonic transport for this event. Finally, distributed top-to-SW shear bands crosscut all previous structures.

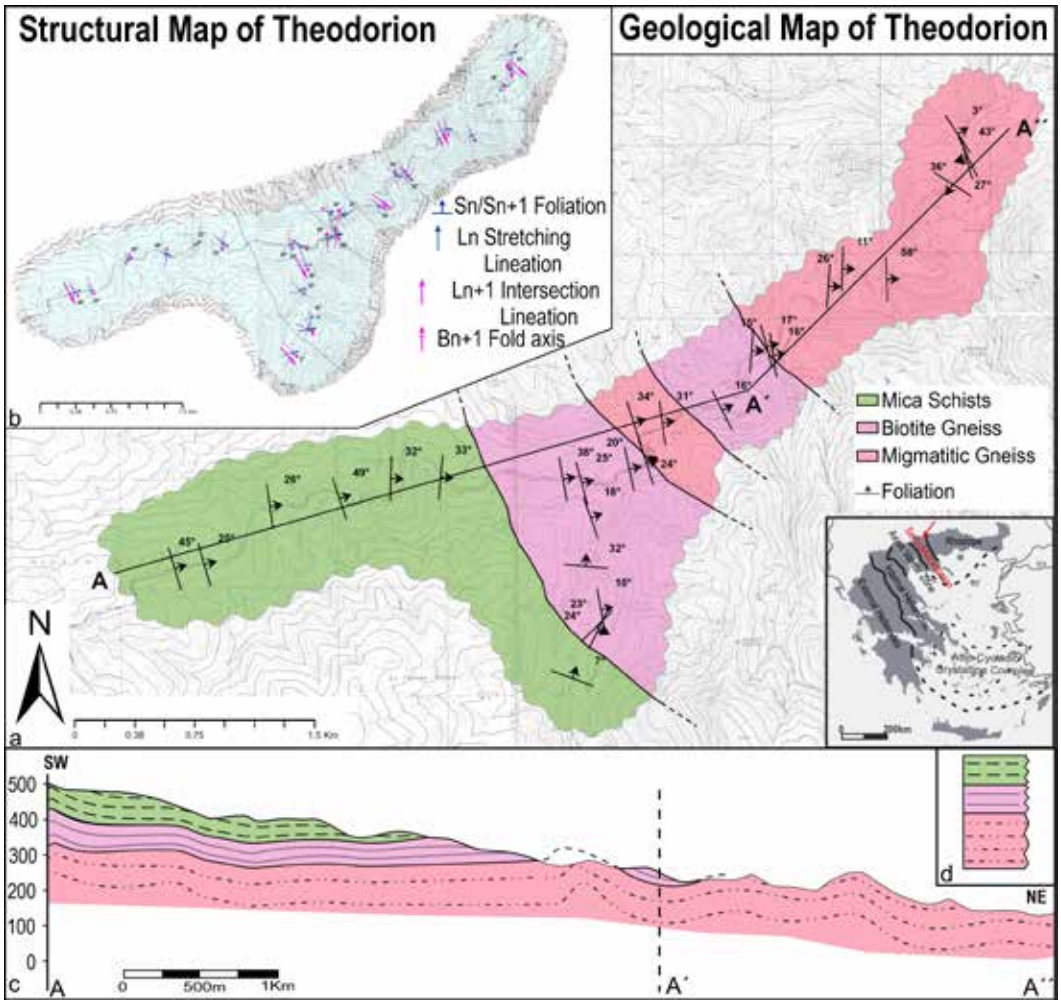

Figure 1a-d. a-b) Geological and structural map of the Theodorion area. Inlet shows the location of the study area. c-d) SW-NE crosssection A-A´-A´´ showing the structure of the Theodorion area and tectonostratigraphic column.

Figure 2a-b a) Close view of the lowermost migmatitic gneiss, red arrow indicating ptygmatic folds. b) Photomicrograph of the biotite gneiss showing the oblique Sn foliation folded by a greenschist-facies Sn+1 foliation (XZ section +polars).

Discussion - Conclusions

Our detailed mapping showed that a northeast-dipping sequence of high-grade rocks exists in the Theodorion area. The lowermost migmatitic gneiss and biotite gneiss represent prealpine basement lithologies of granitic or migmatitic protoliths that underwent high-grade metamorphism through multiple tectonometamorphic events as reported by previous researchers (Pe-Piper and Piper 2002 and references therein; Himmerkus et al., 2007, 2009; Abbo et al., 2020). The origin of the uppermost mica schist is less straightforward to conclude. It could represent a metasedimentary cover, in which case, based on existing geochronological data for the Vertiskos Unit basement rocks, it could be the late Proterozoic to early Paleozoic cover of the granitic precursors. On the other hand, given that these rocks have participated in several orogenic events, a meta-migmatitic origin cannot be excluded.

As for the structural history of these rocks, the early Dn-1 and Dn events could be associated with the Mesozoic (late Jurassic-Cretaceous) history related to the Vardar closure and subsequent deformation. The Dn+1 event could correspond to the Eocene thrusting of the Serbomacedonian Massif on the Circum Rhodope and the Vardar ophiolites. The late-stage top-SW shear bands probably accompanied the late Eocene-Oligocene exhumation of the underlying Kerdylia Unit.

References

Abbo, A., Avigad, D., Gerdes, A., 2020. Crustal evolution of peri-Gondwana crust into present day Europe: the Serbo-Macedonian and Rhodope massifs as a case study. Lithos 356–357, 105295. doi: 10.1016/j.lithos.2019.105295.

Christofides G., Koroneos A., Pe-Piper G., Katirtzoglou K., Chatzikirkou A., 1999. Pre-Tertiary A-Type magmatism in the Serbomacedonian massif (N. Greece): Kerkini granitic complex. Bull. Geol. Soc. Greece, xxxiii, 131-148.

Christofides G., Koroneos A., Liati A., Kral J., 2007. The A-Type Kerkini granitic complex in North Greece: geochronology and geodynamic implications. Bull. Geol. Soc. Greece, xl, 700-711.

Himmerkus, F., Anders, B., Reischmann, T., Kostopoulos, D., 2007. Gondwana-derived terranes in the northern Hellenides. In 4-D Framework of Continental Crust (eds RD Hatcher, MP Carlson, JH McBride and JR Martinez Catalán), pp. 379–90. Geological Society of America, Memoirs no. 200.

Himmerkus, F., Reischmann, T., Kostopoulos, D., 2009. Serbo-Macedonian revisited: a Silurian basement terrane from northern Gondwana in the Internal Hellenides, Greece. Tectonophysics 473, 20–35. doi: 10.1016/j.tecto.2008.10.016.

Kilias, A., Falalakis, G., Mountrakis, D., 1999. Cretaceous–Tertiary structures and kinematics of the Serbomacedonian metamorphic rocks and their relation to the exhumation of the Hellenic hinterland (Macedonia, Greece). International Journal of Earth Sciences 88, 513–31. doi: 10.1007/ s005310050282.

Kockel, F., Mollat, H., Walther, H. W., 1977. *Erlauterungen zur geologicschen karte der Chalkidiki und angrenzender Gebiete 1/100.000 (Nord Griechenland)*. Hanover: Bundesanstalt für Geowissenschaften und Rohstoffe, 119 pp.

Papanikolaou, D.I., 2021. Regional Geology Reviews The geology of Greece. Springer Nature.

Pe-Piper, G. and Piper, D.J.W., 2002. The igneous rocks of Greece. The anatomy of an orogen.–Gebrüder Borntraeger, Berlin, Stuttgart.

Poli, G., Christofides, G., Koroneos, A., Soldatos, T., Perugini, D., Langone, A., 2009. An Early Triassic granitic magmatism—Arnea Kerkini granitic complexes—In the Vertiskos unit (Serbo-macedonian massif, north-eastern Greece) and its significance in the geodynamic evolution of the area. *Acta Vulcanologica*, *21*, 47–70.

Sokoutis D, Brun JP, Van den Driessche J, Pavlides S (1993) A major Oligocene–Miocene detachment in southern Rhodope controlling north Aegean extension. J Geol Soc Lond 150(2), pp.243-246.

17th INTERNATIONAL CONGRESS of the Geological Society of Greece

BULLETIN OF THE GEOLOGICAL SOCIETY OF GREECE, SP. PUBL.

EXTENDED ABSTRACT 003

Fostering FAIR approaches to the seismological data life cycle

Anagnostou V.[1], Bonatis P.[1], Karakostas V.[1], Kourouklas C.[1], Papadimitriou E.[1], Adamaki A.[2], Andriopoulou-Mounteanou S-A.[3], Bathrellos G.D[3], Bitharis S.[1], Foumelis M.[1], Karolos I-A.[1], Kaviris G.[4], Papageorgiou E.[1], Pikridas C.[1], Sakkas V.[1], Skilodimou H.D.[32], Spingos I.[4], Zymvragakis A.[4]

(1) Aristotle University of Thessaloniki, Thessaloniki, Greece, vanagno@geo.auth.gr (2) Lund University, Lund, Sweden (3) University of Patras, Rio, Greece (4) Section of Geophysics – Geothermics, Department of Geology and Geoenvironment, National and Kapodistrian University of Athens, Athens, Greece

Introduction

Natural disasters such as earthquakes floods and landslides expose communities living within hazard-prone areas to significant risks, particularly in today's increasingly interconnected world, making the need for advancement in multi-hazard assessment techniques critical. The HOMEROS project seeks to tackle the challenges presented by those advancements, focusing on seismology, geodesy and geology and leveraging cutting-edge technical solutions tailored to the big data era. HOMEROS makes strides in standardizing research methods, fostering collaboration, and improving the ability to understand and foresee natural hazards through Open Science practices. The project focuses on assessing hazard in high-risk areas in Greece, known for their significant seismic activity, major earthquake occurrence, floods, and landslides, through its transparent, reproducible and widely accessible research products. Data and tools developed by the project will strictly adhere to the FAIR principles (Findable, Accessible, Interoperable, Reusable), thereby maximizing their value for the scientific community, policy makers and stakeholders. HOMEROS will compile earthquake catalogues and assess ground deformation products to provide a comprehensive evaluation of seismic hazard. Furthermore, it will enhance knowledge of flood and landslide hazards, contributing to more effective mitigation efforts.

Project objectives

The HOMEROS project seeks to fulfill the critical need for reliable and standardized methods to assess multiple hazards in an increasingly dynamic risk environment. Harnessing the potential of Open Science and interdisciplinary collaboration, the project strives to expand scientific understanding, support data-informed decision-making, and strengthen community resilience. Its goals are centered around three core pillars:

- Utilization of platforms, such as the European Open Science Cloud (EOSC) and the Environmental Research Infrastructure (ENVRI) (Adamaki & Vermeulen, 2023) for the creation of accessible and efficient ecosystems for interdisciplinary data sharing. This effort builds on prior integration efforts in ENVRI projects and promotes FAIR principles, ensuring usability and reproducibility of research outputs.
- Development of methodologies and workflows for integrating and utilising diverse datasets, including geodetic, seismic and geological data to create detailed physical models, visualization products, such as maps, and data inventories. These efforts seek to aid in the advancement and enhancement of multi-hazard assessment.
- Fostering collaboration and communication among research institutions, infrastructures, and projects. Scientific results will be shared through Open Access publications, workshops, and educational resources.

This paper presents data, workflows and results from the HOMEROS project, related to a specific swarm-like seismic excitation that occurred during the 2024 February – April period in the offshore area to the west of Asos village, Kefalonia island. This work includes preliminary findings from the project, highlighting the collaboration between the participating institutions and the potential for clear and reproducible scientific results by the adherence of available seismic datasets to FAIR principles.

Study area

The areas chosen as case studies for the HOMEROS project are the central Ionian Islands, along with the western Gulf of Corinth. These areas exhibit high deformation rates (Pikridas et al., 2016, Bitharis

et al., 2024), frequent occurrences of strong earthquakes (e.g., Papadimitriou et al., 2017; Kaviris et al., 2021; Sakkas et al., 2022) and destructive floods and landslides (Bathrellos et al., 2017, Skilodimou et al., 2018). More than 50% of the seismic energy in Europe is released in Greece, placing earthquakes among the most impactful geohazards in the country, highlighting the need for a reliable seismic hazard model. A comprehensive evaluation of seismic hazard for such areas can be achieved by Peak Ground Acceleration (PGA) and Peak Ground Velocity (PGV) calculations, alongside site-specific analysis (Uniform Hazard Spectra – UHS and hazard curves) in towns that exhibit the highest population in the study areas (e.g., Kaviris et al., 2022, 2024).

The preliminary results presented in this paper concern the rigorous swarm taking place in 2024 in the offshore area west of Asos village of Kefalonia island. The study area is part of the Kefalonia Transform Fault Zone (KTFZ), which dominates the central Ionian Islands, which is the most seismically active area in the Mediterranean (Figure 1). Specifically, the swarm–like activity that lasted more than two months is located in a thoroughly studied part of the KTFZ, that is recognized as an extensional duplex transfer zone that links the northern (Lefkada) with the southern (Kefalonia) branches of the KTFZ (Karakostas et al., 2015). This stepover zone consists of small sub–parallel fault segments, striking roughly WSW–ENE, deflecting the azimuth of the main fault branches. Since only moderate magnitude earthquakes are known to have occurred in this area, this swarm–like excitation raises scientific concern for the exploitation of the large amount of seismological data that were collected during the activity and the exploitation of the collected data for deciphering the dynamic and kinematic properties of the activated structures. Advancing knowledge of the seismotectonic properties will provide valuable insight in assessing seismic hazard in the broader central Ionian Islands region.

Methods and data

High quality seismic data from regional networks are essential for the compilation of earthquake catalogue and the production of efficient data pipelines ready for multidisciplinary utilization. HOMEROS aims to exploit a benchmark seismic dataset for the February – April 2024 Central Ionian Islands swarm – like activity –among others–, containing more than 2000 earthquakes to explore integration opportunities for enhanced data exchange e.g., data pipelines between research groups of various disciplines, interested in leveraging seismic data for their research. This will be achieved by taking advantage of the resources provided by the EOSC and the ENVRI cluster. This effort also seeks to demonstrate the added value of these services, integrating their tools and services for multi–disciplinary research. Availability of both the relocated benchmark seismic catalogue and the raw waveform dataset will be enhanced following FAIR principles and Open Science practices, ensuring the ease of access to the data. To facilitate interoperability, the relocated catalogue will be provided in the QuakeML schema, a widely used form of seismological data representation, in a modular XML form, able to contain a variety of information, including moment tensors. The waveform dataset will be provided in miniSEED format, accompanied by the corresponding metadata for each station used to collect the data.

Along with providing ease of access to the benchmark data, HOMEROS aims to provide open–source tools for managing, obtaining, processing and visualizing seismic data. To this end, interactive coding platforms such as Jupyter Labs, will be utilized for better dissemination of the developed workflows and tools to scientists from different disciplines (e.g., in the form of Jupyter Notebooks), since an essential component of the project is to ensure the reproducibility, interoperability and ease of access of all research outputs of HOMEROS.

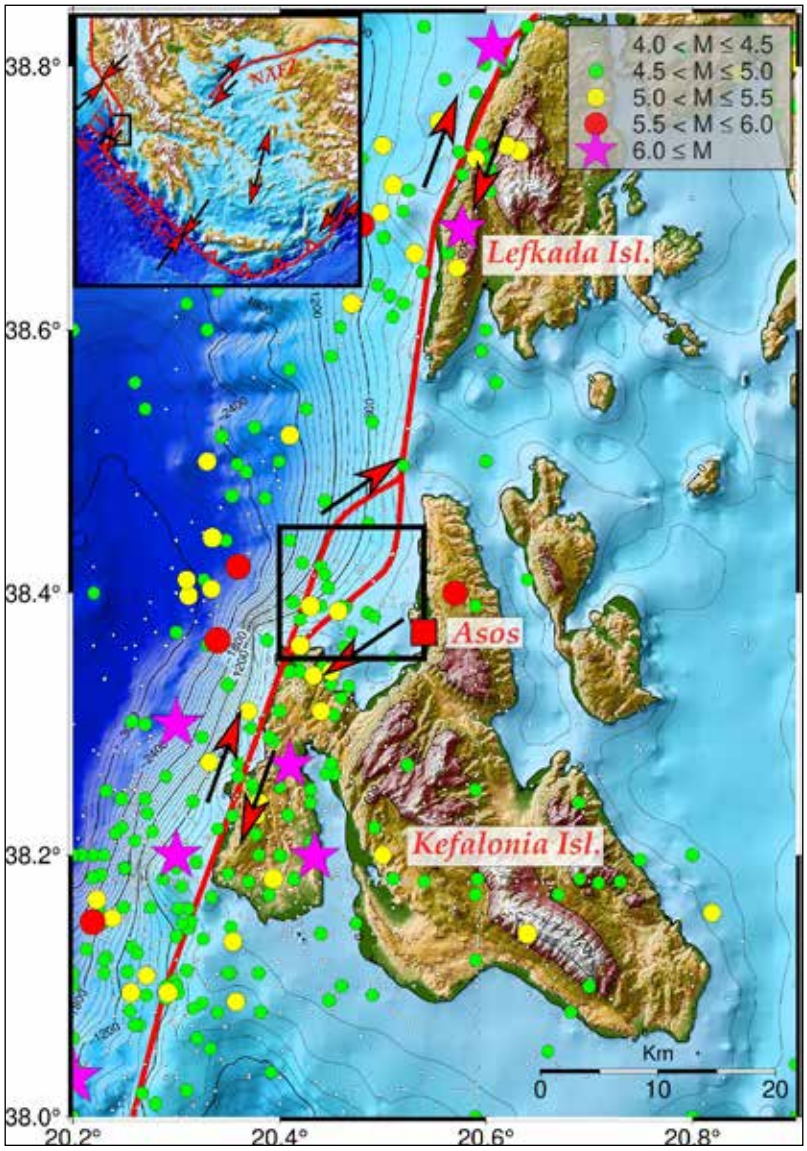

Figure 1: Map of the study area of the central Ionian islands. Circles and stars of different colors and sizes denote seismicity in the region since 1970, according to the legend. The area is placed within the context of the seismotectonics of the Aegean in the map inset, along with major structures of the region, marked with red lines. The main fault segments of the KTFZ, along with the extensional stepover area are denoted with red lines on the map of the study area. Arrows show the relative movement of the faults. The black rectangle encloses the region where the February – April 2024 seismic swarm took place, whereas the red rectangle denotes the location of Asos village

Exploitable results

The primary output for the seismology part of the HOMEROS project multi–hazard outputs, will be open–access datasets, including earthquake catalogues and waveform inventories. It is essential that these datasets will adhere to FAIR principles and be publicly available through platforms such as EPOS ERIC, ENVRI repositories, and other widely used repositories (e.g., GitHub, Zenodo). The benchmark seismic dataset for the February–April 2024 central Ionian Islands swarm-like activity contains over 2000 earthquakes with information on their relocated epicenters, depths, origin time, along with focal

mechanisms for a number of them (Figure 2). The waveform dataset of the swarm contains raw data along with station metadata for 14 seismic stations of the central Ionian Islands. Another key outcome is the development of clear and reproducible research workflows documented through interactive tools such as Jupyter Notebooks. These workflows will showcase the integration of seismic data with various datasets and methodologies, allowing researchers to replicate and tailor the processes for comparable studies, while also providing means of preliminary visualization of the data without the need of prior knowledge of complex tools developed for specific scientific disciplines. In our case, Jupyter notebooks containing complete workflows, along with instructions for waveform data homogenization and earthquake magnitude estimation will be provided.

Type	**Description**	**Format**
Raw data	Seismic Waveforms	miniSEED
Metadata	Station Metadata	StationXML (.xml)
Raw data	Earthquake Catalogues	QuakeML (.xml)
Raw data	Focal mechanisms	QuakeMl (.xml)
Interactive notebook	Waveform dataset homogenization and Magnitude Estimation	Jupyter Notebook
Interactive notebook	Seismic data fetching and simple visualization	Jupyter Notebook

Table 1. Summary of expected data products for the February–April 2024 central Ionian Islands swarm-like activity case study of the HOMEROS project.

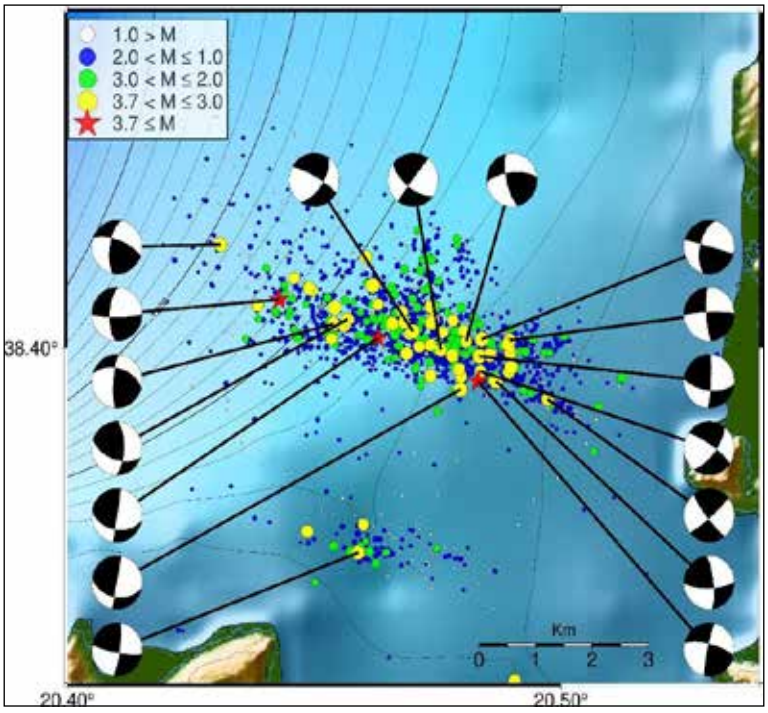

Figure 2: Relocated epicenters of earthquakes that occurred in the study area during the 24/02/2024 – 24/04/2024. Colored dots denote earthquakes with 0.1 ≤ M ≤ 3.7, according to legend. The focal mechanisms of the 17 strongest earthquakes of the excitation are also presented, shown as equal area lower hemisphere projections. The excitation catalog, along with focal mechanisms, is currently available as a preliminary dataset (Anagnostou, 2025) and will be enhanced and finalized with clear metadata and reproducibility information, adhering to FAIR principles through the HOMEROS project.

A workflow along with instructions on obtaining seismic data from open access databases for specific temporal and spatial restrictions and visualizing them on simple maps (Figure 3) will be provided. These workflows will illustrate the combination of diverse datasets and methodologies, empowering researchers to replicate and modify the processes for related studies. Comprehensive documentation for each workflow, presented through interactive notebooks, will act as a best-practice reference for future multidisciplinary research endeavors.

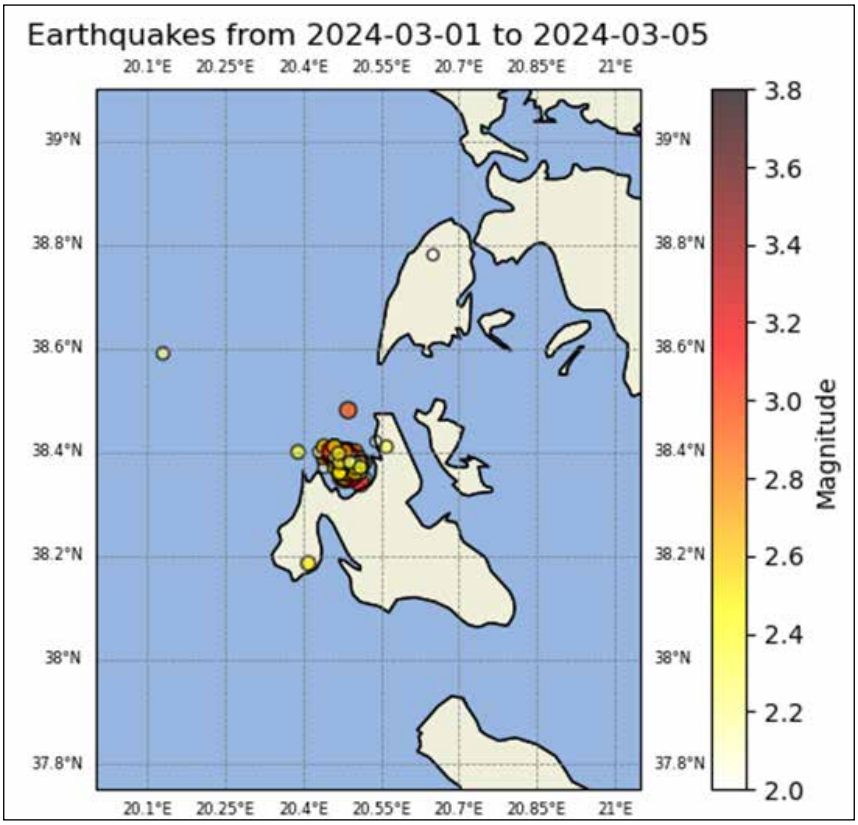

Figure 3: Simple map created using the Seismic data fetching and visualization notebook, presenting earthquakes for the study area during the first 5 days of March 2024, when the excitation activity was peaking. Colored epicenters correspond to the magnitude color bar on the right side of the figure. Data obtained from public EMSC catalogues.

Conclusions

HOMEROS represents an important step forward in addressing the rapidly growing ramifications of multi-hazard assessment. Through unifying data from various scientific fields and embracing Open Science principles, the project addresses critical challenges in making hazard assessment thorough and accessible. By providing seismic datasets and developed workflows following FAIR principles, HOMEROS seeks to propel forward multidisciplinary collaboration and provide clear, reproducible scientific results. The project lays the foundation for scalable and interoperable tools and approaches to understanding natural hazards and their complex interactions. By focusing on a specific case study in a high–risk area such as the central Ionian Islands, we seek to demonstrate the practicality of our developed workflows, the accessibility of our seismic datasets and their potential for further utilization and application from researchers beyond the Earth sciences disciplines. Finally, the outputs comprising open–access data, scientific publications, and training modules, will provide valuable resources for policy–making and disaster management, contributing to a safer and more resilient society.

Acknowledgements

The authors acknowledge the OSCARS project, which has received funding from the European Commission's Horizon Europe Research and Innovation programme under grant agreement No. 10112975.

References

Adamaki, A., & Vermeulen, A. (2023). ENVRI-FAIR D5.7: ENVRI-Hub design study, Zenodo. https://doi.org/10.5281/zenodo.8119522

Anagnostou, V. (2025). February - April 2024 Ionian islands Swarm-like exciation seismic catalog [Data set]. Zenodo. https://doi.org/10.5281/zenodo.14652121

Bathrellos, G. D., Skilodimou, H. D., Chousianitis, K., Youssef, A. M., & Pradhan, B. (2017). Suitability estimation for urban development using multi-hazard assessment map. *Science of the total environment*, *575*, 119-134. https://doi.org/10.1016/j.scitotenv.2016.10.025

Bitharis, S., Pikridas, C., Fotiou, A., Rossikopoulos D., 2024. GPS data analysis and geodetic velocity field investigation in Greece, 2001–2016. *GPS Solutions 28*, 16. https://doi.org/10.1007/s10291-023-01549-8

Karakostas, V., Papadimitriou, E., Mesimeri, M., Gkarlaouni, Ch., Paradisopoulou, P., 2015. The 2014 Kefalonia doublet (Mw6.1 and Mw6.0) central Ionian Islands, Greece: Seismotectonic implications along the Kefalonia Transform Fault Zone. *Acta Geophysica 63*, 1-16. https://doi.org/10.2478/s11600-014-0227-4

Kaviris, G., Elias, P., Kapetanidis, V., Serpetsidaki, A., Karakonstantis, A., Plicka, V., De Barros, L., Sokos, E., Kassaras, I., Sakkas, V., Spingos, I., Lambotte, S., Duverger, C., Lengline, O., Evangelidis, C.P., Fountoulakis, I., Ktenidou, O.-J., Gallovic, F., Bufferal, S., Klein, E., Aissaoui, E.M., Scotti, O., Lyon-Caen, H., Rigo, A., Papadimitriou, P., Voulgaris, N., Zahradnik, J., Deschamps, A., Briole, P., & Bernard, P. (2021). The Western Gulf of Corinth (Greece) 2020–2021 Seismic Crisis and Cascading events: first results from the Corinth Rift Laboratory Network. Seism. Rec., 1, 85–95. https://doi.org/10.1785/0320210021.

Kaviris, G., Zymvragakis, A., Bonatis, P., Kapetanidis, V., & Voulgaris, N. (2022). Probabilistic and Scenario-Based Seismic Hazard Assessment on the Western Gulf of Corinth (Central Greece). *Applied Sciences*, *12*(21), 11152. https://doi.org/10.3390/app122111152

Kaviris, G., Zymvragakis, A., Kapetanidis, V., Kouskouna, V., Spingos, I., Sakellariou, N., & Voulgaris, N. (2024). A logic-tree based probabilistic seismic hazard assessment for the central ionian islands of cephalonia and ithaca (Western Greece). *Journal of Seismology*, *28*(5), 1087-1103. https://doi.org/10.1007/s10950-024-10242-3

Papadimitriou, E., Karakostas, V., Mesimeri, M., Chouliaras, G., & Kourouklas, Ch. (2017). The Mw6.5 17 November 2015 Lefkada (Greece) Earthquake: Structural Interpretation by Means of the Aftershock Analysis. *Pure and Applied Geophysics*, 174(10), 3869–3888. https://doi.org/10.1007/s00024-017-1601-3

Pikridas C., Bitharis S., Fotiou A., Rossikopoulos D., Katsougiannopoulos S., Spanakaki K, Karolos I., 2016. Monitoring seismic displacements using GNSS data with PPP method. *Bulletin of the Geological Society of Greece 50* (3), 1563-1569. https://doi.org/10.12681/bgsg.11870

Sakkas, V., Kapetanidis, V., Kaviris, G., Spingos, I., Mavroulis, S., Diakakis, M., Alexopoulos, J.D., Kazantzidou-Firtinidou D., Kassaras, I., Dilalos, S., Vassilakis, E., Kotsi, E., Tselentis, G., Lekkas, E. & Voulgaris, N. (2022). Seismological and ground deformation study of the Ionian Islands (W. Greece) during 2014–2018, a period of intense seismic activity. *Applied Sciences, 12*(5), 2331. https://doi.org/10.3390/app12052331

Skilodimou, H. D., Bathrellos, G. D., Koskeridou, E., Soukis, K., & Rozos, D. (2018). Physical and anthropogenic factors related to landslide activity in the Northern Peloponnese, Greece. *Land*, *7*(3), 85. https://doi.org/10.3390/land7030085

17th INTERNATIONAL CONGRESS of the Geological Society of Greece

BULLETIN OF THE GEOLOGICAL SOCIETY OF GREECE, SP. PUBL.

EXTENDED ABSTRACT 004

Detailing the stress pattern in the area of central Ionian Islands

Anagnostou V.[1], Papadimitriou E.[1], Karakostas V.[1], Bäck T.[2]
Department of Geophysics, Aristotle University of Thessaloniki, Thessaloniki, Greece, vkarak@geo.auth.gr
Nuclear Science and Engineering department, KTH Royal Institute of Technology, Stockholm

Background

The Kefalonia Transform Fault Zone (KTFZ) is the most seismically active area in the Mediterranean and consists of two major branches, the Lefkada fault segment to the north and the Kefalonia fault segment to the south. KTFZ acts as an active boundary between the subduction zone of the remnants of the oceanic lithosphere of the Eastern Mediterranean that subducts under the Aegean microplate to the south and the continental collision between the Eurasian plate and the Adriatic Microplate to the north. The tectonic activity in the region is reflected in the rapid crustal deformation rates of the region and subsequently the frequent occurrence of strong earthquakes ($M_w \geq 6.0$) that occurred during both the historical and instrumental era of seismology. Those strong earthquakes and their temporal distribution can be explained due to stress transfer between closely located fault segments (Papadimitriou, 2002) and as such, studying those stress interactions is an integral part of understanding the long-term tectonic loading in the region.

For better understanding of the kinematics and the distribution of continental deformation that is occurring within the brittle crustal layer in the study area, we assess the regional stress field by inverting focal mechanisms. Contemporary stress field in an area is a result of processes that operate at significantly different spatial scales (Zoback, 1992). Forces that are linked to major tectonic movements such as ridge push and slab pull affect the stress field at large wavelengths, beyond 2000 km and are considered first–order sources of stress field perturbation. At intermediate wavelengths (between 2000 and 500 km) the crustal stress field is affected by processes such as orogenic lithospheric flexure (Zoback, 1992) with those processes representing second order sources of stress field disturbances. Third order patterns of crustal stress field are linked to small–scale variations (<100km) that are produced by processes such as active faulting and at times these variations may lead to the nucleation of potentially destructive earthquakes (Hergert and Heidbach, 2011). Detailed knowledge of the contemporary stress field characteristics of high–risk areas, such the central Ionian Islands region is valuable for possible investigations of stress triggering sensitivity due to the coseismic slip of strong earthquakes.

Objectives

The main objective of this paper is to present crustal stress data for the area of central Ionian Islands, inferred from the inversion of 485 focal mechanisms using the SATSI inversion method of Hardebeck and Michael (2006) and specifically the MSATSI implementation of the method (Martinez–Garzon et al., 2014). We seek to better detail the stress field by binning the focal mechanism dataset according to known structures in the area and producing a representative focal mechanism for each subarea based on the stress inversion results. Previous work in defining the stress pattern has been done for the Greek region (e.g., Kapetanidis & Kassaras, 2019) including our study area. We focus on detailing the stress pattern around the main branches of the KTFZ along with the transfer zone that connects them and has been identified as an extensional stepover zone (Karakostas et al., 2015).

Data and Method

Our dataset contains 485 focal mechanisms and was compiled from data obtained from a variety of sources, mainly published works (Hatzfeld et al., 1995; Louvari et al., 1999; Benetatos et al., 2004, 2005; Pondrelli et al., 2004, 2007, 2011; Karakostas & Papadimitriou, 2010; Karakostas et al., 2015; Papadimitriou et al., 2017; Kostoglou et al., 2020) along with routine solutions from various observatories (GCMT, ETH, HUSN, GEOFON). In cases of duplicate solutions, we prioritized the focal mechanism computed by published works over routine solutions. MSATSI deals with the ambiguity of the fault-plane solution by allowing the user to explicitly specify the probability that each input fault plane solution is thought to be the real one. We used the typical 50% value for our inversions. Focal mechanisms that correspond to seismicity occurring below crustal depths (>30km) were discarded in order to constrain the stress patterns to crustal, third order levels. The KTFZ comprises five major fault segments with striking from 12° to 40°, with fault lengths between 12–40km and rake values that exhibit right–lateral strike–slip faulting (Kourouklas et al., 2023). Four out of the five segments bound the western coastlines of the Lefkada and Kefalonia Islands and were identified

as the causative faults of four of the strongest earthquakes that occurred in the study area during the 21st century (Karakostas et al., 2004, 2015; Papadimitriou et al., 2017). The fifth segment is located offshore, south of Kefalonia and was associated with the 1983 M_w=7.0 earthquake (Scordilis et al., 1985). The gridding scheme for our focal mechanism dataset follows the segmentation of the KTFZ for its five segments, with an additional grid point located in the stepover zone that connects the northern Kefalonia segment with the southern Lefkada segment (Figure 1).

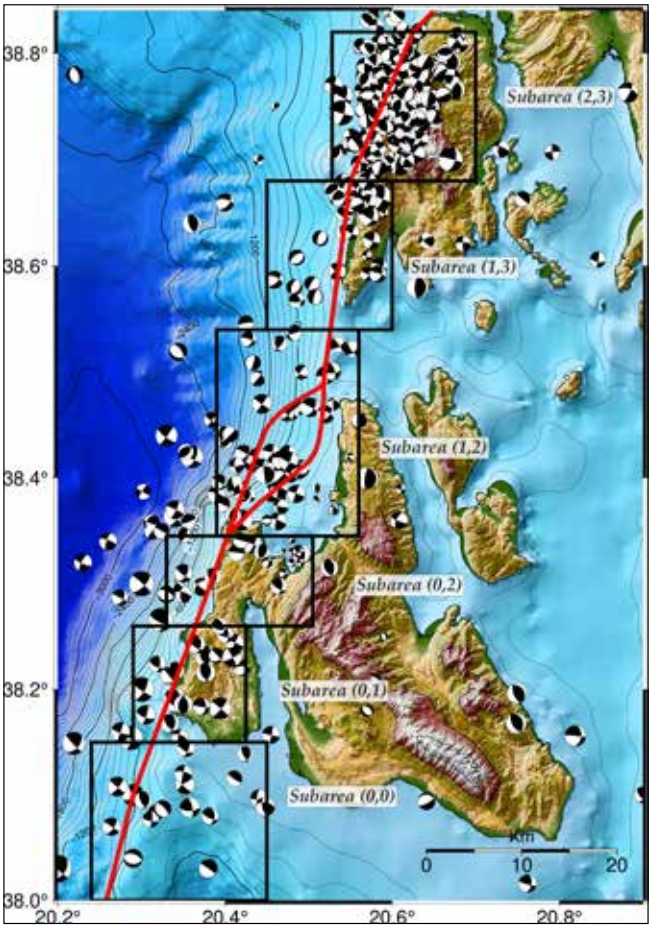

Figure 1: Map of the study area of the central Ionian Islands along with the major fault segments of the KTFZ and the extensional stepover area, denoted with red lines and enclosed by rectangles that correspond to the subareas or grid points containing the focal mechanisms used in the inversion. The focal mechanisms are shown as equal area lower hemisphere projections.

After compiling and subdividing our dataset to their corresponding subareas, securing that each one comprises at least 20 focal mechanisms to ensure robustness of results, we perform stress inversion for each subset, by applying the SATSI inversion algorithm. The algorithm inverts focal mechanism data for spatially and/or temporally variable stress field, using a damped least–squares inversion method to obtain a smoothed solution (stress tensor) for each subarea while avoiding data singularities. MSATSI provides the orientation of the three principal axes, as well as a relative stress magnitude quantity (R):

$$R = \frac{\sigma_1 - \sigma_2}{\sigma_1 - \sigma_3} R = \frac{\sigma_1 - \sigma_2}{\sigma_1 - \sigma_3} \quad (1)$$

where σ_1, σ_2, σ_3 are the magnitudes of the principal stress axes obtained from the deviatoric stress tensor. This way, the R value quantifies whether the magnitude of the intermediate principal stress σ_2 is closer to the magnitude of the most compressive or the least compressive principal stress. MSATSI calculates the optimal damping parameter by performing a series of inversions with varying values and comparing the resulting data misfit to the degree of

heterogeneity of the solution (model length). The chosen damping parameter is found on the trade–off curve of the two values, corresponding to the point that minimizes both the data misfit and the model length. Finally, we assess the uncertainties of our results using a bootstrap resampling method. We perform resamplings at least 20 times the number of our data for each grid point, specifying the confidence interval of the uncertainties at 95%. Finally, we construct a representative focal mechanism for each grid point, according to the best stress tensor derived from our methodology.

Exploitable Results

The results of the damped stress inversion are presented in Figure 2 and Table 1. We observe that in all grid points, the plunge and azimuth of the principal stress axes agree as expected with a strike–slip faulting regime, with low plunge values of both the σ_1 and σ_3 principal stress components. Our data constrain the plunge and azimuth of the principal stress axes adequately for the Kefalonia branch of the KTFZ, the stepover zone north of Kefalonia and the southern Lefkada grid point. In the case of the northern Lefkada (grid point 2, 3) subarea, we observe higher uncertainties in the plunges of both the σ_3 and the σ_2 principal stress components. Assessing these uncertainties through bootstrap resamplings, we find that they are mainly concerned with the plunges of the σ_3 axis. This, along with the value of the relative stress ratio R, indicate a stronger normal faulting component in this subarea and thus extensional characteristics. R values for the southern Lefkada (grid point 1, 3) and the stepover zone (grid point 1, 2) are found to be 0.45 and 0.41, respectively. Values of R closer to 0.0 evidence extensional component of the prevailing regional stress field, whereas values approaching to 1.0 are indicative of rather transpressional regimes. This is present in the north Kefalonia (grid point 0, 2) south Kefalonia (grid point 0, 1) and offshore Kefalonia (0,0) subareas, where the relative stress magnitude values increase, evidencing a stronger compressive stress component as we move towards the southern edge of the KTFZ. Nevertheless, the R values for all subareas under study remain relatively close to the 0.5 value, meaning the dominant faulting that characterize the regional stress regime is strike–slip. Following the World Stress Map project guidelines (Zoback, 1992) we calculate the azimuth of the maximum horizontal stress axis for every grid point. We observe as expected, that the maximum compression axis σ_1 corresponds to the S_{Hmax} and strikes SW–NE. Using the calculated best solutions for the P and T axes geometrical characteristics, we produced six representative focal mechanisms, one for each grid point. All are pointing towards a strike–slip stress regime, with the one nodal plane striking NNE–SSW and the second (conjugate) WNW–ESE.

Grid point (X,Y)	Optimal σ_1 Trend and Plunge	Optimal σ_2 Trend and Plunge	Optimal σ_3 Trend and Plunge	Relative Stress Magnitude	Representative Focal Mechanism					
					Nodal Plane 1			Nodal Plane 2		
					Strike	Dip	Rake	Strike	Dip	Rake
(0,0)	249°/10°	130°/62°	341°/11°	0.76	25°	75°	179°	115°	89°	15°
(0,1)	248°/11°	132°/63°	343°/23°	0.75	21°	68°	171°	114°	82°	21°
(0,2)	246°/11°	123°/70°	340°/16°	0.71	22°	73°	176°	112°	86°	17°
(1,2)	244°/5°	99°/78°	337°/6°	0.41	20°	80°	-177°	290°	87°	-9°
(1,3)	242°/13°	82°/84°	335°/1°	0.45	19°	86°	-177°	289°	87°	-4°
(2,3)	248°/13°	10°/67°	152°/18°	0.47	290°	67°	4°	198°	86°	157°

Table 1: Stress inversion results and representative focal mechanisms corresponding to the optimal principal stress axes for each grid point of our study area.

Summary and Conclusions

An effort has been exerted to detail the third–order stress field patterns that dominate the area of central Ionian Islands, the most seismically active part of the broader Aegean area drawing significant interest for its seismotectonic properties. Taking advantage of the wealth of data provided by the rigorous scientific work done on the region, we find consistent stress field characteristics, typical of dextral strike – slip stress regime. Relative stress magnitude

values for each subarea, point towards a notable extensional component to the northern parts of our study area, corresponding to the Lefkada KTFZ fault segments and the extensional duplex zone that connects the southern and northern KTFZ branches, whereas evidencing a transition towards a more transpressional regime towards the Kefalonia branch to the south. Nevertheless, the study area is dominated by the strike–slip fault motions of the KTFZ, indicated by the maximum compression axis being equal to the SH_{max} while the intermediate stress axis plunging steeply in every grid point.

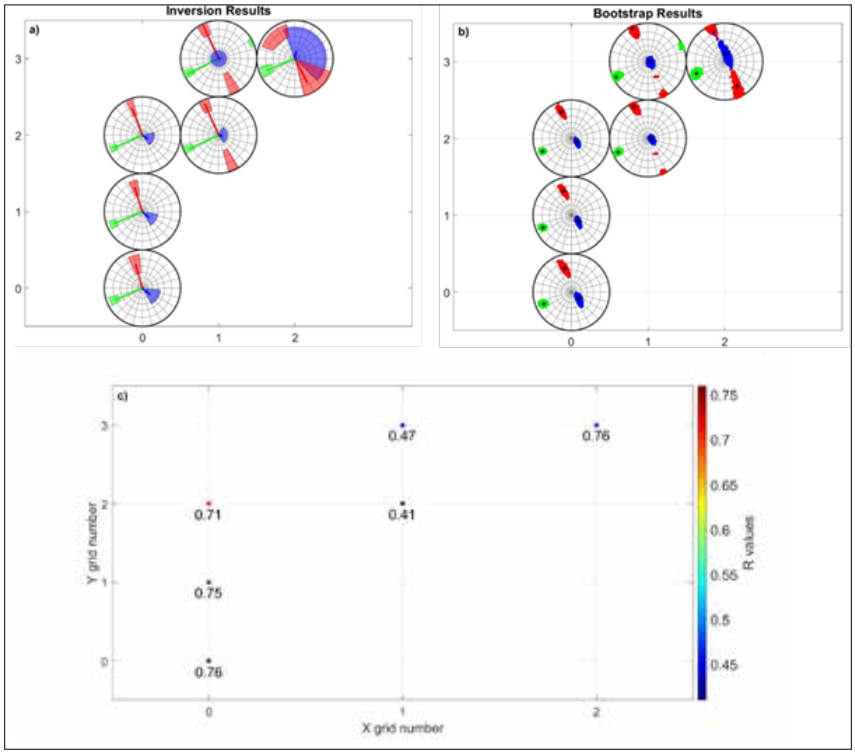

Figure 2: a) Inversion results for the 6 grid points of our study area. Optimal solutions for trend and plunge of the principal stress components σ_1, σ_2, σ_3 (colored green, blue and red, respectively) plotted on Wulff stereographic projection plots, each corresponding to a numbered subarea, according to Table 1. The respective colored areas denote the axes uncertainties in plunge and trend. b) Same as a, but presenting the trend and plunge scatter of the principal stress axes, after 2000 bootstrap resamplings for 95% confidence interval. Black crosses denote the optimal solution for each axis. c) Relative Stress Magnitudes for each of the 6 grid points

Acknowledgements

This research is partially financially supported by the artEmis Project funded by the European Union, under Grant Agreement nr 101061712. The views and opinions expressed are, however, those of the author(s) only and do not necessarily reflect those of the European Union or European Commission–Euratom. Neither the European Union nor the granting authority can be held responsible for them.

References

Hardebeck, J. L., & Michael, A. J. (2006). Damped regional□scale stress inversions: Methodology and examples for southern California and the Coalinga aftershock sequence. *Journal of Geophysical Research: Solid Earth*, *111*(B11). https://doi.org/10.1029/2005JB004144

Hergert, T., & Heidbach, O. (2011). Geomechanical model of the Marmara Sea region—II. 3-D contemporary background stress field. *Geophysical Journal International*, *185*(3), 1090-1102. https://doi.org/10.1111/j.1365-246X.2011.04992.x

Kapetanidis, V., & Kassaras, I. (2019). Contemporary crustal stress of the Greek region deduced from earthquake focal mechanisms. *Journal of Geodynamics*, *123*, 55-82. https://doi.org/10.1016/j.jog.2018.11.004

Karakostas, V. (2004). Properties of the 2003 Lefkada, Ionian Islands, Greece, Earthquake Seismic Sequence and Seismicity Triggering. *Bulletin of the Seismological Society of America*, 94(5), 1976–1981. https://doi.org/10.1785/012003254

Karakostas, V., Papadimitriou, E., Mesimeri, M., Gkarlaouni, C., & Paradisopoulou, P. (2015). The 2014 Kefalonia doublet (Mw 6.1 and Mw 6.0), central Ionian Islands, Greece: Seismotectonic implications along the Kefalonia transform fault zone. *Acta Geophysica*, *63*, 1-16. https://doi.org/10.2478/s11600-014-0227-4

Kourouklas, C., Papadimitriou, E., & Karakostas, V. (2023). Long-Term Recurrence Pattern and Stress Transfer along the Kefalonia Transform Fault Zone (KTFZ), Greece: Implications in Seismic Hazard Evaluation. *Geosciences*, *13*(10), 295. https://doi.org/10.3390/geosciences13100295

Martínez-Garzón, P., Kwiatek, G., Ickrath, M., & Bohnhoff, M. (2014). MSATSI: A MATLAB package for stress inversion combining solid classic methodology, a new simplified user□handling, and a visualization tool. *Seismological Research Letters*, *85*(4), 896-904. https://doi.org/10.1785/0220130189

Papadimitriou, E. E. (2002). Mode of Strong Earthquake Recurrence in the Central Ionian Islands (Greece): Possible Triggering due to Coulomb Stress Changes Generated by the Occurrence of Previous Strong Shocks. *Bulletin of the Seismological Society of America*, 92(8), 3293–3308. https://doi.org/10.1785/0120000290

Scordilis, E. M., Karakaisis, G. F., Karacostas, B. G., Panagiotopoulos, D. G., Comninakis, P. E., & Papazachos, B. C. (1985). Evidence for transform faulting in the Ionian Sea: The Cephalonia Island earthquake sequence of 1983. *Pure and Applied Geophysics*, 123(3), 388–397. https://doi.org/10.1007/BF00880738

Zoback, M. L. (1992), First- and second-order patterns of stress in the lithosphere: The World Stress Map Project, *J. Geophys. Res.*, 97(B8), 11703–11728, doi:10.1029/92JB00132

Data Sources

Benetatos, C., Kiratzi, A., Papazachos, C., & Karakaisis, G. (2004). Focal mechanisms of shallow and intermediate depth earthquakes along the Hellenic Arc. *Journal of Geodynamics*, *37*(2), 253–296. https://doi.org/10.1016/j.jog.2004.02.002

Benetatos, C., Kiratzi, A., Roumelioti, Z., Stavrakakis, G., Drakatos, G., & Latoussakis, I. (2005). The 14 August 2003 Lefkada Island (Greece) earthquake: Focal mechanisms of the mainshock and of the aftershock sequence. *Journal of Seismology*, *9*(2), 171–190. https://doi.org/10.1007/s10950-005-7092-1

Ekström, G., Nettles, M., & Dziewoński, A. M. (2012). The global CMT project 2004–2010: Centroid-moment tensors for 13,017 earthquakes. *Physics of the Earth and Planetary Interiors*, *200–201*, 1–9. https://doi.org/10.1016/j.pepi.2012.04.002

ETH Zurich. (1986). Swiss Seismological Service (SED). In *National Seismic Networks of Switzerland, ETH Zürich*. https://doi.org/10.12686/sed/networks/ch

GEOFON Data Centre. (1993). GEOFON Seismic Network [Data set]. GFZ Data Services. https://doi.org/10.14470/TR560404

Hatzfeld, D., Kassaras, I., Panagiotopoulos, D., Amorese, D., Makropoulos, K., Karakaisis, G., & Coutant, O. (1995). Microseimicity and strain pattern in northwestern Greece. *Tectonics*, *14*(4), 773–785. https://doi.org/10.1029/95TC00839

National Observatory of Athens, Institute of Geodynamics, Athens. (1975). *National Observatory of Athens Seismic Network* [Data set]. International Federation of Digital Seismograph Networks. https://doi.org/10.7914/SN/HL

Karakostas, V., & Papadimitriou, E. (2010). Fault complexity associated with the 14 August 2003 Mw6.2 Lefkada, Greece, aftershock sequence. *Acta Geophysica*, *58*(5), 838–854. https://doi.org/10.2478/s11600-010-0009-6

Kostoglou, A., Karakostas, V., Bountzis, P., & Papadimitriou, E. (2020). The February-March 2019 seismic swarm offshore north Lefkada Island, Greece: Microseismicity analysis and geodynamic implications. *Applied Sciences (Switzerland)*, *10*(13). https://doi.org/10.3390/app10134491

Louvari, E., Kiratzi, A. A., & Papazachos, B. C. (1999). The Cephalonia transform fault and its extension to western Lefkada Island (Greece). *Tectonophysics*, *308*(1-2), 223-236. https://doi.org/10.1016/S0040-1951(99)00078-5

Papadimitriou, E., Karakostas, V., Mesimeri, M., Chouliaras, G., & Kourouklas, C. (2017). The Mw6.5 17 November 2015 Lefkada (Greece) Earthquake: Structural Interpretation by Means of the Aftershock Analysis. *Pure and Applied Geophysics*, *174*(10), 3869–3888. https://doi.org/10.1007/s00024-017-1601-3

Pondrelli, S., Morelli, A., & Ekström, G. (2004). European-Mediterranean regional centroid-moment tensor catalog: solutions for years 2001 and 2002. *Physics of the Earth and Planetary Interiors*, *145*(1–4), 127–147. https://doi.org/10.1016/J.PEPI.2004.03.008

Pondrelli, S., Salimbeni, S., Morelli, A., Ekström, G., & Boschi, E. (2007). European–Mediterranean Regional Centroid Moment Tensor catalog: Solutions for years 2003 and 2004. *Physics of the Earth and Planetary Interiors*, *164*(1–2), 90–112. https://doi.org/10.1016/J.PEPI.2007.05.004

Pondrelli, S., Salimbeni, S., Morelli, A., Ekström, G., Postpischl, L., Vannucci, G., & Boschi, E. (2011). European–Mediterranean Regional Centroid Moment Tensor catalog: Solutions for 2005–2008. *Physics of the Earth and Planetary Interiors*, *185*(3–4), 74–81. https://doi.org/10.1016/J.PEPI.2011.01.007

17th INTERNATIONAL CONGRESS
of the Geological Society of Greece

BULLETIN OF THE GEOLOGICAL SOCIETY OF GREECE, SP. PUBL.

EXTENDED ABSTRACT 005

Flood events over the past 115 years in the Municipality of Patras, southern Greece

Andriopoulou Mounteanou S.A.[1], Bathrellos G.D.[1], Skilodimou H.D.[1]
(1) University of Patras, Greece, geo13014@ac.upatras.gr

Introduction

Natural hazards are physical phenomena that can cause substantial harm to both the natural world and human environments. These hazards arise from endogenic or exogenic processes, such as tectonic activity or climate change, which can alter landforms and influence natural hazards, often directly affecting human activities (Migiros *et al.,* 2011, Kamberis *et al.,* 2012, Skilodimou *et al.,* 2014, Kokinou *et al.,* 2015, Bathrellos *et al.,* 2017, Bathrellos *et al.,* 2018).

Floods are natural events that have occurred throughout geological history, resulting from excessive surface runoff. Floodplains are formed through sediment deposition when rivers overflow their banks. They are considered favorable locations for human settlement due to their fertile soils, flat terrain, ease of excavation, and proximity to water sources. These advantages have encouraged the development and urbanization of floodplains, leading to an increase in flood-related disasters. Despite efforts to mitigate flooding through structures like dams, levees, and river channeling, the damage caused by floods continues to rise (Bathrellos and Skilodimou, 2006, Bathrellos, 2007, Skilodimou *et al.,* 2024).

Floods are a common occurrence in certain regions of the world. In urban settings floods are among the most hazardous natural events. The impacts of flooding extend beyond environmental damage, encompassing social and economic consequences as well. Floods can harm urban infrastructure and agricultural lands, and in severe cases, they can even result in the loss of human lives (Bathrellos *et al.,* 2016).

Between 2000 and 2024, there have been more than 400 major floods, including several catastrophic events floods that affected over 1.9 million people in Europe, claiming more than 2,000 lives and causing economic losses estimated at over 70 billion Euros (EM-DAT, 2024). Flooding is a frequent natural hazard in Greece, with numerous severe events occurring over the 25 years. These floods have led to the tragic loss of over 72 lives and caused extensive damage to properties, buildings, infrastructure, and the environment. Their effects have significantly disrupted both the national and rural economies with the financial impact surpassing 1 billion (Skilodimou *et al.,* 2021, EEA, 2024).

Objectives

This study highlights the flood events and their impacts in the Municipality of Patras from 1909 to 2024. In detail, the study explores the hydrological basins of the rivers within the study area, the occurrences of flooding, the regions impacted, and the damage inflicted on the urban infrastructure, particularly focusing on buildings. Furthermore, the study analyzes the occurrence of floods in particular areas and establishes a correlation between the impacted regions and the damaged structures.

Study area

The study area (Fig. 1A) includes the drainage basins of the Glafkos, Diakoniaris, Meilichos, Haradros and Selemnos river located in the northern Peloponnese region of southern Greece (Fig. 1B). These rivers discharge into the Gulf of Patras. The areas of the drainage basins are as follows: Glafkos River covers 108.5 km², Diakoniaris River spans 26.5 km², Meilichos River encompasses 22 km², Haradros River covers 25 km², and Selemnos River occupies 17.8 km², resulting in a total combined area of 199.8 km².

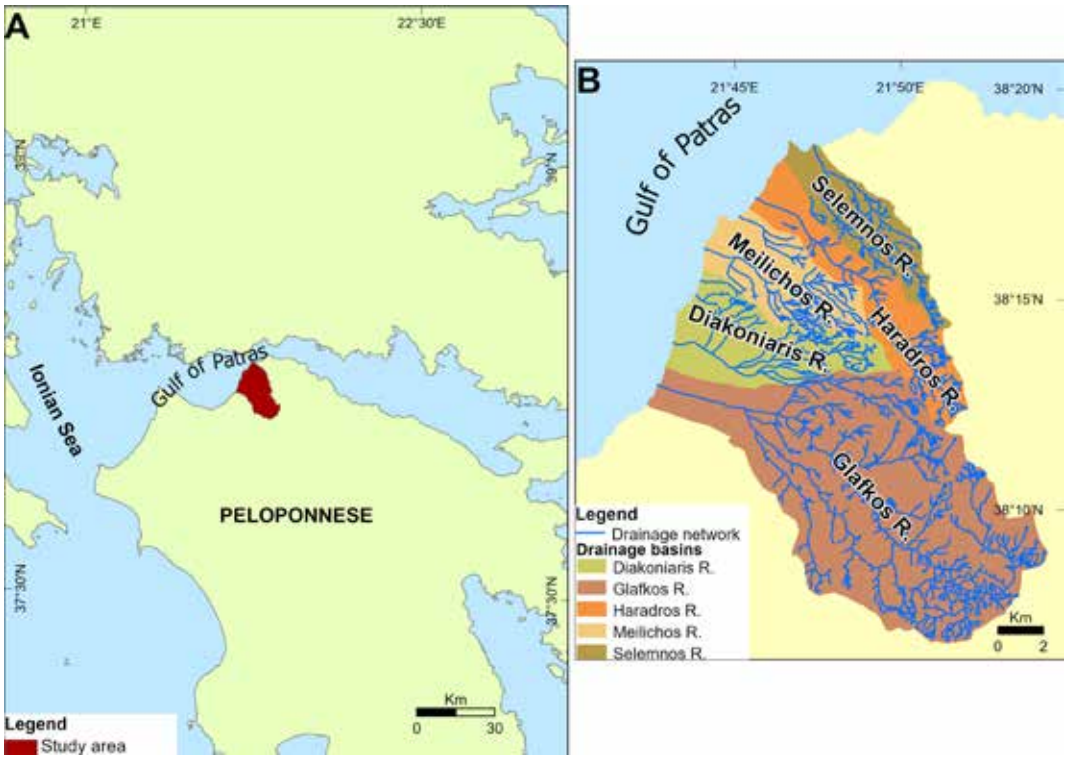

Figure 1. (A) Location map of the study area, (B) a map of the drainage networks and basins of the study area.

Methodology - Data

The data collected in the context of the current research were:

- Collection data from online sources (Ministry of Environment and Energy, 2017, METEO, 2024).
- Fact-checking the provided information and gathering additional details (UEDNPEI, 2014).

This study focused on key elements such as the flood locations, dates of occurrence, extent of the flooded area, types of damages, and the total damage caused by each flood event.

The data collection was initially carried out by consulting meteo.gr, which provides material on floods that have occurred between 2000 and 2024. Additional information, like the number of flooded buildings and the districts that these events occurred, was gathered from local newspapers. Following this, a search was performed on the official Press Museum website using filters and keyword searches to identify older flood events. The affected areas were determined from this data, and Google Earth was utilized for detailed calculations of the impacted regions. Thematic maps were then generated using ArcGIS Pro.

A temporal statistical analysis was performed to determine the number of events, the flooded area (in km^2), the number of affected buildings, and human casualties impacted by floods throughout the 115-year period. The frequency of flood occurrences in each district of Patras during this period was analyzed. Furthermore, data from Urban Atlas 2018 (Copernicus, Urban Atlas 2018, 2021) were used to evaluate the extent of the urban structure and to calculate the Building Cover Ratio (BCR) impacted by flooding.

Results

A total number of 20 flood events were recorded in the drainage basins of the Glafkos, Diakoniaris, Meilichos, Haradros and Selemnos rivers. Table 1 outlines the year in which floods occurred and the corresponding river, the affected area and the specific districts, the number of impacted buildings, and the human casualties. Over the 115-year period, there was only one instance of human casualties, occurring in 2001, which resulted in the loss of two lives.

Table 1. Classes of the year of the flood event, river that contributed for the phenomenon, flooded area, number of buildings that were casualties and people that lost their life

YEAR	RIVER	AREA (km2)	AFFECTED DISTRICTS	FLOODED BUILDINGS
1909	DIAKONIARIS	0.28	PSAROFAI, GIROKOMIO	40
1917	GLAFKOS	0.12	LEFKA	0
1927	GLAFKOS-HARADROS	1.12	MPOZAITIKA, KASTELOKAMPOS, MPEGOULAKI, ITIES	80
1931	GLAFKOS	0.24	ITIES, KRIA ITEON	25
1935	GLAFKOS	0.13	ITIES, KRIA ITEON	20
1940	DIAKONIARIS	0.62	AG. AIKATERINI, AG. PARASKEVI, TASI, GIROKOMIO, VILLA LADOPOULOU, AG. IOANNIS PRATSIKA	100
1956	DIAKONIARIS - GLAFKOS	2.03	MPEGOULAKI, PSAROFAI, AG. GEORGIOS LAGOURA, ZAROUCHLEIKA, AG. IOANNIS PRATSIKA, LAGOURA, AG. AIKATERINI, ITIES, KRIA ITEON	250
1959	HARADROS	0.22	SKAGIOPOULIO	100
1960	GLAFKOS	0.03	ITIES	0
1962	DIAKONIARIS - GLAFKOS-MEILICHOS - HARADROS-SELEMNOS	3.25	EGLIKADA, AG. AIKATERINI, AG. IOANNIS PRATSIKA, ITIES, AGYIA, AG. GEORGIOS LAGOURA, PSAROFAI, PROASTIO, SKAGIOPOULIO	4,000
1965	GLAFKOS	0.06	ITIES, KRIA ITEON	25
1997	DIAKONIARIS	3.01	EGLIKADA, AG. AIKATERINI, AG. IOANNIS PRATSIKA, AG. GEORGIOS, LAGOURA, PSAROFAI, GIROKOMIO	1,500
2001	DIAKONIARIS	0.28	ZAROUCHLEIKA	150
2002	DIAKONIARIS	0.01	CENTER	2
2013	MEILICHOS	0.05	AGYIA	0
2021	MEILICHOS	0.21	VOUTENI, KOTRONI	40
2024	GLAFKOS	0.01	ITIES	0

The Municipality of Patras consists of just over 50 districts, with this study focusing on the main districts, including and those that have experienced flooding.

Figure 2 depicts the drainage basins of the Glafkos, Diakoniaris, Meilichos, Haradros, and Selemnos rivers, along with the spatial distribution of flooded areas across each district and drainage basin. Notably, in the Diakoniaris River basin, the flooded area results from multiple flood events over different years. This basin has the largest flooded area, covering approximately 3 km². It also exhibits the highest level of urban development among the studied hydrological basins and has experienced a significant number of flood events. In contrast, the Selemnos River basin has the smallest flooded area.

Figure 3 illustrates the number of flood events across various districts in Patras. Ities has the highest frequency, with six flooding events, making it the most affected district in Patras, other significantly affected districts include Psarofai (4 flooding events), Ag. Aikaterini, Girokomio, Kria Iteon and several others with 3 events each. Many regions, including Ketes and Anthoupoli recorded only one flooding event. Some, appear to have no significant recorded flooding frequency, indicated by the absence of bars. Notably, 40% of the districts have been affected by flooding multiple times emphasizing the recurrent nature of the issue.

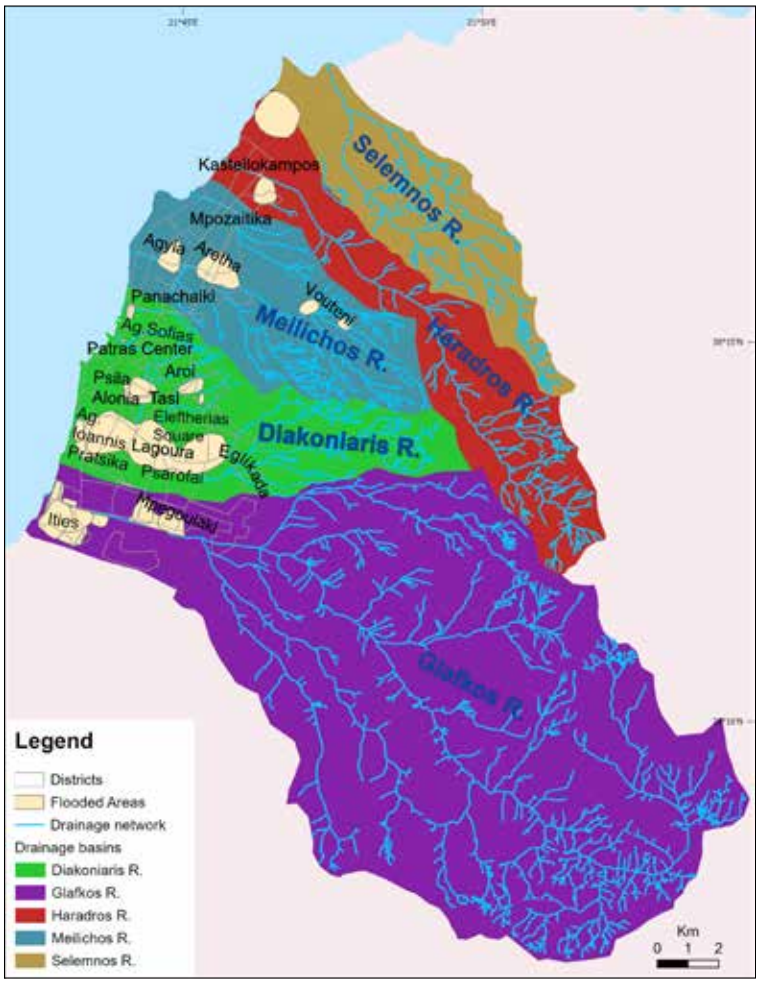

Figure 2. Map of Patras with districts, drainage basins and networks as well as flooded areas.

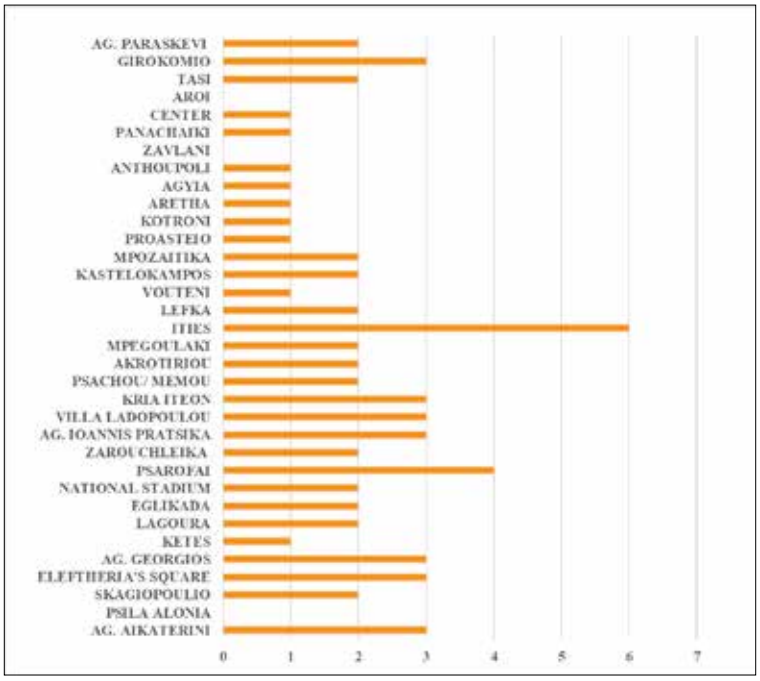

Figure 3. The number of flood events in the districts of Patras.

Figure 4 illustrates the impact of flooding on the Building Cover Ratio (BCR) over the past 115 years. When analyzed alongside the data in Table 1, a clear correlation emerges between the BCR, the extent of the flooded area, and the number of affected buildings in specific years.

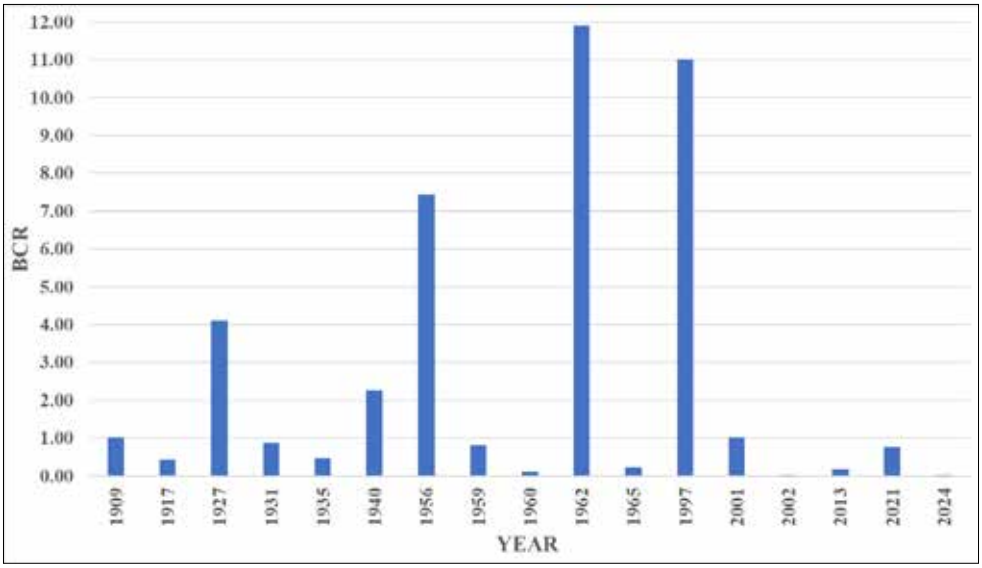

Figure 4. The Building Cover Ratio (BCR) affected by flood over the past 115 years.

Notably, in 1927, the BCR reached a high value of 4.1, which coincided with a significant flooded area of 1.12 km² and a large number of flooded buildings (80). Moreover, in 1956, the BCR was recorded at 7.43, indicating a significant flooding event, with the flooded area extending to 2.03 km² and the number of affected buildings reaching 250, both at considerable levels. In 1962, the BCR reached its peak value of 11.90, corresponding to the largest flooded area of 3.25 km² and the highest number of affected buildings (4,000), marking one of the most catastrophic floods recorded._Similarly, in 1997, the BCR (11.09) was nearly at its peak, corresponding to the flooded area of 3.01 km² and a significant number of affected buildings (1,500). The buildings affected by floods mainly involve basements and ground-floor structures.

Conclusions and discussion

The study of flood events in Patras reveals significant insights into the frequency, impact, and trends over the past 115 years. A total of 20 flooding events were recorded within the drainage basins of Glafkos, Diakoniaris, Meilichos, Haradros, and Selemnos rivers, affecting various districts of Patras.

The year 1962 stands out as the most catastrophic flooding event, followed by 1956 and 1997, with both the flooded area and the number of affected buildings reaching their highest levels. These years highlight the direct relationship between the extent of the flooded area and the resulting damage to infrastructure. While 2001 is the only recorded year with human casualties, emphasizing the severity of the event despite a subsequent reduction in flooded areas.

Ities is identified as the most flood-prone district in Patras, with six recorded flooding events, making it the most severely impacted area. It is worth mentioning, 40% of the regions have experienced flooding more than once, emphasizing the widespread and recurrent nature of the issue.

A distinct relationship is observed between the BCR, the size of the flooded area, and the number of flooded buildings in particular years. The peak BCR of 11.90 was recorded in 1962, coinciding with the largest flooded area of 3.25 km² and the highest number of flooded buildings (4,000).

References

Bathrellos, G., Skilodimou, H., 2006. Geomorphic Hazards and Disasters. Bull. Geol. Soc. Greece, 39 (3), 96–103.

Bathrellos, G.D., 2007. An overview in Urban Geology and Urban Geomorphology. Bull. Geol. Soc. Greece, 40 (3), 1354–1364.

Bathrellos, G.D.; Karymbalis, E.; Skilodimou, H.D.; Gaki-Papanastassiou, K.; Baltas, E.A., 2016. Urban flood hazard assessment in the basin of Athens Metropolitan city, Greece. Environ Earth Sciences, 75(4), 319.

Bathrellos, G.D.; Skilodimou, H.D.; Maroukian, H.; Gaki Papanastassiou, K.; Kouli, K.; Tsourou, T.; Tsaparas, N., 2017. Pleistocene glacial and lacustrine activity in the southern part of Mount Olympus (central Greece). Area, 49 (2), 137-147.

Bathrellos, G. D., Skilodimou, H. D., Soukis, K., Koskeridou, E., 2018. Temporal and spatial analysis of flood occurrences in the drainage basin of pinios river (thessaly, central greece). Land, 7(3), 106.

Copernicus. Urban Atlas 2018. Copernicus Land Monitoring Service, 2021 Available at https://land.copernicus.eu/local/urban-atlas/urban-atlas-2018.

EEA (European Environment Agency), 2024. Economic losses from weather- and climate-related extremes in Europe. Available online: https://www.eea.europa.eu/en.

EM-DAT, 2024. The International Disaster Database. Center for Research on Epidemiology of Disasters. Available online: https://www.emdat.be/ (accessed on 02 December 2024).

Kamberis, E., Bathrellos, G., Kokinou, E., & Skilodimou, H., 2012. Correlation between the structural pattern and the development of the hydrographic network in a portion of the Western Thessaly Basin (Greece). Open Geosciences, 4(3), 416-424.

Kokinou, E.; Skilodimou, H.D.; Bathrellos, G.D.; Antonarakou, A.; Kamberis, E., 2015. Morphotectonic analysis, structural evolution/pattern of a contractional ridge: Giouchtas Mt., Central Crete, Greece. Journal of Earth System Science, 124(3), 587-602.

METEO, 2024. All about weather. Available online: https://www.meteo.gr/weather_cases.cfm (accessed on 22 January 2024).

Migiros, G., Bathrellos, G. D., Skilodimou, H. D., Karamousalis, T. 2011. Pinios (Peneus) River (Central Greece): hydrological—geomorphological elements and changes during the quaternary. Central European Journal of Geosciences, 3, 215-228.

Ministry of Environment and Energy, 2017. Special secretariat for water. Floods, Historic floods., Available online: http://www.ypeka.gr/Default.aspx?tabid=252&language=el-GR (accessed on 03 January 2024).

UEDNPEI, 2014. Press Museum of the Union of Editors of Daily Newspapers of the Peloponnese, Epirus, and the Islands (UEDNPEI). Available online: http://www.mouseiotipou.gr/ (accessed on 10 January 2024).

Skilodimou, H.D.; Bathrellos, G.D.; Maroukian, H.; Gaki-Papanastassiou K., 2014. Late Quaternary evolution of the lower reaches of Ziliana stream in south Mt. Olympus (Greece). Geogr. Fis. Din. Quat. 2014, 37 (1), 43-50.

Skilodimou, H.D., Bathrellos, G.D., Alexakis, D.E., 2021. Flood Hazard Assessment Mapping in Burned and Urban Areas, Sustainability, 13 (8), 4455.

Skilodimou, H. D., Bathrellos, G. D., Pappa, M. I., Youssef, A. M., Kontakiotis, G., Karymbalis, E., 2024. Assessing flood hazard mapping using AHP and GIS in a tectonically active region. Zeitschrift für Geomorphologie. Published online.

17th INTERNATIONAL CONGRESS
of the Geological Society of Greece

BULLETIN OF THE GEOLOGICAL SOCIETY OF GREECE, SP. PUBL.

EXTENDED ABSTRACT 006

HOMEROS project for natural hazards: An example from northern Peloponnese, Greece

Andriopoulou-Mounteanou S.A.[1], Bathrellos G.D.[1], Skilodimou H.D.[1], Adamaki A.[2], Anagnostou V.[3], Bitharis S.[3], Bonatis P.[3], Foumelis M.[3], Karakostas V.[3], Karolos I. A.[3], Kaviris G.[4], Kourouklas C.[3], Papadimitriou E.[3], Papageorgiou E.[3], Pikridas C.[3], Sakkas V.[4], Spingos I.[4], Zymvragakis A.[3]

(1) University of Patras, Patras, Greece, geo13014@ac.upatras.gr (2) Lund University, Lund, Sweden, (3) Aristotle University of Thessaloniki, Thessaloniki, Greece, (4) National & Kapodistrian University of Athens, Athens, Greece.

Background

Natural phenomena such as earthquakes, floods, and landslides, which appear throughout geological history, are now classified as natural hazards. These events pose significant risk to human safety on a global scale (Bathrellos and Skilodimou, 2006). Effective planning is essential for minimizing loss of life and reducing the economic impact of these hazards (Bathrellos *et al.,* 2024). Accurate information on the spatial distribution of natural hazards serves as a crucial resource for environmental planners and engineers, helping them identify suitable sites for land use and development (Bathrellos and Skilodimou, 2019).

Natural hazards are complex phenomena, and most published studies have focused on in-depth analyses of individual hazard types (Bathrellos *et al.,* 2016, Karpouza *et al.,* 2021, Skilodimou *et al.,* 2021, Youssef *et al.,* 2024). However, a particular area is rarely affected by only one hazard; instead, multiple hazards may occur simultaneously or consecutively. In such cases, managing separate hazard zones for each type of disaster becomes impractical, especially when multiple hazards must be considered (Bathrellos *et al.,* 2021, Karpouza *et al.,* 2023). The solution to this challenge lies in adopting a multi-hazard analysis, which allows for a comprehensive assessment of various hazard types. Multi-hazard analysis is an essential tool for selecting appropriate land uses and evaluating the vulnerability and risk of urban areas. It plays a critical role in mitigating natural hazards and managing urban disasters (Karpouza *et al.,* 2024).

Objectives

In this context, the HOMEROS project focuses on enhancing multi-hazard assessment approaches within the fields of seismology, geodesy, geology, geomorphology and engineering geology. It utilizes technical solutions tailored to the big data era, marking a major step forward in standardizing research methodologies, fostering collaboration, and improving the understanding and forecasting of natural hazards through Open Science practices. HOMEROS concentrates on high-hazard regions in Greece, characterized by intense seismic activity, floods, and landslides. It consolidates earthquake, ground deformation, flood, and landslide data to offer a comprehensive assessment of these hazards.

This paper provides data and results from the program related to flood events and the production of flood hazard assessment maps in the northern Peloponnese. This work represents an early example of the findings from the HOMEROS project, stemming from the collaboration between the University of Patras, Lund University, Aristotle University of Thessaloniki, and the National and Kapodistrian University of Athens.

Study area

The study area includes the drainage basins of the Xerias, Phoenix, and Peneus rivers, located in the northern Peloponnese region of southern Greece (Fig. 1). The Xerias drainage basin spans 170 km² with a predominantly north-south elongated shape. Similarly, the Phoenix River basin covers around 94 km² and exhibits a southwest-to-northeast elongated orientation. Both river systems drain into the Gulf of Corinth. In contrast, the Peneus River drainage basin, occupying an area of approximately 900 km², extends in an east-west direction. It flows westward and discharges into the Ionian Sea (Fig. 1).

Methods

HOMEROS adopts an innovative approach by leveraging existing data and services from e-science gateways and platforms at multiple levels (national, research infrastructures, or scientific clusters), as well as external resources like Copernicus. It emphasizes the application of FAIR principles in research to deliver new open-access data products.

In this context, data from existing scientific publications were utilized to implement the project. Specifically, HOMEROS incorporated documented flood events that occurred for the period from 1920 to 2021, in the drainage basins of the Xerias, Phoenix, and Peneus rivers (Fig. 2), as reported by Bathrellos *et al.* (2017), Skilodimou *et al.* (2024) and Skilodimou *et al.* (2019), respectively. Additionally, it utilized information from these works concerning the applied methodologies and flood hazard assessment maps.

Figure 1. The study area comprises the drainage basins of the Xerias, Phoenix, and Peneus rivers.

Five key factors have been identified as the most significant in influencing flood events. These factors include slope, elevation, hydro-lithology, distance to streams, and land use. The Analytical Hierarchy Process (AHP) was integrated with Geographic Information System (GIS) to facilitate the assessment of the chosen factors employed in the production of the flood hazard assessment maps.

Figure 2. Flood events in the drainage basins of the Xerias, Phoenix, and Peneus rivers.

Results

The recorded number of past flood events for each drainage basin is as follows: ten for the Xerias River, eleven for the Phoenix River, and eight for the Peneus River.

The flood hazard assessment maps for the three drainage basins were categorized into five levels of flood hazard: very low, low, moderate, high, and very high (Bathrellos et al., 2016, Skilodimou et al., 2021). As stated by Bathrellos *et al.* (2017), the northern and central regions of the Xerias drainage basin have the most extensive coverage of very high and high flood hazard zones. The moderate hazard zone is primarily located in the northeastern and central parts of the basin, whereas the low and very low hazard zones are concentrated in the southern region (Fig. 3).

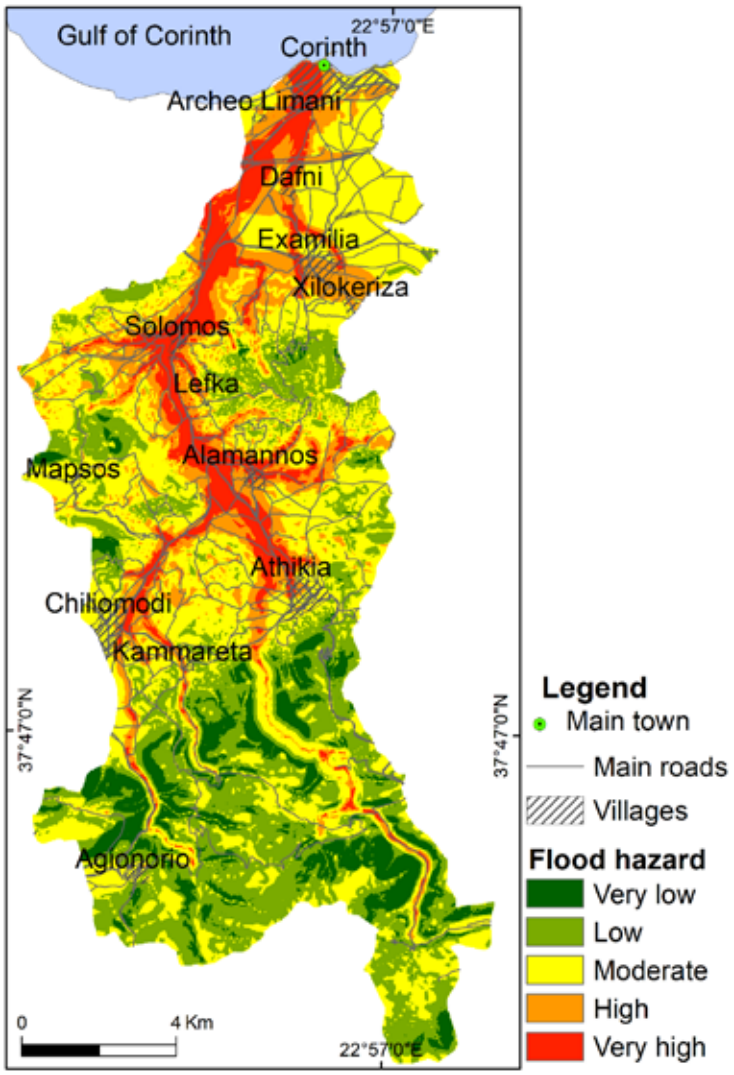

Figure 3. The flood hazard assessment map in the drainage basin of the Xerias River.

The high and very high hazard zones are mainly located along the mainstream of the Xerias drainage network and at the points where it intersects with major tributaries. Notably, most of the recorded flood events in the study area occur within the very high and high flood hazard zones. The lowland terrain, gentle slopes, presence of impermeable formations, and urbanization of these areas contribute to increased surface runoff, creating conditions that are more prone to flooding.

According to Skilodimou *et al.* (2024), the very high and high flood hazard zones are mainly found in the northern and central parts of the Phoenix drainage basin, along the mainstream channel of the drainage network. The moderate hazard zone is largely concentrated in the central area, extending into the northern, western, and southern areas. In contrast, the southern, western, and eastern parts of the study area include many locations within the low and very low hazard zones (Fig. 4).

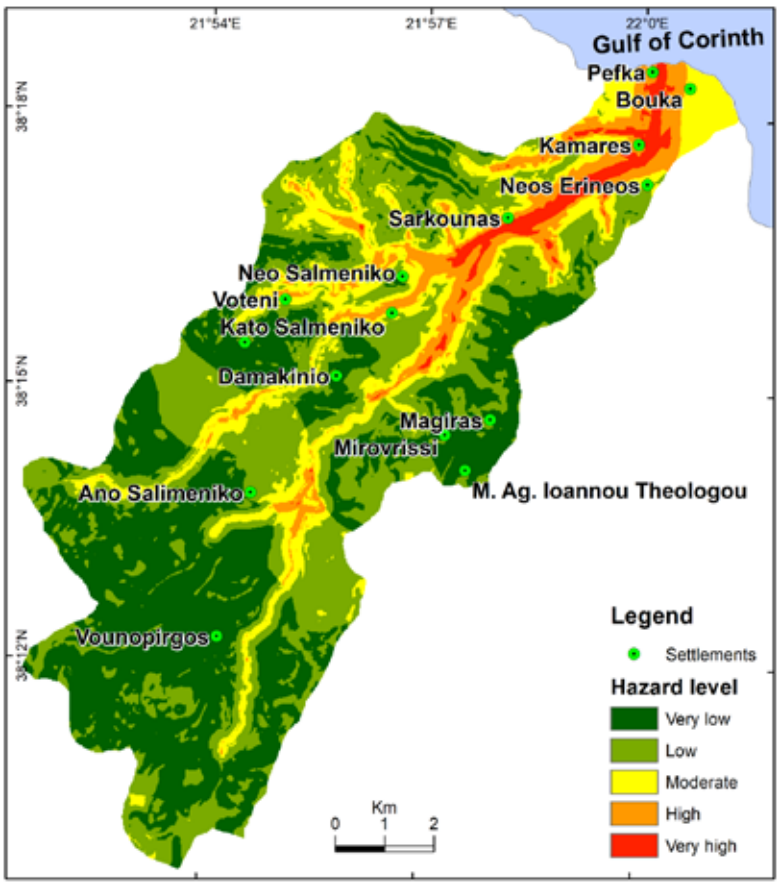

Figure 4. The flood hazard assessment map in the drainage basin of the Phoenix River.

The relatively small size of the Phoenix River drainage basin, along with its ephemeral streams, plays a key role in influencing flood events within the study area. Furthermore, the constricted artificial riverbed in the river's downstream sections, caused by agricultural and urban activities, disrupts the river's natural flow patterns and contributes to flooding incidents.

As reported by Skilodimou et al. (2019), the western, northern, and southwestern parts of the Peneus drainage basin include areas most susceptible to flooding, primarily along the mainstream of the Peneus drainage network. The moderate hazard zone is situated in the western and northern sections of the basin, while the low and very low hazard zones are found in the southern and eastern parts of the area (Fig. 5).

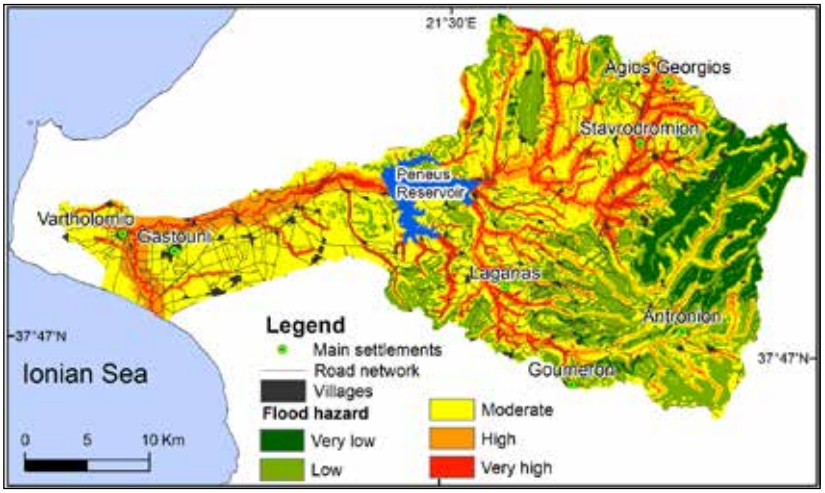

Figure 5. The flood hazard assessment map in the drainage basin of the Peneus River.

Land use changes in areas impacted by extensive fires have contributed to an increase in flood events. Additionally, the constricted artificial riverbed in the lower reaches of the Peneus River, resulting from agricultural land use and urban development, significantly disrupts the natural flow dynamics and exacerbates flooding.
Table 1 displays the percentage of area covered by each flood hazard zone for the Xerias, Phoenix, and Peneus drainage basins.

Table 1. The percentage of area for each flood hazard zone for the Xerias, Phoenix, and Peneus drainage basins.

	Xerias drainage basin	Phoenix drainage basin	Peneus drainage basin
Flood hazard zone	**Area (%)**		
Very low	9	38	8
Low	27	36	24
Moderate	40	16	39
High	15	8	20
Very high	9	2	9

In the Xerias drainage basin, the very high and high flood hazard zones cover a significant portion, making up about one-quarter of the basin. In comparison, the Phoenix drainage basin has a much smaller coverage, with these two zones spanning only 10% of the area. The Peneus drainage basin, however, has the largest extent, with the very high and high hazard zones covering approximately one-third of the basin.

Conclusions

The total number of past flood events across the drainage basins of the Xerias, Phoenix, and Peneus rivers amounts to twenty-nine. The northern and central areas of the Xerias and Phoenix drainage basins are the most flood-prone, while the western, northern, and southwestern regions of the Peneus drainage basin are particularly vulnerable to flooding. Among the three drainage basins, the Peneus drainage basin has the largest areas classified as very high and high flood hazard zones.

The gentle slopes and widespread urban development of the lowland areas in the Xerias drainage basin play a role in flooding. In the downstream sections of the Phoenix River drainage basin, the narrow artificial riverbed, shaped by agricultural and urban activities, also contributes to flooding. Changes in land use in regions affected by extensive fires have led to an increase in flooding events in the Peneus drainage basin.

Acknowledgements

The authors acknowledge the OSCARS project, which has received funding from the European Commission's Horizon Europe Research and Innovation programme under grant agreement No. 10112975.

References

Bathrellos, G., Skilodimou, H., 2006. Geomorphological Hazards and Disasters. Bulletin of the Geological Society of Greece, 39(3), 96-103.

Bathrellos, G.D., Skilodimou, H.D., 2019. Land Use Planning for Natural Hazards. Land, 8(9), 128.

Bathrellos, G.D., Karymbalis, E., Skilodimou, H.D., Gaki-Papanastassiou, K., Baltas, E.A., 2016. Urban flood hazard assessment in the basin of Athens Metropolitan city, Greece. Environmental Earth Sciences, 75(4), 319.

Bathrellos, G. D., Skilodimou, H. D., Chousianitis, K., Youssef, A. M., Pradhan, B., 2017. Suitability estimation for urban development using multi-hazard assessment map. Science of the Total Environment, 575, 119-134.

Bathrellos, G. D., Skilodimou, H. D., Zygouri, V., Koukouvelas, I. K., 2021. Landslide: A recurrent phenomenon? Landslide hazard assessment in mountainous areas of central Greece. Zeitschrift für Geomorphologie, 63, 95-114.

Bathrellos, G. D., Koukouvelas, I. K., Skilodimou, H. D., Nikolakopoulos, K. G., Vgenopoulos, A. L., 2024. Landslide causative factors evaluation using GIS in the tectonically active Glafkos River area, northwestern Peloponnese, Greece. Geomorphology, 109285.

Karpouza, M., Chousianitis, K., Bathrellos, G.D., Skilodimou, H.D., Kaviris, G., Antonarakou, A., 2021. Hazard zonation mapping of earthquake-induced secondary effects using spatial multi-criteria analysis. Natural Hazards, 109, 637-669.

Karpouza, M., Bathrellos, G. D., Kaviris, G., Antonarakou, A., Skilodimou, H. D., 2023. How could students be safe during flood and tsunami events? International Journal of Disaster Risk Reduction, 95, 103830.

Karpouza, M., Skilodimou, H. D., Kaviris, G., Zymvragakis, A., Antonarakou, A., Bathrellos, G. D., 2024. Escape routes and safe points in natural hazards. A case study for soil. Engineering Geology, 340, 107683.

Skilodimou, H.D., Bathrellos, G.D., Chousianitis, K., Youssef, A.M., Pradhan, B., 2019. Multi-hazard assessment modeling via multi-criteria analysis and GIS: A case study. Environmental Earth Sciences, 78(2), 47.

Skilodimou, H. D., Bathrellos, G. D., Alexakis, D. E., 2021. Flood hazard assessment mapping in burned and urban areas. Sustainability, 13(8), 4455.

Skilodimou, H. D., Bathrellos, G. D., Pappa, M. I., Youssef, A. M., Kontakiotis, G., Karymbalis, E., 2024. Assessing flood hazard mapping using AHP and GIS in a tectonically active region. Zeitschrift für Geomorphologie. Published online.

Youssef, A.M., El-Haddad, B.A., Skilodimou, H.D. Bathrellos, G. D., Golkar, F., Pourghasemi, H. R., 2024. Landslide susceptibility, ensemble machine learning, and accuracy methods in the southern Sinai Peninsula, Egypt: Assessment and Mapping. Natural Hazards 120, 14227–14258.

17th INTERNATIONAL CONGRESS of the Geological Society of Greece

BULLETIN OF THE GEOLOGICAL SOCIETY OF GREECE, SP. PUBL.

EXTENDED ABSTRACT 007

Digital Visualization of Geological Heritage at Lesvos UNESCO Global Geopark: The Role of 3D Animations in Educational Experiences

Antonakis Emmanouil 1, Nicholas Zouros 2
(1) University of the Aegean, Mytilene, Greece, manolis.antonakis@rocketmail.com (2) University of the Aegean, Mytilene, Greece

Introduction / Background

In this paper, we use 3D animation technologies to visualize, interpret and communicate geological heritage in Lesvos UNESCO Global Geopark. Our objective is to make geological heritage more accessible to the general public. 3D animations have been utilized as a means to periodically monitor and document changes in geological sites over time, supporting conservation initiatives. Additionally, they can replicate geological events, describe the formation and evolution of landscapes, simulate how we believe paleoenvironments looked for a holistic learning experience. Their interactive and dynamic nature can boost engagement and facilitate learning in an educational context, while it can also engage tourists by offering previews, virtual tours of inaccessible or fragile sites. In this paper, we select 21 case studies of geosites or monuments of geological heritage to 3D geo-visualize. The selection method is based on three criteria: accessibility, supervision and relief of the geosite out of the total number of 151 designated geosites of the Geopark. The results were verified with a pilot study to participants of environment educational programs in the Natural History Museum of Lesvos Petrified Forest in 2024. . Overall, the approach promotes visitor democracy, as all groups have access to the visualized geosites and can be used to further improve the visibility of the geosites and that of the Geopark.

Objectives

In this paper, we use 3D animation technologies to visualize, interpret and communicate geological heritage of Lesvos UNESCO Global Geopark. Our objective is to make geological heritage more accessible to the general public.

Methodology

This research included the creation of 3D animation in Google Earth Studio to introduce the most important geosites within Lesvos UNESCO Global Geopark, it was divided into four topics: geosite selection, data collection and preparation, animation creation and visualizations evaluation. The main goal is to use these 3D animations in educational activities for students and non-experts.

Selection of Geosites:

The first phase involved identifying key geosites within the Lesvos UNESCO Global Geopark that would benefit from enhanced visual representation. Criteria for selection included accessibility of Geosite, Supervision of the location of the geosite,, and The topography of a geosite's location. Key sites, such as volcanic formations, petrified parks, and notable tectonic features, were chosen to highlight the geological diversity of the region.

Data Collection and Preparation:

for each selected geosite, topographic and geological data were gathered to accurately represent the site in 3D animation. Sources included geological maps, high-resolution satellite imagery, and geospatial data accessible through Google Earth. Historical and interpretive information on each site was also collected to provide context for the animations.

Animation Development with Google Earth Studio:

Using Google Earth Studio, each geosite was visualized in a sequence of animations. The development process included defining camera paths to capture distinct perspectives, zooming into details of geological formations, and incorporating dynamic movements to simulate real-world exploration. Attention was given to camera angles and framing to ensure that animations were both engaging and informative.

For added educational value, labels, annotations, and shapes were embedded directly in the animations, highlighting significant geological features and processes relevant to each site. This interactive approach aimed to increase viewer comprehension of the complex geological structures and their historical importance.

Evaluation of Visualizations:

The educational activities focus on presenting complex geosites with one more easy and interactive way. After completing the educational activity, we made it for students and educators. The users give us feedback through questionaries. was collected to assess the animations' comprehensive, engaging, and educational impact, The responses guided further refinements, with adjustments made to optimize the balance between scientific accuracy and accessibility for a non-specialist audience.

Dissemination and Public Engagement:

The finalized 3d animation were presented to students and public due to guided tour in fieldtrips in Lesvos UNESCO Global Geopark and in educational trips at Natural History Museum of the Petrified Forrest of Lesvos, also were shared through the official Lesvos UNESCO Global Geopark website and social media platforms to reach a wider audience. By incorporating Google Earth Studio's animations, the project aimed to make complex geological phenomena more comprehensive and engaging for the public, fostering a broader appreciation of Lesvos's geological heritage.

This methodology demonstrates a structured approach to utilizing 3D animation as a powerful tool for geosite interpretation and education, highlighting the potential of Google Earth Studio to enhance public understanding of geological heritage sites.

Table 1 Methodology Flowchart

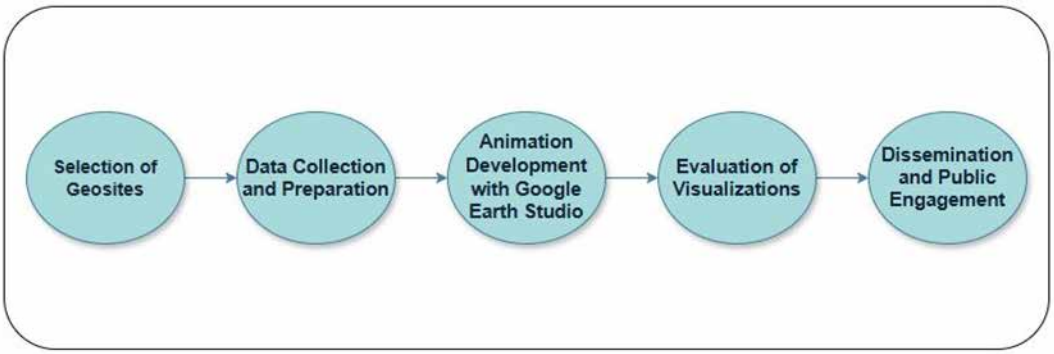

The study area

Lesvos UNESCO Global Geopark has a unique wealth of geological monuments and landscapes of natural beauty, habitats and cultural monuments which have contributed to its recognition and inclusion in the Global Geoparks Network of UNESCO.

In its western part, the Petrified Forest dominates, a unique piece of geological history, which has been declared a "Preservable Monument of Nature". Lesvos is scattered with a multitude of geological monuments and landforms of unique value and importance. Some of them are impressive volcanoes, hot springs, important fossil sites, large geological faults, waterfalls, coastal landforms that are important evidence of geological history that testify to the evolution of the Aegean basin.

The geosites: selection process

In this paper, we select 21 case studies of geosites or monuments of geological heritage to 3D geo-visualize. The selection method is based on three criteria: accessibility, supervision and relief of the geosite out of the total number of 151 designated geosites of the Geopark.

Geological Heritage, Education, and Geotourism

Geological heritage encompasses the unique geological formations, landscapes, and features that hold scientific, educational, and cultural significance. The integration of geological heritage into education fosters a deeper understanding of Earth's processes, history, and conservation needs. Geotourism, which focuses on showcasing geological attractions, bridges education and sustainable tourism by engaging visitors in immersive, place-based learning experiences. By blending science with storytelling, geotourism not only raises awareness about geological phenomena but also supports the local economy and conservation efforts, creating a holistic approach to promoting and preserving geosites like the Lesvos UNESCO Global Geopark.

3D Tools and Geoheritage

Digital tools, particularly 3D technologies, have revolutionized the way geological heritage is presented and understood. Otherwise, 3D animations, virtual reconstructions, and interactive visualizations, it is possible to bring to life geological features and processes that are otherwise inaccessible or difficult to comprehend. In the context of Lesvos UNESCO Global Geopark, these tools offer a dynamic platform for engaging educational experiences, allowing students and visitors to explore virtual landscapes, simulate volcanic activity, or visualize tectonic faults. This innovative approach not only enhances learning but also deepens appreciation for geoheritage by making abstract or hidden processes tangible and memorable.

Results

In this study, a total of 225 students and educators from Greece and other EU countries were surveyed during their visit to the Natural History Museum of the Lesvos Petrified Forest and various geosites within the Lesvos UNESCO Global Geopark. These participants were provided with scientific information regarding the geological heritage of the area, with the consideration of 3D geosite animations incorporated into the presentations to facilitate enhanced comprehension of the geosites. After the educational activity the users asked questionnaires, the findings of the study indicated the following:

To the question "On a scale of 1 to 5, how understandable was the concept of a geosite » 54% of respondents reported that the use of 3D animations made geosites highly comprehensive, while 33% found them very comprehensive.

Table 3 Methodology Flowchart

Discussion

The implementation of 3D animations through Google Earth Studio as educational tool for geosites within the Lesvos UNESCO Global Geopark has provided significant insights into the potential of digital tools for geoheritage promotion and education in other geoparks. This discussion addresses the benefits, challenges, and future implications of using this approach in geoscientific communication.

Enhanced Public Engagement and Education

Mixing geoeducation with the tours is an optimal way to keep tourism interesting. the tour guide and educational boards play an important role (Wang et al., 2023) The results demonstrate that 3D animations can serve as an effective tool for increasing public interest and comprehension of complex geological processes and formations. By offering an immersive, interactive view of geosites, animations make the scientific details of the landscape accessible to a broader audience, including those with limited geoscientific knowledge. Enhanced engagement aligns with findings in prior studies, where 3D visualization has been shown to effectively support educational initiatives in geoparks and geoscience education more generally.

Accessibility and Preservation of Geoheritage

The virtual nature of 3D animations also addresses key challenges in geoheritage conservation. By providing virtual access to sensitive or inaccessible areas, these animations help minimize the environmental impact of tourism, reduce the risk of physical degradation, and allow continuous public engagement without compromising the integrity of the geosites. This approach aligns with current geoheritage conservation goals, which advocate for minimal environmental impact while promoting public awareness and educational

outreach. Virtual flights over larger territories, supported by relevant commentaries highlighting relationships between nature and humans, may in turn be an attractive means to become acquainted with areas which lack singular spectacular sites (Migoń and Pijet-Migoń, 2024)

Technical and Methodological Limitations

Despite the successes observed, google earth is not perfect there exist several limitations, that is the inconsistent quality of images, insufficient capability for quantitative measurement (Yu and Gong, 2012),

lack of analytical functionalities, the study faced limitations in terms of data resolution and platform capabilities. Google Earth Studio, while powerful, has constraints regarding data detail and may not fully capture subtle geological features. Future studies could explore supplementary tools like high-resolution GIS mapping software or custom 3D modeling to complement Google Earth Studio, thus enhancing the accuracy of the representations. Additionally, labeling and annotation tools within Google Earth Studio could be expanded to improve the educational value of animations.

Future Research and Practical Applications

The use of 3D animation for geoheritage could be expanded in future research to include more comprehensive datasets, interdisciplinary collaborations. Also, it can be a useful tool for geoparks with hard accessible and fragile geosites.highlighting the role of 3D animations in geoheritage education and conservation.

However, it could further elaborate on the specific technical constraints of Google Earth Studio. For example, while the paper mentions data resolution issues, a deeper analysis of how these limitations affect the accuracy of geological feature representations such as fine-scale in different variations or subtle geomorphological changes—would be beneficial. Additionally, a comparison with alternative 3D modeling tools, such as GIS-integrated software or photogrammetry-based reconstructions, could provide a more comprehensive perspective on the advantages and trade-offs of the chosen methodology.

Furthermore, expanding the future research directions section to explore AI-driven enhancements, such as machine-learning-assisted geosite identification or automated annotation features, could significantly enhance the study's impact. Integrating AI could help refine data visualization, allowing for real-time user interaction and adaptive learning experiences tailored to different audiences. These aspects would not only strengthen the study's contribution to digital geoheritage visualization but also position it within the broader context of emerging technologies in geoscience education.

Conclusion

This study highlights the strong potential of using 3D animations as educational tools for geoheritage promotion, offering a way to communicate advanced geological science contents in an effective and enjoyable manner that can effectively engage the public in learning about culturally complex geological knowledge. Considering these benefits, while digital solutions will remain a powerful asset in the future of geoscience education and conservation, both technical innovations and methodological optimizations are necessary to enhance the impact of such visualizations. The combinations of Guided tour with 3D animation it can be an educational approach, and it can contribute to geological heritage management for fragile and inaccessible geosites.

Overall, the approach promotes visitor democracy, as all groups have access to the visualized geosites and can be used to further improve the visibility of the geosites and that of the Geopark

References

Migoń, P. and Pijet-Migoń, E. (2024) 'Non-Uniform Distribution of Geoheritage Resources in Geoparks—Problems, Challenges and Opportunities', Resources, 13(2). doi: 10.3390/resources13020023.

Wang, Y. et al. (2023) 'From Geoparks to Regional Sustainable Development: Geoheritage Protection and Geotourism Promotion of Geoparks in Hebei Province, China', Geoheritage. Springer Berlin Heidelberg, 15(3). doi: 10.1007/s12371-023-00870-5.

Fassoulas, C., Nikolakakis, E. and Staridas, S. (2022) 'Digital Tools to Serve Geotourism and Sustainable Development at Psiloritis UNESCO Global Geopark in COVID Times and Beyond', pp. 1–22.

Wang, J. and Zouros, N. (2021) 'Educational Activities in Fangshan UNESCO Global Geopark and Lesvos Island UNESCO Global Geopark', Geoheritage. Springer Berlin Heidelberg, 13(3), pp. 1–16. doi: 10.1007/s12371-021-00570-y.

Yu, L. and Gong, P. (2012) 'Google Earth as a virtual globe tool for Earth science applications at the global scale: progress and perspectives', International Journal of Remote Sensing, 33(12), pp. 3966–3986. doi: 10.1080/01431161.2011.636081.

Pringle, H. (2010) 'Google earth shows Clandestine worlds', Science, 329(5995), pp. 1008–1009. doi: 10.1126/science.329.5995.1008.

Zouros N and Valiakos I (2010) 'Geoparks management and assessment', Bulletin of the Geological Society of Greece, XLIII(2), pp. 965–975. Available at: www.europeangeoparks.org.

SHARPLES, C. (2007) 'Geoconservation in forest management-principles and procedures.', Research Gate, 62(December 1995), pp. 37–50.

17th INTERNATIONAL CONGRESS of the Geological Society of Greece

BULLETIN OF THE GEOLOGICAL SOCIETY OF GREECE, SP. PUBL.

EXTENDED ABSTRACT 008

Land Subsidence and Flooding in the East Thessaly Plain: A Historical Overview

Antoniadis N.1, Loupasakis C.1

(1) School of Mining & Metallurgical Engineering, National Technical University of Athens, nikolaosantoniadis@metal.ntua.gr

Background

The East Thessaly Plain, a critical region for agricultural production in Greece, has a rich and complex geological and hydrological history that has shaped its current environmental and socio-economic landscape. Prehistorically, Lake Voivida, a vast body of water, covered the Plain and influenced early human settlements (Thermou, 2023). Over centuries, the lake experienced fluctuating water levels, with humans adapting to the changing environment. The region's evolution saw a transition from lake-based ecosystems to large-scale agricultural land use, particularly as drainage and flood management projects were implemented in the late 19th and early 20th centuries. In the 1960s and 1970s, rapid agricultural expansion, combined with intensive groundwater extraction for irrigation, led to significant hydrological changes. As a result, the East Thessaly Plain became one of the most important agricultural areas in Greece, contributing significantly to the country's grain production. However, this transformation came at a significant environmental cost, including land subsidence, water shortages, and vulnerability to flooding (Arapostathis et al., 2024). In recent decades, the Plain has experienced recurring land subsidence, particularly in areas that rely heavily on groundwater for irrigation. These subsidence phenomena, linked by the overexploitation of the aquifers, have been influenced by extreme weather events, including the 2023 Daniel storm, which caused widespread flooding and infrastructural damage. The interaction between land subsidence, flooding, and land use changes, compounded by climate change, has created a complex set of challenges for the region's future.

Objectives

This paper aims to provide a comprehensive historical overview of the evolution of the East Thessaly Plain emphasizing on the land subsidence, as well as explore its interaction with flooding events, land use changes, and extreme storms, particularly in the context of the intensification of agricultural practices over the past century. The study draws upon existing research, reports, satellite-based InSAR data, and historical accounts.

Methods

A detailed review of historical documents, archaeological excavations, and scientific literature has been conducted to track the region's evolution from prehistoric lake systems to modern agricultural landscapes. Key sources include studies of early human settlements in Thessaly, geological, geotechnical and geophysical surveys, and flood records. The study incorporates data from geological surveys, such as reports conducted by the Hellenic Survey of Geology and Mineral Exploration (HSGME), Central Laboratory Public Works (KEDE), as well as reports from the Ministry of Environment and Energy of Greece.

Open-access InSAR (Interferometric Synthetic Aperture Radar) products, such as Copernicus European Ground Motion Service have been used to track land subsidence over the last decade, providing a unique opportunity to assess the long-term impacts of groundwater extraction and flooding phenomena on the region's land stability.

Field surveys and ground-based observations have been combined with remote sensing data to assess the physical and hydrological changes in the East Thessaly Plain, focusing on key areas such as Larissa, Tyrnavos, and Velestino. This multi-method approach allows for a more comprehensive understanding of the historical and ongoing processes affecting the region.

Results

The results of the study reveal a clear relationship between land subsidence, changes in land use, and extreme weather events. Historical records suggest that the area has long been subject to fluctuating surface water levels, with periods of lake expansion and contraction. The draining of Lake Karla in 1962, which transformed large parts of the Thessaly Plain into cultivated land, marked a significant turning point in the region's hydrological history. This, along with the intensification of irrigation practices, created a situation where groundwater extraction reached unsustainable levels, leading to the onset of land subsidence.

Satellite-based InSAR data has shown that subsidence is most pronounced in areas that experienced intensive groundwater extraction, with significant subsidence recorded in the regions of Larissa and Tyrnavos. The rate of subsidence has increased since the 1990s, coinciding with the period of progressive intensification of agricultural practices in the region. InSAR data also highlights that the subsidence is not uniform, with certain areas showing localized shifts in the ground level that correspond with faults and tectonic zones (Fakhri & Kalliola, 2015; Parcharidis et al., 2011; Vassilopoulou et al., 2013). Land subsidence phenomena are still ongoing as shown by the European Ground Motion Service's products (Figure 1).

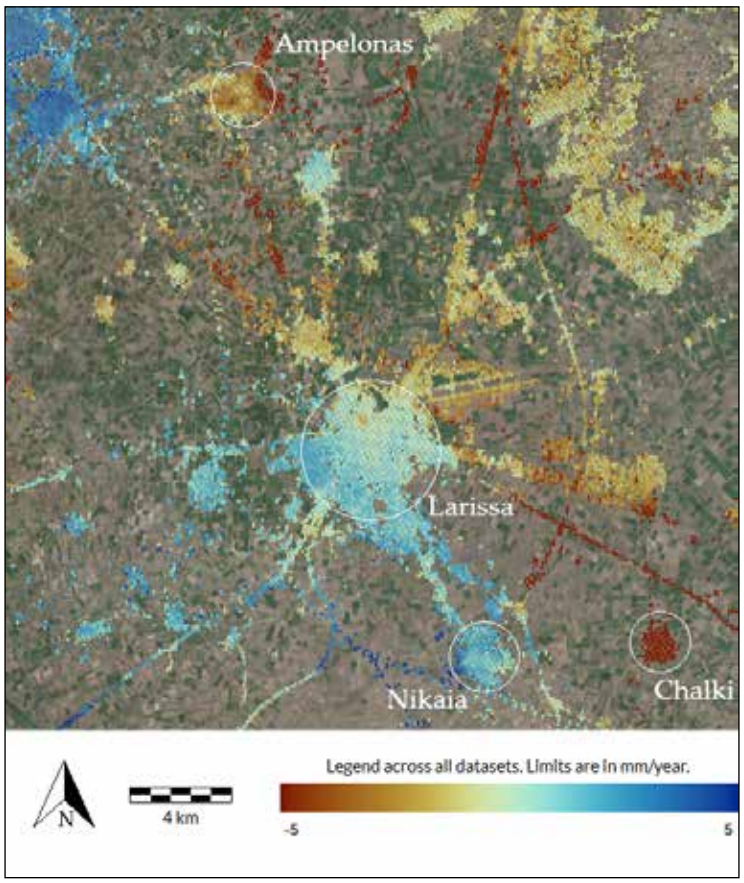

Figure 1. Ground deformation phenomena in the greater area around Larissa from EGMS Copernicus

Field surveys and studies reported land subsidence phenomena in several villages such as Rizomylos, Stefanovikeio, Kastrio, Melia, and Niki, where the drop in the water table reached up to 35 meters by the early 1990s (Soulios, 1997), while similar patterns have been identified in the villages of Halki and Magoula (Kaplanides A. & Fountoulis D., 1997). Land subsidence has also been observed in the Karla area, where excessive groundwater extraction took place. Marginal fractures appeared as the thickness of

the Quaternary sediments diminished (Rozos, 2007). These findings were aligned with tectonic patterns in the region, where subsidence appeared more pronounced along fault zones, suggesting a combination of natural tectonic activity and human-induced groundwater extraction as primary contributors to subsidence in the region.

On the other hand, flooding events, particularly those caused by extreme storms like the Daniel storm in 2023, have further affected the impact of subsidence on the region. These floods have caused widespread inundation, damaging infrastructure and agricultural land. The interaction between land subsidence and flooding is particularly problematic in areas with poor drainage systems, such as the Lake Karla area, where water remains stagnant for extended periods after heavy rainfall.

Conclusions

The East Thessaly Plain's evolution has been shaped by a complex interaction between geological processes, human activity, and climate change. The expansion of irrigation systems and exploitation of the underground water have transformed the Plain into one of the most productive agricultural regions in Greece. However, this transformation has come at the cost of land subsidence, which has been exacerbated by groundwater overexploitation. The review underscores the need for more sustainable water management practices to mitigate further subsidence and flooding risks. The integration of satellite-based monitoring techniques like InSAR offers a powerful tool for tracking ground deformation and assessing the long-term impacts of land use changes.

The findings highlight the importance of continued monitoring of groundwater levels and the implementation of flood control measures to protect the agricultural productivity of the East Thessaly Plain. Furthermore, the ongoing challenges posed by land subsidence and extreme weather events underscore the need for adaptive strategies to address the evolving risks associated with climate change and urbanization in the region. The study also calls for further research into the interactions between groundwater extraction, land subsidence, and storm-related flooding to develop more comprehensive and effective risk management strategies for the future.

Acknowledgements

This publication has been prepared using the European Union's Copernicus Land Monitoring Service information (https://egms.land.copernicus.eu/). The key elements of the European Ground Motion Service (EGMS) are stated in the White Paper, available online at https://land.copernicus.eu/user-corner/technical-library/egms-white-paper (EU-GMS Task force, 2017).

References

EU-GMS Taskforce. (2017). *EGMS White Paper*. https://land.copernicus.eu/en/products/european-ground-motion-service/egms-white-paper

Fakhri, F., & Kalliola, R. (2015). Monitoring ground deformation in the settlement of Larissa in Central Greece by implementing SAR interferometry. *Natural Hazards*, *78*(2), 1429–1445. https://doi.org/10.1007/s11069-015-1779-6

Kaplanides A., & Fountoulis D. (1997). Subsidence phenomena and ground fissures in Larissa, Karla basin, Greece: their results in urban and rural environment. In P. Marinos, G. Koukis, G. Tsiambaos, & G. Sambatakakis (Eds.), *Eng Geol Environ* (pp. 729–735). Balkema.

Parcharidis, I., Foumelis, M., & Katsafados, P. (2011). Seasonal ground deformation monitoring over Southern Larissa Plain (Central Greece) by SAR interferometry. In *Advances in the Research of Aquatic Environment* (pp. 497–504). Springer Berlin Heidelberg. https://doi.org/10.1007/978-3-642-24076-8_58

Soulios, G. (1997). Subsidence de terrains alluviaux dans le sud-est de la plaine de Thessalie. *International Symposium on Engineering Geology and the Environment*, 1067–1072.

Vassilopoulou, S., Sakkas, V., Wegmuller, U., & Capes, R. (2013). Long term and seasonal ground deformation monitoring of Larissa Plain (Central Greece) by persistent scattering interferometry. *Open Geosciences*, *5*(1). https://doi.org/10.2478/s13533-012-0115-x

Arapostathis, E., Vlachos, G., Gousios, D., Danalatos, N., Hliou, N., & Tsimpoukas, K. (2024). *AGRICULTURAL DEVELOPMENT PLAN OF THESSALY*. (in Greek) https://www.thessaly.gov.gr/images/right/sxedio.pdf

Thermou, M. (2023, September 15). *Same picture: The Thessaly plain today, as it was 10,000 years ago*. (in Greek) Mononews. https://www.mononews.gr/politismos/idia-ikona-o-thessalikos-kampos-simera-opos-prin-apo-10-000-chronia

Rozos, D. (2007). *Engineering Geology I - Manual, Landslides - Land subsidence - Settlements*. Department of Geological Sciences, Laboratory of Engineering Geology and Hydrogeology, School of Mining and Metallurgical Engineering, NTUA.

17th INTERNATIONAL CONGRESS of the Geological Society of Greece

BULLETIN OF THE GEOLOGICAL SOCIETY OF GREECE, SP. PUBL.

EXTENDED ABSTRACT 009

Geological suitability in remote mountainous settlements using the AHP method. The case study of the settlement of Klepa in Greece

Antonopoulou A.[1], Depountis N.[1], Kokkalas S.[1]*

*(1) Department of Geology, University of Patras, 26504 Patras, Greece. *up1065387@ac.upatras.gr*

Research Highlights: **GIS-based Analytical Hierarchy Process (AHP) for geological suitability evaluation in remote mountainous settlements**

Introduction

The evaluation of geological suitability is crucial in managing and planning residential development in settlements, where geological conditions are harsh, and accessibility is limited. This becomes even more critical in areas affected by geohazards, such as landslides that primarily occur in remote mountainous regions due to their complex terrain, geological characteristics, and human activities. These studies are compulsory in every case of urban planning or demarcation of a settlement and aim to safeguard the built environment from natural hazards or hazards resulting from human intervention and activities (Depountis, 2023).

Focusing on mountainous remote settlements influenced by landslide events, this study employs a GIS-based multicriteria analysis using the Analytical Hierarchy Process (AHP) to evaluate geological suitability. This methodology incorporates various geological factors affecting the study area to produce a suitability map and categorize existing settlement conditions into safe or unsafe building zones. The Analytical Hierarchy Process (AHP) assigns certain weights to the chosen criteria and spatial datasets are produced within a GIS environment to create a geological suitability map that identifies optimal areas for development; thus, categorizing them as suitable, unsuitable, or suitable under specific conditions.

Background

The settlement of Klepa, located in the Central Western Greece, belongs to the regional unit of Aitoloakarnania. The geology of the study area is characterized by the presence of Alpine bedrock, specifically the Pindos unit. The formations in the study area are primarily comprised of flysch, limestone and cherts. In addition, Quaternary deposits are present, including fluvial deposits, scree and landslide materials.

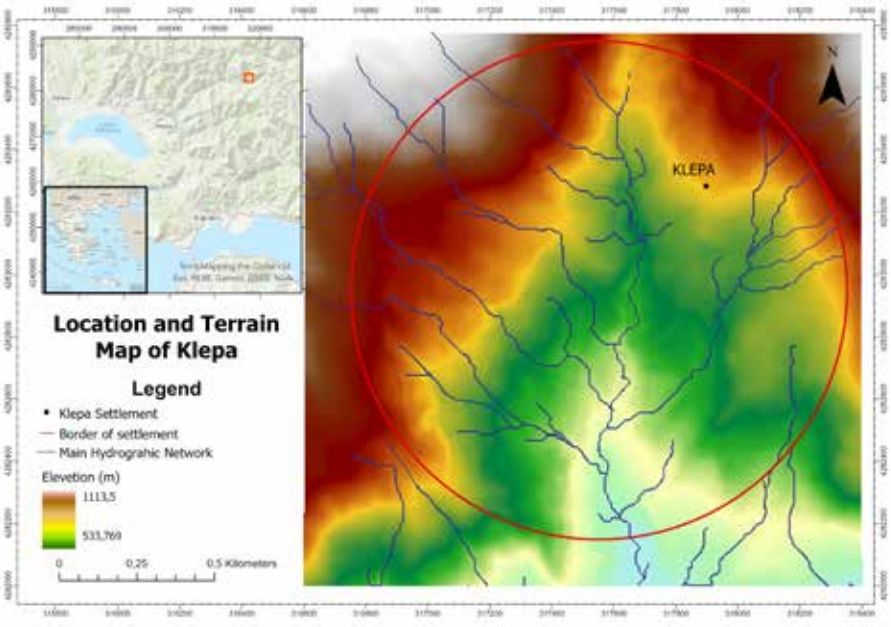

Figure 1. Location and terrain map of the study area.

The landslide problem in the wider area of Klepa is well-known and has been repeatedly examined by the Hellenic Survey of Geology and Mineral Exploration. In particular, the area has recorded activations of old or recent landslides at least four times in the last 35 years, with the most recent and severe occurred in 2015. The impact of landslides was severe, destroying several houses and a section of the provincial road about 120 meters long.

Methodology

The methodology of this study is divided into four key phases: a) criteria selection, b) AHP application, c) spatial analysis and standardization, and d) suitability assessment. The criteria were selected from the study by Depountis (2023), which proposes an outline for the application of various parameters for MCE suitability related to different land uses. The selected criteria are (1) Geohazards/Landslides, (2) Geomorphology/ Slope, (3) Geology/Lithology, (4) Hydrology/Rivers, (5) Ground Seismicity Hazard and (6) Tectonics/Faults. The current study employs the Analytic Hierarchy Process by Saaty (1980), a multicriteria decision method that uses eigenvalue theory to compute weights and maintain consistency in pairwise comparisons. The AHP is a comprehensive measurement theory, which allows the creation of ratio scales through comparison of discrete and continuous variables (Hajar, 2017) and is a globally recognized technique aiding in risk assessment and mitigation planning (Mokhtari et al., 2023).

The pairwise comparison of the chosen criteria was performed to assess their relative importance to a defined objective, using Saaty's weighting scale 1-9. After the process of the matrix's normalization to ensure logical consistency, the Consistency Ratio (CR) is calculated, which includes the following indices:

- Random Index (RI): A constant derived from Saaty's random index scale, based on the number of criteria.
- Maximum Eigenvalue (λmax): The mean obtained by multiplying elements of the normalized comparison matrix by the priority vector (weights).
- Consistency Index (CI): A measure of matrix consistency, using the number (n) of criteria and calculated as:

$$CI = \frac{\lambda_{max} - n}{n - 1} \quad (1)$$

The CR is computed by dividing the CI by the RI, with values ≤0.10 deemed acceptable; higher values suggest the need for revised comparisons (Saaty, 1980).

The main purpose of the application of the analytical hierarchy process is to determine the weight values of the criteria discussed to solve the problem and their place in the hierarchical structure at the solution stage (Topuz & Deniz, 2023).

The criteria (or factors) used in this study and their calculated weights are presented in Table 1. In Table 2 the criteria used are presented as data layers imported in the GIS framework and divided into four classes (1-4) for proper suitability assessment.

Table 1. Pairwise matrix of the criteria and produced weightage W_i.

Criteria	Geohazards/ Landslides	Geomorphology/ Slope	Geology/ Lithology	Hydrology/ Rivers	Ground Seismicity Hazard	Tectonics/ Faults	Weight W_i.
Geohazards/ Landslides	1	2	3	4	4	4	0.368
Geomorphology/ Slope		1	2	3	3	3	0.236
Geology/ Lithology			1	2	2	2	0.144
Hydrology/ Rivers				1	2	2	0.106
Ground Seismicity Hazard					1	1	0.073
Tectonics/Faults						1	0.073

Table 2. Division of criteria into classes and Suitability assessment.

Data Layer	Class	SC	Data Layer	Class	SC	Data Layer	Class	SC
Landslides	Active/ recent	4	Slope (%)	<10	1	Lithology	Recent loose Landslide materials	4
	Inactive/ older	3		10-20	2		Paleo & Older semi-compacted Landslide materials	3
	Absence	1		20-35	3			
				>35	4			
Distance from Streams (m)	<10	4	Ground Seismicity Hazard	A	1		River bed deposits	3
	10-50	3		B	2		River terrace	1
	50-100	2		C	3		Scree	3
	>100	1		D, X	4		Sandstone/ Flysch Pindos Unit	2
Distance from Faults (m)	0-20	4					Siltstone/ Flysch Pindos Unit	2
	>20	1					Limestone/ Pindos Unit	1
							Cherts/ Pindos Unit	2
CR= 0.0192 ≤ 0.10								

1: Suitability Class (SC) refer as; (1) Highly Suitable, (2) Moderately suitable, (3) Marginally suitable and (4) Unsuitable.

The spatial analysis was conducted in ArcGIS Pro 3.1 software. To illustrate the spatial distribution of the relevant criteria, six thematic maps were developed based on the data layers and classification categories specified in Table 2. These maps provide a detailed spatial representation, contributing to a more thorough understanding of the patterns and relationships within the study area (Figure 2, 3). The data necessary for the creation of the aforementioned layers were sourced from various references, which are detailed subsequently. Moreover, a modification and validation of vector data was performed, specifically for the limits of the area of active landslides. Figure 2A depicts the landslide inventory, classifying areas into three distinct classes: (i) absence, (ii) inactive/older landslides, and (iii) active/recent landslides. This classification is crucial for identifying regions with historical or ongoing instability. Slope plays a pivotal role in affecting the occurrence of landslide events. Steeper slopes are more prone to instability due to the greater gravitational force acting along the slope surface, which increases the probability of failure. A slope map was generated by processing the Digital Elevation Model (DEM) of the area, which has a grid size of 5x5m. The layer was classified into four distinctive categories that are: (i) less than 10, (ii) 10 to 20, (iii) 20 to 35 and (iv) greater than 35, each representing different slope percentages (Figure 2B).

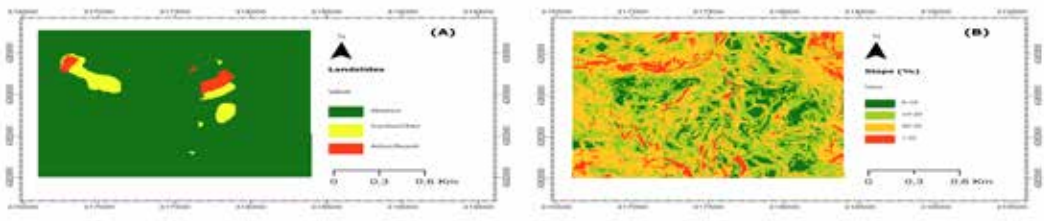

Figure 2. Thematic layer maps: (A) Landslides, (B) Slope.

Figure 3C presents the lithological classification, detailing various geological formations. The geological and lithology features were digitized from a large-scale (1:2.000) Engineering Geological map produced by the Hellenic Survey of Geological and Mineral Exploration (T-2855/2016) and an update was made after an on-site geological surveying.
The distance from streams portrays a critical hydrological factor influencing slope stability. The drainage network was derived from the Digital Elevation Model (DEM) and subsequently verified against the Engineering Geological map. The vector data was modified to define the boundaries of the river banks, and buffer zones were established around the streams, categorized as follows: (i) less than 10 meters, (ii) 10 to 50 meters, (iii) 50 to 100 meters, and (iv) greater than 100 meters. These buffer zones are represented as a layer in Figure 3D.
Furthermore, Figure 3E illustrates the proximity to fault lines, categorizing the study area into two classes: (i) areas within 0 to 20 meters from faults and (ii) areas beyond 20 meters, based on the provided data of the Engineering Geological map. Figure 3F represents the ground seismicity hazard of the geological formations, with the layer classified into four categories: (i) A, (ii) B, (iii) C, (iv) D, X, corresponding to the Engineering Geological map of the area and the Greek Code for Seismic Resistant Structures (EAK 2000). It is important to note that the third class is not represented in the thematic map, as no geological formations were classified within this category.

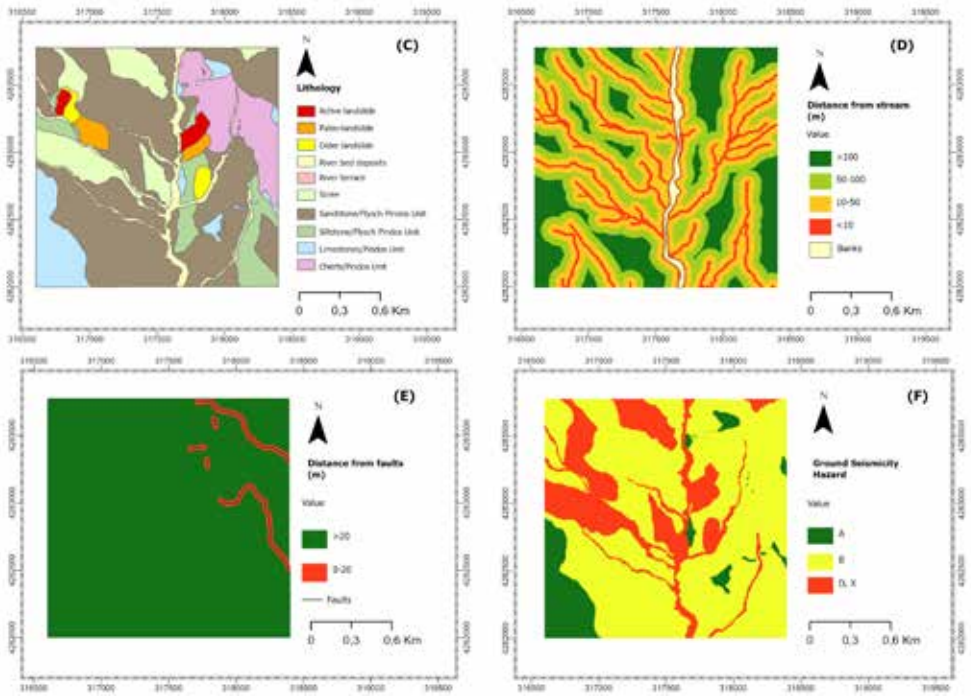

Figure 3. Thematic layer maps: (C) Lithology, (D) Distance from stream, (E) Distance from faults and (F) Ground Seismicity Hazard.

The raster layers were exported and then a scale of 1-4 was applied for the process of reclassification, following the scale of suitability values mentioned in Table 2. The levels of suitability were evaluated based on the relative significance of the contribution made by each criterion as has been suggested by Feizizadeh (2012). The reclassification of the spatial layers was made in order to eliminate the units of measurement and transform the data into a unitless format as has been suggested by Mansour et al. (2019). This process enhances compatibility, allowing for smoother integration with other datasets, regardless of their measurement system.
Following spatial analysis, a geological suitability map was obtained by the Weight Linear Combination

(WLC) method, then reclassified with Jenks natural break, categorizing the study area into four suitability categories (Figure 4). The WLC approach is one of the most frequently used in GIS-MCDA (Malczewski, 2000). The criteria and their individual weights are summed up in WLC, and the combined sum presents the final suitability map using the equation:

$$\sum_{i=1}^{n} = w_i \cdot c_{ij} \quad (2)$$

Where Wi: weights of selected criterion i, Cij: Reclassified criteria and n denotes total number of criteria.

Results

Each individual category of the final map corresponds to a unique geological suitability level with a specific color (Figure 4). For example, the lowest suitability level, represented by the highest weighted score, is highlighted in red. In this study, the suitability map shows four suitability categories as follows: (a) Unsuitable, (b) Marginally suitable, (c) Moderately suitable and (d) Highly suitable.

The analysis reveals that 38.58% of the total area is classified as highly suitable for residential development. The largest share of the land, 44.85%, falls under the “Moderately suitable” category, making it the most dominant classification in the analysis. While considering the land area that is not suitable, it is seen that a small area of the field consists of the Marginally suitable class 12.77%, whereas 3.80% of the study area is considered unsuitable for residential development.

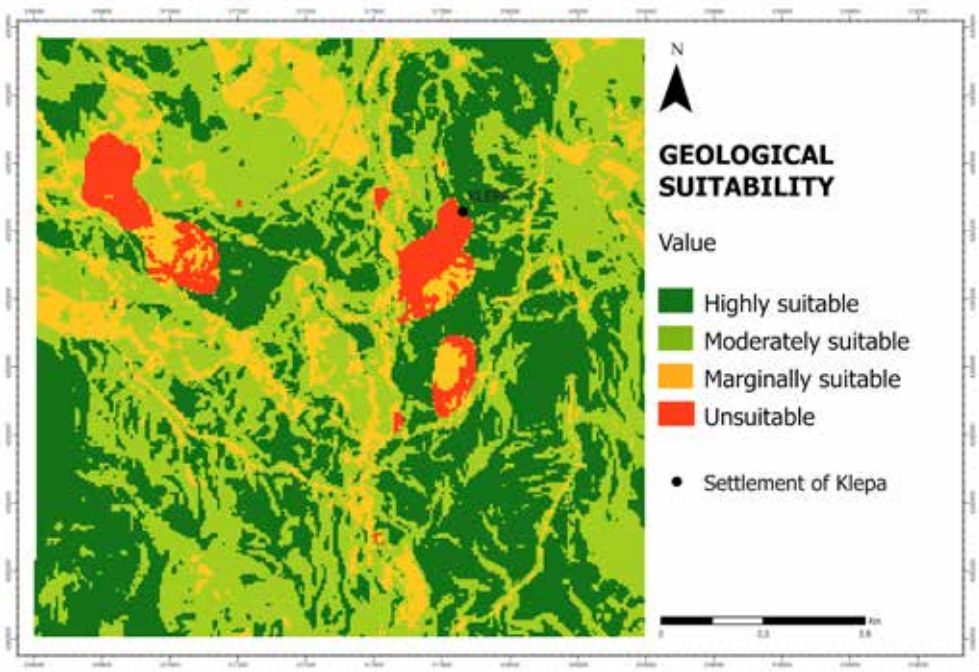

Figure 4. Geological Suitability map of the study area with color classification for each suitability category.

Conclusions

This study effectively combines Geographic Information Systems (GIS) and the Analytic Hierarchy Process (AHP) to assess geological suitability and residential development in mountainous settlements impacted by landslide events. By prioritizing key criteria through AHP and via GIS for spatial analysis, a geological suitability map is obtained. The produced map presents four levels of suitability: Unsuitable, Marginally Suitable, Moderately Suitable, and Highly Suitable. The analysis reveals that 38.58% of the investigated area is highly suitable for development, whereas 44.85%, of the total area falls under the Moderately

Suitable category. A smaller portion, 12.77%, is Marginally Suitable and 3.80% is classified as Unsuitable. This comprehensive approach provides a valuable decision-making tool for sustainable residential development and planning, particularly in remote settlements and geohazard-prone areas, that can be adapted to diverse cases and assess the influence of multiple factors in a region.

References

Depountis, N. (2023). Geological studies for regional and urban planning in Greece. European Geologist, 56.

Elhadj Mokhtari, Farouk Mezali, Brahim Abdelkebir, Bernard Engel, (2023). Flood risk assessment using analytical hierarchy process: A case study from the Cheliff-Ghrib watershed, Algeria. Journal of Water and Climate Change 14 (3): 694–711.

Feizizadeh, B., & Blaschke, T. (2012). Land suitability analysis for Tabriz County, Iran: a multi-criteria evaluation approach using GIS. Journal of Environmental Planning and Management, 56(1), 1–23. https://doi.org/10.1080/09640568.2011.646964

Hajar YAA, (2017). Using Analytical Hierarchy Process (AHP) to build suppliers' selection model. Int J Acad Res Bus Soc Sci. Pages 772-787. ISSN: 2222-6990. http://dx.doi.org/10.6007/IJARBSS/v6-i12/2552

Hellenic Survey of Geology and Mineral Exploration (2016). Engineering Geological study of the Kato Klepa settlement, Municipality of Nafpaktia, Regional Unit of Etoloakarnania (T-2855).

Malczewski J (2000) On the use of weighted linear combination method in GIS: common and best practice approaches. Trans GIS 4(1):5–22

Mansour, Shawky & Al-Awadhi, Talal & Al-Hatrushi, Salim. (2019). Geospatial based multi-criteria analysis for ecotourism land suitability using GIS & AHP: a case study of Masirah Island, Oman. Journal of Ecotourism. 19. 1-20. 10.1080/14724049.2019.1663202.

Saaty, Thomas. (1980). The Analytic Hierarchy Process. McGraw-Hill, New York.

Topuz, M., Deniz, M. (2023). Application of GIS and AHP for land use suitability analysis: case of Demirci district (Turkey). Humanit Soc Sci Commun 10, 115. https://doi.org/10.1057/s41599-023-01609-x

17th INTERNATIONAL CONGRESS
of the Geological Society of Greece

BULLETIN OF THE GEOLOGICAL SOCIETY OF GREECE, SP. PUBL.

EXTENDED ABSTRACT 010

Legacy data analysis combined with an integrated geological and geophysical survey for geothermal site exploration at Petra-Lesvos, Greece

Apostolopoulos G.[1], Malehmir A.[2], Vakalas I.[1], Kranis C.[3], Leontarakis K.[1], Orfanos C.[1], Konstantinidis E.[2], Markovic M.[2], Papadopoulou M.[2], Chailas S.[3], Skourtsos E.[3], Tzanis A.[3], Spyridonos E.[4]

(1) National Technical University of Athens, Athens, Greece, gapo@metal.ntua.gr
(2) Uppsala University, Uppsala, Sweden
(3) National and Kapodistrian University of Athens, Athens, Greece
(4) Public Power Corporation Renewables S.A., Athens, Greece

Introduction / Background

Geothermal source of energy has become a priority in the energy sector providing a precious transition from hydrocarbons. Geothermal energy has the great advantage to be used when it is needed especially in islands when there is a boost in consumption in the summer period. Public Power Corporation Renewables SA (PPCR) has sponsored geological and geophysical surveys for many years now for geothermal exploration leading to important results through geophysical surveys (Tzanis et al., 1991, Lagios et al., 1994, Lagios and Apostolopoulos, 1995, Apostolopoulos et al., 1997, Tzanis et al., 2018, Tzanis et al., 2020) in various sites of geothermal fields of interests. In the Lesvos Island, faults that may act as thermal circulation zones have been speculated through geothermal springs and through geophysical studies (Thanassoulas and Xanthopoulos, 1991, Apostolopoulos et al., 1997). A good correlation between geology, seismicity and geothermics has been found using remote sensing data and GIS in the island (Voulgaris et al., 2004)

Kontis et al. (1994) state that the active geothermal system in the Megala Therma (Northern Lesvos) is probably a late evolutionary stage in the formation of mineralization with different types of alterations from silicification, propylitization, argillic alteration and potassic to phyllic. This is important because in the gravity Bouguer anomaly map of Lesvos Island (Figure 1) this area is part of a low gravity anomaly trending in south-westwards towards Stipsi and extending to the south with relatively low gravity values where Kalloni and Polychnitos area are also of geothermal interest.

Figure 1. Northern Central part of the Bouguer gravity anomaly map (in mGals) of Lesvos Island over Google Earth map.

Geothermal exploration today involves geophysical method such as magnetotellurics (MT), a method of great detection depth, which is sensitive to zones of conductivity and possibly associated with geothermal circulation or reservoir but also with saline water presence. In the case of Lesvos, 3D interpretation of legacy magnetotelluric data (Tzanis, 2024) provide resistivity distributions at various depths with one particular at depth of approximately 1.25 km below mean sea level (Figure 2) showing great correlation between low resistivity values and low gravity regions previously inferred.

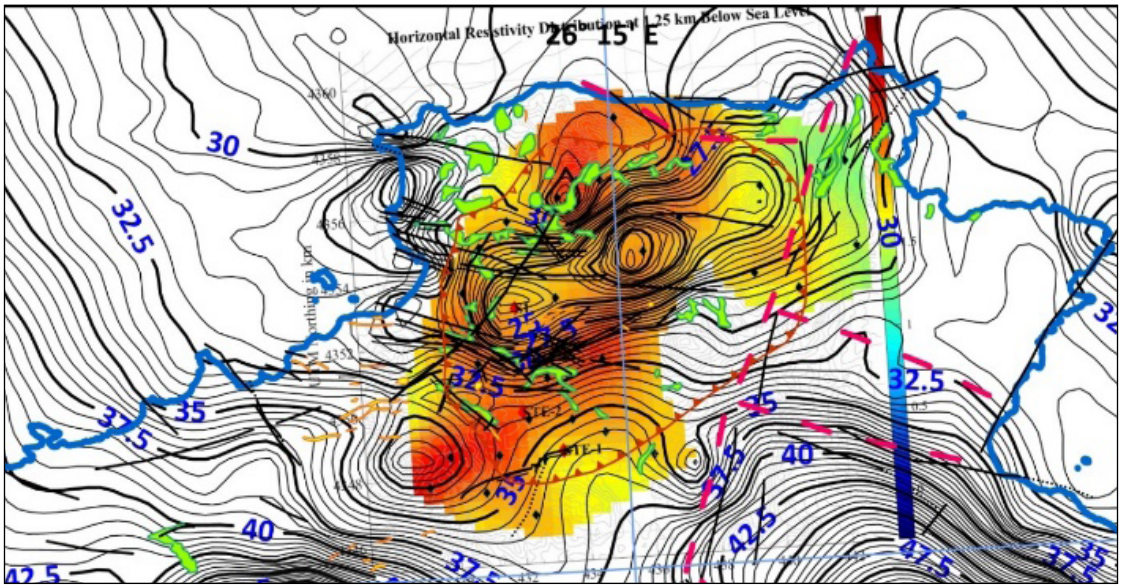

Figure 2. Northern Central part of Lesvos Island with horizontal electrical resistivity slice at the depth of 1.25km below mean sea level over the Bouguer gravity anomaly map (in mGals). The resistivity slice among others was extracted from the 3-D model elaborated by Tzanis (2024) on legacy magnetotelluric data.

PPCR has sponsored a renewed geothermal project under the coordination of National Technical University of Athens (NTUA, School of Mining and Metallurgical Engineering, Laboratory of Hydrocarbon's Exploitation & Applied Geophysics) in collaboration with Uppsala University (UU, Department of Earth Sciences) and National and Kapodistrian University of Athens (NKUA, Faculty of Geology and Geoenvironment) that consists a geological-tectonic and geophysical study in an integrated mode that will provide a better understanding of the geothermal field through the positioning of faults that act as geothermal circulation zones and areas of geothermal alteration. The project goal is to propose the best position for a new deep borehole in the area for geothermal exploration. The project involves the evaluation of all available geological and geophysical data, new geological field survey including the use of UAV imaging for remote sensing in areas of interest such as fault zones, new gravity, and magnetic data along with an active seismic survey.

Geology of the Petra area

The geological formations (Figure 3) presented in Mythimna and Ayia Paraskevi work (Hecht, 1973, 1974), were verified macroscopically in the field. The main lithological types are the following: i) entirely silicified lava, ii) Dykes (rhyodacitic or dacitic), iii) Upper lava unit (dacitic, latitic, latitandesitic and quartz-andesitic; minor rhyodacitic lavas), iv) Lowermost parts of the upper lava unit (mostly latitic to latitandesitic), v) Pyroclastic layer (lapilli tuff and tuff breccia containing increasing amounts of volcanic bombs towards the west region of Scalochori), vi) Lower lava unit of the Stipsi and Vatoussa areas (mostly latitandesitic, partly andesitic or latitic, lavas; kaolinized zones of the lower lava unit, locally silicified. Basic lapilli tuff, magmatic breccia, or agglomerate within the lower lava unit).

Figure 3. Geological map of Lesvos Island Northern Central part (geographical coordinates UTM 35N) (Hecht 1973, 1974).

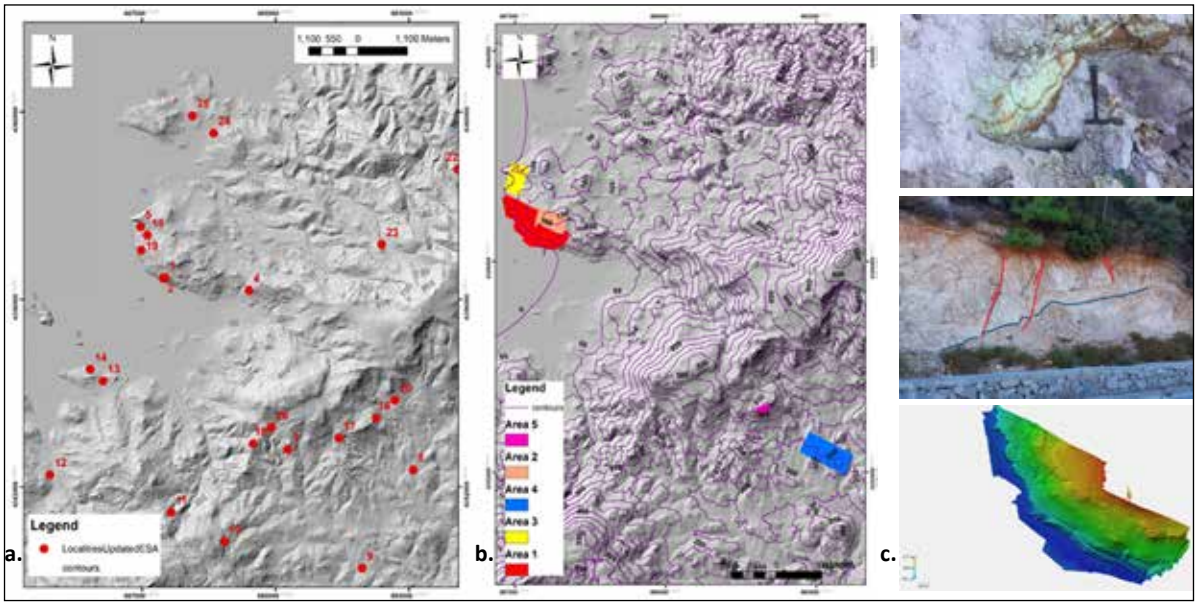

Figure 4. a) Geological data acquisition map in Petra study area, b) areas were drone surveyed (geographical coordinates Greek Grid), c) Hydrothermal alterations in the contact of pyroclastic sediments with the lower part of the Upper Lava Unit, faults affecting the silicified lavas (East of Stipsi), digital elevation model of Area 1.

The field geological survey (Figure 4a) focused on the following objectives:

- Identifying the rock units in the study area, using the geological map sheets of Mythimna and Ayia Paraskevi (HSGME, scale 1:50000) as reference.
- Conducting structural measurements, including faults and joints.

Additionally, in areas of interest, such as fault zones, data collection was enhanced using UAV imaging for remote sensing (Figure 4b).

Macroscopical identification of the lithological units in the study area, identification and measurement of potential fault zones and remote sensing data acquisition in 5 areas utilizing a set of 1373 aerial images were accomplished (Figure 4c) with the next step to be the construction of the structural model of the area in collaboration of the geophysical team.

Geophysical surveys

After considering all legacy data, geological and geophysical, in parallel with the geological survey, an integrated geophysical survey was designed in such a way to cover all interesting geological and tectonic features around the Petra area and the areas with low gravity and resistivity values the extended gravity map and magnetotelluric results.

The gravity and magnetic measurements designed and operated by NTUA-NKUA teams as well as the seismic profiles designed and operated by UU groups covered areas from Molyvos to Anaxos and Lafionas and from Petra to Petri and Stipsi (Figure 5). The gravity measurements were acquired from two groups with the Lacoste Romberg gravity meters and the magnetic measurements with the magnetometers Scintrex Envipro and Geometrics 852 (Figure 5). Differential RTK LEICA GPS instruments and Metrica Network were used for the positioning of the measurements. Four seismic profiles were positioned for a total of 24 km long across several suspected geological structures. UU subcontracted the Geological Survey of Denmark and Greenland (GEUS) in order to provide their new vibro-truck (Innova UV2 weighs approximately 17 tons, operates at a peak force equal to 115.6 kN and configured to produce a time-synchronised and phase-locked linear sweep signal from 10-140 Hz over 18 seconds) and its operation, while coordinated the survey and design with its own recording instrumentations (1000 wireless or nodal recorders connected with 10 Hz geophones for autonomous data recording). Receiver and shot points had a spacing of 10 m, except for P4 which was 20 m. At every shot point, 3 sweeps were generated to improve signal-to-noise ratio by vertical stacking of the repeated shot records. The recording time was set to 25 s with a sampling rate of 2 ms. Aiming for upper 2-3 km subsurface imaging and capitalizing from the large number of nodal recorders, long offset data were aimed for during the acquisition, reaching sometimes to up to 7.2 km.

Bouguer gravity and magnetic anomaly, reduced to the pole, maps show in the eastern region lower values something that was expected from the Bouguer gravity map of the Island (part of it in Figure 1). These lower values are very well associated with the Upper Lava Unit and possibly with geothermal alteration of the underground formations.

The unmigrated seismic section of P1 (Figure 6) shows an interesting cross-section of the subsurface with various characters appearing to suggest fault systems. Noteworthy the Bouguer gravity values show similar general behavior as the reflection seismic section (Figure 6). A gravity low correlates well with a seismic depression zone in the Petra area.

Figure 5. Gravity and magnetic measurements along with seismic profiles in the survey area on Google Earth map. Photos from gravity and magnetic measurements (left) and seismic survey (right).

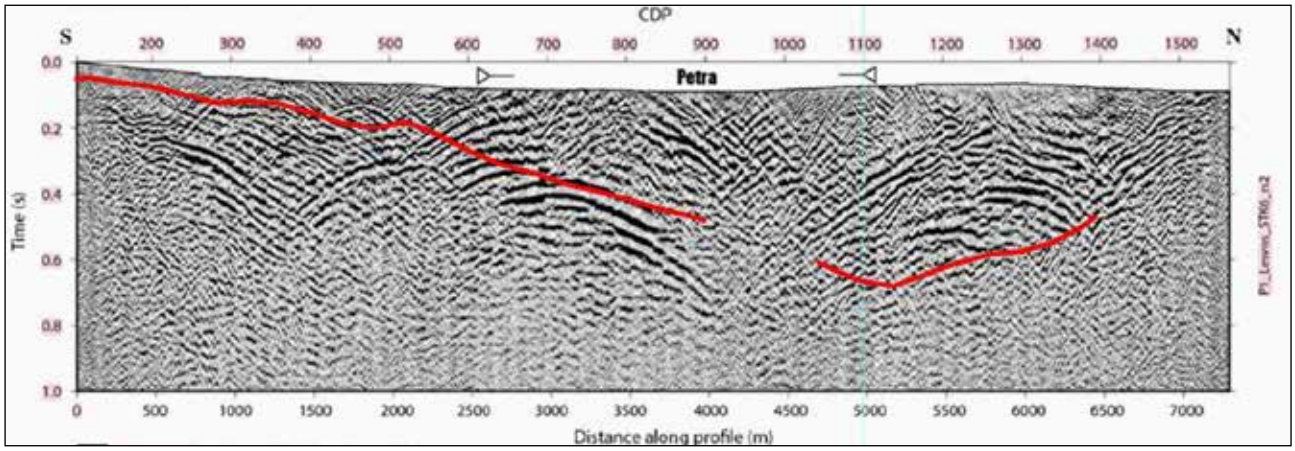

Figure 6. Unmigrated reflection seismic section of "P1" profile with the red line showing the of Bouguer gravity anomaly values extracted along the same profile.

First comments

According to the legacy data analysis, the geophysical and geological data coverage that was followed in the field with the final survey area extended as much to the east reaching Stipsi village to include in a substantial way the area of gravity low (Figure 1) as well as the resistivity low (Figure 2), the boreholes "S1" and "STE-2" (Figure 5) and most of the proposed faults. All data as expressed in maps or sections look of great quality and very good coincidence of what previous data were suggesting. The geophysical maps (Bouguer gravity anomaly map, magnetic anomaly reduced to the pole) which are considered reference map as uniquely represent the underground response already give interesting areas for geothermal activity. It is expected that further processing and data interpretation will lead to 3D models of the underground. The seismic shot gathers and unmigrated CDP sections show useful information of subsurface structures. This information will be useful both for density models as well as to refine the geological model suggested by surface geological observations. The fact that many of the features to be interpreted in the gravity maps as well as the surveyed geological and tectonic features are in seismic profiles gives the benefit of the integrated interpretation this project has as a target.

Acknowledgements

The authors wish to thank firstly Public Power Corporation Renewables for sponsoring the project. We also thank the Geological Survey of Denmark and Greenland (GEUS), which provided their new vibro-truck and their geoscientists Dr. G. Donoso and Mr. L. Solheim who operated it. Thanks to the important contribution in the field survey of Ms. K. Polychronopoulou (M.Sc.), Mr. S. Karizonis, Mr. D. Karaiskos, Mr. T. Ntagiantas, mining engineers, Ms. A. Dromiadi, Ms. T. Tzovara, Mr. A. Tsiftsidis NTUA students, Ms. K. Kantareli, Ms. N. Kranidioti, NKUA students, Mr. E. Konstantinidis, Mr. S. Zappala, Ms. J. Putnaite, Mr. V. Stender, Ms. K. Kucinskaite, PhD students of UU.

References

Apostolopoulos, G., Louis, I. and Lagios, E., 1997. The self-potential method in the geothermal exploration of Greece. Geophysics v.62, No. 6, pp.1715-1723. **[Journal Article].**

Hecht, J., 1973. Geological Map of Greece (Scale 1:50,000), Lesbos Island, Ayia Paraskevi Sheet, (N.I.G.M.R. publisher).

Hecht, J., 1974. Geological Map of Greece (Scale 1:50,000), Lesbos Island, Mithimna Sheet, (N.I.G.M.R. publisher).

Kontis, E., Kelepertsis, E. and Skounakis, S., 1994. Geochemistry and alteration facies associated with epithermal precious metal mineralization in an active geothermal system, northern Lesvos, Greece. Mineral Deposita 29,

430-433. **[Journal Article]**

Lagios, E., Tzanis, A., Delibasis, N., Drakopoulos, J. and Dawes, G.K.J., 1994. The geothermal exploration of Kos Island, Greece: Magnetotelluric and microseismicity studies. Geothermics, 23 (3), 267-281. **[Journal Article]**

Lagios, E. and Apostolopoulos, G., 1995. Integrated geophysical study of the geothermal system in the Southern Part of Nisyros Island, Greece. Journal of Applied Geophysics v.34, pp.55-61. **[Journal Article]**

Thanassoulas, C. and Xanthopoulos, N., 1991. Location of possibly productive geothermal fracture zones/faults using integrated geophysical methods over Lesvos Island geothermal field, Greece. Geothermics 20, 5/6, 355-368. **[Journal Article]**

Tzanis, A. and Lagios, E. 1991. Magnetotelluric Exploration of Geothermal Potential in Greece. Pro-ceedings, 1st Gen. Conf. of Balkan Phys. Union, Thessaloniki, Greece, September 26-28 1991, v 1, 520-522. **[Conference Proceedings]**

Tzanis, A., Sakkas, V. and Lagios, E., 2018, Magnetotelluric Reconnaissance of the Nisyros Caldera and Geothermal Resource (Greece). In: Dietrich, V.J. and Lagios, E. (eds), "Nisyros Volcano: The Kos - Yali - Nisyros Volcanic Field", Springer Verlag, 203-225; doi: 10.1007/978-3-319-55460-0_6. **[Book]**

Tzanis, A., Efstathiou, A., Chailas, S., Lagios, E. and Stamatakis, M., 2020b. The Methana Volcano – Geothermal Resource, Greece, and its relationship to regional tectonics, Journal of Volcanology and Geothermal Research, 404, 107035; doi: 10.1016/j.jvolgeores.2020.107035. **[Journal Article]**

Tzanis, A., 2024. Investigation of the geothermal potential of the wider area of Stıpsi, Lesvos: 3D inversion of digitized old (year 2000) magnetotelluric measurements. Technical Report to Public Power Corporation Renewables under the contract PO77000646.

Voulgaris, N., Parcharidis, I., Pahoula, M., and Pirlis, E., 2004. Correlation of tectonics, seismicity and geothermics of Lesvos Island using remote sensing data and geographical information systems. Bulleting of the Geological Society of Greece vol. XXXVI, Proceedings of the 10th International Congress, Thessaloniki. **[Conference Proceedings]**

17th INTERNATIONAL CONGRESS of the Geological Society of Greece

BULLETIN OF THE GEOLOGICAL SOCIETY OF GREECE, SP. PUBL.

EXTENDED ABSTRACT 011

Modelling Coastal Protection as an ecosystem service in the Greek coastal zone

Konstantina Apostolopoulou[1], Efthimios Karymbalis[1], Maria Salomidi[2], Evangelia G. Drakou[1]

(1) Department of Geography, Harokopio University, El. Venizelou 70, 176 76 Kallithea, Attica, Greece (2) Institute of Oceanography, Hellenic Centre for Marine Research, 46.7 km Athens Sounio Ave., 19013, Anavyssos, Greece

Research Highlights

Structural connectivity within seagrass meadows can enhance the ecosystem service of coastal protection capacity. This work provides an integrated modelling approach of biotic and abiotic seascape features while incorporating the role of structural connectivity to existing coastal protection ES models.

Background

Coastal areas are known to contribute to human well-being through the supply of ecosystem services (ES) (Liquete et al., 2013) or nature's contributions to people (NCP) (Díaz et al., 2018). Among these ES, coastal protection is of particular importance , especially in the face of increasing climate change impacts. Coastal protection is defined as the ecosystem service which provides natural defense of the coastal zone against inundation and erosion from waves, storms and sea level rise (Liquete et al., 2013). Coastal habitats, such as mangroves, saltmarshes, seagrasses, coral reefs and dunes, can act as natural defense against coastal flooding and erosion through wave attenuation, storm surge reduction and seabed elevation, thereby enhancing the resilience of coastal communities against these hazards (Trégarot et al., 2021). This is very timely, as climate change is expected to increase the frequency and magnitude of extreme weather events, such as storms and hurricanes, as well as lead to accelerated sea level rise. This increasing frequency and intensity of extreme events, along with anthropogenic activities such as coastal development, which degrade the coastal zone, pose a great threat to coastal populations and economies through increased erosion, flooding, and damage to infrastructure.

Greece has a diverse array of coastal habitats that are crucial for coastal protection. Sandy beaches act as dynamic buffers, absorbing wave energy and dissipating storm surge. Rocky shores provide refuge for marine life and offer resistance to erosion. Wetlands, such as salt marshes and lagoons, absorb floodwater. Seagrass meadows, stabilize sediments, and reduce wave energy. Among them, *Posidonia oceanica* meadows, endemic to the Mediterranean, as well as *Cymodocea nodosa*, are particularly important for coastal protection in Greece. *Posidonia oceanica* is identified as the most abundant seagrass species in Greece, being present in almost 70% of the Greek coastline (Panayotidis et al., 2022). In more shallow, brackish and sheltered areas, especially in the northern Aegean latitudes, *Cymodocea nodosa* also forms extensive meadows, playing a respective key role in coastal dynamics. Other seagrass species namely *Zostera noltei* and *Halophila stipulacea* also have a restricted presence in the Greek coastal zone (Panayotidis et al., 2022). Greece's complex coastal geomorphology with numerous bays, gulfs, peninsulas and islands, influences wave patterns, currents, and sediment transport, which in turn affect the distribution and resilience of coastal habitats. For instance, the steep slopes and narrow coastal plains characteristic of Greece's coastline, influence the vulnerability of coastal communities to sea-level rise and extreme weather events. Understanding the complex relationship between geomorphology, coastal habitats and their distribution, and biophysical processes is essential for developing effective coastal management strategies in Greece (Hasan et al., 2022).

In Greece, there have been many studies focusing on different aspects of coastal protection. Anastasiou and Sylaios (2016) investigated shoreline dynamics and evaluated coastal protection approaches in an erosion-vulnerable deltaic region of Northern Greece. Tragaki et al. (2018) assessed the physical and social vulnerability of Peloponnese to coastal hazards through variables like geomorphology, shoreline change rate, coastal slope, relative sea-level rise, mean wave height, and mean tide range. Hasan et al. (2022) adapted a regional coastal protection model proposed by Liquete et al. (2013) to Greece by mapping three

indicators, coastal protection capacity, exposure, and societal demand.

Objectives

The aim of this work is to assess and map the ecosystem service of coastal protection in Greece with a more holistic and integrated manner. The work presented uses existing knowledge and modelling approaches on coastal protection as an ES and enhances it with estimates of structural connectivity and fragmentation within coastal habitat types. The paper focuses on seagrass meadows, particularly *Posidonia oceanica* and *Cymodocea nodosa*, being the most abundant along the Greek coasts, and assess their distribution and connectivity patterns, in order to assess the role of seascape patterns in coastal protection.

Methods

The paper focuses on the role of the connectivity of seagrass meadows in enhancing coastal protection. The dataset developed by Panayotidis et al (2022) was used to account for the spatial distribution of seagrass meadows in the Greek coastal zone (Figure 1). Extra emphasis is given on *Posidonia oceanica*, a seagrass species endemic to the Mediterranean Sea, considered a priority habitat under the European Union's Habitats Directive (92/43/EEC). Seagrass beds form extensive underwater meadows up to 40 meters depth that provide essential ES, such as coastal protection. Coastal protection provided by seagrasses is based on their capacity to mitigate flooding and erosion, which are the primary natural threats to coastlines (Ondiviela et al., 2013). Seagrass beds and even more, *Posidonia oceanica* are well known for their ability to provide coastal protection through mechanisms such as wave attenuation and sediment stabilization (Campagne et al., 2015). They reduce wave energy, thereby mitigating the hydrodynamic force impacting the shoreline. The effectiveness of wave attenuation is influenced by factors such as meadow extent, density, blade length, and the overall health of the seagrass ecosystem. Beyond direct habitat effects, seagrass banquettes— formed on the shoreline by beach-cast dead leaves and rhizomes from the meadows— also absorb wave energy, acting as natural barriers that further enhance coastal resilience against erosion and storm surges. (Boudouresque et al., 2016; Ottero et al., 2018).

While there is little research on the contribution of *Cymodocea nodosa* on coastal protection, it has been shown that the species' meadows in combination with *Posidonia oceanica* meadows could significantly reduce the average annual wave height, reducing the amount of energy reaching the beach and enhancing the defense against flooding and erosion. Also, the largest wave damping can be observed in water depths between 1 and 5 meters, because of the greater submergence ratio (canopy height over water depth) (Sierra et al., 2023). In the Greek coastal zone, *C. nodosa* replaces *P. oceanica* at these depths in almost every semi-enclosed gulf where muddy-sand substrata prevail (Panayotidis et al., 2022).

Continuous and dense meadows provide a larger surface area for interaction with water flow, enhancing their capacity to reduce wave and current energy. Fragmented meadows, however, may not offer the same level of protection due to reduced biomass and connectivity. Also, fragmented meadows may lead to increased coastal erosion as the protective barrier they provide is compromised (Ondiviela et al., 2013). In addition, fragmentation can lead to increased sediment resuspension and transport, as the cohesive structure of the meadow is disrupted, reducing its ability to trap and stabilize sediments effectively (Montefalcone et al., 2010).

Incorporating this information within existing models of coastal protection is achieved through the identification and quantification of biophysical and socioeconomic variables. An adaptation of the model developed by Liquete et al. (2013) and downscaled by Hasan et al. (2022), is used. They assessed coastal protection through three indicators: coastal protection capacity, exposure and demand. Through these indicators they calculated the flow of the ES and eventually the benefit of coastal protection. Data on 20 biophysical and socio-economic variables were collected. For coastal protection capacity, slope, geomorphology, seabed and emerged habitat and sediment accretion rate were considered. Within the seabed and emerged habitat variables, an additional to the original model variable to capture the connectivity impact on coastal protection, was included. To assess the structural connectivity and fragmentation patterns

of the meadows, spatial pattern metrics using the FRAGSTATS software were calculated. Metrics and indicators that describe density and shape of the habitat patches, but also those which are dedicated connectivity measures, such as Splitting and Aggregation Indices were selected. For coastal protection exposure, wave height, storm surge height, sea level rise and tidal range, as well as wind speed and eastward and northward current were considered. Coastal protection demand was calculated based on population density, transportation network, artificial surface and cultural sites density, with the addition of port area density, ecologically important site density and mineral extraction site density.

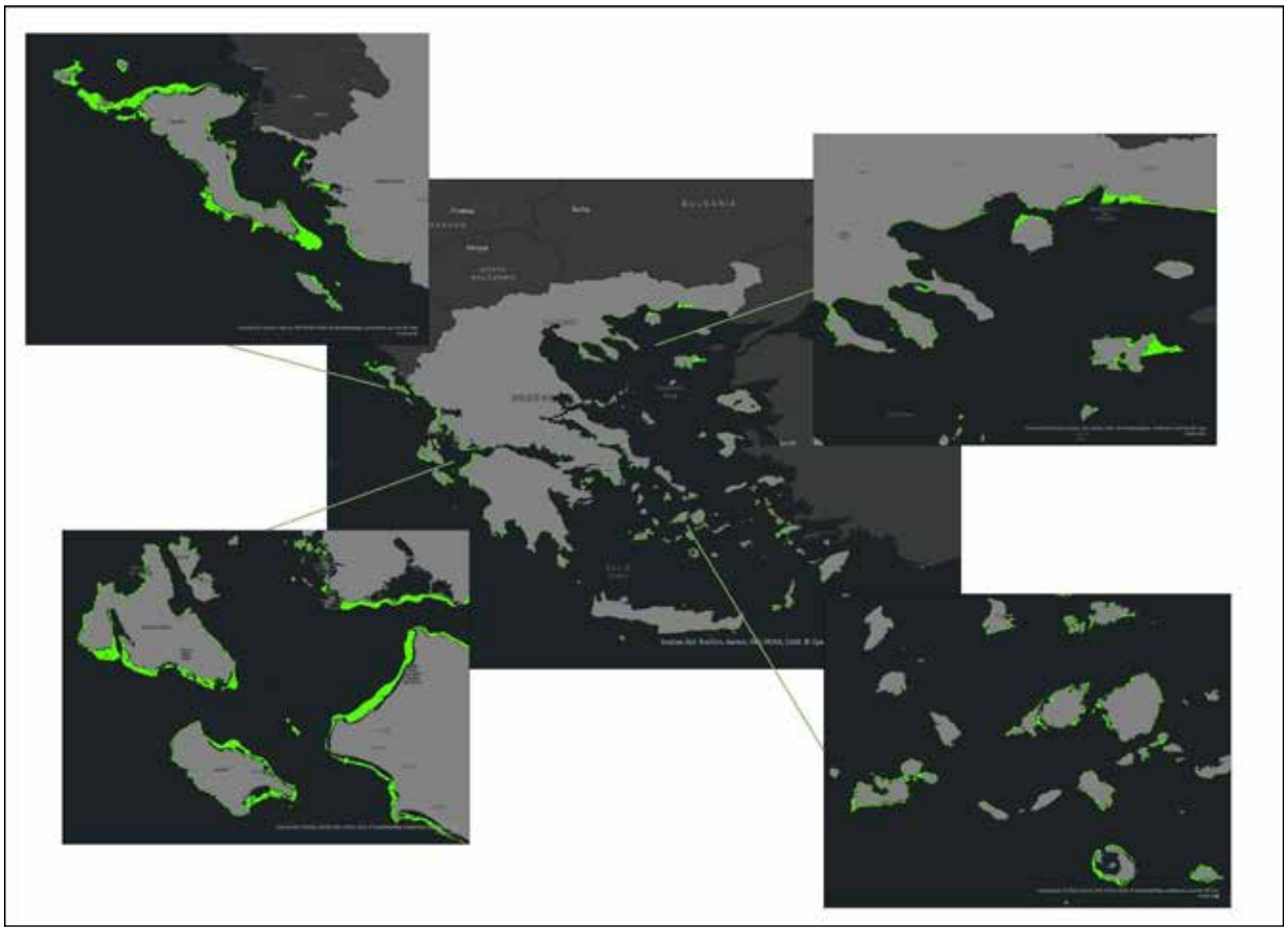

Figure 1. Seagrass meadows in the Greek coastal zone adapted from Panayotidis et al., 2022.

Results

The results are analyzed at two levels: i) the understanding of the spatial patterns emerging across the seascape and ii) the coastal protection ES across the coastal zone of Greece, and its linkage with the spatial patterns of seagrass meadows. For the connectivity assessment, a series of landscape metrics were applied on the locations of seagrass meadows across the coastal seascape. The indicators used were analyzed statistically to identify those that can better describe the variability in structure of submerged coastal vegetation. The results indicated that Shape and Aggregation metrics were able to reveal differences across locations. For instance, the islands of the north Aegean Sea such as Lemnos, or the Western part of the country such as Peloponnese and Corfu (in the Ionian Sea), had largely connected habitats, while the coastline of the mainland or Crete had a quite patchy and dispersed habitat.

Connectivity indicators were then included in the modelling of coastal protection and the results indicate

that there might be a shared pattern across the two. The largest cities in Greece, particularly Athens and Thessaloniki, seem to have low natural protection capacity since seagrass meadows are absent or at low density. Many of the islands show a pattern of high demand and exposure to coastal threats, yet only those with presence of seagrasses have medium natural capacity for protection. Also, certain regions within Peloponnese, particularly in the northern and eastern parts, experience high exposure and demand for coastal protection while simultaneously having low protection capacity. Only areas that have high density of seagrass meadows, such as the southern west and east part of Attica, coasts of Western Greece and north Aegean islands have a relatively high coastal protection capacity. The results indicate a positive correlation between well-connected seagrass vegetation with areas that show higher coastal protection capacity.

Conclusions

This research highlights the critical role of seagrass meadows and particularly *Posidonia oceanica* and *Cymodocea nodosa* in enhancing coastal protection within the Greek coastal zone, particularly in the context of increasing climate change impacts. By integrating biotic and abiotic factors to assess structural connectivity, the study underscores the importance of understanding the spatial dynamics of seagrass meadows and their contribution to mitigating coastal erosion and flooding. The findings indicate that while urban areas such as Athens and Thessaloniki face high demand for coastal protection, they simultaneously exhibit low natural protection capacity due to the natural absence or decline of seagrass meadows. Conversely, regions with dense seagrass coverage demonstrate a greater ability to withstand coastal threats. The research emphasizes the need for comprehensive coastal management strategies that prioritize the protection and restoration of these important ecosystems, particularly in areas most vulnerable to extreme weather events.

References

Anastasiou, S., & Sylaios, G. (2016). Assessment of Shoreline Changes and Evaluation of Coastal Protection Methods to Mitigate Erosion. Coastal Engineering Journal, 58(2), 1650006-1-1650006–1650024. https://doi.org/10.1142/S0578563416500066

Boudouresque, C. F., Pergent, G., Pergent-Martini, C., Ruitton, S., Thibaut, T., & Verlaque, M. (2016). The necromass of the Posidonia oceanica seagrass meadow: Fate, role, ecosystem services and vulnerability. Hydrobiologia, 781(1), 25–42. https://doi.org/10.1007/s10750-015-2333-y

Campagne, C. S., Salles, J.-M., Boissery, P., & Deter, J. (2015). The seagrass Posidonia oceanica: Ecosystem services identification and economic evaluation of goods and benefits. Marine Pollution Bulletin, 97(1–2), 391–400. https://doi.org/10.1016/j.marpolbul.2015.05.061

Díaz, S., Pascual, U., Stenseke, M., Martín-López, B., Watson, R. T., Molnár, Z., Hill, R., Chan, K. M. A., Baste, I. A., Brauman, K. A., Polasky, S., Church, A., Lonsdale, M., Larigauderie, A., Leadley, P. W., Van Oudenhoven, A. P. E., Van Der Plaat, F., Schröter, M., Lavorel, S., … Shirayama, Y. (2018). Assessing nature's contributions to people. Science, 359(6373), 270–272. https://doi.org/10.1126/science.aap8826

Hasan, M. U., Drakou, E. G., Karymbalis, E., Tragaki, A., Gallousi, C., & Liquete, C. (2022). Modelling and Mapping Coastal Protection: Adapting an EU-Wide Model to National Specificities. Sustainability, 15(1), 260. https://doi.org/10.3390/su15010260

Liquete, C., Zulian, G., Delgado, I., Stips, A., & Maes, J. (2013). Assessment of coastal protection as an ecosystem service in Europe. Ecological Indicators, 30, 205–217. https://doi.org/10.1016/j.ecolind.2013.02.013

Montefalcone, M., Parravicini, V., Vacchi, M., Albertelli, G., Ferrari, M., Morri, C., & Bianchi, C. N. (2010). Human influence on seagrass habitat fragmentation in NW Mediterranean Sea. Estuarine, Coastal and Shelf Science, 86(2), 292–298. https://doi.org/10.1016/j.ecss.2009.11.018

Ondiviela, B., Losada, I. J., Lara, J. L., Maza, M., Galván, C., Bouma, T. J., & Van Belzen, J. (2013). The role of seagrasses in coastal protection in a changing climate. Coastal Engineering, 87, 158–168. https://doi.org/10.1016/j.coastaleng.2013.11.005

Otero M.M., Simeone S., Aljinovic B., Salomidi M., Mossone P., Giunta Fornasin M.E., Gerakaris V., Guala I., Milano P., Heurtefeux H., Issaris Y., Guido M., Adamopoulou M. (2018). POSBEMED: Governance and management of the Posidonia beach/dune systems. Final Report. 66pp & Annexes.

Panayotidis, P., Papathanasiou, V., Gerakaris, V., Fakiris, E., Orfanidis, S., Papatheodorou, G., Kosmidou, M.,

Georgiou, N., Drakopoulou, V., & Loukaidi, V. (2022). Seagrass meadows in the Greek Seas: Presence, abundance and spatial distribution. Botanica Marina, 65(4), 289–299. https://doi.org/10.1515/bot-2022-0011

Sierra, J. P., Gracia, V., Castell, X., García-León, M., Mösso, C., & Lin-Ye, J. (2023). Potential of Transplanted Seagrass Meadows on Wave Attenuation in a Fetch-Limited Environment. Journal of Marine Science and Engineering, 11(6), 1186. https://doi.org/10.3390/jmse11061186

Tragaki, A., Gallousi, C., & Karymbalis, E. (2018). Coastal Hazard Vulnerability Assessment Based on Geomorphic, Oceanographic and Demographic Parameters: The Case of the Peloponnese (Southern Greece). Land, 7(2), 56. https://doi.org/10.3390/land7020056

Trégarot, E., Catry, T., Pottier, A., El□Hacen, E. M., Sidi Cheikh, M. A., Cornet, C. C., Maréchal, J., & Failler, P. (2021). Coastal protection assessment: A tradeoff between ecological, social, and economic issues. Ecosphere, 12(2), e03364. https://doi.org/10.1002/ecs2.3364

17th INTERNATIONAL CONGRESS of the Geological Society of Greece

BULLETIN OF THE GEOLOGICAL SOCIETY OF GREECE, SP. PUBL.

EXTENDED ABSTRACT 012

Simulation of Domestic Rainwater Harvesting Systems on Fourni Island, Aegean Sea: Assessing Efficiency Under Historic and Climate Change Scenarios.

Apostolou K.-M.[1] ,Feloni E.[2] ,Stergiadou A.[1]
1. Department of Forestry and Natural Environment, Faculty of Agriculture, Forestry and Natural Environment, Aristotle University of Thessaloniki, 54124 Thessaloniki, Greece; nanty@for.auth.gr
2. Department of Surveying and Geoinformatics Engineering, University of West Attica, 28 Ag. Spiridonos, 12243 Egaleo, Athens, Greece; efeloni@uniwa.gr

Introduction and scope

Rainwater harvesting (RWH) has long been an essential practice for ensuring water availability, especially in regions with limited freshwater resources. With increasing global concerns about climate change, the demand for sustainable water management systems has grown (EEA, 2009). Climate change is exacerbating existing water scarcity problems, contributing to prolonged droughts, extreme heat events, and shifting precipitation patterns (Eckstein, 2009). The Greek islands, particularly small islands like Fourni, face significant challenges in water security due to their limited natural water sources (Feloni and Nastos, 2024). This underscores the potential of rainwater harvesting systems to provide an efficient alternative for in-house water needs, such as toilet and laundry use, while enhancing the sustainability of both the island's water resources and the agricultural sector (Essendi, 2014; Koumoura et al., 2018; Londra et al., 2015, 2022).

Fourni Island, located in the Aegean Sea, is characterized by its small population, limited freshwater supply, and vulnerable water resources. This makes it an ideal case study for assessing the potential role of rainwater harvesting systems in addressing local water scarcity.

This study focuses on evaluating various domestic RWH scenarios to simulate the system's efficiency under both historical climatic conditions and projected future scenarios based on the Representative Concentration Pathways (RCP) 4.5 and 8.5 models. These scenarios allow for an exploration of how climate change might influence the feasibility of RWH systems for domestic use, with specific attention given to factors such as household size, tank volume, and rooftop collection area. In this work, we simulate a range of scenarios involving different household sizes (2, 3, and 4 residents), rooftop areas (40-140 m²), and tank volumes (5-30 m³) to assess their impact on the efficiency of RWH systems in achieving coverage targets of 30%, 40%, and 50% of daily water consumption needs. We also consider how these systems would perform under both current climate conditions and the future projections of the RCP 4.5 and RCP 8.5 models, using available timeseries of the EURO-CORDEX regional climate downscaling (Jacob et al., 2020) provided by the DEAR-Clima web application (DEAR-Clima, 2023). While rainwater harvesting systems have the potential to offer significant benefits in arid regions (e.g., Preka et al., 2017), this study highlights the challenges faced by Fourni Island in meeting the desired coverage targets, especially considering future climate projections.

Methods

To evaluate the performance of the rainwater harvesting (RWH) system and compare different scenarios, a water balance simulation model was employed (Tsihrintzis and Baltas, 2013). This model simulates the daily operation of the RWH system, focusing on the collection, storage, and utilization of rainwater. The system collects rainwater from rooftops and other available surfaces and stores it in tanks, which vary in material and size.

To implement the model, it is crucial to have accurate rainfall data for the region. This data serves as input to the simulation model, determining the volume of rainwater that can be captured. Additionally, the volume of rainfall influences the sizing of the storage tank and helps assess the percentage of demand that the system can meet.

The amount of stored water is calculated using a daily water balance equation:

$$St = St{-}1 + Rt - Dt \ , \ 0 \le St{-}1 \le Vtank$$

Where: St the volume of water that can be stored in the tank on t days (m^3), $St-1$ the volume of water that can be stored in the tank on the previous day (m^3), Rt the volume of the rainwater that runoff from the collection water and enters the tank on t days (m^3), Dt the demands on water on day t (m^3) και $Vtank$ the capacity of the water tank (m^3).

The efficiency of the rainwater harvesting system is determined for the simulation period using the efficiency factor Re. To calculate the efficiency factor Re, several equations are used in the simulation model (Rosas et al., 2024). These equations account for daily storage, runoff, and demand, and allow for the determination of the system's performance across different scenarios, including variations in household size, collection area, and tank volume. In this analysis, this factor is the ratio of the number of days in which the tank water meets the household's full water needs to the total number of days over which the rainfall data is recorded and used in the model.

$$Re = \frac{D_{eff}}{D_{total}}$$

Where: Re is the Efficiency factor, as the ratio of effective days (D_{eff}) to the total number of simulation days (D_{total}).

In this study, daily rainfall data for the area of Fourni were used to simulate the performance of the rainwater harvesting system. The data covered a period from 2012 to 2023, encompassing a total of 10 hydrological years. This data was used as input for the simulation model to determine the volume of rainwater that could be harvested over the specified period.

Several different scenarios were analyzed to assess the impact of various factors on the efficiency of the rainwater harvesting system. The scenarios considered the following parameters:

- Household Size: Two different household sizes were modeled: one with 2 members and another with 4 members. These values were represented as N_{cap}, reflecting the number of people in the household and their corresponding water demands.
- Rooftop Area: The area of the rooftop used for rainwater collection was varied between 40 m² and 140 m². This range covers typical household roof sizes, affecting the volume of rainwater that can be harvested each day.
- Rainwater Tank Volume: The capacity of the rainwater storage tank was varied between 5 m³ and 30 m³. Larger tank volumes allow for more significant storage and provide greater flexibility to manage periods of lower rainfall.
- Coverage Target: The primary objective of the study was to meet a coverage target of 30% of the household's total daily water demand that is about the water amount required for toilet demand (Domènech and Saurí, 2011, after Domene et al., 2004). Further analysis also provided regarding the target of meeting the 40% and 50% of the total daily water demand. The daily water demand was set at 180 L per person, a standard value based on typical household usage for non-potable needs, such as toilet flushing and laundry. Each of these factors was simulated across a range of possible configurations, with the efficiency of the system being evaluated based on the ability to meet the target coverage. The simulations allowed for the comparison of different scenarios and helped to identify which combinations of household size, collection area, and tank volume provide the most efficient solutions for rainwater harvesting on Fourni Island.

The efficiency of the rainwater harvesting system was further examined under future climate change scenarios. To simulate the potential impacts of climate change on the system's performance, EURO-CORDEX climate projections were used, focusing on two representative concentration pathways (RCPs): RCP4.5 (moderate scenario) and RCP8.5 (adverse scenario). These climate scenarios provide projections of future climate conditions, offering insights into how temperature, precipitation, and other climate variables may evolve over time. The time series for future estimates was set to cover 30 hydrological years, from October 1st, 2030 to September 30th, 2060. It is important to note that these projections are not forecasts but tools used to simulate potential climate conditions based on current climate models.

For the future climate scenarios, the following parameters were considered:

- Household Size: The simulations included household sizes of 2 and 3 members (N_{cap} =2,3), reflecting

different household configurations and their corresponding water needs.

- Rooftop Area: The rainwater collection area was adjusted to a range of 60 m² to 100 m². This represents a slightly larger minimum collection area compared to the historical scenarios, accommodating potential increases in demand or larger household sizes in the future.
- Rainwater Tank Volume: The tank volume was limited to a smaller range, between 5 m³ and 10 m³, reflecting the more conservative storage capacity designed for future needs, potentially due to anticipated changes in rainfall patterns and storage efficiency under climate change. These sizes are also available in the market.
- Coverage Target: As with the historical scenarios, the coverage target was set at 30% of the household's total daily water demand. This target was chosen to match non-potable water usage such as toilet flushing, with the daily demand still set at 180 L per person.

The climate scenarios were used to simulate the effect of changing precipitation patterns and other climate variables on the efficiency of the rainwater harvesting system. The simulations aimed to determine how the system's ability to meet the daily water demand would be affected under the moderate scenario (RCP4.5) and high emissions scenario (RCP8.5). This analysis helps to assess the potential future performance of the system and identify how climate change may influence the viability and effectiveness of rainwater harvesting as a sustainable water supply solution for Fourni Island.

To better illustrate the system's performance under varying scenarios, the daily fluctuation of water storage in the domestic tank is presented for cases involving two (2) household members and tank volumes ranging from 5 to 20 m³ (Figure 1). Calculations are based on the daily water balance method. Additionally, for the smallest tank volume, changes in water storage are shown for several rooftop areas (60–100 m²). As observed, rooftop area is the most critical parameter influencing model efficiency. Under the first scenario, overall performance reaches 89%; when rooftop area increases, the system fully satisfies the target demand coverage.

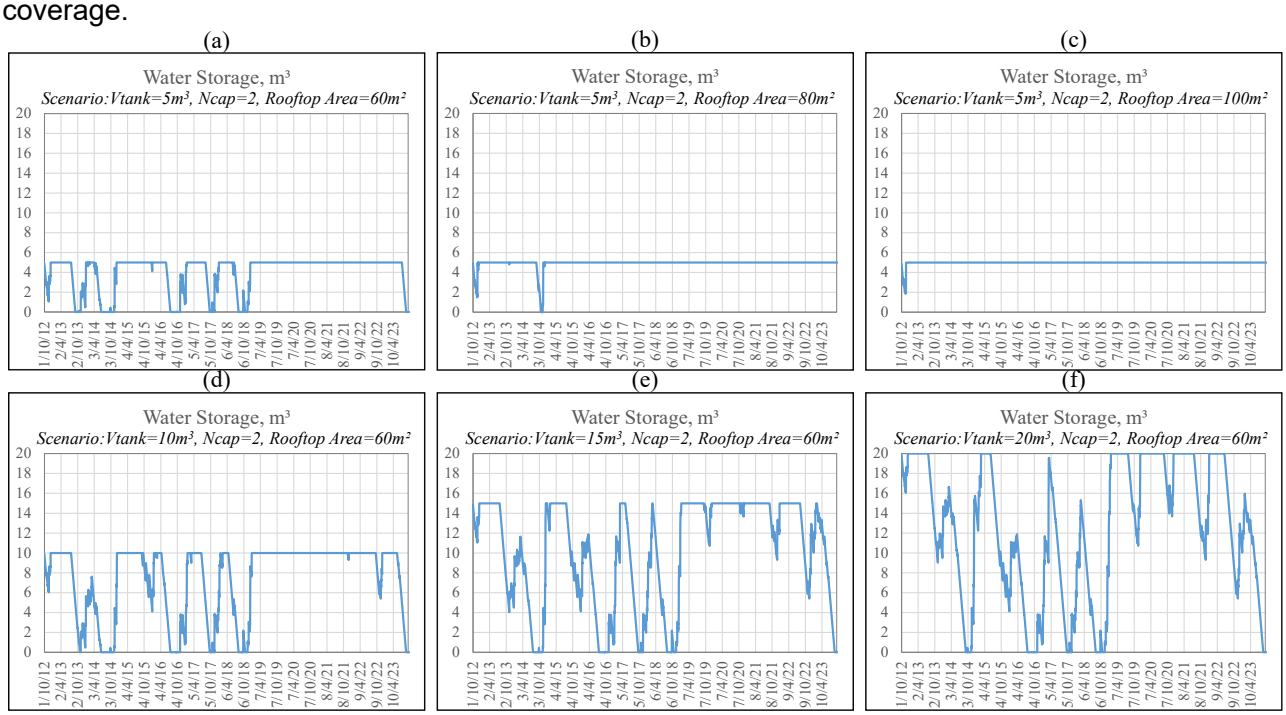

Figure 1. Daily water storage fluctuation in the domestic tank under different combinations of tank volume and rooftop area for two household members, using the water balance method. Sub-figures represent: (a) V = 5 m³, rooftop area = 60 m²; (b) V = 5 m³, rooftop area = 80 m²; (c) V = 5 m³, rooftop area = 100 m²; (d) V = 10 m³, rooftop area = 60 m²; (e) V = 15 m³, rooftop area = 60 m²; (f) V = 20 m³, rooftop area = 60 m².

Results

Initial simulations (historic timeseries of a ten-year period)

The results of the rainwater harvesting system simulation highlight the impact of rooftop collection area and tank volume on system efficiency, expressed through the reliability factor Re. The system's performance was assessed for different household sizes and water demand coverage targets.

- Household with 2 Members (N_{cap}=2): As shown in Figure 2, for a rooftop area of 80 m² or larger, the system meets the 30% water demand coverage target. The efficiency of the system increases with larger rooftop areas, reaching near 100% for collection areas of 120 m² regardless of the size of the tank. In other words, tank volume has a lesser impact on efficiency compared to the rooftop area, as even smaller tanks (5-10 m³) provide sufficient storage when combined with a large collection surface.
- Household with 3 Members (N_{cap}=3): As seen in Figure 2 (right panel), when the household size increases, the system struggles to meet the 30% coverage target for most scenarios. The target is only achieved for collection areas of 140 m² with large tank volumes. For smaller rooftop areas (≤100 m²), the system remains inefficient, indicating that a larger roof area is essential for sustaining a 3-member household.
- Higher Coverage Targets (40% and 50%): When the target coverage is increased to 40% and 50% of total water demand, the system's reliability significantly drops for smaller collection areas. The system is only effective ($Re \geq 90\%$) when the collection area is at least 100 m². Tank volume remains a less sensitive parameter, meaning that increasing storage capacity does not significantly improve efficiency unless the collection area is also sufficiently large.

The graphical results provide valuable insights into selecting the optimal tank size based on individual household conditions. By examining the figures, it becomes evident that the coverage target is more frequently achieved in the 2-member household compared to larger households.

- For 2-member households , the system successfully meets the 30% coverage target for collection areas starting from 80 m².
- For 3-member households, achieving the 30% target is significantly more challenging and is only possible for the largest rooftop area (140 m²) with maximum tank volumes.
- For 4-member households, the system fails to meet the 30% coverage target in all cases, indicating that rainwater harvesting alone cannot be a reliable solution for larger families under current conditions.

When the coverage target increases beyond 30%, the system's performance declines, as seen in Figure 3.

The key observations are:

- Only collection areas of 100 m² or larger provide acceptable efficiency ($Re \geq 90\%$) for 40% and 50% demand coverage.
- Tank size has a limited impact compared to rooftop area, reinforcing the importance of maximizing the collection surface rather than solely increasing storage capacity.
- The system's reliability remains low overall, as it rarely meets higher demand coverage targets, emphasizing the need for supplementary water sources on Fourni Island.

These findings underline the limitations of RWH systems in semi-arid environments and suggest that their effectiveness is highly dependent on household size, available rooftop area, and target water demand levels.

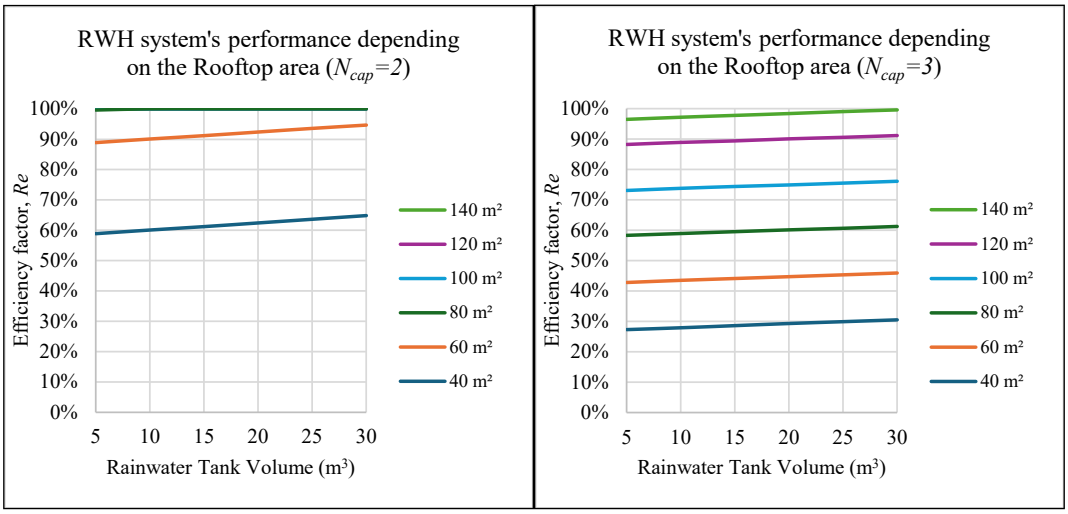

Figure 2. RWHS' performance for two-member (left panel) and three-member household (right panel), and for a 30% coverage target, using the historic timeseries.

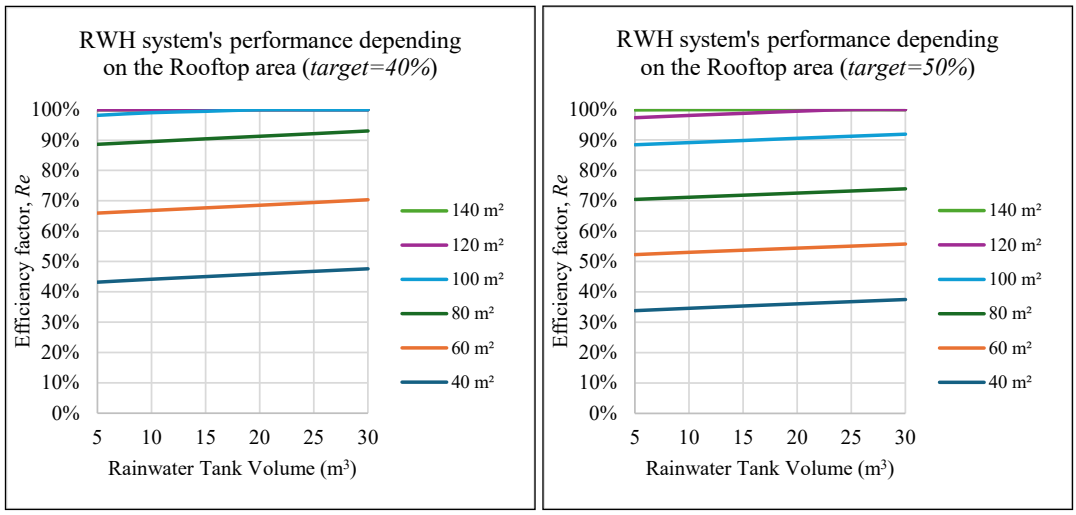

Figure 3. RWHS' performance for a two-member household, and for a coverage target of 40% and 50% (historic period).

B. Impact of Climate Change on System Performance

The results of the rainwater harvesting system simulations (Table 1; codes 1-8) under climate change conditions (RCP 4.5 and RCP 8.5) reveal notable variations compared to the historical timeseries (Table 1; code = 0). The system's efficiency, represented by the reliability factor, Re, is particularly affected for the cases of smaller collection areas, demonstrating the potential impact of altered precipitation patterns in future scenarios.

Key observations from Climate Change (CC) simulations and for a two-member household are presented in Figures 4-5, for RCP4.5 and RCP8.5, respectively. The performance of the rainwater harvesting system under climate change scenarios exhibits significant variability across models. The CC6 scenario (SMHI-RCA4_IPSL-IPSL-CM5A-MR) consistently results in the lowest system performance for both RCP 4.5 and RCP 8.5, irrespective of tank size (5 m³ or 10 m³), indicating that rainfall projections under this model predict less favorable conditions for rainwater harvesting efficiency. In contrast, CC3 and CC4 slightly overestimate system efficiency, yielding performance levels marginally higher than those observed in the historical period; however, these improvements are negligible and do not significantly alter the overall conclusions regarding RWH feasibility. A general decline in system reliability is evident, as most climate

change simulations indicate a decrease in the *Re* factor, with system effectiveness projected to deteriorate under future climate conditions. On average, the *Re* factor under climate change scenarios is approximately 15% lower than in the historical period for a rooftop area of 60 m², suggesting that reduced precipitation and increased variability may challenge the reliability of RWH systems on Fourni Island. These findings underscore the vulnerability of rainwater harvesting systems to climate change, particularly for smaller collection areas, with potential consequences for households reliant on rainwater as a primary source of water. To ensure long-term water security, additional water management strategies may be necessary. Meanwhile, larger collection areas (≥100 m²) remain the most effective approach to maintaining system efficiency despite changing climatic conditions. Overall, the results highlight the need for adaptive planning in water resource management to mitigate the adverse effects of climate change on domestic rainwater harvesting, especially in small island environments.

Table 1. Summary of Climate Change Scenario Simulations for Precipitation Inputs

code	Timeseries/ EURO-CORDEX Models Used for Future Rainfall Projections
0	historic period daily precipitation timeseries
1	CLMcom-CCLM4-8-17_CNRM-CERFACS-CNRM-CM5
2	CLMcom-CCLM4-8-17_MPI-M-MPI-ESM-LR
3	IPSL-INERIS-WRF331F_IPSL-IPSL-CM5A-MR
4	KNMI-RACMO22E_ICHEC-EC-EARTH
5	SMHI-RCA4_CNRM-CERFACS-CNRM-CM5
6	SMHI-RCA4_IPSL-IPSL-CM5A-MR
7	SMHI-RCA4_MOHC-HadGEM2-ES
8	SMHI-RCA4_MOHC-HadGEM2-ES

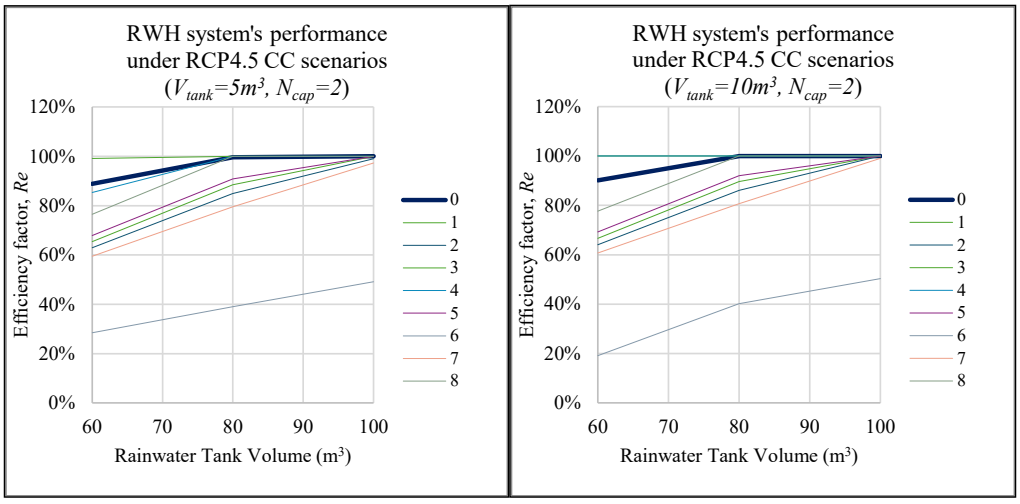

Figure 4. Performance of the Rainwater Harvesting System (RWHS) under Various Climate Change Scenarios (RCP 4.5).

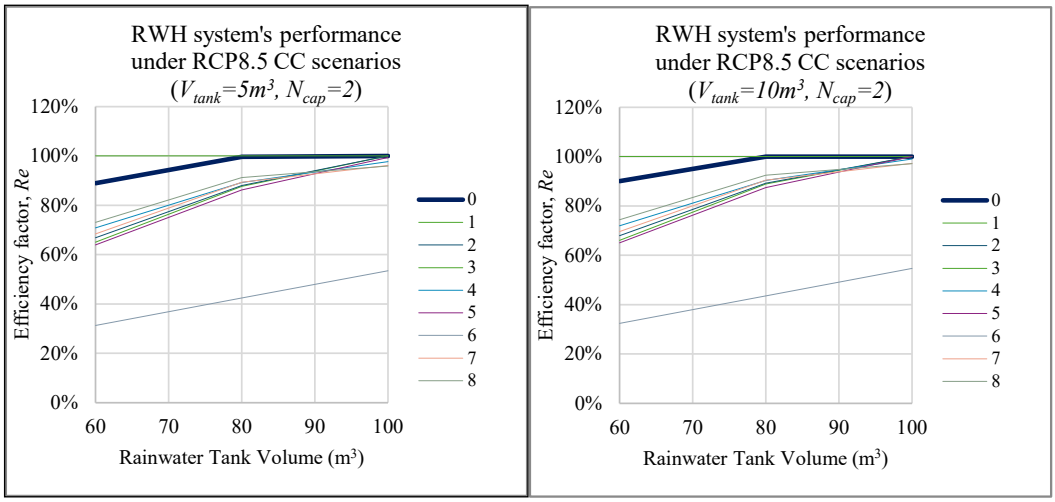

Figure 5. Performance of the Rainwater Harvesting System (RWHS) under Various Climate Change Scenarios (RCP 8.5).

Conclusions

This study assessed the efficiency of domestic rainwater harvesting (RWH) systems on Fourni Island, Greece, under various household and climate change scenarios. The findings highlight the potential and limitations of RWH as a supplementary water source in an arid island environment with limited freshwater resources.

The results demonstrated that rooftop collection area is the most significant factor influencing the system's performance. Larger collection surfaces (≥100 m²) improve system efficiency, ensuring higher rainwater availability. Tank volume plays a secondary role; once a sufficient storage capacity is reached (10-30 m³), additional increases in volume provide diminishing returns in performance.

For two-member households, the system achieved the 30% coverage target in several scenarios, particularly when collection areas exceeded 80 m². However, for three- and four-member households, meeting the coverage target proved significantly more challenging. The four-member household scenario failed to reach the target under any conditions, highlighting the system's limitations in larger households. Higher coverage targets (40% and 50%) further reduced the system's efficiency, requiring rooftop areas of at least 100 m² to maintain reliability (Re ≥ 90%).

When assessing the impact of climate change (RCP 4.5 & RCP 8.5) on system reliability, most scenarios projected a decline in efficiency. Most climate models indicated an average 15% reduction in Re compared to historical conditions, particularly for smaller collection areas (60 m²). The CC6 scenario (SMHI-RCA4_IPSL-IPSL-CM5A-MR) consistently showed the lowest efficiency across both climate pathways, indicating that future rainfall projections under this model predict less favorable conditions for RWH. In contrast, CC3 and CC4 models slightly overestimated system performance but did not significantly alter overall conclusions.

Despite these challenges, RWH remains a viable water management strategy, particularly during peak demand periods such as the tourist season, when water needs increase sharply. While it may not fully replace conventional water sources, RWH can serve as a reliable supplementary resource, reducing dependence on external water supply systems.

Future research should focus on cost-benefit analysis, assessing whether the implementation of RWH systems is economically viable for households in the short and long term. Additionally, exploring hybrid solutions, such as integrating RWH with desalination or greywater reuse, could enhance water security on small islands like Fourni.

In conclusion, while RWH offers potential benefits, its effectiveness depends on site-specific factors such as rooftop area, storage capacity, and climate conditions. Policymakers and local authorities should consider

adaptive planning strategies, including financial incentives for larger collection areas and optimized tank sizing, to improve the feasibility and long-term sustainability of RWH in water-scarce island regions.

References

DEAR-Clima, Data Extraction Application for Regional Climate (2023). Web Application Tool. Available online: http://meteo3.geo.auth.gr:3838/ (accessed on October 12, 2023).

Domene, E., Saurí, D., Martí, X., Huelin, S., Boada, M., Garriga, N. and Molina, J., 2004. Estudi del consum d'aigua als edificis de la Regió Metropolitana de Barcelona. Situació actual i possibilitats d'estalvi. Fundació Abertis, Universitat Autònoma de Barcelona, Departament de Medi Ambient i Habitatge and Fudació Agbar [online]

Domènech, L. and Saurí, D., 2011. A comparative appraisal of the use of rainwater harvesting in single and multi-family buildings of the Metropolitan Area of Barcelona (Spain): social experience, drinking water savings and economic costs. Journal of Cleaner production, 19(6-7), pp.598-608.

Eckstein, G.E., (2009). Water scarcity, conflict, and security in a climate change world: challenges and opportunities for international law and policy. Wis. Int'l LJ, 27, p.409.

EEA, European Environment Agency (2009). Water resources across Europe – confronting water scarcity and drought, Copenhagen. Retrieved in January 2011 from http://www.eea.europa.eu/publications/water-resources-across-europe/at_download/file (Last accessed on December 30, 2024).

Essendi, S.M., (2014). Enhancing household water use efficiency and domestic rainwater harvesting potential in Nairobi county (Doctoral dissertation, University of Nairobi).

Feloni, E. & Nastos, P.T., (2024). Evaluating Rainwater Harvesting Systems for Water Scarcity Mitigation in Small Greek Islands under Climate Change. Sustainability, 16(6), p.2592.

Jacob, D., Teichmann, C., Sobolowski, S., Katragkou, E., Anders, I., Belda, M., Benestad, R., Boberg, F., Buonomo, E., Cardoso, R.M. & Casanueva, A., (2020). Regional climate downscaling over Europe: perspectives from the EURO-CORDEX community. Regional environmental change, 20, pp.1-20.

Koumoura, K.A., Feloni, E.G., Londra, P.A., Baltas, E.A. and Tsihrintzis, V.A., 2018. Uncertainty analysis in sizing rainwater harvesting tanks in an isolated island with limited water resources. Glob. NEST Int. J, 20, pp.534-540.

Londra, P.A., Theocharis, A.T., Baltas, E. & Tsihrintzis, V.A., (2015). Optimal sizing of rainwater harvesting tanks for domestic use in Greece. Water resources management, 29, pp.4357-4377.

Londra, P.A., Gkolfinopoulou, P., Mponou, A. & Theocharis, A.T., (2022). Effect of Rainfall Regime on Rainwater Harvesting Tank Sizing for Greenhouse Irrigation Use. Hydrology, 9(7), p.122.

Preka, M., Feloni, E., Londra, P., Kotsifakis, K. & Baltas, E. (2017). Rainwater harvesting tanks' efficiency in Thera Island. 15th International Conference on Environmental Science and Technology, Rhodes, Greece, 31 August to 2 September 2017.

Rosas, D.F., de Oliveira, F.G., de Castilho Carvalho, L., de Almeida, J.C.A., Souza, A.B., de Souza Lemos, J., Júnior, A.A.O. & Obraczka, M., (2024). Method of Calculation the Efficiency and Economic Viability of Rainwater Harvesting Systems. Revista De Gestão Social E Ambiental, 18(2), pp.e04471-e04471.

Tsihrintzis, V. and Baltas, E., (2013). Sizing of rainwater harvesting tank for in-house water supply. In 13th International Conference on Environmental Science and Technology, Athens, Greece (pp. 5-7).

17th INTERNATIONAL CONGRESS of the Geological Society of Greece

BULLETIN OF THE GEOLOGICAL SOCIETY OF GREECE, SP. PUBL.

EXTENDED ABSTRACT 013

Metapelitic assemblages in the contact metamorphic zone of the Varnous plutonite (NW Macedonia, Greece): preliminary results.

Aravani F.[1], Papadopoulou L.[1], Koroneos A.[1], Chatzipetros A.[2]

(1) Department of Mineralogy-Petrology-Economic Geology, School of Geology, Aristotle University of Thessaloniki, 54124 Thessaloniki, Greece, faravani@geo.auth.gr. (2) Department of Structural, Historical & Applied Geology, School of Geology, Aristotle University of Thessaloniki, 54124 Thessaloniki, Greece

Introduction

The area of the Varnous plutonite is located in northwestern Macedonia, Greece. It lies west of the town of Florina, east of Mikri Prespa Lake, and extends northward across the border between Greece and North Macedonia. The southern boundary extends to the foothills of Mount Vernon (Fig. 1). The plutonite is differentiated, comprising various petrological types ranging from leucogranite to monzodiorite (Katerinopoulos, 1983; Koroneos & Christofides, 1990; Koroneos, 1991; Koroneos et al., 1991; Koroneos 1993, Koroneos et al., 1994). It intruded the basement of the Pelagonian Nappe in 297 Ma (Koroneos et al., 1993).

Although several studies have mentioned the existence of thermally metamorphosed rocks in contact with plutonite, this aspect has not been thoroughly investigated (Kilias, 1980; Katerinopoulos, 1983; Kilias & Mountrakis 1989; Koroneos, 1991). There is ongoing debate regarding whether these rocks are thermally or regionally metamorphosed (Mposkos et al., 2001). The aim of this study is to identify the different metamorphic assemblages and clarify the presence or absence of a thermal aureole.

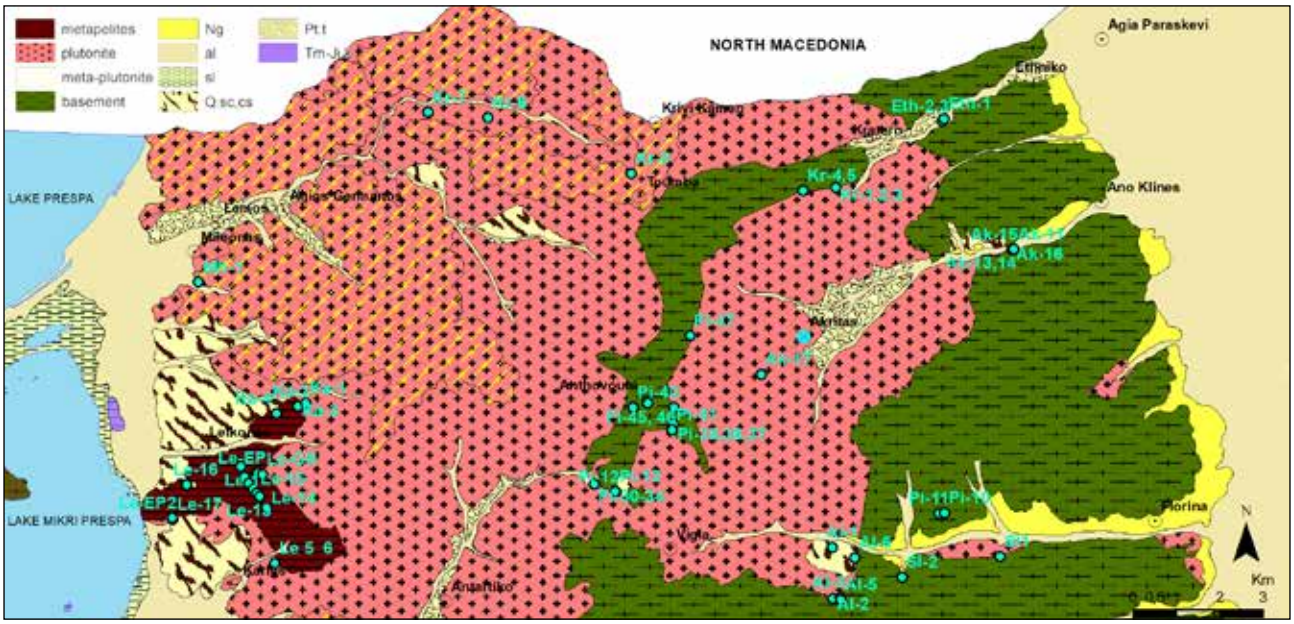

Figure 1. Geological map of the study area., Ng=Neogene sands, clays and conglomerates, al=alluvial deposits, sl=marshy areas, Q.sc,cs=old and recent scree and talus cones, Pt.t=old terrestrial terraces, Tm-Ji.k= Middle Triassic-Lower Jurassic limestones and dolomitic limestones. With cyan sampling locations

Materials and Methods

Seventy-eight polished-thin sections of the rocks surrounding the plutonite were studied by optical and scanning electron microscope for the determination of their mineralogical composition and their textures (see Figure 1 for sampling locations). The scanning electron microscope used was a JEOL JSM-6390LV type equipped with an energy dispersive spectrometer INCA 300, at the Laboratory of Scanning Electron Microscopy at Aristotle

University of Thessaloniki. Analytical conditions were 20 kV operating voltage, 0.4 mA beam current, 80 s analysis time and ≈1 μm beam diameter.

Results

For better data management, the study area has been subdivided into three regions: the eastern part, parallel to the Florina-Agia Paraskevi Road; the western part, parallel to the Andartiko-Mileonas road; and the southern part, parallel to the Florina-Pissoderi-Andartiko road. The southern and eastern parts exhibit the most similarities, while the western part is considerably different.

The eastern part contains the most complex assemblages within the study area. In the same thin section, minerals from a wide range of temperatures and pressures can be observed. The samples can be divided into those that contain sillimanite and those that do not. The main assemblages are as follows (abbreviations after Whitney and Evans 2010)

- Qtz + Mica (Ms-Ph+Pg) + Bt + Grt + St + Sil ± Chl ± Ilm ± Pl ± Ap, and
- Qtz + Mica (Ms-Ph+Pg) + Chl + Grt + Cld ± Bt ± Ilm

Analyses of the minerals are presented in Table 1.

Similar assemblages are found in the southern part; however, in some cases, St occurs alongside Cld. Evidence of overprinting in the samples (Figs. 2 and 3) suggests that the minerals formed as a result of polymetamorphism. Large garnet crystals contain inclusions of sillimanite and appear broken and deformed. A new generation of garnet is observed, characterized by small euhedral crystals. Staurolite and chloritoid occur in some locations, forming euhedral crystals that do not conform to the rock's overall texture. In some samples, sillimanite appears broken and/or replaced by mica, while in other cases, it occurs in the form of fibrolite.

In contrast, the main assemblage in the western part is Qtz + Mica (Ph + Par + Mrg) + And + Crd + Bt ± Pl ± Kfs ± Chl ± Ilm ± Rt ± Sil ± Cld. Crd is, in some cases, almost completely replaced by Ms, Mrg, Bt, and Chl (Fig a,b). In other cases, Crd rim is altered to pinite (Fig. 2 c,d).

Table 1. Representative compositions of minerals from the samples of the area. The structural formulae were calculated on the basis of fixed oxygens. FeOt=total.

	Ms-Ph	Mrg	Pg	Bt	Chl	And	Sil	Crd	Cld	Grt	Pl	Kfs
	Le-1a	Ka-2	Le-2	Le-2	Le-4a	Le-17	Le-10	Le-14	Ka-2	Ka-4a	Le-11	Le-13
SiO_2	45.57	32.04	46.87	39.40	29.66	37.00	37.06	46.90	23.83	38.67	63.16	64.22
TiO_2	0.31	-	0.25	3.28	0.18	0.09	0.04	-	-	0.25	-	18.78
Al_2O_3	34.67	49.77	39.02	20.11	21.20	62.55	61.51	32.67	40.94	20.36	23.01	-
FeOt	1.75	0.30	0.29	18.23	24.29	0.03	0.14	11.25	24.23	30.9	0.1	0.12
MnO	0.08	0.25	-	0.88	1.01	-	0.4	0.11	2.12	6.74	-	-
MgO	0.48	0.03	0.10	6.00	8.44	-	-	5.62	1.48	2.77	-	-
CaO	0.12	11.27	0.53	0.17	-	0.16	0.49	0.43	0.16	1.23	4.02	0.22
Na_2O	0.29	1.35	6.19	-	0.75	-	-	0.38	0.22	-	9.09	0.91
K_2O	9.84	0.06	1.75	8.58	0.26	-	0.23	0.64	0.30	-	0.46	15.43
Total	95.1	95.06	95.03	96.66	85.72	99.84	99.65	98.01	93.29	100.92	99.83	99.68
O	22	22	22	22	28	20	20	18	14	12	8	8
Si	6.31	4.25	6.02	5.78	6.17	4.00	4.027	4.95	1.97	3.00	2.80	2.97
Al^{IV}	1.69	3.75	1.98	2.22	-	-	-	1.05	3.00	-	1.20	1.02
Al^{VI}	3.73	4.02	3.93	1.26	5.20	7.97	7.88	3.01	1.00	1.92	-	-
Ti	0.03	-	0.02	0.36	0.03	0.01	-	-	-	0.02	-	-
Fe^{2+}	0.19	0.03	0.03	2.24	3.45	-	0.01	0.99	1.68	2.07	-	-
Mn	0.01	0.03	-	0.11	0.18	-	0.04	0.01	0.18	0.46	-	-
Mg	0.09	0.01	0.02	1.31	2.62	-	-	0.88	0.15	0.33	-	-
Ca	0.02	1.60	0.07	0.03	-	0.02	0.06	0.05	0.01	0.11	0.19	0.01
Na	0.07	0.35	1.54	-	0.60	-	-	0.08	0.04	-	0.78	0.08
K	1.67	0.01	0.29	1.61	0.14	-	0.03	0.09	0.03	-	0.03	0.91

All minerals that form solid-solution series with Fe-Mg are iron rich. Chl is classified as brunsvigite, a type of chamosite, with Fe/Fe+Mg ratio of 0.62, while in Bt the same ratio is 0.63. In Cld the ratio Fe/Fe+Mg ratio is 0.8, whereas in Crd it is 0.53. As shown by the representative analyses, micas exhibit a wide range of compositions. The underlying causes of these variations in mica composition are still under investigation. Garnet, where present, is almost always represented by the following composition: $Alm_{66}Sps_{14}Py_{9}Grs_{4}Adr_{2}$. Plagioclase is classified as albite in some samples, while in others it is identified as oligoclase.

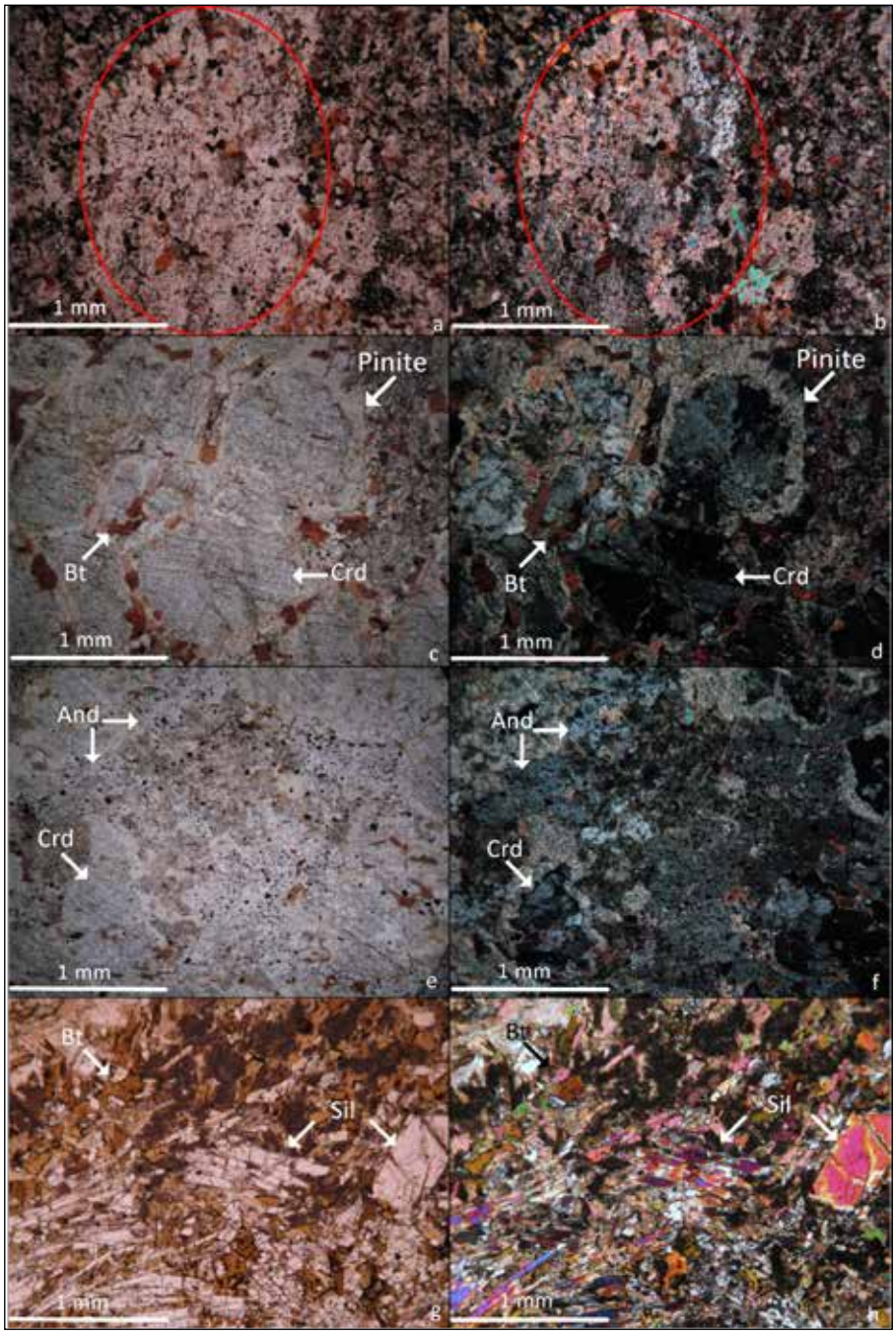

Figure 2. Microscopic images of metapelitic samples of the area. On the left are images with //N and on the right images with +N. Pictures a) and b) show pseudomorphs of mica, biotite and chlorite after cordierite from the western part. Pictures c) and d) show cordierite crystals with pinitic alteration and biotite from the western part. Pictures e) and f) show andalusite and cordierite from the western part. Pictures g) and h) show prismatic sillimanite and biotite with diablastic texture from the eastern part.

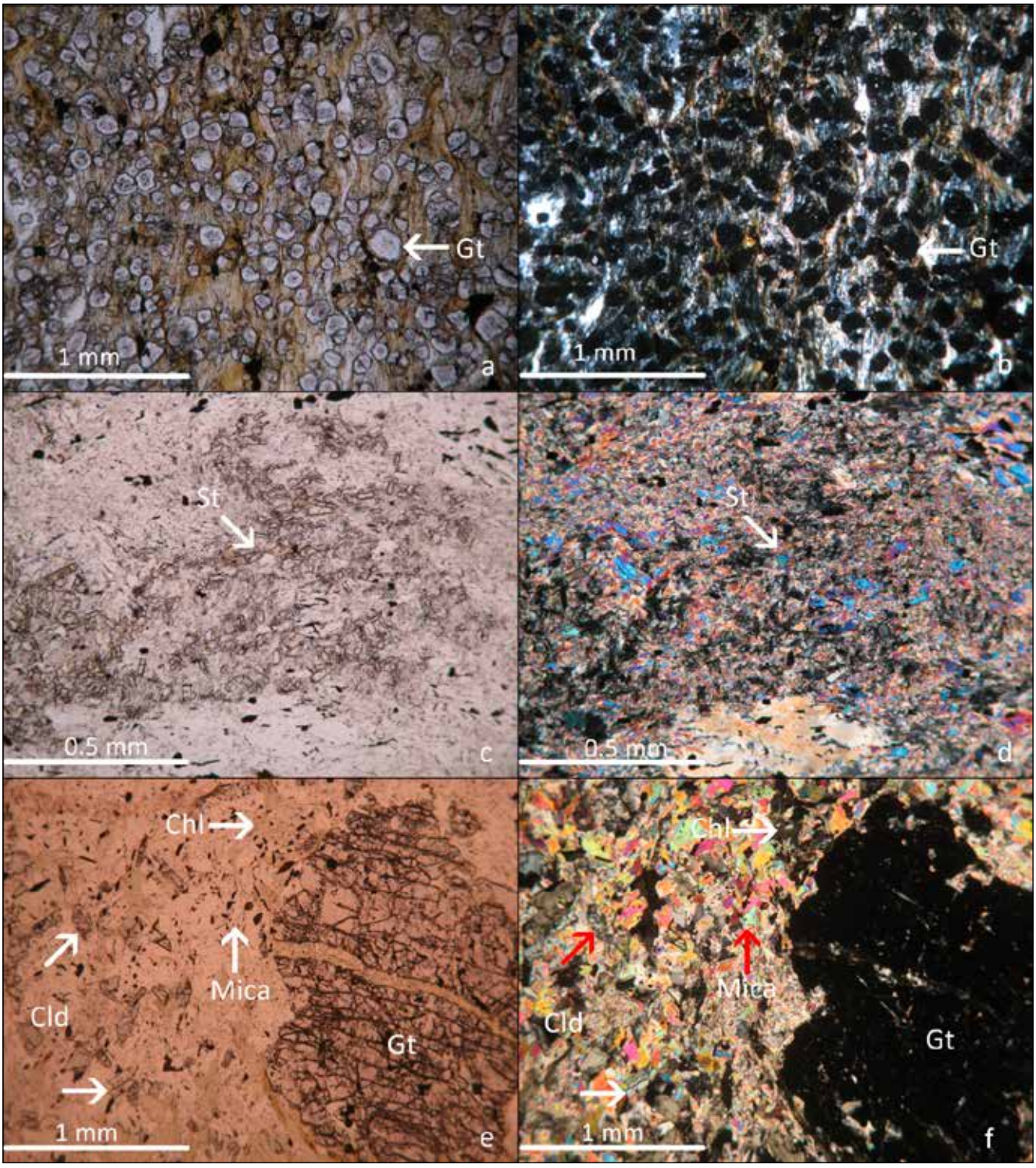

Figure 3. Microscopic images of Alpine metamorphosed rocks of the area. On the left are images with //N and on the right images with +N. Pictures a) and b) show newly formed small garnets in a biotite, chlorite, mica lepidoblastic mass from the eastern part. Pictures c) and d) show staurolite crystals with sericite mass from the eastern part. Pictures e) and f) show prismatic crystals of chloritoid with chlorite and mica and an old garnet with sillimanite inclusions, partially altered to chlorite

Discussion and Conclusions

The eastern and southern parts of the study area exhibit significant similarities, whereas the western part is distinctly different. It is important to note that the basement of the Pelagonian Nappe is considered to represent a continental fragment of Gondwana. Having been formed before the Alpine orogenesis, it has undergone all the tectonic and metamorphic stages associated with this event. Since the plutonite intruded the basement, the surrounding rocks must predate the intrusive rock, with some studies estimating their age at approximately 700 Ma (Anders, 2005; Zlatkin et al., 2014). Consequently, the tectonic history of the area supports the evidence of polymetamorphism observed in the samples.

The Alpine metamorphism in the study area has been well-documented (Avgerinas, 2014; Kilias et al., 2010). According to these studies, a metamorphic event occurred between 150 and 130 Ma, resulting in the formation of an assemblage comprising Cld + Mica + Chl + Kfs + Pl + Qtz + Grt. Another metamorphic event, dated to 110–90 Ma, overprinted the previous assemblage, as evidenced by the alteration of mica to sericite and garnet to chlorite, along with quartz and plagioclase. Finally, a mylonitic event occurred between 90 and 70 Ma.

Based on these studies, it can be inferred that the samples collected from the eastern and southern parts demonstrate these Alpine assemblages, as well as older ones. The older assemblages include Sil-Bt-Grt, characterized by a diablastic texture with large prismatic crystals of sillimanite (Fig. 2 g, h). In some samples, sillimanite occurs as small fibrolite crystals forming an ino-lepidoblastic texture together with chlorite and chloritoid. Samples from the western part also exhibit a diablastic texture, which strongly suggests that these rocks formed under low-pressure/high-temperature conditions.

The assemblages Sil-Bt-Grt in the eastern part and And-Crd-Bt-Ms in the western part are older than the Alpine metamorphic events. These assemblages are attributed to thermal contact metamorphism associated with the intrusion of the Varnous plutonite. This conclusion is further supported by the overprinting of Alpine metamorphic events onto these earlier assemblages.

The sequence of metamorphic events in the area can be summarized as follows:

1. Formation of Sil + Bt + Grt and And + Crd + Bt + Ms at approximately 297 Ma.
2. Development of Cld + Mica + Chl + Kfs + Pl + Qtz + Grt ± St during the Alpine event at 150–130 Ma.
3. Alteration of these assemblages by sericite, chlorite, and margarite at 110–90 Ma.
4. Mylonitization of all previous assemblages at 90–70 Ma.

Further research is ongoing to determine the factors responsible for the formation of different assemblages in the eastern and western parts of the contact aureole.

References

Anders, B. 2005. The pre-Alpine evolution of the basement of the Pelagonian Zone and the Vardar Zone, Greece (Doctoral dissertation, Mainz, Univ., Diss., 2005).

Avgerinas, A. 2014. Deformation and kinematics analysis of the pelagonian zone in Northern Greece. Faculty of Sciences, School of Geology. PhD Thesis, Aristotle University of Thessaloniki

Katerinopoulos, A. 1983. Contribution in the study of plutonic rocks from Western Varnountas, School of Geology. PhD Thesis, University of Athens.

Kilias, A. 1980. Geologische und tectonische Untersuchung des Gebietes von östlichen Varnous (NW Makedonien). Thesis, Univ. of Thessaloniki, Greece

Kilias, A., Mountrakis, D., 1989. The Pelagonian nappe: tectonics, metamorphism and magmatism. Δελτίον της Ελληνικής Γεωλογικής Εταιρίας, 23(1), 29-46.

Kilias, A., Frisch, W., Avgerinas, A., Dunkl, I., Falalakis, G., & Gawlick, H. J. 2010. Alpine architecture and kinematics of deformation of the northern Pelagonian nappe pile in the Hellenides. Austrian Journal of Earth Sciences, 103(1), 4-28.

Koroneos, A., 1991. Mineralogy, Petrology and Geochemistry of Eastern Varnountas plutonite (NW Macedonia), Faculty of Sciences, School of Geology. PhD Thesis, Aristotle University of Thessaloniki

Koroneos, A., 1993a. Study of the coexisting biotites and amphiboles from the eastern Varvountas plutonite (NW Macedonia). Ορυκτός Πλούτος, 1993(085), 31-46.

Koroneos, A., 1993. Comparative, mineralogical-petrological and geochemical study of the plutonic and gneissic

rocks of eastern Varnountas (NW Macedonia) Annales Géologiques des pays helléniques, Athènes, Départment des sciences de la terre de l'université.

Koroneos, A., Christofides, G., 1990 Petrology and geochemistry of the Eastern Varnountas plutonite (NW. Macedonia): preliminary presentation. Δελτίον της Ελληνικής Γεωλογικής Εταιρίας, 22, 97-113.

Koroneos, A., Christofides, G., Eleftheriadis, G., 1991. Evolution of Eastern Varnountas plutonite (NW. Macedonia): major and trace element fractional crystallization models. Δελτίον της Ελληνικής Γεωλογικής Εταιρίας, 25(2), 81-99.

Koroneos, A., Christofides, G., Del Moro, A., & Kilias, A., 1993. Rb-Sr geochronology and geochemical aspects of the Eastern Varnountas plutonite (NW Macedonia, Greece). Neues Jahrbuch für Mineralogie. Abhandlungen, 165(3), 297-315.

Koroneos, A., Soldatos, T., Christofides, G., Eleftheriadis, G., 1994. Origin of eastern Varnountas plutonite (NW Macedonia). Δελτίον της Ελληνικής Γεωλογικής Εταιρίας, 30(1), 193-204.

Mposkos, E., Kostopoulos, D., Krohe, A. 2001. Low-P/High-T pre Alpine metamorphism and medium-P Alpine overprint of the Pelagonian z;one documented in high-alumina metapelites from the Vernon massif, western Macedonia, Northern Greece. Bulletin of the Geological Society of Greece, 34, 3-949

Whitney, D. L., & Evans, B. W. (2010). Abbreviations for names of rock-forming minerals. American mineralogist, 95(1), 185-187.

Zlatkin, O., Avigad, D., & Gerdes, A., 2014. Peri-Amazonian provenance of the Proto-Pelagonian basement (Greece), from zircon U–Pb geochronology and Lu–Hf isotopic geochemistry. *Lithos*, *184*, 379-392.

17th INTERNATIONAL CONGRESS of the Geological Society of Greece

BULLETIN OF THE GEOLOGICAL SOCIETY OF GREECE, SP. PUBL.

EXTENDED ABSTRACT 014

Balancing Precision and Resources: The Effect of Sampling Density in Regional Soil Geochemical Mapping

Argyraki A.[1], Kontomichalou A.[1], Kypritidou, Z.[1], Liakopoulos, A.[2]
(1) Department of Geology and Geoenvironment, National and Kapodistrian University of Athens, Athens, Greece, argyraki@geol.uoa.gr (2) Hellenic Survey for Geology and Mineral Exploration, Athens, Greece

Research Highlights

This study investigates the impact of field sampling density on the quality and reliability of regional geochemical maps using chromium (Cr) and lead (Pb) as case studies due to their contrasting geochemical behaviour within the mapped area. Two data sets, comprising 117 and 24 evenly distributed sampling locations within the same study area of 2500 km^2, were used to produce geochemical maps for each element. Key statistical metrics, including the mean, median, and standard deviation were compared to assess the impact of varying sampling densities. The Inverse Distance Weighting (IDW) interpolation method was then applied to generate maps, enabling visualisation of spatial variability.

Introduction

Geochemical mapping is a method of "revealing the invisible", initially involving systematic sampling, followed by sample preparation, chemical analysis, interpretation of the results, and the plotting of geochemical maps. This valuable tool is used today in various fields, including mineral resource exploration, development planning, contaminated site inventory, epidemiology, agriculture, and forestry.

The work presented here is part of a preliminary study on establishing the soil geochemical baselines of a pilot area (Attiki-Voiotia region), with the ultimate aim of publishing the first Soil Geochemical Atlas of Hellas. The project is implemented by the Hellenic Survey for Geology and Mineral Exploration, Department of Geochemistry and Environment, through the National Funds Programme in collaboration with the Laboratory of Economic Geology and Geochemistry of the University of Athens. The dominant lithological types identified across the entire extent of the pilot area can be categorised into three groups: (a) Carbonate rocks of the Alpine orogeny (limestones, dolomites, and marbles), (b) Argillaceous-siliceous rocks of the Alpine orogeny (schists and schist-chert sequences) in stratigraphic or tectonic contact with the carbonates, and (c) Post-Alpine sedimentary rocks (marls, conglomerates, sandstones, etc.) and looser sediments (colluvium, alluvial clastic material), which occupy the lower topographic areas and plains. Mineralogical analysis by semi-quantitative powder X-Ray Diffraction of selected soil samples from the study area assisted in their classification into two major groups depending on the proportion of carbonate minerals, related to the underlying lithology. Specifically, samples of significantly lower carbonate mineral content are associated with the alpine rocks (Kypritidou et al., 2024).

The objective of the present study is to investigate the impact of field sampling density on the quality and reliability of regional geochemical maps using chromium (Cr) and lead (Pb); they are used as case studies due to their contrasting geochemical behaviour within the mapped area. Chromium is a primarily lithogenic element enriched in mafic-ultramafic rocks and their weathering products, and Pb is an element typically associated with diffuse anthropogenic contamination as well as areas of enrichment, related to massive sulphide ore bodies.

Methods

Top-soil (0-20 cm) samples were collected from 117 locations on a 5 x 5 km grid within an area of about 2500 km^2 by following and appropriately adjusting the guidance of the International Union of Geological Sciences Manual of Standard Methods for Establishing the Global Geochemical Reference Network (Demetriades et al., 2022). Dried and sieved (<2 mm) soil samples were analysed by ICP-AES / ICP-MS following hot aqua regia dissolution. The present study is focused on the analytical results of Cr and Pb.

To prepare the geospatial database for the pilot project, which incorporated the results of laboratory determinations and chemical analyses, a corresponding file was compiled in ArcGIS Pro. Sampling locations were integrated into the file by importing the complete KML format file exported from the GPS. The eastern coastline boundary, along with the

boundaries of HNHS (Hellenic National Mapping Agency) maps, or the municipal and community boundaries of the pilot area, were used to isolate and clip thematic layers to the extent of the pilot project area from broader national data sets. For the purposes of this study, a subset of 24 sampling points out of the total 117 locations, was used, i.e., by reducing the number of samples by 80%. The selection of the samples was based on their uniform spatial distribution, the different land uses, and litho-geological types of the area. It is noted that since the overall objective of the project is to establish the geochemical baselines, this thinned-out sample distribution did not include any samples within the urban area of Athens, in line with the prescribed methodology by the Manual of Standard Methods for Establishing the Global Geochemical Reference Network to "sample natural residual soil, meaning soil that is not affected by any anthropogenic activities" (Batista et al., 2022). The resulted sampling scheme is equivalent to a sampling density of approximately 1 sample per 10 x 10 km grid. This thinning-out of the grid would correspond to saving a great deal of resources during sampling, sample preparation and analysis.

The statistical treatment of the concentrations of Cr and Pb at the two sampling densities included the calculation of the basic statistical parameters, and the plotting of probability curves in order to test normality and calculate appropriate percentiles for defining the concentration classes in the produced colour-surface geochemical maps. Notched box-and-whisker plots were constructed to allow pairwise comparison of the medians to be performed at the 95% confidence level by examining whether the two notches overlap. One-way analysis of variance (ANOVA) was used to indicate the statistical significance of the differences between results by the two sampling densities. The subsequent geochemical mapping procedure followed the typical steps of spatial data posting and interpolation by using the deterministic IDW technique with output cell size set at 200, power of 2 and search radius variable with 12 points in ArcGIS Pro. Error analysis, by applying exploratory interpolation in ArcGIS Pro, was used to calculate mean error enabling comparison of interpolated results between the datasets.

Results and discussion

The descriptive statistics for the two elements at the two sampling densities, and their probability plots are presented in Table 1 and Figure 1, respectively.

Table 1. Summary statistics for Cr and Pb (mg/kg) in soil for the two sampling densities.

Element	N	Mean	Median	Standard Deviation	Minimum	Maximum
Cr	117	134	86	190	2	1273
Cr	24	185	89	225	2	990
Pb	117	213	29	969	5	10000
Pb	24	238	31	558	8	2138

The statistical parameters of the raw data (Table 1) indicate that both elements display non-normal, right skewed statistical distributions with mean values significantly higher than their corresponding medians and several outlying values. A comparison of the median values for the two sampling densities demonstrates nearly similar results for both elements. One-way ANOVA (95% confidence level) on log-transformed data indicated no statistically significant differences in mean Cr and Pb concentrations between the two sampling densities. Particularly for Pb, the median values of 29 mg/kg for the dense and 31 mg/kg for the sparse sampling locations are comparable with the values of 26 and 45 mg/kg measured for rural and suburban soil within the area in a previous study by Argyraki et al. (2018).

Although Cr data approach a log-normal distribution, Pb data after log-transformation are not normalised, probably due to the presence of multiple populations within the study area. Indeed, the effect of elevated Pb concentrations in soil samples from the sulphide-ore bearing Lavreotiki peninsula is profound as a separate geochemical domain within the study area. Following these observations, and the number of samples classified in each interval, concentrations corresponding to the 25^{th}, 50^{th}, 75^{th}, 90^{th}, and 95^{th} percentiles of the data were selected to define the class limits for mapping both elements at the two sampling densities.

The boxplot comparison (Figure 1) shows that the notches at the 95%-confidence interval about the medians overlap, indicating that there is no significant difference between the median values of Cr and Pb at the two sampling

densities. However, the folding-in behaviour of the Cr low sampling density boxplot is caused by the notch extending beyond the first quartile, suggesting that more samples are needed to define the background population.

For plotting the interpolated surfaces, the deterministic IDW technique was used. The resulting maps are displayed in Figure 2. Graduated size symbol layers are superimposed on the colour surface maps to provide the exact concentration measured at each sampling site. Visual inspection of the maps indicates that although the spatial variability is better captured by the dense sampling data set, anomalous areas can still be delineated even when using the 24 sampling locations. This observation highlights that careful selection of sampling sites in conjunction with a thorough study of the underlying lithology plays a crucial role in regional geochemical mapping, and that a 10 x 10 km sampling grid would still be fit-for-purpose for the delineation of regional geochemical trends.

Within the study area, elevated Cr concentrations correspond to areas of laterite occurrences in the north-west part of the map, serpentinised rocks in Hymettus Mt., and greenstones in the south-east part of the map. A gradual increase in Pb concentration is observed from north-west towards south-east areas on the map, peaking in the Lavreotiki area, which hosts the well-known galena ore deposits. These trends are captured by both the dense and the sparse sampling data sets. However, error analysis on the interpolated results indicated a 6-fold and a 3-fold increase of mean error for Pb and Cr respectively when the number of samples is reduced to 24.

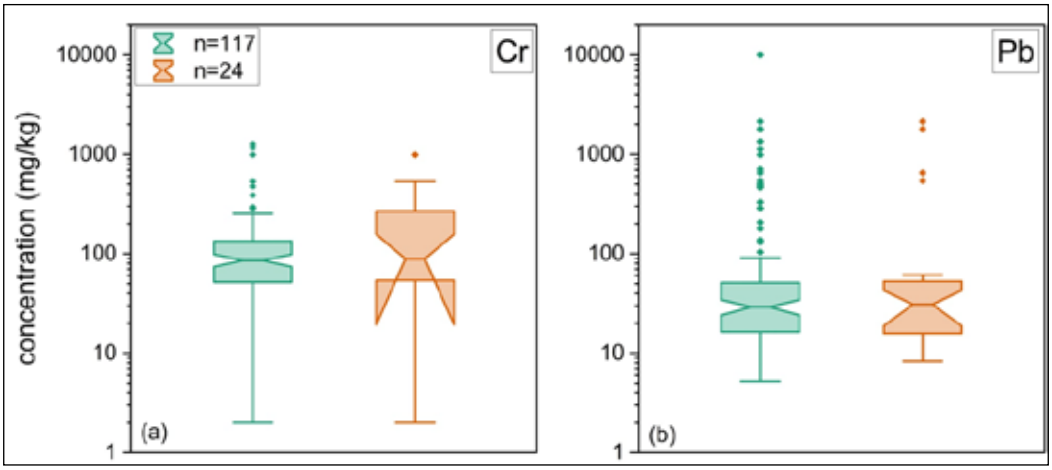

Figure 1. Notched box-and-whisker plots of Cr (a) and Pb (b) for comparison at different sampling densities.

Conclusions

The main findings of the comparison presented between the two sampling densities and the Cr and Pb spatial distribution are as follows:

- The geochemical patterns of both elements in soil are explained by bedrock lithology.
- No significant differences were identified between the descriptive statistics for both elements and sampling densities; the overall trend of the statistical distribution was captured with sufficient precision by the lower sampling density data set.
- The interpolated surfaces in the geochemical maps show anomalous concentrations in the same areas. The lower sampling density captured most of the anomalous areas. However, the spatial variability is better attained by the dense sampling data set for both elements.

Overall, the results of this study suggest that soil sampling locations for mapping the geochemical baseline of chemical elements at the regional scale should be selected by adopting a combination of statistical and judgmental approaches with careful consideration of the local conditions at each sampling site. In this way the balance between effort and final map precision can be achieved.

Further work should focus on testing the results for additional elements of interest and for different sampling densities. The current sampling data set on the 5 x 5 km sampling grid provides the opportunity for such trials, which

could be of paramount importance for optimising available resources for sampling, sample preparation and analysis when expanding the project to the national scale.

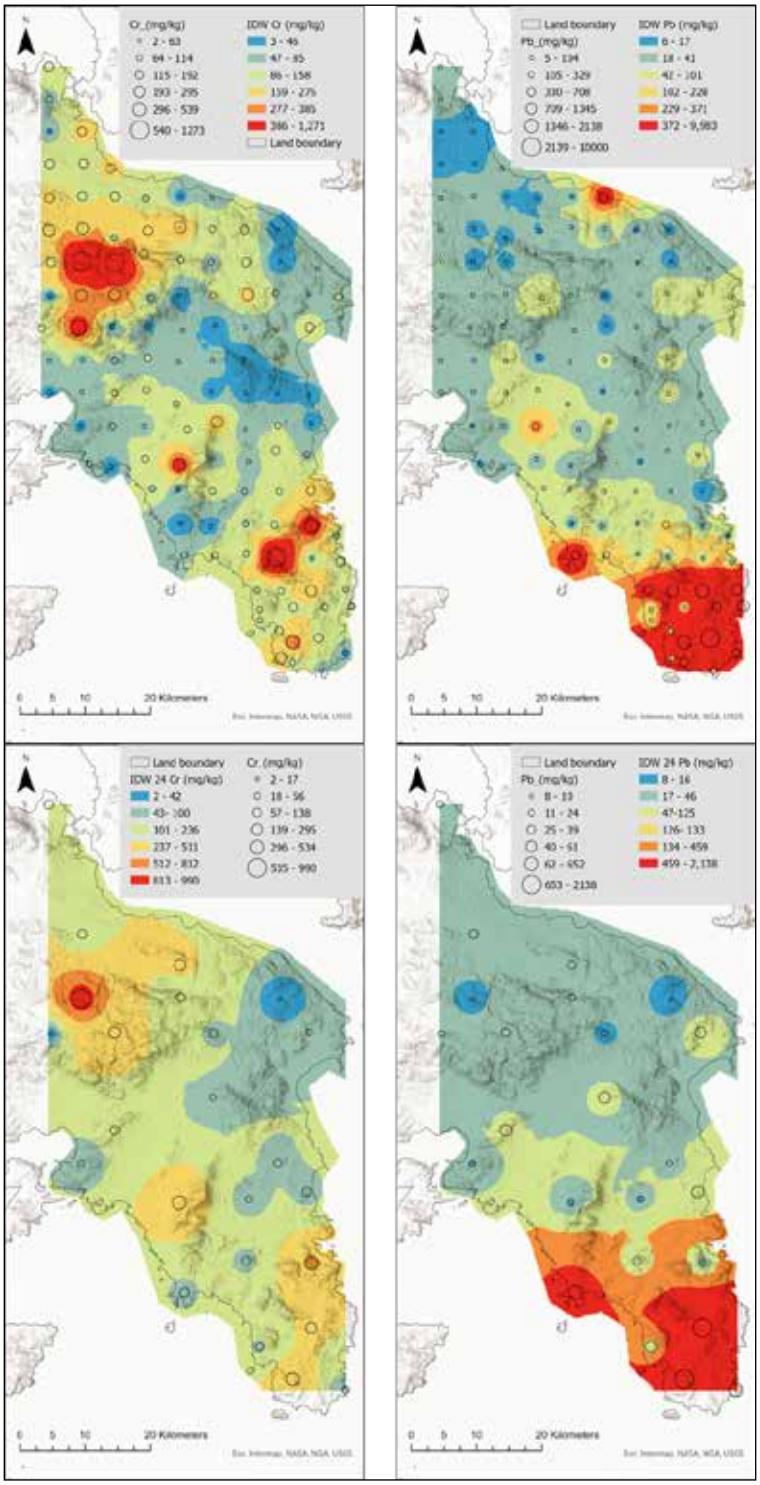

Figure 2. IDW interpolated colour surfaces of Cr and Pb based on 117 samples (top) and 24 samples (bottom).

Acknowledgements

We acknowledge financial support by HSGME through the National Funds Programme, project no. 2020ΣΕ06100004 (HSGME no 22204). We thank Dr. Alexandros Demetriades and an anonymous reviewer for the thorough review of this extended abstract.

References

Argyraki, A., Kelepertzis, E., Botsou, F., Paraskevopoulou, V., Katsikis, I., Trigoni, M., 2018. Environmental availability of trace elements (Pb, Cd, Zn, Cu) in soil from urban, suburban, rural and mining areas of Attica, Hellas. In: Demetriades, A., Johnson, C. and Birke, M. (Eds.), Urban Geochemical Mapping: The EuroGeoSurveys Geochemistry Expert Group's URGE Project, Journal of Geochemical Exploration, 187, 201−213; https://doi.org/10.1016/j.gexplo.2017.09.004

Batista, M.J., Demetriades, A., Johnson, C.C., Tarvainen, T., Savin, I., Smith, D.B., Haslinger, E., Salminen, R., Gregorauskienė, V., Zomeni, Z., Lacassie Reyes, J.P., Astudillo, F. & Oliva Vicentelo, P.S, 2022. *Residual Soil and Humus Sampling*. Chapter 3.2 In: Demetriades, A., Johnson, C.C., Smith, D.B., Ladenberger, A., Adánez Sanjuan, P., Argyraki, A., Stouraiti, C., Caritat, P. de, Knights, K.V., Prieto Rincón, G. & Simubali, G.N. (Editors), International Union of Geological Sciences Manual of Standard Methods for Establishing the Global Geochemical Reference Network. IUGS Commission on Global Geochemical Baselines, Athens, Hellenic Republic, Special Publication, **2**, 91−119.

Demetriades, A., Johnson, C.C., Smith, D.B., Ladenberger, A., Adánez Sanjuan, P.A., Argyraki, A., Stouraiti, C., Caritat, P. de, Knights, K.V., Prieto Rincón, G., Simubali, G.N. (Eds.), 2022. International Union of Geological Sciences. Manual of Standard Methods for Establishing the Global Geochemical Reference Network. IUGS Commission on Global Geochemical Baselines, Athens, Hellenic Republic, Special Publication, 2, 515 pp.; https://doi.org/10.5281/zenodo.7307696..

Kypritidou, Z., Kontomichalou, A., Botsou, F., Argyraki, A., Liakopoulos, A., 2024. Soil mineralogy in support of a regional geochemical baseline study in Greece. Joint Conference of ISEH ICEPH & ISEG, Galway, Ireland, Book of Abstracts p. 410; https://www.universityofgalway.ie/media/ineh/files/ISEH-ICEPH-ISEG-Book-of-Abstracts.pdf.

17th INTERNATIONAL CONGRESS of the Geological Society of Greece

BULLETIN OF THE GEOLOGICAL SOCIETY OF GREECE, SP. PUBL.

EXTENDED ABSTRACT 015

Seismic resilience of primary water transfer network at Lagadas municipality, North Greece

Arnaouti, S.[1], Ktenidou O.-J.[2]

(1) Civil Engineer at Municipal Water Supply and Sewerage Company of Lagadas, Greece

(2) Senior Researcher at National Observatory of Athens, Greece

Introduction

Among natural disasters, earthquakes have the most destructive potential to water pipe networks. The induced damages to the water supply can be the main reason for post seismic economical disruptions. Thus, it is of utmost importance to recognize the most vulnerable elements of the water pipe network under seismic load, in order to manage effectively prevention and post seismic actions.

At the present work, we estimate the seismic resilience of the external water network - based on Balaei et al (2020) methodology - at Lagadas municipality, one of the ten largest area municipality in Greece, as a measure of the system's ability to absord a shock when occurs and to recover quickly after that (Bruneau, 2003). The results can be used to rank the prevention actions necessary to reduce earthquake consequences to water network performance.

Background

The term 'resilience' was first introduced by Holling (1973) at ecology field, as a measure of the system capacity to absorb parameter changes. The term was imported to engineering by Klein et al. (2003), that study the characteristics of mega-cities resilience to natural hazards. The conceptual work of Bruneau et al. (2003) defines seismic resilience as 'the ability of social units to mitigate hazards, contain the effects of disasters when they occur and carry out recovery activities in ways that minimize social disruption and mitigate the effects of future earthquakes.' As such, a resilient system entails the properties of robustness, redundancy, resourcefulness and rapidity to recovery.

Focusing at the water pipe networks, the works of Menoni et al. (2002) and Borzi (2023) estimate the network's vulnerability. In respect of the 'resilience' term, Arcadis company (2016) ranks fifty cities worldwide regarding their ability to secure constant water supply. Cimellaro et al. (2015) propose a resilience index for the water distribution network (WDN) as a product of three parameters: the number of users that lose their access to water, the water level in the tank and the water quality. The same year, Matthews analyses the water and sewage network resilience during natural hazards. In his study, the key parameters of the water infrastructure are quantified, based on Katrina and Rita hurricane events. Farahmandfar et al. (2016) propose a metric for seismic resilience of WDNs dependent on hazard intensity, estimated pipeline response and network topology in order to prioritise pipeline replacement works. Makropoulos et al. (2018) recognize three failure states for the WDNs, namely insufficient water quantity, insufficient water quality and infrastructure failure and suggest a toolbox to assess network resilience. Mo'Tamad et al. (2022) applied 27 different earthquake senarios to the WDN of an M-city in Ontario and examined how the expected failures affect its hydraulic resilience, in terms of pressure, water serviceability and population impacted. The analysis showed that for medium to large earthquakes, water supply can be lost for days and affect more than 90% of the city population.

Balaei et al. (2020) propose an index-based methodology to estimate WDN resilience under seismic load; the technical factors that affect WDN resilience are established through literature review and expert interviews and then quantified through expert judgement. The study showed that vulnerability, redundancy and criticality are the major technical factors affecting system resilience.

Methodology

The methodology used to estimate water system resilience is based on the work of Balaei et al. (2020) and is described in detail at Arnaouti, 2020. Balaei et al. (2020) initially state that system resilience consists of two principal terms: the residual functionality of the system after shock (robustness) and the swiftness of the system to return to its initial functionality (recovery rapidity). For the first part, the authors consider

that it mainly depends on the physical characteristics of the system rather than in social, economic and organizational parameters. For the latter part, the authors assume that the recovery time depends on the same parameters as the robustness, in the sense that an organization that creates a robust system usually develops quick time responses as well. By taking those simplified assumptions under consideration, Balaet et al. (2020) convert the resilience estimation problem to a robustness estimation problem. Literature review and field expert interviews resulted in the selection of three technical factors that define water system robustness under seismic load: vulnerability, redundancy and criticality. The authors suggest index values for those three factors through provided tables. For the vulnerability index assessment, the authors take account of the three main seismic hazards to the water network, namely fault rupture, slope failure and liquefaction. Once the vulnerability index (V_i), the redundancy index (ρ_i) and the criticality index (C_i) are determined for each pipeline section i, the robustness index R_i is given by the following equation:

$$R_i = 1 - \frac{V_i \cdot C_i}{\rho_i} \quad (1)$$

If L_i is the length of pipe section i and N is the number of the network pipe sections of the settlement water network, then the total robustness of the network is:

$$R = \frac{\sum_i^N L_i \cdot R_i}{\sum_i^N L_i} \quad (2)$$

Study area

The Municipality of Lagadas is located about 20 klm northeast of Thessaloniki and is the 10th larger municipality in Greece in terms of area (1220.3 km^2). It consists of seven municipality units, namely Assiros, Vertiskos, Kallindia, Koronia, Lagadas, Lahanas and Sohos) and its total population is 37.022 inhabitants (ELSTAT data, 2021).

The present study focuses on to the primary transfer water network of the total 37 housing areas/ settlements of Lagadas municipality, since there are scarce data for their water distribution network.

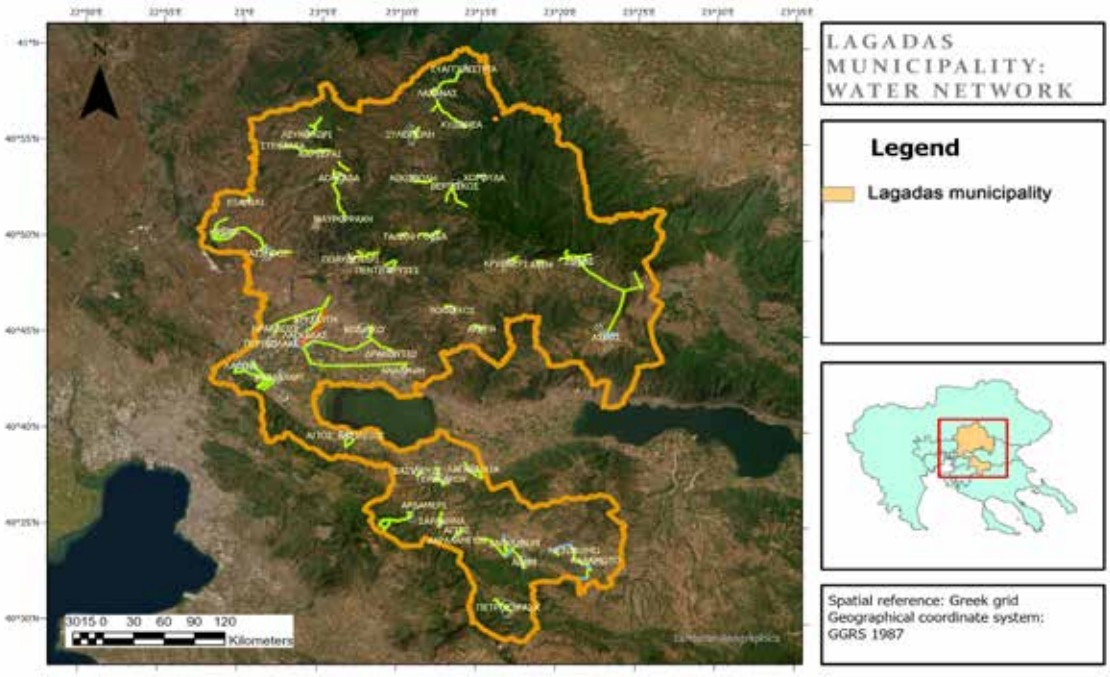

Figure 1: Primary water transfer network of the 37 settlements of Lagadas municipality

- **Fault ruptures at Lagadas**

Caputo et al. (2012) report two main fault ruptures in Lagadas area, the Sohos-Mavrouda fault and the Mygdonia fault. The Sohos-Mavrouda fault has a W-E direction, its length is about 41 km and it is an antithetic fault, since it is the only one with south-dipping structure. The Mygdonia fault with a total length of 69 km, is divided in three parts, that follow the borders of the homonymous basin: from west to east, there is Lagadas segment, Gerakarou segment and Apollonia segment. The Gerakarou segment with a W-E direction dips to the North and was the causative fault of the 1978 Mw=6.5 Thessaloniki earthquake, while the Lagadas segment strikes NW-SE and caused the M6.5 Assiros earthquake in 1902. The authors state that some researchers consider that Lagadas segment is not related to the current stress field, though oblique-slip kinematics show evidence of reactivation. On the other hand, some researchers believe that the seismic activity has abandoned Lagadas segment and been transferred to the south, towards Asvestohori fault. In addition, Chatzipetros et al. (2006) have detected a fault in Lagyna region with a NW-SE strike that was not included to the IGME geological map. This fault is parallel to the rest of the active faults of the area and is considered to be caused by recent over pumping activity. The map with the aforementioned fault ruptures available at Chatzipetros et al. (2006) was digitized through ArcGIS Pro program.

- **Landslides at Lagadas**

Koukis et al. (2005) recorded landslide occurrences in Greece for the time period 1950-2004 and provide a landslide hazard zonation map of Greece. According to this map, the Lagadas area exhibit a number of 0-1 landslides per 100 km^2 area. In addition, Wilde et al. (2018) and Günther et al. (2014) created a landslide susceptibility map of Europe with a 200x200m resolution based on a semi-quantitative method that relates the number of landslide occurrences to slope angle, lithology and land cover. The map was received in a raster form through the ESDAC Dataset Access service, after digital request.

- **Liquefaction at Lagadas**

As stated by Papathanassiou (2006), the 1902 Assiros earthquake caused liquefaction phenomena in Assiros and at the Thermal Springs of Lagadas, as written descriptions of mud puddles in dry tributary reveal. Papathanassiou et al. (2010) created a liquefaction susceptibility map of Greece by correlating liquefaction occurrences with geological, geomorphological and seismological data. Though a susceptibility map in a regional scale instead of national scale would have been more appropriate for the present study, the lack of such data led to the use of the data available.

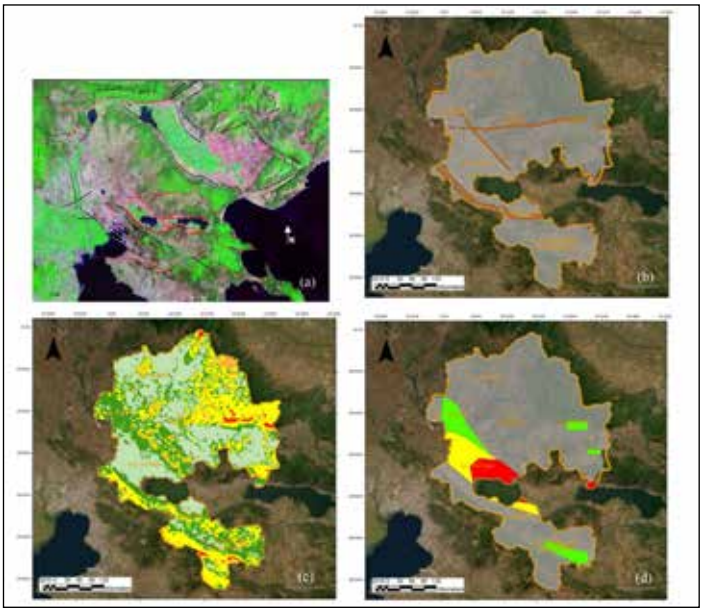

Figure 2: (a) Fault rupture maps at Lagadas area, taken from Chatzipetros et al. (2006), (b) Active faults of Lagadas municipality used for the present study, based on Chatzipetros et al. (2006) map, (c) Landslide susceptibility map of Lagadas municipality used for the present study (based on ESDAC data) and (d) Liquefaction susceptibility map of Lagadas municipality used for the present study (based on Papathanassiou et. Al, 2010 susceptibility map)

Calculations

- **Vulnerability index Vi**

According to the literature, vulnerability index Vi of the pipelines can be estimated based on their technical characteristics. For example, Menoni et al. (2002) propose a method for estimating Vi based on pipe age, pipe depth, construction material and pipe diameter. However, Menoni's methodology results in an almost uniform vulnerability index throughout Lagadas municipality, since the primary water transfer network share common characteristics (their diameter is usually below 300 mm, their material is PVC besides a few cases made of asbestos and the majority of the networks was constructed at the decade 1999-2009, just before the beginning of economic crisis in Greece).

According to the technicians of Municipal Water Supply and Sewerage Company of Lagadas, this is not the case in practice; transfer water pipe networks exhibit a considerable different performance under regular conditions, with damages ranging from almost none to too many damages per year. This different performance is attributed to three main reasons: (a) the asbestos pipelines that haven't been replaced yet (as Commission Directive 1999/77/EC defines), exhibit leaks at their joints, because the rubber joints have been worn with time. In addition, their repair is demanding due to the lack of special joints for large diameters, (b) inadequate initial design, since in practice the need to serve houses outside the settlement boundaries (in greater elevations and/or great distances from the settlement) lead to water pressures greater than initially designed and (c) inadequate compliance with technical specifications during construction; for example, non-appropriate pipe depth, no use of pipe sand-enacased or concrete-encased techniques when appropriate.

In order to import our technical staff knowledge about pipe actual vulnerability into our analysis, we have introduced five vulnerability categories (categories 0 to 4, where category 0 is for a pipe that is not in use, and categories 1 to 4 for pipes that exhibit damages 0, 1-2, 3-4 and more than 4 per year respectively) and set the vulnerability index according to the actual pipe performance under standard conditions. The most vulnerable sections of the transfer water pipe network are located at the municipal unit of Lagadas and more specifically at Lagadas, at Lagynas and at Irakleion – Perivolaki asbestos networks. At the rest of the municipal units, vulnerable sections can be found where elongated pipelines are used to transfer water to adjacent settlements, like in Stefania and Ossa.

- **Criticality index C_i**

Following Balaei et al. (2020) study, we used five categories for the criticality index (categories 1 to 5, when the population served was 0-50, 51-200, 201-500, 501-1000 and more than 1000 inhabitants respectively).

- **Redundancy index ρ_i**

Balaei et al. (2020) set five categories for the redundancy index (categories 1 to 5, for very high, high, some, low and no redundancy respectively). Since the redundancy description of Di Nardo et al (2016) is applied to water distribution networks and not to transfer water networks, we defined new categories and definitions for the redundancy index, shown at Table 1 below:

Table 1. Redundancy index categories for standpipes and downpipes, used in the present study

Redundancy index (ρ)	Standpipe (water transfer from drilling to the tank)	Downpipe (water transfer from tank to the settlement)
1	-	>2 downpipes
2	>5 functioning standpipes OR >2 standpipes with at least one spare	-
3	4-5 functioning standpipes OR 2 standpipes with at least one spare	2 downpipes
4	2-3 functioning standpipes	-
5	one functioning standpipes	One downpipe

- Rupture impact index $I_{RP,i}$, landslide impact index $I_{LD,i}$ and liquefaction impact index $I_{LQ,i}$

The impact indexes are estimated based on the tables provided by Balaei et al. (2020).

- **Robustness index**

The robustness index of pipe section i for seismic hazard j is:

$$R_{j,i} = \frac{1}{(V_i \cdot C_i \cdot \rho_i \cdot I_{j,i})}$$

Five categories were selected for the robustness index (index values: 1 for high robustness to 5 for very limited robustness), when robustness is 15-100%, 5-15%, 1-5%, 0.5-1% and 0-0.5% respectively. The robustness index in total, by taking account all three seismic hazards, is considerer to be the robustness of the worst-case scenario, thus it is the max robustness index: . $R_i = \max_{j=1\ldots3} R_{j,i}$. Through Eq.2, the robustness category per settlement network can be estimated.

All the calculations and maps of the present study were performed using ArcGIS Pro software, v.3.3.0, @ ESRI Inc 2024 (free license was available to MSc students of University of Aegean).

Results

Figure 4 shows the robustness of the water transfer network per pipeline section and per settlement.

The study reveals the very limited robustness of the water transfer pipelines at Lagadas, Lagyna, Perivolaki, Gerakarou and Lagadikia due to its proximity to faults. Liquefaction phenomena affect the water network at Lagadas, Xrisavgi and Irakleion. Regarding landslides, pipelines at Lagadas, Xrisavgi and Lagyna exhibit very limited robustness.

In terms of settlement networks, the only settlement with high robustness is Galini. Indeed, Galini is relatively protected by the seismic hazards and it has small population. Settlements at Lagadas municipality unit show very limited robustness due to the network's high vulnerability, the large population relative to the other municipality units, the proximity to fault ruptures and the liquefaction susceptibility. Very limited robustness can also be met at settlements of Koronia municipality unit, mostly because these networks lack redundancy and they are close to fault ruptures.

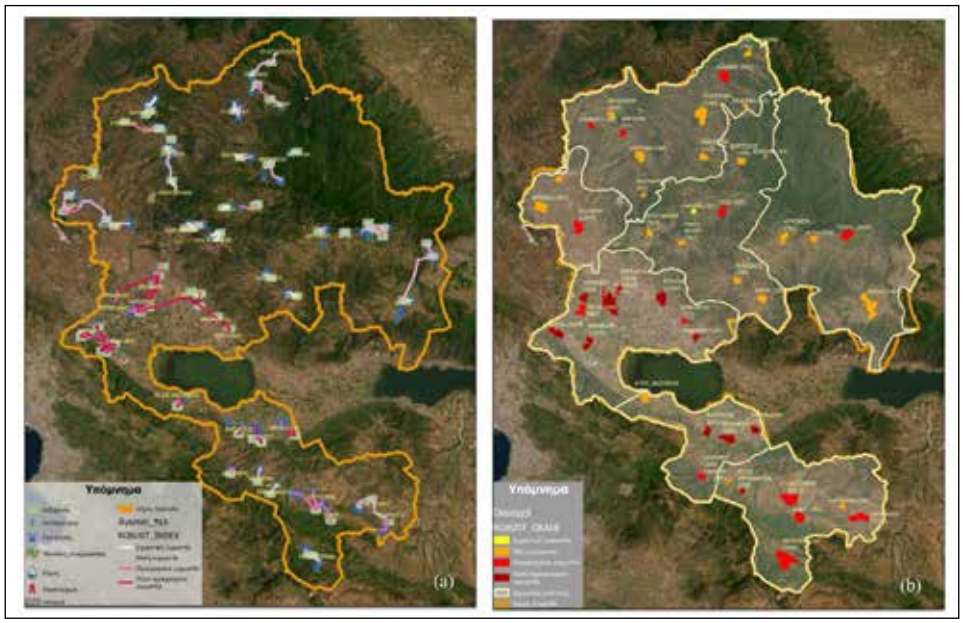

Figure 4: Water transfer network robustness. (a) Robustness per pipeline (white: high robustness, light pink: medium robustness, pink: limited robustness, magenta: very limited robustness. (b) Robustness per settlement of Lagadas municipality (yellow: high robustness, orange: medium robustness, red: limited robustness, brown: very limited robustness)

Conclusions

According to literature, the basic reason of failure of the water pipelines after earthquake is soil displacement, that can be caused by fault rupture displacements, landslide effects and liquefaction phenomena. The methodology proposed by Balaeti et al. (2020) takes account of all three seismic hazards.

Although literature review offers many approaches for estimating pipe vulnerability based on their physical characteristics, the use of our technical staff knowledge seems more appropriate, since it integrates critical aspects of the network, like inadequate initial design and not compliance with technical specifications during construction.

The results reveal that the majority of settlements in Lagadas municipality are not that robust and severe disruptions to water supply is expected after earthquake. Increasing pipeline vulnerability and enhancing network's redundance are prevention works for the least robust systems. Settlement robustness offers a valuable indicator to prioritize the prevention measures.

Acknowledgements

I would like to express my sincere appreciation to Municipal Water Supply and Sewerage Company of Lagadas and to its technical staff for providing all the necessary data for the water network providing and sharing their experience on its performance.

References

Holling, C., 1973. Resilience and stability of ecological systems. Annual Review of Ecology and Systematics, 4, 1-23.

Klein, R., Nicholls, R., & Thomalla, F., 2003. Resilience to natural hazards: How useful is this concept? Environmental Hazards, 5, 35-45.

Bruneau, M., Chang, S., Eguchi, R., Lee, G., O'Rourke, T., Reinhorn, A., Shinozuka, M., Tierney, K., von Winterfield, D., 2003. A Framework to Quantitatively Assess and Enhance the Seismic Resilience of Communities. Earthquake Spectra, 19(4), 733-752.

Menoni, S., Pergalani, F., Boni, M., & Petrini, V., 2002. Lifelines earthquake vulnerability assessment: a systemic approach. Soil Dynamics and Earthquake Engineering, 22, 1199-1208.

Borzi, I., 2023. Vulnerability assessment of water supply infrastructures through multiple indicator methodology. Journal of Water and Climate Change. doi:10.2166/wcc.2023.148

Arcadis Company, 2016. Sustainable cities water index. Amsterdam: Arcadis-Design and Consultancy for Natural and Built Assets. https://www.arcadis.com/media.

Cimellaro, G., Tinebra, A., Renschler, C., & Fragiadakis, M., 2015. New resilience index for urban water distribution networks. Journal of Structural Engineering, C4015014-1-13. https://doi.org/10.1061/(ASCE)ST.1943-541X.0001433.

Matthews, J., 2015. Disaster resilience of critical water infrastructure systems. Journal of of Structural Engineering, 142(8), C6015001.

Farahmandfar, Z., Piratla, K., & Andrus, R., 2016. Resilience evaluation of water supply networks against seismic hazards. Journal of Pipeline Systems Engineering and Practice, 8(1), 04016014. doi:10.1061/(ASCE)PS.1949-1204.0000251.

Makropoulos, C., Nikolopoulos, D., Palmen, L., Kools, S., Segrave, A., Vries, D., Koop, S., von Alphen, H.J., Vonk, E., van Thienen, P., Rozos, E. & Medema, G. 2018. A resilience assessment method for urban water systems. Urban Water Journal. https://doi.org/10.1080/1573062X.2018.1457166.

Mo'Tamad, H., Carriveau, R., & Ting, D.-K., 2022. Urban water supply systems' resilience under earthquake scenario. Scientific Reports, 12: 20555. https://doi.org/10.1038/s41598-022-23126.

Balaei, B. W., 2020. Investigating the technical dimension of water supply resilience to disasters. Sustainable Cities and Society, 56(102077). https://doi.org/10.1016/j.scs.2020.102077.

Arnaouti, S., 2024. Resilience of the external water supply network of Lagadas municipality (Northern Greece) to earthquake-related hazards. Dissertation of the Inter-Institutional Master Course 'Natural Hazards and Disaster Mitigation'. University of the Aegean, June 2024 (in Greek).

Caputo, R., Chatzipetros, A., Pavlides, S., & Sboras, S., 2012. The Greek Database of Seismogenic Sources (GreDaSS): state-of-the-art for northern Greece. Annals of Geophysics, 55(5), 859-894. doi:10.4401/ag-5168.

Chatzipetros, A., Tsapanos, Th. & Pavlidis, S. 2006. Geological-seismological investigation for the fault of the

Lagynas area in Lagadas Municipalitu. Thessaloni: Geology departhment of A.U.Th..

Koukis, G., Sabatakakis, N., Nikolaou, N., & Loupasakis, C., 2005. Landslide hazard zonation in Greece. Proceedings of open symposium on landslide risk analysis and sustainable disaster management in the First General Assembly of International Consortium on Landslides, pp. 291-296.

Wilde, M., Günther, A., Reichenbach, P., Malet, J.-P., & Hervás, J., 2018. Pan-European landslide susceptibility mapping: ELSUS Version 2. Journal of Maps, 14(2), 97-104. doi:10.1080/17445647.2018.1432511.

Günther, A., Van Den Eeckhaut, M., Malet, J.-P., Reichenbach, P., & Hervás, J., 2014. Climatephysiographically differentiated Pan-European landslide susceptibility assessment using spatial multi-criteria evaluation and transnational landslide information. Geomorphology, 224, 69-85.

ESDAC dataset, 2024. European Soil Data Centre, Joint Research Centre, European Commission. https://esdac.jrc.ec.europa.eu/resource-type/datasets.

Papathanassiou, G., 2006. Soil liquefaction phenomena in Hellenic region. Ph.D. thesis. Aristotle University of Thessaloniki.

Papathanassiou, G., Valkaniotis, S., Chaztipetros, A., & Pavlides, S., 2010. Liquefaction susceptibility map of Greece. Bulletin of the Geological Society of Greece, 43(3), 1383–1392. https://doi.org/10.12681/bgsg.11314.

Di Nardo, A., Di Natale, M., Giudicianni, C., Musmarra, D., Rodriguez Varela, J., Sntnastaso, G., . . . Tzatchkov, V. (2017). Redundancy features of water distribution systems. XVIII International Conference on Water Distribution Systems Analysis, WDSA2016. 186, pp. 412 – 419. Elsevier.

17th INTERNATIONAL CONGRESS
of the Geological Society of Greece

BULLETIN OF THE GEOLOGICAL SOCIETY OF GREECE, SP. PUBL.

EXTENDED ABSTRACT 016

Implementing the Critical Raw Materials Act to explore strategic minerals potential in Greece

Arvanitidis N.[1], Laskaridis K.[2], Christidis C.[2]

(1) President of the Mineral Raw Materials Committee of the Association of Greek Geologists, nikolaos.arvanitidis@gmail.com (2) Hellenic Survey of Geology and Mineral Exploration, Greece, klaskaridis@eagme.gr, christidisc@hotmail.com

Introduction / Background

Vast amounts of raw materials from minerals will be needed to meet the demand for a global economy free of hydrocarbons. Some are categorised as Critical and Strategic Minerals (CSMs) due to their high economic significance and supply risk. Of the 34 minerals and metals on the current EU list of CSMs, established in 2023, 16—such as copper, nickel, and aluminium—are strategically significant (Grohol et al., 2023). The CSMs are the foundation on which modern technology is built. From photovoltaics to semiconductors, wind turbines, and lithium batteries, to transport and store the produced renewable energy. In addition to lithium, battery value chains need cobalt, graphite, nickel, and manganese (Rachovides, et al., 2024). The electrification of cars requires permanent magnets, whose value chains use rare earth elements (REE) such as neodymium, dysprosium, and praseodymium, but also increase the use of nickel, copper, zinc, and lead. The CSMs are also essential in digital technology. Without CSMs, there cannot be an energy and digital shift. As a result, the resilience and sustainability of the CSM value chains that deal with technology facilitating the energy transition are highly valued by the EU. The EU would need up to 18 times more lithium and 5 times more cobalt by 2030 and almost 60 times more lithium and 15 times more cobalt by 2050 to cope with the increase in the production of electric vehicle batteries. By 2030, the demand for graphite is expected to reach 4 million tons per year, with 75% going to lithium battery anodes (Rachovides, et al., 2024). A shortfall of around 780,000 tons per year is estimated by 2030. Given that several of the Green Deal's goals, such as reducing greenhouse gas emissions by at least 55%, must be addressed and achieved by 2030, the growing need for CSMs becomes even more urgent.

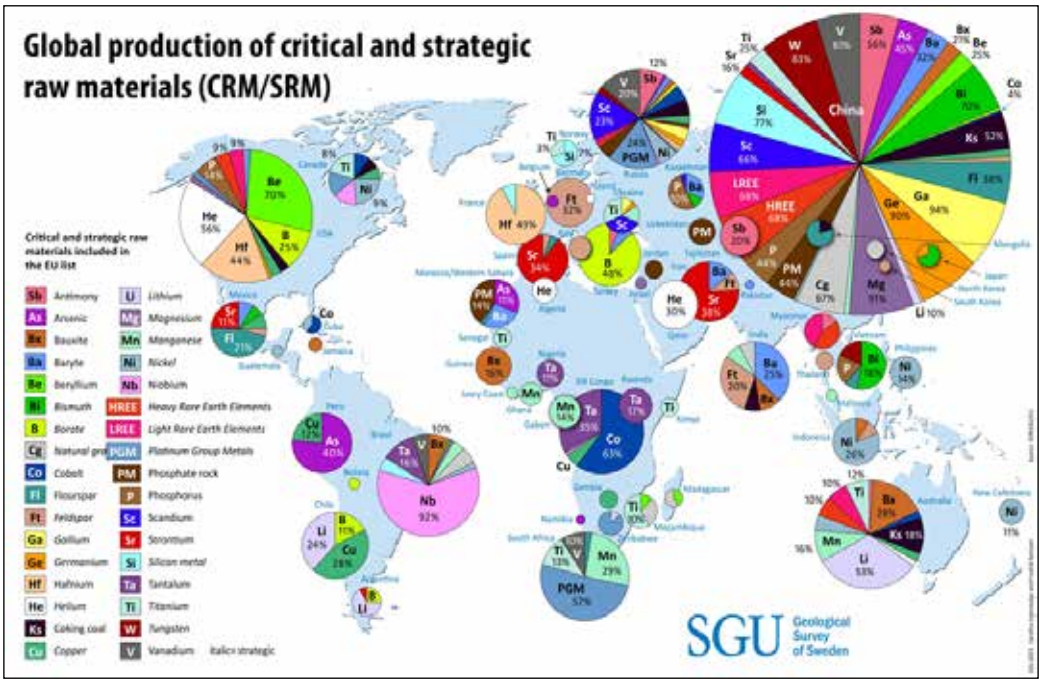

Figure 1. Map of world production of CSMs according to the current European list. Source: Geological Survey of Sweden.

The above forecasts seem "scary" considering that the EU depends on 75 to 100% of imports for most CSMs. It also happens that the production and processing of many CSMs are geographically controlled, making their geopolitical access and disposal vulnerable, accompanied by a series of social, economic, environmental, and other risks. So, some CSMs, but also their related value chains, tend to a large extent to be productively monopolized by specific regions of the planet, sometimes by essentially one country. For example, about 60% of the world's cobalt comes from the Democratic Republic of Congo (Fig. 1). China mines around 60% of the world's REE production, produces 85% of associated processed and metallurgical products, and consumes 70% (Arvanitidis, 2024). The urgent need for a global hydrocarbon-free economy will require therefore increasing quantities of raw materials. Therefore, it is important to know which and how many raw materials are needed to understand and assess the implications of their scarce access or scarcity for the European, and hence the Greek, economy. This article views why and how strategic and criticality in mineral resources arises, the geopolitical dominance of China, the European Regulation on Strategic and Critical Mineral Resources Act(CRMA), the key deposit of strategic and critical mineral raw materials resources, the need for increased investment in mineral exploration, new methodological approaches to mineral exploration, dynamic CRM systems in Europe and Greece and proposals for projects in mineral bearing areas of Greece.

The European Critical Raw Materials Act (CRMA)

The CRMA (European Commission, 2024) has become the political and strategic tool, but also the operational platform seeking to promote the implementation of the Green Deal, the new industrial strategy, the European partnership for innovation, the circular economy, and the integrated intra-European mining production, with the primary objective of making Europe climate neutral. This regulatory initiative is timely and necessary in formulating a policy for exploiting the European CSMs.

The main targets of the CRMA are until 2030

- At least 10% of CSM's annual consumption comes from European mineral deposits.

Europe's geology and metallogenetic evolution considerably favour its capability to capitalise on domestic CSM resources and become self-sufficient, resilient, and sustainable. Mineral exploration technologies for CSM deposits must be further developed to provide reliable resource estimates and feasibility studies. The national Geological Surveys of the member states must review the economic geology of their potential CSM systems, with the aim of a more documented and systematic assessment, to identify any exploitable targets.

- At least 40% of processed minerals are produced within the EU.

The integrated operation of resilient strategic value chains for the energy transition requires developing sustainable processing and refining technologies.

- At least 25% of the annual need in CSMs should come from recycling.

Most CSMs are mainly found as minor components in sulfide and oxide deposits of base metals (e.g. copper, lead, zinc, nickel, iron, aluminum). With mining and processing focused on base metal minerals, any accompanying CSM concentrations end up in various mining wastes, such as waste rocks and beneficiation tailings. Historical mining waste makes up the secondary resources that through their recycling and reuse, can potentially lead to the recovery of the CSMs they contain.

- Less than 65% dependence of each CSM on one country.

Minerals have been the missing link in the climate debate for many years. It is now clear that the EU's climate targets cannot be achieved without them. More specifically, any disruptions to the access and adequacy of CSMs, have implications for ensuring the energy transition and achieving the climate goals.

- Strengthening the resilience of strategic value chains for more effective implementation of energy and digital transition.

The value chains for CSMs include upstream mineral exploration and extraction, midstream processing (concentration, metallurgy), and downstream industrial processing and recycling. Unfortunately, in Europe today there are limited possibilities for the sustainable and integrated operation of CSM-based technology value chains

- Simplifying and speeding up licensing procedures.

The rapidly growing demand for mineral raw materials has also increased the need to update mining policy and research and innovation projects. The CRMA aims to reduce licensing time, and Member States will ensure that the overall permitting process related to such projects becomes faster. The governments of the EU Member States

agreed, in cooperation with the European Commission, the European Council, and the European Parliament, to highlight and implement strategic projects that would benefit from shorter and more efficient authorization procedures and easier access to finance.

- Development of environmentally friendly mining and production methods.

A common European understanding of best practices in the responsible mining of mineral resources, concerning social, environmental, and economic commitments and applications, set a trajectory toward the UN Sustainable Development Goals (SDGs).

- Channeling strategic partnerships between the EU and third countries to ensure sustainable and resilient CSM supply chains.

The CRMA aims to pave the way for long-term partnerships, with knowledge and technology transfer, training, and skills development for new jobs with better working conditions and income, as well as sustainable/ESG compliant extraction and processing in the partner countries from where Europe will be able to access and import some of the CSMs.

Metallogenetic settings sourcing CSMs

Most of the CSMs are minor accompanying components of important sulfides, oxides, and other metallic mineral systems. In nickel ore exploration, cobalt should also be a complementary target. Examples of CSMs found in subordinate concentrations along with known metallogenetic systems are,

- cobalt (Co) with nickel (Ni) and copper (Cu) deposits
- gallium (Ga), germanium (Ge), indium (In), antimony (Sb) with mixed sulfides
- gallium (Ga), rare earths (REE), scandium (Sc) with aluminum (Al) deposits
- platinum-based (PGM) with chromium (Cr), nickel (Ni) and copper (Cu)
- tungsten (W), niobium (Nb), indium (In), tantalum (Ta) with tin (Sn) deposits
- rare earth (REE) with phosphate (P) deposits.

"Critical" need for increased investment in mineral exploration.

Increasing the degree of self-sufficiency from 2-3% to 10% in 2030 means a 300-400% increase in intra-European production in 7 years. Huge efforts are therefore required for an increase in investment in mineral exploration to at least an equivalent degree to make the 10% degree of self-sufficiency possible. In this direction, innovative and sustainable approaches must be applied, using innovative prospecting technologies, thus improving economic performance and obtaining information that could not be obtained with conventional methods. The CRMA requests the member states to implement national CSM exploration projects through systematic economic geology approaches.

CSM potential mineral systems in Greece

Europe's geological environment and metallogenetic evolution substantially favour its ability to become self-sufficient, resilient, and sustainable in CSMs from domestic deposits.

In Greece (Fig. 2), potential CSM systems (Melfos and Voudouris, 2012; Stergiou, et al., 2023) relate to:

- active areas of mining base metal, magnesite, laterite, and aluminum bauxite mineral deposits (Fig. 2). Elevated geochemical values to higher grades of arsenic and antimony have been determined in the polymetallic ores in northern Greece. Along with nickel, the potential of exploitable cobalt contents in the laterites is a challenging target. A current project addresses the recovery of gallium, scandium, and REE with bauxite extraction and aluminium production.
- systems of metallic minerals in mainly Northern Greece (Figure 2, where mining activity (brownfields) or various scales (regional scale, deposit scale) of mineral exploration have been conducted in the past. The epithermal gold system in the Thrace region is connected to Tertiary volcanic basins and rocks with typical examples being the exploitable deposits of Sappes (Shaw and Constantinides, 2001; Border et al., 1999; Bridges et al., 1998; Cheliotis et al., 1999; Voudouris et al. 2006, Voudouris 1993), Agios Dimitrios (Michael, 1993; 2004; 2005; Michael et al., 1988), and Perama (Voudouris and Skarpelis, 1998; Lescuyer et al., 2003; McAlister et al., 1999; Michael C., 2002; Voudouris et al., 2011). In the case of this system, bismuth might be a potential target, as well as the challenging

target of locating deeper-seated copper mineralisation (Melfos et al., 2002). In the metamorphic basement of the Thrace region, there is a CSM exploration potential for antimony, with typical examples of mineralisation in Kallintiri (Michael, et al., 2012; Michael, et al., 2013; Kanellopoulos, et al., 2014), A prominent antimony prospect is found in Chios (Tsamantouridis and Chorianopoulou, 1977; Dimou et al., 1986).

- potential CSM exploration targets in central Macedonia are associated with the carbonate-replacement polymetallic mineral systems in the Serbo-Macedonian and Rhodope zones. In the lead-zinc-silver-gold ore deposits of Olympias and Mavres Petres in NE of Halkidiki arsenic and antimony, are mineralogically and geochemically also determined. The mineralisation in Thermes belongs to the same system (Arvanitidis et al., 1987) and the volcanogenic massive base-metal sulfide deposit (VMS) in Polykastro, where germanium and indium could also be of potential exploration interest. The VMS Molai base metal deposit in Peloponnese having a similar mineralogical composition, shows feasible germanium exploration results. While exploitable resources are mostly associated with the palladium-containing porphyry copper-gold mineral systems in the central Macedonian regions of Skouries and Kilkis, copper is the focus of exploration attention in the Kimmeria skarn mineralisation. The pyrolusitic manganese ores of the Varvara area in NE Halkidiki, which was explored in the past, probably needs a new review. Regarding antimony, the historical mining in the central Macedonia Lahanas area should not be ignored.
- to the mineral system of magmatic mineralisations, which is largely genetically linked to the ophiolite zones in mainly western Macedonia, with the predominant occurrence of Vourinos chromite deposits and the hydrothermally formed and ultrabasic rock-hosted magnesite in Halkidiki and Evia. Bauxites and laterites, formed by alteration, weathering and re-working of ophiolite-related ultramafic rocks and associated rocks (Valeton, et al, 1987), are exploratory placed in this system, with particularly increased contents of CSMs of gallium, scandium, REE, and cobalt, as mentioned with the respective active bauxite and laterite mines (Fig. 2). As far as nickel and cobalt are concerned, the mineral deposits in the western and eastern Vermio (e.g., Flamouria area), an exploration project previously implemented, concluded that an economic geology re-evaluation is highly recommended.
- the resource dimension and perspective of historical mining waste (mining tailings, beneficiation tailings, metallurgical residues), as part of the circular economy practices promoted and recommended by the CRMA, with exploring the potential of contained CSM resources, based on the UNFC classification system.

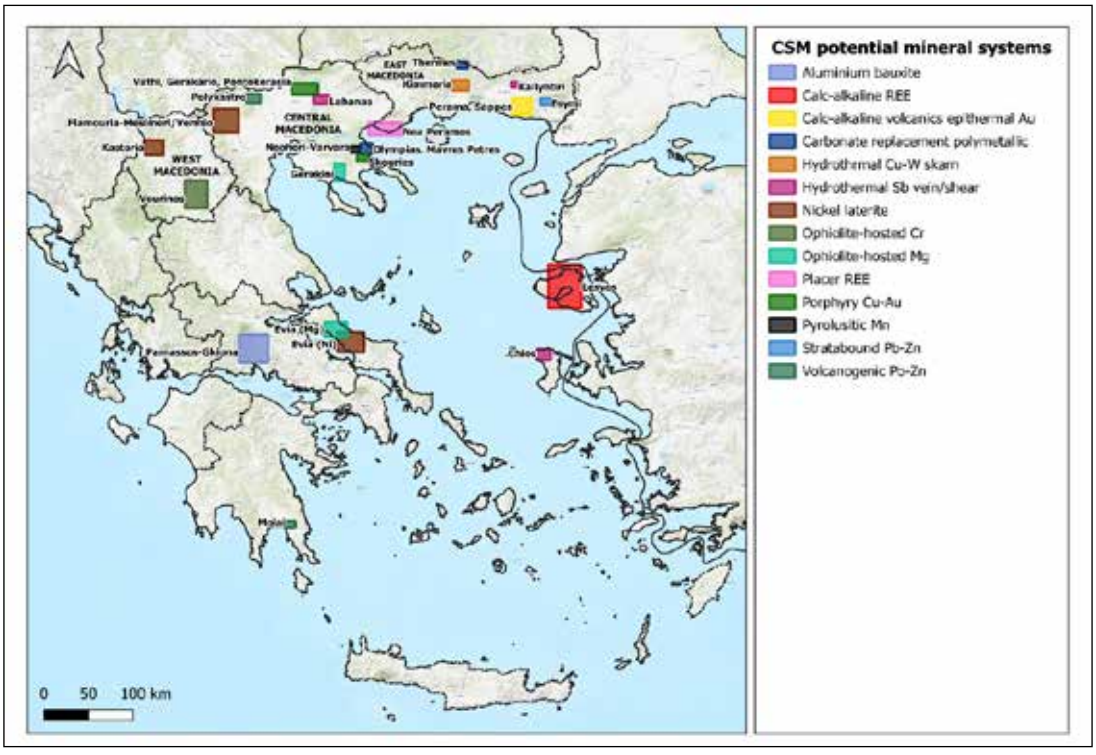

Figure 2. Map showing CSM potential mineral systems in Greece.

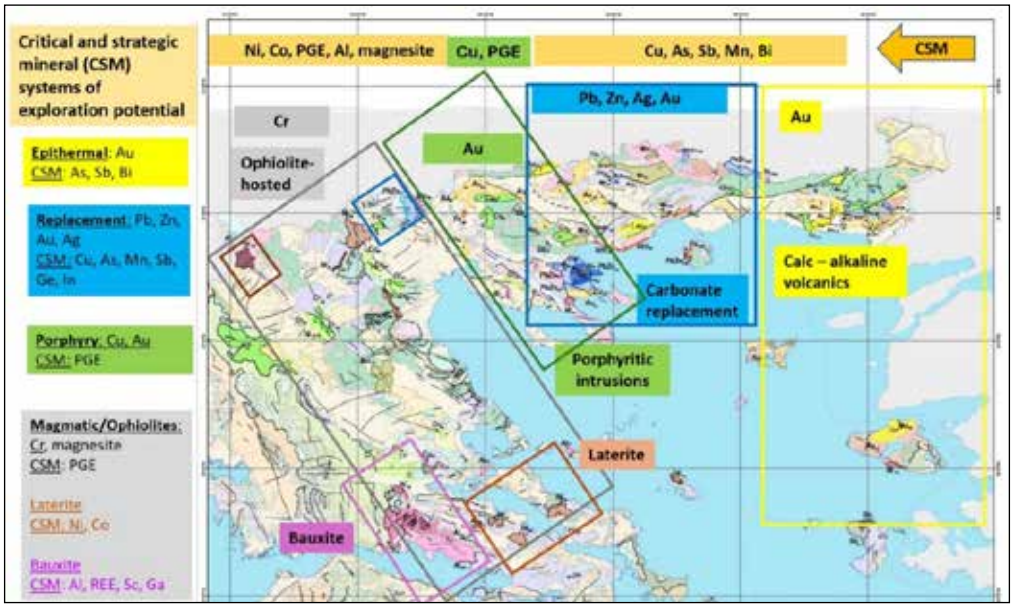

Figure 3. Mineral systems of CSM exploration potential in central and northern Greece.

- greenfields where the regional geology and lithological features justify conducting further economic geology approaches and exploration to target CSMs. For example, monazitic concentrations of REE have been identified in the coastal area of Nea Peramos. Exploring the granitic country rocks is necessary since they may be the sources of the REE found in the monazitic sands. The volcanic rocks in the NW part of Lesvos are found in the western extension of the Mesozoic-Cenozoic REE belt (Goodenough, et al., 2016) where a Turkish REE mineralisation was also made known. The REE geochemistry of these alkaline volcanics needs to be further explored. As far as lithium is concerned, several European Geological Surveys are exploring its potential in pegmatites. That could also be the case for the Greek pegmatites, particularly the ones of magmatic origin.

High-priority CSM exploration projects in Greece

Porphyry copper mineral systems. The project aims to explore economic geology and the feasibility of exploiting the porphyry copper mineralisations in Kilkis County's Pontokerasia, Vathi, Gerakario, and Mylohori areas (Apostolou and Stefanidis, 1987; Tsamadouridis, 1982; Drougas et al., 1981; Arvanitidis, 2010; Kelepertsis et al., 1986). The demand for strategic copper will increase rapidly and its price will follow the same upward trend, due to its use in energy transition technologies. Important copper resources can be found in Greece, such as Skouries, where mining is about to start. These developments are a motivation and an opportunity to highlight the CSM value of other porphyry copper-gold mineral systems, as they are in Pontokerasia, Vathi, Gerakario, and Mylohori. The resource potential is estimated at over 80 million tons, with typical grades of 0.30% copper and 0.8 grams/ton of gold. Porphyry copper systems typically develop a cylindrical structure, sometimes in the form of an inverted cone, and extend to an average depth of 2000 meters, with 1000 meters being a feasible exploration target.

Carbonate-replacement and VMS polymetallic sulfide minerals systems. The project addresses the economic geology and ore feasibility of Polykastro, Mavro Dendro, and Thermes base metal deposits, focused on the CSMs of copper, tungsten, germanium, and indium. The Polykastro mineral deposit, in Kilkis County, has an estimated resource of 4.7 million tons with about 6 % zinc and lead together, while the corresponding potential resources were estimated at 12 million tons. New exploration efforts will target deeper-seated copper mineralisation. In the neighboring area, the porphyry style Mavro Dendro deposit, amounts 4.8 million tons with 0.25% molybdenum and increased contents of copper and tungsten were

identified. In Thermes, in the County of Xanthi, there are confirmed 5.1 million tons with 6.9% zinc and lead, and 28 grams/ton of silver. In the same area, a graphite reserve of 400,000 tons with a content of 6% is found.

Manganese mineral systems. Previous exploration in Neohori and Varvara, including drilling, resulted in an estimated 1.5 million tons with 25-30% of pyrolusitic manganese, suitable for batteries. These mineralisations are found in the western part of the Stratoni fault, a regional structure known for its polymetallic sulfide minerals underlying iron-manganese oxidations. Characteristic examples of the Stratoni fault-controlled structural link between manganese oxides and base metal sulfides, as they move from shallower to deeper levels, are the Mavres Petres sulfide ore deposit in the eastern part of the fault and the Piavitsa sulfide mineralisation in the middle part.

Base and precious mineral sulfide systems. This project will target further exploration of several prospects of the County of Evros, in the Thrace region, which have been studied for lead, zinc, molybdenum, silver, and gold, including beneficiation testing. The potential occurrence of the CSMs of copper and bismuth will be in focus. Characteristic examples are the Esymi base metal deposit with 14 million tons of 6% zinc, and the adjacent Myli copper mineralisation. Excellent examples of feasible epithermal gold mineral systems are the ore deposits at Perama and Sappes.

Lateritic nickel mineral systems. The project will address the economic geology and exploitation potential of the lateritic nickel mineralisation in the Flamouria and Mesimeri areas of the prefecture of Pella. According to recent estimates (Source: Raw Materials Group, Future Mine & Mineral), global demand for stainless steel will continue to grow, with a projected increase of over 90% during the period 2021-2050. This is predicted to increase demand for nickel over the same period, by over 115%. Electric vehicles, which weren't on investors' radars in the early 2000s, are the new price engine for the anticipated nickel booms this time. Greece has a long-standing relationship with nickel mining production in LARCO's mining centers in Evia, Viotia, and Kastoria. Strategic nickel exploration was carried out in the Flamouria and Mesimeri areas, estimating a resource potential of over 1.5 million tons with approximately 0.9% Ni and 0.04% Co. Since cobalt and nickel are both now CSMs and the mineralisations are open downward geologically, more exploration is required. It should be noted that the need for deposits with high nickel grades has been greatly lowered by using hydrometallurgy rather than pyrometallurgy.

These selected exploration projects will contribute to access to increase the CSMs resource potential in Greece and the EU, as the CRMA targets, and to enable shortening the current timelines, to take no more than 27 months for mining licenses and 15 months for processing and recycling licenses.

References

Apostolou N. and Stefanidis P., 1987. Report on the geological and mineralogical mapping in the Gerakario area – Central – Gavras N. Kilkis. Report in Greek by I.G.M.E. **[Report]**

Arvanitidis N., Constantinides D., Dimadis E., Favas N., Nikolaou S., Romaidis Y., Iliev I., Katzkov N., Manev D., Milev V., Yanev V. 1987. Greek - Bulgarian joint project on the Geology, Metallogeny and prospecting of the Thermes ore-field, Northern Greece - Special volume I.G.M.E. Xanthi. **[Report]**

Arvanitidis N., 2010. New metallogenetic concepts and sustainability perspectives for non-energy metallic minerals in Greece. - 12th International Congress of The Geological Society of Greece. Bulletin of the Geological Society of Greece Volume XLIII, No 5. 2010. **[Conference Proceedings]**

Arvanitidis, N. 2024. Europe's economic geology generates exploitable critical mineral resources enabling to reduce its geopolitical dependence- Progress beyond state-of-the-art. Technical Annals. 1. 10.12681/ta.36119. **[Journal Article]**

Border A. J.M., Constantinides D. C., Michael C., Abatzioglou M., 1999. Discovery and Evaluation of the Sappes gold deposits, North-eastern Greece. - New Generation gold mines 99. Conference proceedings, 22-23, November, Perth, Western Australia, 1999. **[Conference Proceedings]**

Bridges P. S., Gordon M. J., Michael C., Abazioglou M., 1998. Gold mineralization at Sappes, Northern Greece. - In: Europe's major gold deposits, Irish Association for Econ. Geol., Abstracts volume, IAEG, Geological survey of Ireland, 95-107, 1998. **[Conference Proceedings]**

Cheliotis I., Naden J., Michael C., Shepherd T., Bitzios D., Leng M., Eliopoulos D., Spyro B., Dimitroula M., Kilias

S., Constantinidou E., 1999. Creation of models of Epithermal systems in the Rhodope and Aegean areas. - Final report (In Greek) **[Report]**

Dimou E., Papastavrou St., Serment R., 1986. The Sb in Greece (Part Two) - Study of occurrences and deposits of antimony in South Chios and Pelion (Metallic Paragenesis - Metallogenesis), Report in Greek by I.G.M.E. **[Report]**

Drougas I., Pantazis M., Papaioannou K. Polychronakis I., Spanos N., Tsamadouridis P., Charalambidis P., 1981. Economic and technical study on the feasibility of exploiting the mixed sulfide deposit in the Polykastro-Skra area, I.G.M.E. Unpublished Report in Greek No. 5, p. 111. **[Report]**

European Commission, 2024. Critical Raw Material Act https://single-market-economy.ec.europa.eu/sectors/raw-materials/areas-specific-interest/critical-raw-materials/critical-raw-materials-act_en **[Report]**

Geological Survey of Sweden, 2024. Critical and strategic raw materials. https://www.sgu.se/en/mineral-resources/critical-raw-materials/ **[Report]**

Grohol, M. and Veeh, C., 2023. Study on the critical raw materials for the EU – Final report. European Commission: Directorate-General for Internal Market, Industry, Entrepreneurship and SMEs, Publications Office of the European Union, 2023, https://data.europa.eu/doi/10.2873/725585. **[Report]**

Goodenough, K.M., Schilling, J., Jonsson, E., Kalvig, P., Charles, N., Tuduri, J., Deady, E.A., Sadeghi, M., Schiellerup, H., Müller, A., Bertrand, G., Arvanitidis, N., Eliopoulos, D.G., Shaw, R.A., Thrane, K., Keulen, N. (2016). Europe's rare earth element resource potential: An overview of REE metallogenetic provinces and their geodynamic setting, Ore Geology Reviews, Volume 72, Part 1, 2016, Pages 838-856, ISSN 0169-1368, https://doi.org/10.1016/j.oregeorev.2015.09.019. **[Journal Article]**

Kanellopoulos, Christos & Voudouris, Panagiotis & Moritz, Robert., 2014. Detachment-related Sb-Pb-Zn-Ag-Au-Te mineralization in Kallintiri area, northeastern Greece: Mineralogical and Geochemical constraints. Bul. Shk. Gjeol. 1/2014 - Special Issue Proceedings of XX CBGA Congress, Tirana, Albania, 24-26 September 2014. **[Conference Proceedings]**

Kelepertsis, A. E., Reeves, R., and Androulakis, J., 1986. Geochemical studies of porphyry type mineralization at Gerakario-Vathi of Kilkis area, northern Greece. Mineral Wealth, 42, pp. 43-48. **[Journal Article]**

Lescuyer J. L., Baily L., Cassard D., Lips A.L. W., Piantone P., Mc Alister M. 2003. Sediment-hosted gold in South-eastern Europe: the epithermal deposits of Perama, Thrace Greece: - Mineral Exploration and Sustainable Development. **[Conference Proceedings]**

McAlister M., Hammond J.M., Normand D. & Kampasakakis M., 1999. Discovery case history for the Perama Hill gold deposit, Greece - New Generation Gold Mines Conference in Perth, p. 10, West Aust., 22-23rd Nov. 1999**[Conference Proceedings]**

Melfos V., Voudouris P. (2012) Geological, mineralogical and geochemical aspects for critical and rare metals in Greece. Minerals 2, 300-317, https://doi.org/10.3390/min2040300

Melfos, V., Vavelidis, M., Christofides, G., Seidel, E., 2002. Origin and evolution of the Tertiary Maronia porphyry copper-molybdenum deposit, Thrace, Greece. Mineralium Deposita 37, 648-668. **[Journal Article]**

Michael C, Arvanitidis N., Iliadis, A., Papavasiliou, K., Christidis C., 2013. Orogenic mineralisations – A new exploration target for gold-polymetallic ore deposits in Greece. Proceed. 6th Conf. Sustain. Devel. Min. Industry, Milos Island, Greece, pp. 139-145. **[Conference Proceedings]**

Michael C., 1993. Geology and Geochemistry of epithermal gold deposit in Konos area. - Internal report of I.G.M.E. (In Greek). **[Report]**

Michael C., 2002. Exploration - valuation study of primary gold - IGME, internal report (In Greek). **[Report]**

Michael C., 2004. Epithermal systems and gold mineralization in western Thrace (North Greece). - Bulletin of the Geological Societies of Greece, vol. xxxvi. Proceedings of the 10th International Congress, Thessaloniki, April 2004. **[Conference Proceedings]**

Michael C., 2005. Mineralogical and Geochemical characteristics of Sappes epithermal system in western Thrace (Northen Greece). - In: Comptes rendus de l'Academie bulgare des sciences. Vol. 58, No 6, p. 691-698, 2005. **[Conference Proceedings]**

Michael C., Arvanitidis N., Gaál G., Papavasileiou K., Iliadis A., Christidis C., 2012. Orogenic mineralisations – A new exploration target for gold-polymetallic ore deposits in Greece. 34th International Geological Congress (IGC): Australia. **[Conference Proceedings]**

Michael C., Papadopoulos P., Marantos I., Evagelou E., 1988. Epithermal mineralization of gold in the Konos area (Eastern Rhodope). - Internal report of I.G.M.E. (in Greek), 1988. **[Report]**

Rachovides M., Arvanitidis N., Constantinides D., Anderhuber F., 2024. Critical minerals and rare earth elements: Ethical and societal considerations. Chapter 19. Editor(s): Silvia Peppoloni, Giuseppe Di Capua, Geoethics for

the Future, Elsevier, 2024, Pages 249-267, ISBN 9780443156540. **[Book chapter]**

Shaw A., Constantinides D., 2001. The Sappes gold project. - Bulletin of the Geological Society of Greece vol. 34,3, 1073 - 1080. Proceedings of the 9th International Congress, Athens, September 2001. **[Conference Proceedings]**

Stergiou, C.L.; Sakellaris, G.A.; Melfos, V.; Voudouris, P. 2023. A Review of the Distribution of Critical and Strategic Mineral Raw Materials in the Vein-Type Mineralisations of Vertiskos Unit, Northern Greece. Mater. Proc. 2023, 15, 51. https://doi.org/10.3390/materproc2023015051. **[Conference Proceedings]**

Tsamadouridis P., 1982. The polymetallic deposit Pb-Zn-Cu of Polykastro – Skra N. Kilkis, Report in Greek by I.G.M.E. **[Report]**

Tsamantouridis P., Chorianopoulou P., 1977. Report on the mineralogical assessment of the island of Chios (Occurrences of Antimony – Mixed Sulfides). Report in Greek by I.G.M.E. **[Report]**

Valeton I., Biermann M., Reche R., Rosenberg F., 1987.Genesis of nickel laterites and bauxites in Greece during the Jurassic and Cretaceous, and their relation to ultrabasic parent rocks, Ore Geology Reviews, Volume 2, Issue 4, Pages 359-404,

Voudouris P (1993): Mineralogical, geochemical and microthermometric studies of epithermal Au-Ag mineralization at Kassiteres/Sappes area (northeastern Greece) University of Hamburg, Germany, 218p (in German).

Voudouris P. and Skarpelis, N. 1998. Mineralisations of Epithermal gold-silver in Perama (Thrace) and Limnos. - Bulletin in Greek Geological Society. 32 (3) 1998, pages 125-135, 19 ref. 1998. **[Conference Proceedings]**

Voudouris P, Tarkian M, Arikas K 2006 Mineralogy of telluride-bearing epithermal ores in Kassiteres-Sappes area, western Thrace, Creece. Mineralogy and Petrology, 87, 31-52

Voudouris, P., Melfos, V., Spry, P.G., Moritz, R., Papavassiliou, C., Falalakis, G., 2011. Mineralogy and geochemical environment of formation of the Perama Hill high-sulfidation epithermal Au-Ag-Te-Se deposit, Petrota Graben, NE Greece. Mineralogy and Petrology 103, 79-100. **[Journal Article]**

17th INTERNATIONAL CONGRESS of the Geological Society of Greece

BULLETIN OF THE GEOLOGICAL SOCIETY OF GREECE, SP. PUBL.

EXTENDED ABSTRACT 017

Assessing the effect of 2023 Evros Wildfire: a new Post-Fire Rockfall Hazard System

Asteriou P.[1], Sotiriadis D.[1], Petala E.[1], Kazelis L.[1], Klimis N.[1]

(1) Democritus University of Thrace, Civil Engineering Dpt. Xanthi, Greece, pasterio@civil.duth.gr

This paper proposes a risk and hazard assessment system for rockfalls in fire-affected areas. The system has the ability to efficiently prioritize hazardous sites and evaluate post-fire rockfall risks, supporting rapid decision-making for mitigation actions.

Introduction

The Evros forest fire in August 2023 burned more than 90,000 hectares, making it the largest wildfire ever recorded on European soil since 2000. During the two-day period of August 21–23, the fire spread at an explosive rate, growing from approximately 8,500 hectares on August 21 to over 65,000 hectares by August 23, accounting for 60% of the total burned area. The explosive growth of the wildfire was driven by extremely dry atmospheric conditions during the incident and the prolonged drought that had affected the broader region in the preceding months. These factors led to exceptionally low moisture levels in the forest material, significantly facilitating the rapid spread of the fire.

Wildfires cause significant economic and social impacts, as they result in severe damage to infrastructure, area evacuations, livestock and wild animals, crops, farmlands, human lives and are associated with serious ecological consequences (Cunningham et al., 2024). Beyond the immediate effects of a wildfire, other natural phenomena and extreme events may arise. Wildfires can increase the susceptibility, frequency, magnitude, and area of influence of geohazards such as shallow landslides, rockfalls, debris flows, and soil erosion, triggering a destructive chain reaction with adverse consequences (Vahedifard et al., 2024). The occurrence of rockfalls depends on various factors related both to the slope, such as its gradient, geology, weathering, and vegetation, as well as, external factors, including climate, seismic activity, and exposure to human activities (Scheidl et al., 2020).

When a block detaches above a forested area, its movement will be constrained due to the impacts with the tree trunks. However, the destruction of vegetation, following a wildfire, cancels out this benefit. As a result, the block's travel distance is extended, and the severity of the impact increases. Consequently, the effects of a rockfall become more pronounced, posing a hidden threat to the safety of the exposed activities. The presence of vegetation makes the implementation of protective measures more cost-effective or even unnecessary (Scheidl et al., 2020). According to Moos et al. (2017), it has been found that protective forests can reduce the occurrence of rockfalls by up to 90% and their intensity by up to 70%, depending on variations in parameters such as the forest coverage, tree density and diameter, trunk arrangement, and the volume of the falling blocks. An overview of the current scientific knowledge and practical methods for addressing rockfall hazards in forested slopes can be found in Stoffel et al. (2006), Dorren et al. (2007), and others.

Recent studies report an increase in rockfall activity during and after wildfires (e.g., DeGraff et al., 2015; Perez-Rey et al., 2023). A combination of factors affects both the detachment areas and the propagation zones. Such factors include changes in the mechanical properties of the rocks and their fragmentation due to the high temperatures, the loss of vegetation's protective capacity, the impact of firefighting activities, and/or the destruction of existing protective measures (Sarro et al., 2021; Perez-Rey et al., 2023).

Objectives

The impacts of climate change, including rising temperatures and severe droughts, have intensified the occurrence of wildfires globally, leading to increased frequency, severity, and extent (Liu et al., 2010). Consequently, higher rockfall activity in burnt areas is expected, even in locations previously deemed safe due to vegetation. Thus, the objectives of this study are:

- Develop a user-friendly rockfall risk assessment system that accounts for the effects of wildfires. The system is designed to serve as a quick and efficient decision-support tool for identifying vulnerable locations.
- Apply the system to the area affected by the 2023 Evros wildfire, with the goal of identifying prone areas

and prioritizing them to facilitate decision-making regarding the restoration strategy, contributing to the area's restoration process.

Rockfall risk-hazard rating system

Ferrari et al. (2016) highlight the need for effective risk management by conducting a comprehensive review of existing methodologies for rockfall hazard and risk assessment. These methodologies are categorized into two main types: qualitative and quantitative. Qualitative methods rely on descriptive or classified criteria, requiring fewer data and allowing for quicker application, making them suitable for preliminary assessments or areas with limited data. In contrast, quantitative approaches involve numerical calculations and probability estimates, offering higher accuracy but demanding extensive data, complex models, and higher costs. When sufficient data are available, quantitative methods are preferred for detailed analyses of specific locations.

Classification Systems are widely used qualitative methods, that classify slopes based on their characteristic parameters. They have proven particularly effective for road networks, where slopes are evaluated to prioritize mitigation measures. The primary advantages of qualitative methods over quantitative ones are their cost-effectiveness and flexibility, enabling rapid hazard assessments across large areas. Their value lies in identifying high-risk zones that require further analysis. However, their main drawbacks are subjectivity and lack of precision.

The most popular hazard assessment system is the Rockfall Hazard Rating System (RHRS), developed in the late 1980s by the Oregon Department of Transportation (Pierson, 1992) as a standardized tool for assessing and prioritizing rockfall risks along roadways. Each slope section is rated based on factors influencing rockfall risk, such as slope height, ditch effectiveness, average traffic exposure, sight distance, road width, geological conditions, and rock fragment size. These parameters are rated on an exponential scale ranging from 3 to 81 points, depending on the severity of the risk. The original RHRS has been adapted to various regions to address local geological, climatic conditions, and infrastructure needs. These adaptations often involve modifications to rating criteria and the inclusion of additional parameters to enhance accuracy under specific site conditions. Examples include customized systems tailored to regional requirements, such as mRHRs (Budetta, 2004), the proposition of Saroglou et al. (2012) for Monemvasia, Greece, and others.

The precise assessment of rockfall hazard involves evaluating: a) susceptibility; b) magnitude; c) intensity; d) potential runout area; and e) frequency of rockfalls. Susceptibility is determined by the rock mass properties and possible factors that may weaken it. Magnitude refers to the size (volume) of the detached rock blocks, while intensity relates to the kinetic energy of the trajectory. Although precise intensity is typically calculated through simulations, it can be estimated indirectly in a hazard-risk assessment system by considering the maximum height from which a block can detach. Similarly, the potential runout area is often determined via trajectory simulation, but simpler parameters such as slope height and angle can also be used for estimation. Finally, frequency is rarely based on detailed data; instead, it is typically inferred from general information and field observations that indicate recent activity, such as rock block at the slope base, impact marks on the slope face, or damage to the roadway.

For the development of the rockfall hazard-risk assessment system (Figure 1) for the area affected by 2023 Evros wildfire, the aim was to include the essential parameters without requiring time-consuming procedures during field surveys. Following this approach and after reviewing existing systems in the literature, seven parameters were selected, all of which can be measured or estimated through on-site observations. Five of these parameters are related to the hazard (H) of the slope, while the remaining two are related to exposure and vulnerability (R).

Rating for all parameters follows an exponential scale, consistent with the original system proposed by Pierson (1992), but have been modified to have a maximum value of 100. The parameters H1 (slope height), H2 (block size), and H3 (rainfall height) are derived from the original RHRS, while the parameters H4 (rock mass condition) and H5 (rockfall frequency) are based on the proposal by Eggers et al. (2021). To calculate the total rockfall hazard (E), the scores of each H parameter are summed.

To assess risk, in addition to hazard, it is essential to determine and rate exposure and vulnerability. Parameter R1 is determined from measurements made during the field survey along with a correlation of reach angle that considers the influencing parameters and was developed for this study. It is worth noting that for calculating the score of the R1 parameter, vulnerability factors of the infrastructure are considered, such as road width, and exposure is also assessed using the reach angle concept. Therefore, the R1 parameter is a combination of both vulnerability and

exposure.

Reach angle (r) is defined as the angle formed by the horizon and the line that connects the detachment position and the furthest trajectory endpoint. As demonstrated from a detailed site-specific study in Avantas settlement, that was severely affected by the 2023 Evros wildfire (Asteriou et al., 2024), the parameters influencing reach angle are: a) slope height; b) slope angle; c) vegetation density; and d) block size. To estimate the potential area affected by rockfalls, parametric analyses were conducted using RocFall2 by varying those parameters within their typical range for the broader study area. Table 1 presents the values used in the analyses, which combined result to a total of 216 analyses.

Table 1. Parameters and their discrete values used in parametric analysis.

Parameter	Discrete values
Slope height, H [m]	15, 30, 45
Slope angle, θ [°]	45, 60, 75
Vegetation density, ρ [m²/m²]	0, 0.01, 0.03, 0.05
Block volume, V [m³]	0.01, 0.05, 0.1, 0.25, 0.5, 1.0

Figure 1. The proposed Post-fire Rockfall Hazard-Risk Assessment System, FiRo-RiS.

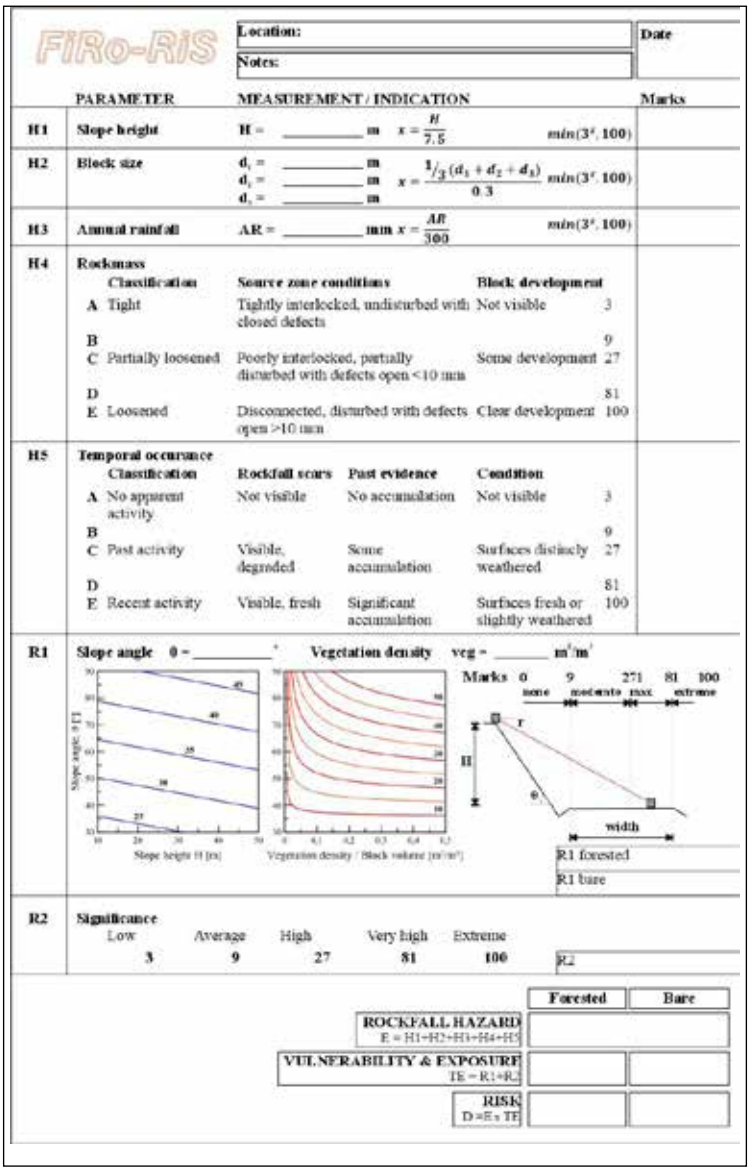

Reach angle (r) was divided into two components: a) the basic reach angle (r_{bas}), which depends on the slope height and slope angle (without vegetation), and b) the surplus reach angle (r_{sur}), which depends on the block size and vegetation density. This allows for directly identifying the impact of vegetation loss due to a wildfire on the trajectory length, which affects the exposure. Before a wildfire, the reach angle (r) is the sum of these components. After the wildfire, the reach angle equals the basic reach angle, since the vegetation has been destroyed.

Utilizing the results of the parametric analyses conducted without the vegetation (bare slope), the basic reach angle (r_{bas}) is correlated with the slope height (H) and the slope angle (θ). The additional effect of vegetation on reach angle is correlated with the vegetation density (ρ), expressed as the total area of stems at breast height per square meter, the block volume (V), and the slope angle (θ). These correlations are embedded in the developed hazard-risk system (Figure 1) as nomographs.

Through the reach angle and the slope height, the runout distance or exposure is calculated. Parameter R1 is rated depending on the position that is influenced by the incident. In case that a road is affected, the following cases are discerned: a) the falling block does not reach the road, so no consequences are expected (R1 = 0); b) the falling block reaches the road but leaves a free width of 3 m width, allowing vehicle movement, thus the road maintains serviceability (R= 9 to 27, depending on the unaffected width); c) the falling block affects the entire road cross-section, resulting in maximum consequences (R1 = 81); and d) .the falling block exceeds the road area and threatens additional infrastructure, having extreme consequences (R1 = 100). The consequences are considered extreme (R1=100) when a resident or a facility is located within the rockfall propagation zone.

The R2 parameter refers to the significance of the potential impacts. It has a subjective nature and is based on the importance of exposed elements from a socio-economic perspective. For example, when the main infrastructure affected is the road network, criteria for assessing its importance could include daily traffic volume, the presence of alternative routes, or others.

The sum of the individual scores for the R1 and R2 parameters gives the total score for the combination of vulnerability and exposure, according to TE = R1 + R2. The final risk score is calculated as the product of the total hazard score and the total vulnerability-exposure score, according to $D = E \times TE$. To avoid excessively large values, the total scores of E and TE are normalized by dividing them to their maximum possible scores, which are 500 and 200, respectively. The proposed system is named FiRo-RiS, derived from the initials of the words Fire Rockfall Risk System.

Application to the area affected by the 2023 Evros Wildfire

The developed Rockfall Hazard-Risk System FiRo-RiS was applied to the area of Evros that was severely affected by the devastating wildfire (see Figures 2 to 4), during an on-site inspection carried out between September 16–18, 2024. The surveyed routes included the mountainous road network and settlements that were impacted by the wildfire. Along these routes, 36 slopes were identified and examined.

Figure 2 presents the hazard map of the examined locations, as derived from the normalized score, E_{norm}. The five classes of the E_{norm} were obtained by applying the Jenks algorithm (Jenks, 1968), according to which the classes are designed to minimize the standard deviation of the scores within the same class, while maximizing the distances between the central values of the classes. Since the system has a comparative character between the slopes examined, each class is given a qualitative description as follows: a) Low; b) Moderate; c) High; d) Very High; and e) Extreme, respectively.

The impact of vegetation loss is highlighted through the comparison of the maps in Figures 3 and 4, which show the distribution of the total risk score before and after the wildfire. It is noteworthy that before the fire, the majority of the locations (61%) were characterized by ‘Low’ risk, with the remaining classes occupying 6%, 14%, 5%, and 14% of the examined slopes, respectively. After the loss of vegetation, there is a significant decrease in the number of locations classified as ‘Low’ risk (19%), and a notable increase in the number of locations categorized as ‘Moderate’ risk (39%). For the ‘High’, ‘Very High’, and ‘Extreme’ risk classes, there is a slight increase, reaching percentages of 17%, 8%, and 17%, respectively.

Figure 2. Normalized hazard map of the investigated area.

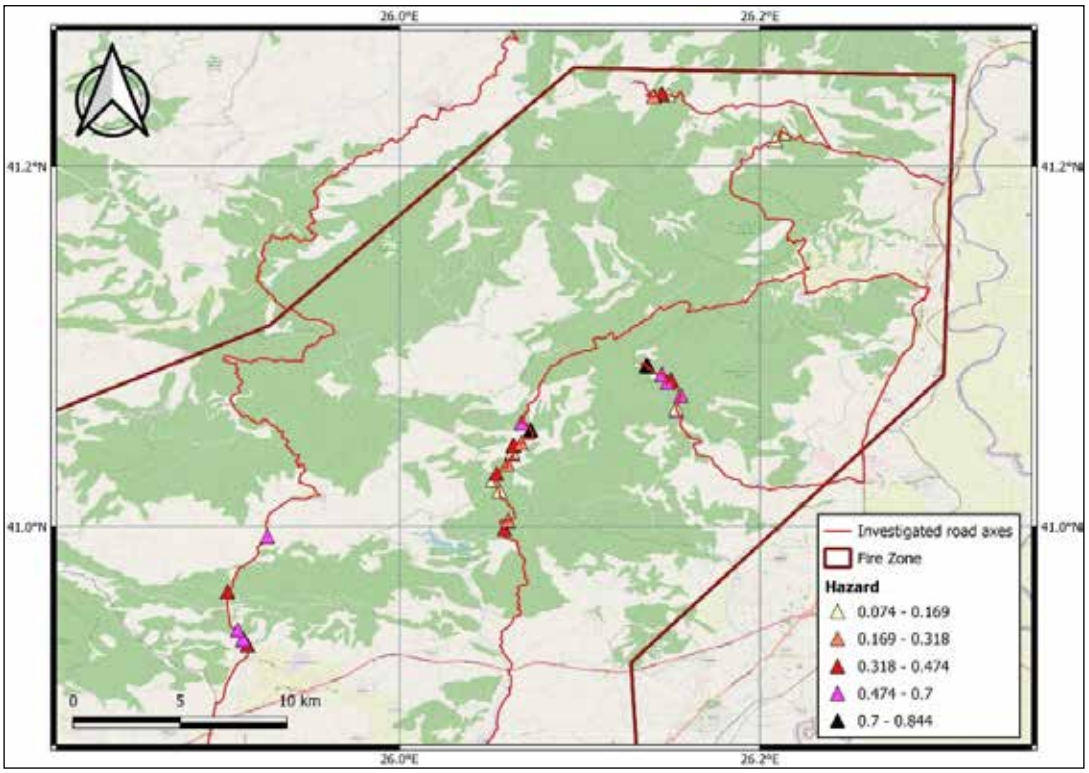

Figure 3. Normalized risk map before the wildfire of the investigated area.

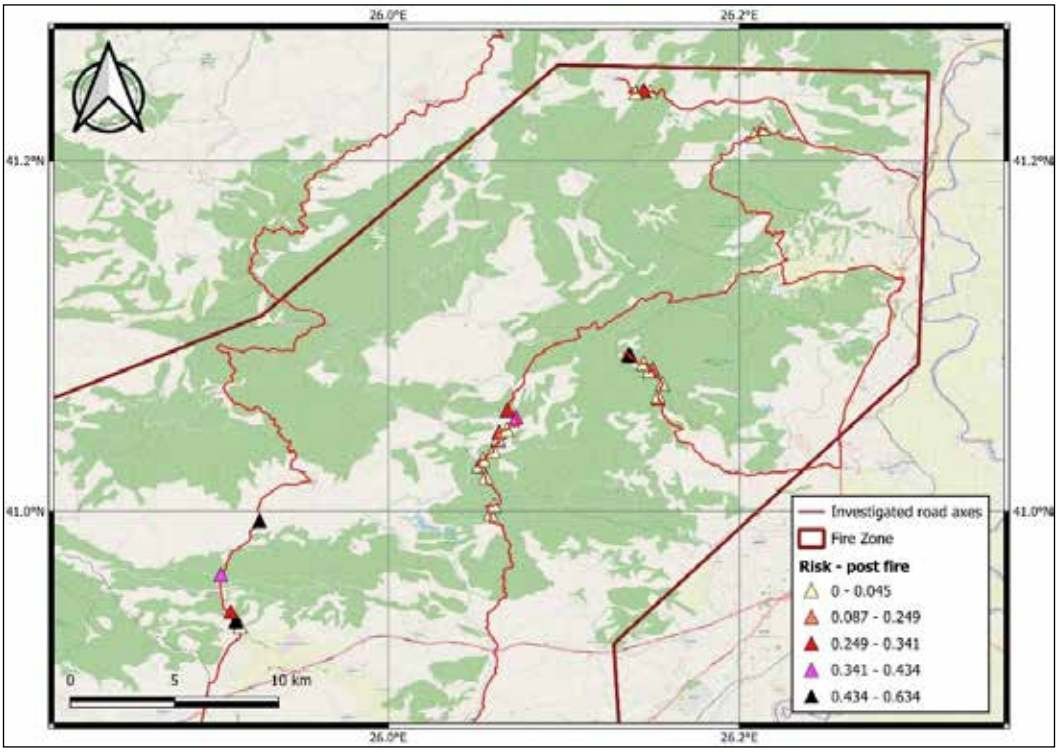

Figure 4. Normalized risk map after the wildfire of the investigated area..

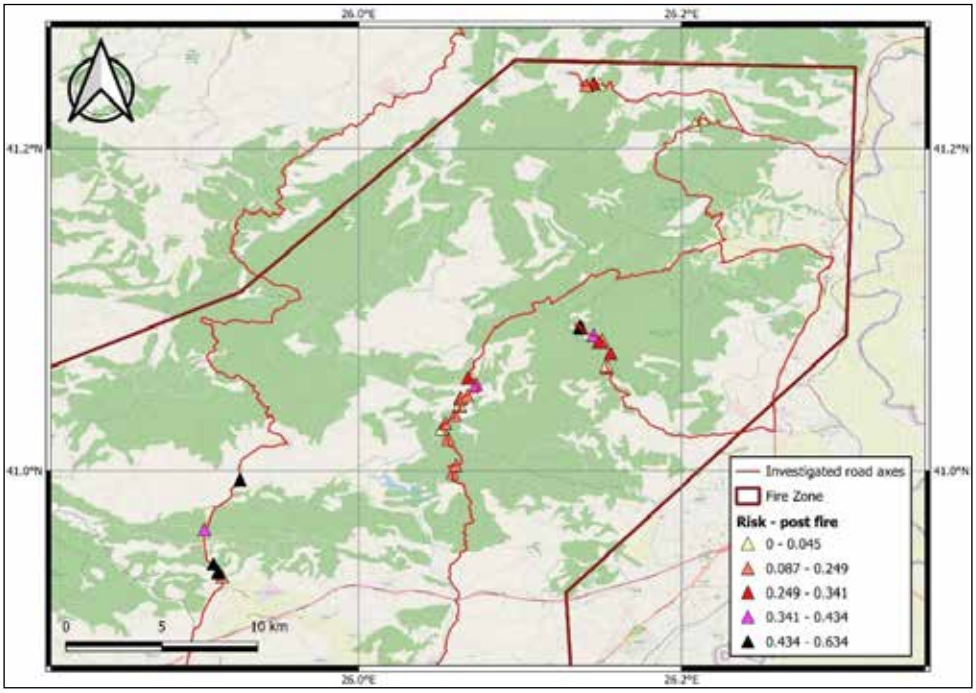

Conclusions and Discussion

The FiRo-RiS (Fire Rockfall Risk System) was developed and successfully applied to the wildfire-affected region of Evros. By incorporating critical parameters from existing international methodologies and introducing modifications to account for the impacts of vegetation loss, the system provides an efficient and systematic approach for assessing rockfall hazard and risk. The system includes factors that consider susceptibility (via geological characterization of the rockmass), magnitude, intensity (through parameters such as block size and slope height), frequency of occurrence, and potential extent (through the calculation of the reach angle). The results demonstrate the system's utility in identifying high-risk sites and prioritizing them for mitigation actions, offering a practical decision-support tool for infrastructure managers and local authorities.

A key innovation of FiRo-RiS lies in its ability to quantify the impact of wildfire-induced vegetation loss on exposure and risk, a feature that addresses a growing concern in regions increasingly affected by climate change. By combining quantitative and qualitative evaluations, the system is both robust and user-friendly. Furthermore, the system can be adapted to diverse geomorphological and environmental conditions.

Despite its strengths, the proposed system has limitations, as is the case with any such system. It relies on predefined parameters that may not fully capture complex geological settings. Some criteria are based on empirical formulas derived from site-specific data. Additionally, the inclusion of subjective parameters, such as the socio-economic impact assessment, introduces variability in risk evaluations depending on the user's perspective. However, when the system is implemented by the same user, ensuring consistency and comparative evaluation of the sites, the ranking of locations remains reliable.

Acknowledgements

This project (KE83226) was funded by Democritus University of Thrace under the initiative "DUTh To The People: Actions to Mitigate the Effects of the Devastating Fires in Thrace."

References

Asteriou, P., Sotiriadis, D., Petala, E., Kazelis, L., Evaggelou, E., Tzevelekis, T., Klimis, N. 2024. Assessing rockfall hazards post-wildfires: a case study in Evros, Greece. EURONGEO 2024. 4th European Regional Conference

of IAEG. Dubrovnik, Croatia.
Budetta, P., 2004. Assessment of rockfall risk along roads. Nat Hazards Earth Syst Sci 4, 71–81.
Cunningham, C.X., Williamson, G.J., Bowman, D.M.J.S., 2024. Increasing frequency and intensity of the most extreme wildfires on earth. Nat Ecol Evol 8, 1420–1425.
De Graff, J.V., Shelmerdine, B., Gallegos, A., Annis, D. 2015. Uncertainty associated with evaluating rockfall hazard to roads in burned areas. Env Eng Geosc 21(1), 21–33.
Dorren, L.K.A., Berger, F., Le Hir, C., Mermin, E., Tardif, P. 2007. Mechanisms, effects and management implications of rockfall in forests. For Ecol Manage 215, 183–195.
Eggers, M.J., Nash, T., Dwumfour, D., Turbitt, S., Dixon, J. 2021. Natural slope hazard management and integration with mining operations, in PM Dight (ed.), SSIM 2021: Second International Slope Stability in Mining, Australian Centre for Geomechanics, Perth, pp. 261-276.
Ferrari, F., Giacomini, A., Thoeni, K. 2016. Qualitative Rockfall Hazard Assessment: A Comprehensive Review of Current Practices. Rock Mech Rock Eng 49, 2865–2922.
Jenks, G.F. 1967. The Data Model Concept in Statistical Mapping. International Yearbook of Cartography 7, 186–190.
Liu, Y., Stanturf, J., Goodrick, S. 2010. Trends in global wildfire potential in a changing climate. For. Ecol. Manag. 259, 685–697.
Moos, C., Dorren, L.K.A., Stoffel, M. 2017. Quantifying the effect of forests on frequency and intensity of rockfalls. Nat Hazards Earth Syst Sci 17, 291–304.
Pierson, L.A., Davis, S.A., Van Vickle, R. 1990. Rockfall hazard rating system implementation manual, federal highway administration (FHWA), report FHWA-OR-EG-90–01, FHWA. US Department of Transporation, Oregon.
Perez-Rey, I., Sarro, R., Tomás, R., Alejano, L.A., Hernández Gutiérrez, L.E., Mateos, R.M., Riquelme, A.2023. A brief review of the effect of wildfires on rockfall occurrence. IOP Conf. Ser.: Earth Environ. Sci. 1124. September 11-15, Helsinki, Finland
Saroglou, H., Marinos, V., Marinos, P., Tsiambaos, G. 2012. Rockfall hazard and risk assessment: an example from a high promontory at the historical site of Monemvasia, Greece- Natural Hazards and Earth System Sciences 12(6), 1823-1836
Sarro, R, Pérez-Rey, I., Tomás, R., Alejano, L.R., Hernández-Gutiérrez, L.E., Mateos, R.M. 2021. Effects of wildfire on rockfall occurrence: A review through actual cases in Spain. Appl Sci 11, 2545.
Scheidl, C., Heiser, M., Vospernik, S., Lauss, E., Perzl, F., Kofler, A., Kleemayr, K., Bettella, F., Lingua, E., Garbarino, M, Skudnik M, Trappmann, D., Berger, F., 2020. Assessing the protective role of alpine forests against rockfall at regional scale. European J For Res 139, 969–980.
Stoffel, M., Wehrli, A., Kühne, R., Dorren, L.K.A., Perret, S., Kienholz, H. 2006. Assessing the protective effect of mountain forests against rockfall using a 3D simulation model. For Ecol Manag 225, 113–122.
Vahedifard, F., Abdollahi, M., Leshchinsky, B., Stark, T., Sadegh, M., AghaKouchak, A. 2024. Interdependencies between wildfire□induced alterations in soil properties, near□surface processes, and geohazards. Earth and Space Science 11(2)

17th INTERNATIONAL CONGRESS of the Geological Society of Greece

BULLETIN OF THE GEOLOGICAL SOCIETY OF GREECE, SP. PUBL.

EXTENDED ABSTRACT 018

Estimation of the displacement components in South Aegean islands as a response to the early 2025 seismicity of the Anydros Islet using Sentinel-1 imagery.

Athinelis I.[1], Basiou E.[2], Falaras, T.[1, 3] and Parcharidis I.[1]

(1) Department of Geography, Harokopio University of Athens, 176 76 Athens, Greece, gp222301@hua.gr (A.I.), falaras@hua.gr (F.T.), parchar@hua.gr (P.I.)

(2) Department of Geology and Geoenvironment, National and Kapodistrian University of Athens, 15771 Athens, Greece, eleutheriaba@geol.uoa.gr (B.E.)

(3) SUPCO - sustainable urban planning consultants, Thessalonikis 121, 18346 Moschato, Attica, Greece.

Research Highlights

- DInSAR analysis of Sentinel-1 data reveals significant coseismic deformation between Santorini and Amorgos, with uplift in South Thira (+2.1 cm) and subsidence near Oia (-2.8 cm), paired with a horizontal distancing trend between Thirasia (-2.7 cm), Nea Kameni (-1.5 cm) and Oia (+4.0).
- Amorgos and Anafi show westward displacement (-4.0 cm, -2.3 cm), indicating active faulting.

Abstract

The region between Santorini and Amorgos is seismically active and recently has seen a noticeable increase in earthquake frequency, causing significant tectonic deformation linked to active faulting and, potentially, magmatic processes. This extended abstract focuses on the analysis of the coseismic displacement components of Santorini, South Ios, Anafi and Amorgos islands, using Sentinel-1 satellite data and the DInSAR (Differential Interferometric Synthetic Aperture Radar) method, which revealed noteworthy vertical (up-down) and horizontal (E-W) ground displacement. Results indicate uplift in South Thira (+2.1 cm), subsidence near Oia (-2.8 cm), and significant east-west displacement in Santorini, where Thirasia, Nea Kameni and Oia seem to move away from each other. SW and NE Amorgos show a significant westward motion (-4.0 cm in Kalofana, -3.5 cm in Aigiali), while Anafi and Ios exhibit localized subsidence and uplift. These findings seem to reference ongoing fault activity and strain accumulation, presenting the need for continued monitoring of the seismically active area.

Key words: Santorini, Amorgos, earthquake, coseismic displacement, DInSAR, Sentinel-1.

Introduction / Background

Greece and the islands of the South Aegean sea particularly are no strangers to seismic activity, due to their proximity to the Hellenic subduction zone of the African plate moving at a pace of ~ 0.9 cm/year under the Aegean plate (Reilinger et al., 2006; McClusky et al., 2000; Andinisari et al., 2021; Krassakis, 2024). For a long time, the South Aegean Islands, such as Santorini, Amorgos, Anafi, and Ios have been the focus of seismological studies, due to the complex tectonic setting and frequent seismic activity in the region between Santorini and Amorgos. More specifically, in the shear zone found NE of Santorini and NW of Amorgos, known as the Santorini-Amorgos Fault Zone (Tsampouraki-Kraounaki et al., 2021), a large number of significant earthquakes has been recorded, some reaching Mw > 5.0 (Nomikou et al., 2016; Andinisari et al., 2021). Such a seismic occurrence, arguably one of the most important events in the region were the twin earthquakes, M 7.8 and 7.2, of 1956, which caused a lethal tsunami 20 m in height (Nomikou et al., 2016; Andinisari et al., 2021).

In recent weeks, Santorini Island and the surrounding region (Figure 1) have experienced a series of earthquakes, with magnitudes reaching up to M 5.3 (10/2/2025). Most of the seismic activity is occurring approximately 25 km northeast of the Santorini complex, near Anydros, at an average depth of about 7 km beneath the seabed. Seismic activity has been gradually increasing since June 2024, with a notable surge in the first weeks of February. Initially, the earthquakes were centered around the Santorini caldera,

but their epicenters have gradually migrated northeast toward Amorgos, specifically around the small, uninhabited islet of Anydros.

The threat that earthquakes and other natural disasters pose have led to significant advancements in the field of remote sensing throughout the years, in an effort to study these events and their deformation effects more effectively. Specifically, techniques utilizing Synthetic Aperture Radar (SAR) satellite images, such as those of the Sentinel-1 mission of the European Space Agency's (ESA) Copernicus program, have been extremely reliable in the study of earthquake-induced deformation (Wright et al., 2004; Suresh & Yarrakula, 2019; Li et al., 2021). More particularly, the method of Differential SAR Interferometry (DInSAR) has been extensively utilized to estimate ground displacement due to earthquakes, using the phase difference between pre and post event images (Wright et al., 2004; Suresh & Yarrakula, 2019; Li et al., 2021).

In this research, the impact of the early 2025 earthquake swarm on the islands of Santorini, Amorgos, Anafi and South Ios was studied using Sentinel-1 SAR data and the DInSAR method. Via differential interferometry, the Line-of-Sight (LOS) displacement of the four islands was estimated and then analyzed into vertical (up-down) and horizontal (E-W) displacement components.

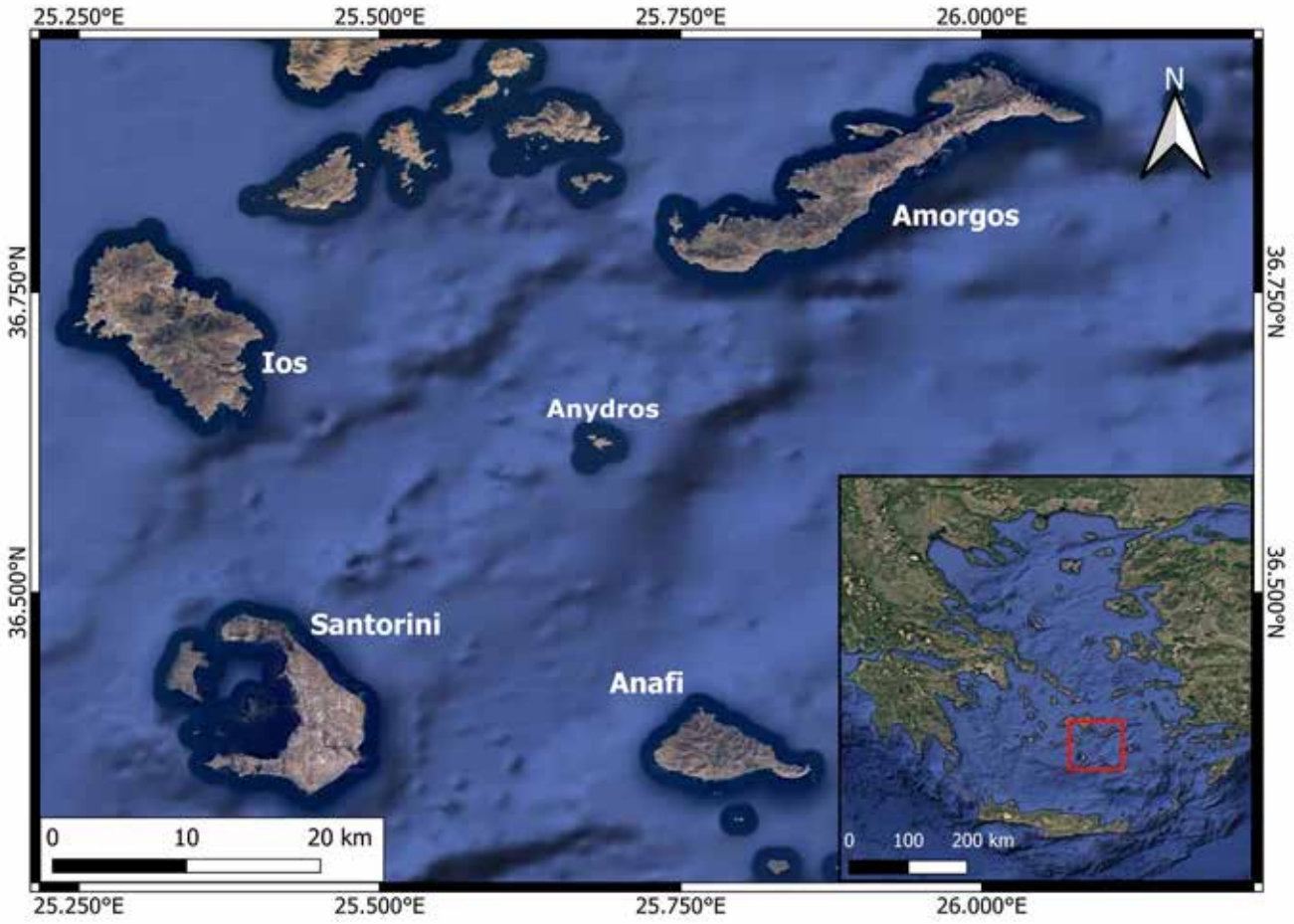

Figure 1. Study area map in QGIS v3.28.1 using the Google Satellite basemap based on Google Earth Pro. Projection: WGS84. (After Athinelis).

Data & Methodology

To study the deformation caused by the recent earthquake in the area around Anydros Island and its effects on the close islands, D-InSAR (Differential Interferometric Synthetic Aperture Radar) was utilized.

InSAR has gained widespread recognition for monitoring surface deformation, due to its many benefits (Calvet et al., 2023). SAR images were utilized for this study, obtained from the Copernicus Data Space Ecosystem browser (Copernicus Data Space Ecosystem). The time-frame studied in this research was of the seismicity during the transitional period from January 2025 to early February 2025, especially between 30/01/2025 and 05/02/2025. As such, the SAR images selected were covering this time-period while having the least time-difference possible. Specifically, a pre-event image on 30/01/2025 and a post-event image on 11/02/2025 were used for the ascending orbit pass and a pre-event image on 24/01/2025 and a post-event image on 05/02/2025 were acquired for the descending orbit pass. The Level-1 Single Look Complex (SLC) Interferometric Wide Swath (IW) data products from the Sentinel-1 are derived from the satellite's C-band SAR C-SAR instrument with a wavelength of approximately 5.5 cm (Kotzerke et al. 2022). The ESA STEP Sentinel Application Platform (SNAP v11.0) software was utilized for the process (ESA). Two pairs of Sentinel-1 IW SLC images were used in this research, for ascending and descending orbits respectively.

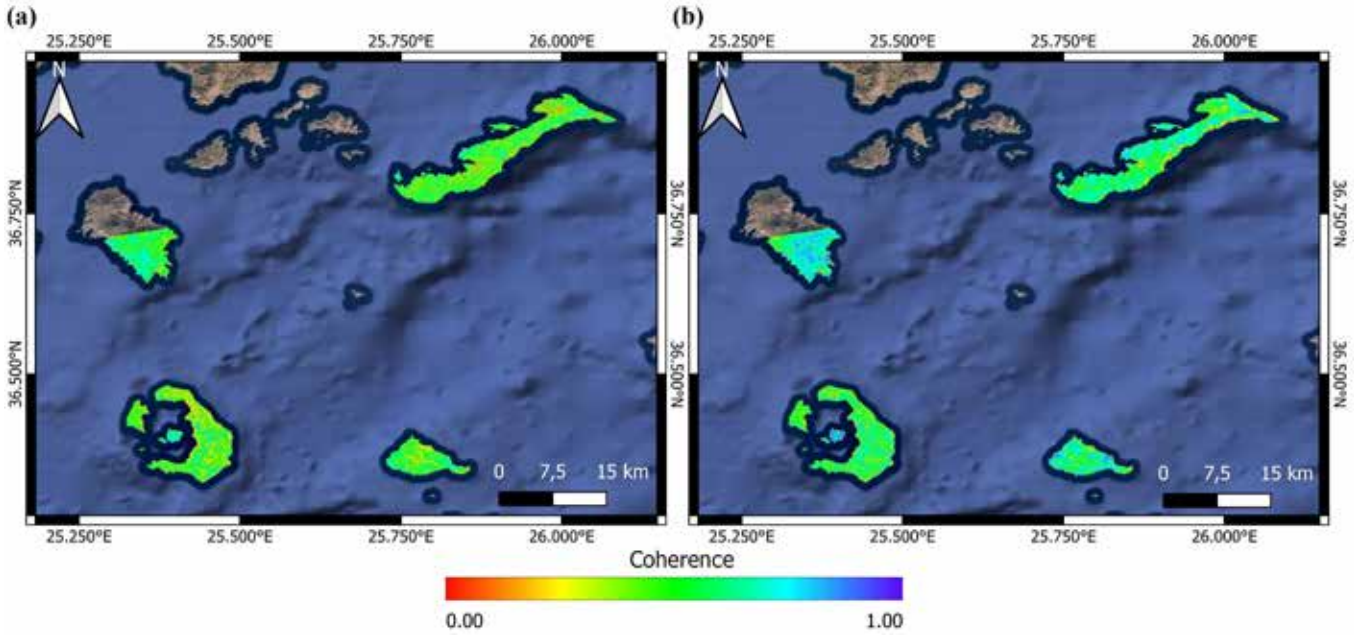

Figure 2. Coherence maps of the studied islands in ascending (a) and descending (b) pass geometry. Made in QGIS v3.28.1 using the Google Satellite basemap based on Google Earth Pro. Projection: WGS84.

The first step is to align two SAR images—a master image and a "slave" image—into a single stack, the pixels in the "slave" image are adjusted to match those in the master image. During this process, orbit correction is applied, and a DEM is utilized with back-geocoding co-registration. In this case the SRTM 1Sec HGT DEM was used, automatically downloaded by the software. The next step involves interferogram generation and coherence estimation, where the interferometric phase and coherence (Figure 2) are computed. This was accomplished through the Interferogram Formation tool, which, unlike other software, does not require the use of a specific reference point and automatically utilizes an area of multiple points for the creation of the interferograms but has been known to provide reliable results (Mavroulis et al., 2021). The interferograms were generated by pairing the aforementioned images as seen in Table 1.

Table 1. List of the interferometric image pairs used for each island.

	Interferometric image pairs		Orbit / Frame	Baseline	
Santorini	S1A	S1A		**Perpendicular**	**Temporal**
Ascending pair	30/01/2025	11/02/2025	29 / 113	49m	12d
Descending pair	24/01/2025	05/02/2025	109 / 471	39m	12d
Amorgos					
Ascending pair	30/01/2025	11/02/2025	29 / 113	49m	12d
Descending pair	24/01/2025	05/02/2025	109 / 471	39m	12d
Anafi					
Ascending pair	30/01/2025	11/02/2025	29 / 113	49m	12d
Descending pair	24/01/2025	05/02/2025	109 / 471	39m	12d
South Ios					
Ascending pair	30/01/2025	11/02/2025	29 / 113	49m	12d
Descending pair	24/01/2025	05/02/2025	109 / 471	39m	12d

Additionally, applying TOPSAR deburst eliminates the boundary areas between consecutive bursts (Marbuti et al. 2017). Before unwrapping, the SRTM 1Sec HGT was used again to remove the topographic phase and the images were multi-looked at 6 range pixels and 2 azimuth pixels. The SNAPHU software plugin (Stanford University) was utilized for the phase unwrapping. Phase unwrapping is essential for eliminating the ambiguity associated with the multiple-wavelength factor in the interferometric phase, allowing for the determination of motion (Goldstein et al. 1998). In this stage it important to specify that no tropospheric phase delay removal was applied to these results. The unwrapped phase is converted into displacement, which is geocoded, resulting in the LOS displacement (Monterroso et al. 2018). Finally, the LOS displacement (D) of the study areas is split into two components, vertical (dz) and horizontal (de), using the incidence angle (θ) of ascending (a) and descending (d) geometries, calculated in radians and the following formulas (Manzo et al., 2006; Dalla Via et al., 2012):

$$dz = \frac{Dd \cdot \sin(\theta a) + Da \cdot \sin(\theta d)}{\sin(\theta d + \theta d)} \quad (1)$$

$$de = \frac{Dd \cdot \cos(\theta a) - Da \cdot \cos(\theta d)}{\sin(\theta d + \theta d)} \quad (2)$$

The positive values of dz signify uplifting, while the negatives are attributed to subsidence. Similarly, negative de values suggest westward displacement, while positive are of an eastward displacement. The decomposition of the deformation into vertical and horizontal displacement was performed in QGIS v.3.28.1, through Raster Calculator tool, by inserting the raster layers of the incidence angles and the LOS displacement into the formulas (1) and (2) respectively (Mavroulis et al., 2021).

Results

Analyzing the resultant vertical (up-down) deformation component (Figure 3) of the four islands a few observations can be made. Santorini (fig. 3-a) shows an upward displacement trend in the southern part of Thira island, reaching up to ~ +2.1 cm (+0.021 m). Most of the rest of the island complex seems relatively stable, while the northwestern part of the island, ESE of Oia, shows an abrupt subsidence reaching up to ~ -2.8 cm (-0.028 m). This subsidence could be related to the SW - NE trending active fault found in the same region. Despite this, the uplifting in South Thira is relatively unexpected. Uplifting can be noticed in the western edge of Anafi island (fig. 3-b), as well as the southeastern coastal areas between the Katsouni

and Roukounas beaches, reaching +0.7 - +1.0 cm. The areas of Agios Nikolaos (Saint Nikolaos) northeast of Klisidi, the area southeast of Agios Nikolaos and the easternmost part of the island present subsidence, with the first two zones reaching ~ -2.2 cm, while eastern Anafi reached ~ -2.4 cm. Amorgos (fig. 3-c) shows subsidence mainly in the northeastern edge of the island reaching up to ~ -2.7 cm. While most of the island seems stable in terms of vertical up-down displacement, a zone of ~ +1.0 cm uplifting can be seen southwest of the Amorgos settlement. In the case of South Ios (fig. 3-d), northward, near the center of the island a subsidence zone of up to ~ -2.0 cm can be seen. East of that zone, a slight uplifting trend can be viewed of about ~ +1.0 cm, while uplifting of ~ +0.5 cm is presented in Petalidi. A maximum of ~ +1.7 cm is seen in the islet of Varvaronisi, southeast of the Magganari settlement off the coast.

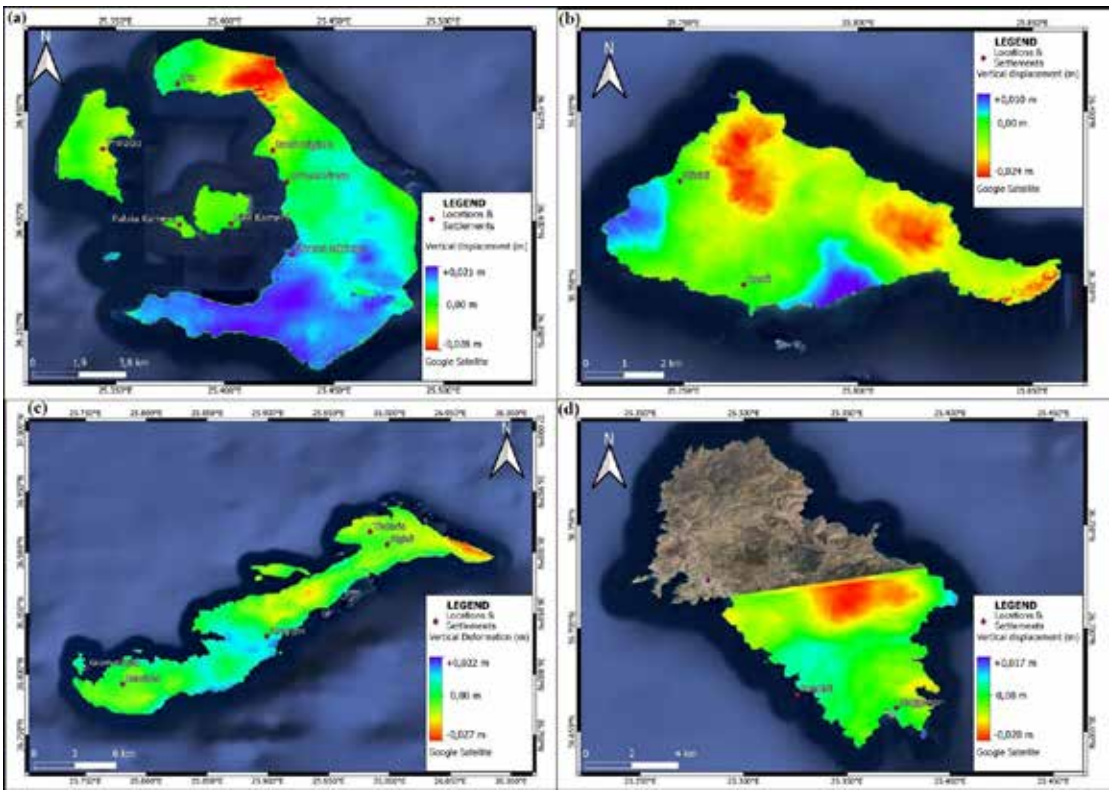

Figure 3. Interferograms showing the vertical displacement taking into account the images before and after the seismic events which happened between 24/01/2025 and 11/02/2025. The layers were overlayed on a Google Satellite basemap in QGIS v3.28.1.

The horizontal, E-W displacement of these islands (Figures 4 & 5) can also highlight some intriguing information, especially in the case of Santorini (fig 4-a). Specifically, the Thirasia island of the Santorini complex showed displacement westward at ~ -2.7 cm, while the eastern Thira island, in the Oia region, saw a significant eastward displacement of up to ~ +4.0 cm. The Nea Kameni island was displaced westward to a smaller degree of ~ -1.5 cm. In Anafi island (fig. 4-b), between the Klisidi and Anafi settlements there's a region presenting westward displacement of up to ~ -2.3 cm. The East-Southeast edge of the island presents eastward displacement of ~ +1.0 cm. Amorgos island (fig. 4-c) is particularly interesting as the entire island seems to have a mild trend westward with the SW part, in Kalofana and the NE part, east of Aigiali, presenting a more significant westward displacement of ~ -4.0 cm and ~ -3.5 cm respectively. The Gramvoussa islet shows an eastward displacement of ~ +1.3 cm. Lastly, South Ios (fig. 4-d) seems fairly stable in the E-W direction with a westward ~ -3.6 cm displacement southeast of Magganari and an eastward displacement zone of ~ +0.4 cm in the coast southeast of Ios settlement.

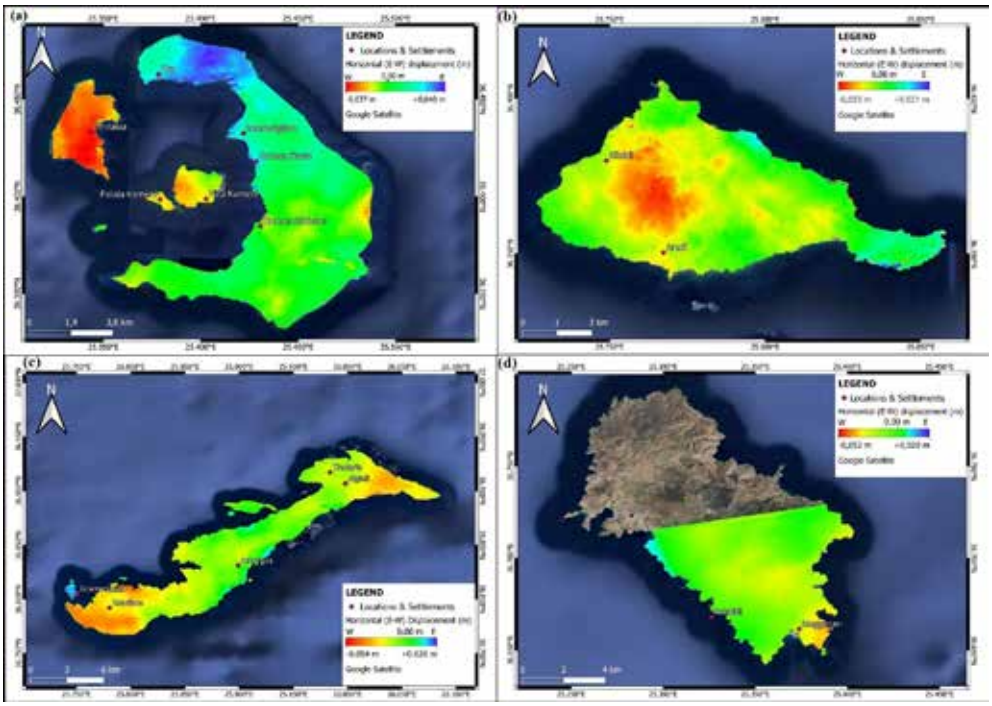

Figure 4. Interferograms showing the horizontal displacement taking into account the images before and after the seismic events which happened between 24/01/2025 and 11/02/2025. The layers were overlayed on a Google Satellite basemap in QGIS v3.28.1.

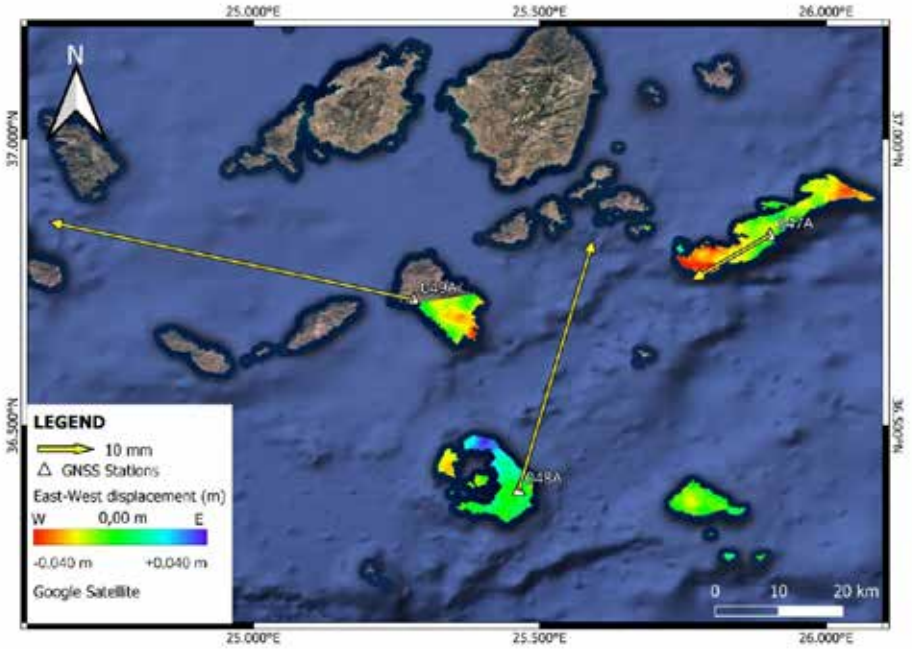

Figure 5. Horizontal shift of the South Aegean Islands shown through GNSS station data, for the period between 28/01/2025 and 20/02/2025, compared to the horizontal displacement trends of the current study. The vectors were created by the Dionysos Satellite Observatory of the National Technical University of Athens (NTUA) using data from the HEPOS GNSS station network. The layers were overlayed on a Google Satellite basemap in QGIS v3.28.1.

Conclusions

Santorini showed a spreading trend in-between the islands of Thirasia, Nea Kameni and North Thira, which were moving away from, seemingly, an underwater center. This might be caused by active tectonic and/or magmatic processes within the submerged caldera found in that region. Despite this, the uplifting trend observed in South Santorini does not seem to fit with that hypothesis and might be the result of residual atmospheric disturbances. Both Anafi and Amorgos showed significant westward displacement where, in Anafi's case, this horizontal shift seems to be due to internal stress. Moreover, uplift was noticed in western and southeastern Anafi, along with subsidence in Agios Nikolaos and the eastern island, possibly connected to similar tectonic processes. In Amorgos there was northeastern subsidence and minor uplift southwest. In the case of South Ios, the island was characterized by localized subsidence and minor uplift. The displacement in these islands does not seem to be related, necessarily, to the seismicity in Anydros, due to their geographic distribution. Overall, these trends found in the four islands studied in this research, seem to indicate ongoing fault activity and, possibly, magmatic processes, though concrete conclusions may require further research and investigation.

Acknowledgements

We would like acknowledge the contribution of Andreas Karavias (NTUA) in his support and advice during the processing phase. We also acknowledge Dionysos Satellite Observatory of NTUA for their displacement vector analysis using HEPOS GNSS data. Acknowledgements should be given to the Hellenic Cadastre, for their ownership of the HEPOS GNSS network. Moreover, we would like to thank Dr A. Ganas (National Observatory of Athens) and Prof. M. Foumelis (Aristotle University of Thessaloniki) for their help in the GNSS explanation as well as during all the crisis. Last but not least, we acknowledge ESA for openly and freely providing the Sentinel-1 satellite data of the Copernicus program through the Copernicus Data Space Ecosystem platform.

References

Andinisari, R., Konstantinou, K.I., Ranjan, P., 2021. Seismicity along the Santorini-Amorgos zone and its relationship with active tectonics and fluid distribution. Phys. Earth Planet. Inter. 312, 106660. https://doi.org/10.1016/j.pepi.2021.106660

Calvet, A., Balbarani, S., Gende, M., 2023. DinSAR coseismic deformation measurements of the Mw 8.3 Illapel earthquake (Chile). Journal of Geodetic Science 13(1), 20220154. https://doi.org/10.1515/jogs-2022-0154.

Copernicus Data Space Ecosystem. Copernicus Browser. Available at: https://browser.dataspace.copernicus.eu/ [Accessed 12 February 2025].

Dalla Via, G., Crosetto, M., Crippa, B., 2012. Resolving vertical and east-west horizontal motion from differential interferometric synthetic aperture radar: The L'Aquila earthquake. J. Geophys. Res. Solid Earth 117(B2). https://doi.org/10.1029/2011JB008689

Dionysos Satellite Observatory. *Santorini Volcano*. National Technical University of Athens. Available at: https://dionysos.survey.ntua.gr/dsoportal/_projects/supersites/santorini/ [Accessed 12 February 2025].

European Space Agency (ESA). Sentinel Application Platform (SNAP). Available at: https://step.esa.int/main/toolboxes/snap/ [Accessed 12 Feb. 2025].

Goldstein, R.M., Werner, C.L., 1998. Radar interferogram filtering for geophysical applications. Geophys. Res. Lett. 25, 4035–4038.

Krassakis, P. 2024. Geospatial intelligence for multi-hazard assessment in coastal areas of the Hellenic volcanic arc. Ph.D. Thesis, Harokopio University, Athens, Greece, 283 p. https://doi.org/10.12681/eadd/56709

Kotzerke, P., Siegmund, R., Langenwalter, J., Andersen, H.S., 2022. End-to-End Implementation and Operation of the European Ground Motion Service (EGMS) Product User Manual. European Environment Agency, Copenhagen, Denmark. [Google Scholar]

Marbouti, M., Praks, J., Antropov, O., Rinne, E., Leppäranta, M., 2017. A study of landfast ice with Sentinel-1 repeat-pass interferometry over the Baltic Sea. Remote Sens. 9, 833. https://doi.org/10.3390/rs9080833

Manzo, M., Ricciardi, G.P., Casu, F., Ventura, G., Zeni, G., Borgström, S., Berardino, P., Del Gaudio, C., Lanari, R., 2006. Surface deformation analysis in the Ischia Island (Italy) based on spaceborne radar interferometry. J. Volcanol. Geotherm. Res. 151(4), 399–416. https://doi.org/10.1016/j.jvolgeores.2005.09.010

McClusky, S., Balassanian, S., Barka, A., Demir, C., Ergintav, S., Georgiev, I., Gurkan, O., Hamburger, M., Hurst, K., Kahle, H., Kastens, K., Kekelidze, G., King, R., Kotzev, V., Lenk, O., Mahmoud, S., Mishin, A., Nadariya, M., Ouzounis, A., Paradissis, D., Peter, Y., Prilepin, M., Reilinger, R., Sanli, I., Seeger, H., Tealeb, A., Toksoz, M.N., Veis, G., 2000. Global positioning system constraints on plate kinematics and dynamics in the eastern Mediterranean and Caucasus. J. Geophys. Res. 105, 5695–5719. https://doi.org/10.1029/1999JB900351

Monterroso, F., de Luca, C., Bonano, M., Lanari, R., Manunta, M., Manzo, M., Zinno, I., Casu, F., 2018. Automatic generation of co-seismic displacement maps by using Sentinel-1 interferometric SAR data. Procedia Comput. Sci. 138, 332–337. https://doi.org/10.1016/j.procs.2018.10.047

Mavroulis, S., Triantafyllou, I., Karavias, A., Gogou, M., Katsetsiadou, K.-N., Lekkas, E., Papadopoulos, G.A., Parcharidis, I., 2021. Primary and secondary environmental effects triggered by the 30 October 2020, Mw = 7.0, Samos (Eastern Aegean Sea, Greece) earthquake based on post-event field surveys and InSAR analysis. Appl. Sci. 11, 3281. https://doi.org/10.3390/app11073281

Nomikou, P., Hübscher, C., Ruhnau, M., Bejelou, K., 2016. Tectono-stratigraphic evolution through successive extensional events of the Anydros Basin, hosting Kolumbo volcanic field at the Aegean Sea, Greece. Tectonophysics 671, 202–217. https://doi.org/10.1016/j.tecto.2016.01.021

QGIS Development Team. QGIS v.3.28.1. Available at: https://qgis.org/ [Accessed 12 Feb. 2025]

Reilinger, R., McClusky, S., Vernant, P., Lawrence, S., Ergintav, S., Cakmak, R., Ozener, H., Kadirov, F., Guliev, I., Stepanyan, R., Nadariya, M., Hahubia, G., Mahmoud, S., Sakr, K., ArRajehi, A., Paradissis, D., Al-Aydrus, A., Prilepin, M., Guseva, T., Evren, E., Dmitrotsa, A., Filikov, S.V., Gomez, F., Al-Ghazzi, R., Karam, G., 2006. GPS constraints on continental deformation in the Africa–Arabia–Eurasia continental collision zone and implications for the dynamics of plate interactions. J. Geophys. Res. 111. https://doi.org/10.1029/2005JB004051

Stanford University. *SNAPHU: Statistical-Cost, Network-Flow Algorithm for Phase Unwrapping*. Stanford University. Available at: https://web.stanford.edu/group/radar/softwareandlinks/sw/snaphu/ [Accessed 12 February 2025]

Tsampouraki-Kraounaki, K., Sakellariou, D., Rousakis, G., Morfis, I., Panagiotopoulos, I., Livanos, I., Manta, K., Paraschos, F., Papatheodorou, G., 2021. The Santorini-Amorgos shear zone: Evidence for dextral transtension in the south Aegean back-arc region, Greece. Geosciences 11(5), 216. https://doi.org/10.3390/geosciences11050216

17th INTERNATIONAL CONGRESS of the Geological Society of Greece

BULLETIN OF THE GEOLOGICAL SOCIETY OF GREECE, SP. PUBL.

EXTENDED ABSTRACT 019

Employing Sentinel-1 imagery to monitor the deformation rate over the caldera of the Santorini Volcanic Island Complex using multitemporal InSAR from January 2023 up to February 2025.

Athinelis I.[1], Castro-Melgar I.[1,2], Gatsios T.[1], Krassakis P.[1] and Parcharidis I[1].
(1) Department of Geography, Harokopio University of Athens, 176 76 Athens, Greece, gp222301@hua.gr (A.I.) icastromelgar@ig.cas.cz (C.-M.I.), gatsios@hua.gr (G.T.), pkrassakis@hua.gr (K.P.), parchar@hua.gr (P.I.)
(2) Institute of Geophysics, Czech Academy of Sciences, 141 00 Prague, Czech Republic

Research Highlights

- MT-InSAR processing of Sentinel-1 data unveiled significant uplifting deformation velocity in the northwestern part of the caldera, focusing in Nea Kameni, Thirasia, Imerovigli & Oia, possibly connected to swelling of the magmatic chamber due to magma accumulation.
- Increased deformation velocity was noticed past June 2024, suggesting increasing volcano-tectonic activity relating to the increased seismicity in Anydros.

Abstract

Santorini is one of the most significant islands in the South Aegean Sea and a well-known volcanic center in the South Aegean Volcanic Arc. It is known for its seismicity, caused by active volcanic and tectonic processes, such as the occurrences of 2011-2012 and 2024-2025. This study focuses on estimating the ground deformation velocity of Santorini's caldera by utilizing Multitemporal InSAR method of SBAS (Small Baseline Subset) and Sentinel-1 satellite imagery. The research found increased uplifting deformation rate in northwestern Nea Kameni and Imerovigli, up to ~ +17.6 mm/yr and ~ +17 mm/yr respectively. A lesser uplifting trend was recorded in Northwestern Thira (Oia) and Thirasia. Significant horizontal westward deformation was seen in south Thirasia and west Oia (up to -20 mm/yr) and Palaia Kameni (~ -39 mm/yr), while an eastward pattern was representing Imerovigli (up to ~ +21 mm/yr), which might signify swelling of the caldera due to magmatic and tectonic processes in the volcanic chamber. Time-series vertical and horizontal deformation diagrams attribute a more impactful effect after June of 2024.
Key words: Santorini, caldera, seismicity, ground deformation, SBAS, Sentinel-1.

Introduction / Background

Santorini (fig. 1), a prominent volcanic island complex in the Aegean Sea, is part of the South Aegean Volcanic Arc, which extends from Methana to Nisyros (Greece) (Krassakis, 2024). This arc is associated with the subduction of the African plate beneath the Eurasian plate, a process that has driven volcanic activity in the region for at least 4.7 million years (Vougioukalakis et al., 2019). The Santorini Volcanic Complex (SVC) consists of five main islands—Thira, Thirasia, Aspronisi, Palea Kameni and Nea Kameni—formed through successive eruptions, the most significant being the Minoan eruption (~1600 BCE). This event shaped the current morphology of the caldera and deposited widespread tephra layers (Vougioukalakis et al., 2019). Since then, the volcanic activity has been concentrated in the central part of the caldera, mainly at Nea Kameni, with the last eruption occurring in 1950.

The island remains an active volcanic system, experiencing recurrent unrest episodes. The most recent significant period of activity occurred between 2011 and 2012, marked by increased seismicity, ground deformation, and magmatic inflation at shallow depths (Vougioukalakis et al., 2016). During this episode, uplift reached up to 14 cm at Cape Skaros and 9 cm at Nea Kameni, as detected by geodetic techniques such as GPS and Interferometric Synthetic Aperture Radar (InSAR) (Foumelis et al., 2013). Seismicity was concentrated along the Kameni and Kolumbo fault zones, indicating a strong structural control on magma emplacement (Vougioukalakis et al., 2016). Despite these significant signals, no eruption followed, and subsequent geodetic studies from 2015 to 2021 confirmed a return to quiescence (Castro-Melgar et al., 2025).

Since June 2024, a new seismic sequence has been developing in the region, reaching its peak in a Mw 5.3 earthquake on 10 February 2025, located approximately 25 km northeast of the Santorini caldera, near the islet of Anydros, at an average depth of ~7 km. Over 7,000 earthquakes have been recorded in the broader Santorini-Amorgos area, suggesting a gradual reactivation of the regional stress field. Given the complex interplay between magmatic processes, tectonic stresses, and hydrothermal activity in Santorini, continuous geodetic monitoring is essential for understanding the current unrest. Remote sensing techniques, particularly multitemporal InSAR (MT-InSAR), offer a valuable tool for detecting and quantifying ground deformation, enabling the identification of subtle precursory signals.

Objectives

In this study, we employ Sentinel-1 imagery and the MT-InSAR method of Small BAseline Subset (SBAS) to monitor progression of the deformation rate in vertical (up-down) and horizontal (east-west) direction around the Santorini caldera from January 2023 up until February of 2025. More specifically, we aim on studying the entire development of non-linear deformation from the early 2023 rest period going into the unrest phase of late 2024 to early 2025, through the use of time-series diagrams. This approach allows for precise quantification of surface displacement patterns, offering valuable insights into the ongoing deformation dynamics of the Santorini caldera.

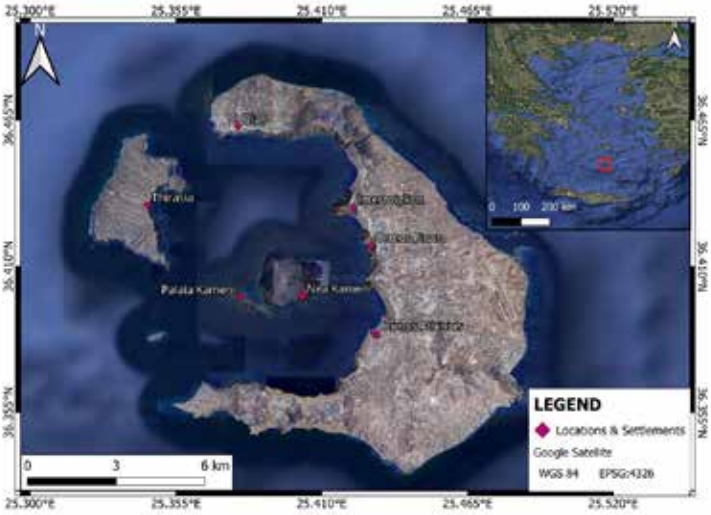

Figure 1. Study area map in QGIS v3.28.1 using the Google Satellite basemap based on Google Earth Pro. Projection: WGS84. (After Athinelis)

Methods

In recent years, MultiTemporal Interferometric Synthetic Aperture Radar (MT-InSAR) has emerged as the most effective method for detecting ground deformations and mapping potential landslides on a regional scale. This is primarily due to its cost efficiency, extensive spatial coverage, and capability to provide high-frequency and high-precision measurements of surface displacement (Zhang,2020). The interferometric processing was performed, using the GAMMA software (GAMMA Remote Sensing AG, Gümligen, Switzerland) and the SBAS technique (Berardino et al., 2002). The SBAS method is an MT-InSAR technique based on the use of multiple SAR images to estimate phase differences in time between image pairs and convert them into a pixel-based deformation time-series (Chen et al., 2024). The basis for the method is that the baseline of the interferometric pairs is smaller than the critical, thus reducing the decorrelation (Ferretti, 2014).

The study area can be characterized as peri-urban. Certain towns exhibit a high density of buildings, whereas some villages contain a comparatively lower number of structures. In the areas that the buildings

are absent, there are some objects that scatter radar signal stronger and more coherent than their surroundings. In this case, the pixel-based SBAS method was selected, which is based on DS, due to its better coverage of natural areas with less dense urban structures (Ferretti, 2014), such as the Santorini Island Complex. Moreover, this method has been found to provide more reliable results when estimated non-linear deformation (Gheorghe & Armaş, 2016; Chen et al., 2021), such as this case where both rest and unrest periods are studied in a singular dataset. The processing can be distinguished into two sub-processing stages: the pre-processing and the main processing.

The methodology for this research utilized 127 Sentinel-1 Interferometric Wide (IW) Single Look Complex (SLC) images from the Copernicus program of the European Space Agency (ESA with an orbital tube less than 100m), which were collected from the Vertex platform of the Alaska Satellite Facility Distributed Active Archive Centers (ASF DAAC).

The generation of parametric files for the 64 SLC images of ascending orbit took place during pre-processing and also the orbital refinement using precise orbits. The stack of ascending SLC images were co-registered using as reference image the scene of 12/03/2024, resulting in a stack of 186 differential interferograms. Similarly, 63 SLC descending orbit images were coregistered with the reference image of 18/03/2024 and 183 differential interferometric pairs were formed. The Shuttle Radar Topography Mission (SRTM) 1-arcsec (i.e., 30 m/pixel) Digital Elevation Model (DEM) (Farr, 2007) was used for the elimination of the topographical contribution from the interferograms. A minimum coherence threshold of 0.8 was used in this phase.

The first step in the primary SBAS processing involved the generation of a multi-reference stack, incorporating both single-look and multi-look differential interferometric phases. The differential interferograms were constructed by comparing each scene to the three consecutive scenes. The reference point was chosen near the airport area, which is regarded as the most stable on the island. After estimating height corrections and atmospheric phase delays, they were subtracted from the interferometric phase and a deformation model was produced. By repeating the final step several times, this model was improved. Ultimately, the ground deformation phases were masked based on a maximum standard deviation threshold of 1.2 for ascending and 1.3 for descending orbit and were then converted into LOS deformation time-series.

The Line-of-Sight (LOS) deformation velocity (D) of Santorini was estimated using the SBAS method. This velocity is then decomposed into vertical (dz) and horizontal (de) components by incorporating the incidence angle (θ), expressed in radians, from both ascending (a) and descending (d) acquisition geometries, following the approach of Manzo et al. (2006) and Dalla Via et al. (2012):

$$dz = \frac{Dd * sin(\theta a) + Da * sin(\theta d)}{sin(\theta d + \theta d)} \quad (1)$$

$$de = \frac{Dd * cos(\theta a) - Da * cos(\theta d)}{sin(\theta d + \theta d)} \quad (2)$$

The negative de values signify a westward displacement, while the positives are attributed to an eastward displacement. Similarly, negative dz values suggest subsidence, while positive are indicative of an uplifting trend. The corresponding results were visualized in a QGIS environment.

Results

The results of the SBAS method showed a smooth deformation pattern throughout the area, especially in the Thirasia and Oia. Particularly, the vertical (up-down) deformation component (fig. 2) suggested that Thirasia is relatively stable in this direction, with the deformation rate in the eastern part being around ~ +6 mm/yr and increasing up to ~ +9 mm/yr towards the northeastern area. Similarly, a vertical deformation rate of about +3 to +5 mm/yr was observed in the Oia region in northwestern Thira island. The most significant vertical deformation velocity was estimated in the Nea Kameni and Palaia Kameni islands, with the latter showing deformation rates in the range of ~ +6 to +8 mm/yr. Most importantly, however, Nea Kameni was represented by velocities > +10.00 mm/yr with an increasing pattern towards the northern and northwestern parts, reaching up to ~ +17.6 mm/yr. Similar deformation rates were noticed in Imerovigli with velocities exceeding +10 mm/yr up to ~ +17 mm/yr.

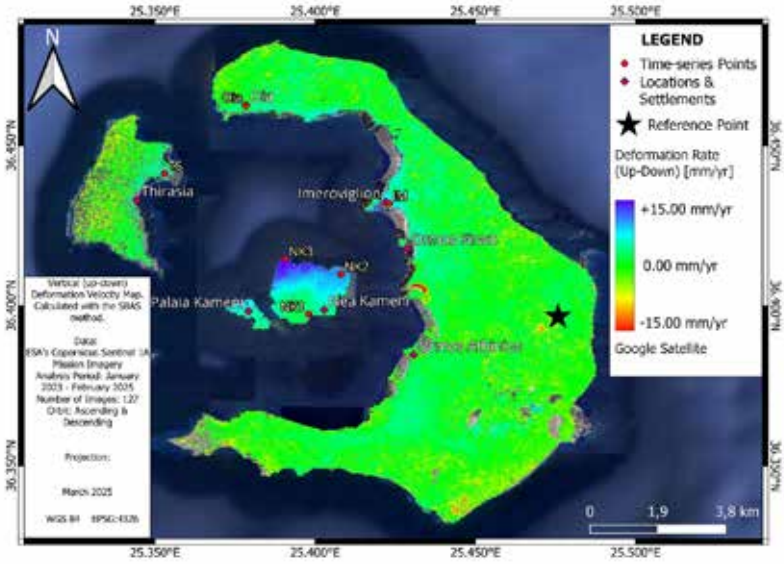

Figure 2. Vertical deformation map of Santorini using the SBAS method. Time period: January 2023 – February 2025. The layers were overlayed on a Google Satellite basemap in QGIS v3.28.1.

Analyzing the horizontal (East - West) deformation rate component (fig. 3), southern Thirasia and the northwestern edge of Thira, west of Oia, suggests a westward movement mostly between -12 to -15 mm/yr while reaching up to ~ -20 mm/yr. The remaining Thira island is dominated by a general eastward deformation, peaking in Imerovigli with velocities near ~ +7 mm/yr and even exceeding +15, up to a maximum of ~ +21 mm/yr. Palaia Kameni represents the highest horizontal deformation rate, showing significant westward displacement, mostly between -15 to -18 mm/yr, with the northern part reaching up to ~ -39. mm/yr. Juxtaposed to this, Nea Kameni seems to be rather stable in the horizontal direction with a slight westward movement of ~ -2 mm/yr.

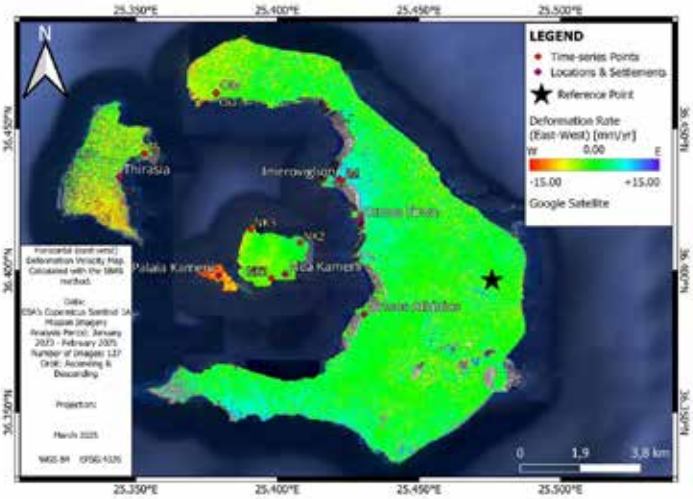

Figure 3. Vertical deformation map of Santorini using the SBAS method. Time period: January 2023 – February 2025. The layers were overlayed on a Google Satellite basemap in QGIS v3.28.1.

It is important to mention that, due to both rest and unrest phases being included in this analysis, the deformation rates calculated may be rather underestimated, as the deformation of both periods is averaged. As such, in order to better comprehend the progression of the deformation in the caldera, it is required that the deformation trend is thoroughly observed through the multitemporal time-series diagrams. The

time-series diagrams show that the multitemporal vertical deformation in Imerovigli (fig. 4-c), Nea Kameni (fig.4-a) and Thirasia (fig. 4-g) has increased significantly since June 2024,continuing climbing up until the end of the study period. More specifically, all three points in Nea Kameni (NK1, NK2 & NK3) suggest a pronounced increase in vertical deformation since June 2024, with NK3 representing a higher deformation rate in northwestern Nea Kameni compared to the eastern (NK2) and southern (NK1) parts. By the end of the study period, uplift values at NK1, NK2, and NK3 reached approximately +10mm, +25mm and 48mm, respectively, relative to the stable reference position. Thirasia presents a more anomalous increase in vertical deformation after June 2024, reaching ~ +12 mm in February 2025. Similarly, Imerovigli, located in western Thira, experienced progressive deformation beginning slightly earlier, near the end of April 2024, with a marked acceleration from June 2024 onward. This deformation reached up to ~ +16 mm by the end of the studyperiod. In contrast, the vertical deformation trend in Oia is less clear (fig. 4-e). Specifically, the time-series diagram of the vertical deformation shows an uplifting trend beginning in December of 2023, declining in June 2024 but increasing again from October 2024 onward. January 2025 presented the highest uplift in Oia at +8mm, dropping to ~ +5.5 mm by February 2025. Regarding horizontal deformation, Nea Kameni (fig. 4-b) shows a clear eastward movement beginning in June 2024 onwards in the northwestern island (NK2) up to ~ +17 mm. A similar but more significant eastward trend is observed in Imerovigli (fig. 4-d), culminating in a deformation of +40 mm east. Oia (fig. 4-f) and Thirasia (fig, 4-h) show westward deformation beginning in October 2024 which appears to reverse after January 2025, stabilizing around-6 mm in both cases.

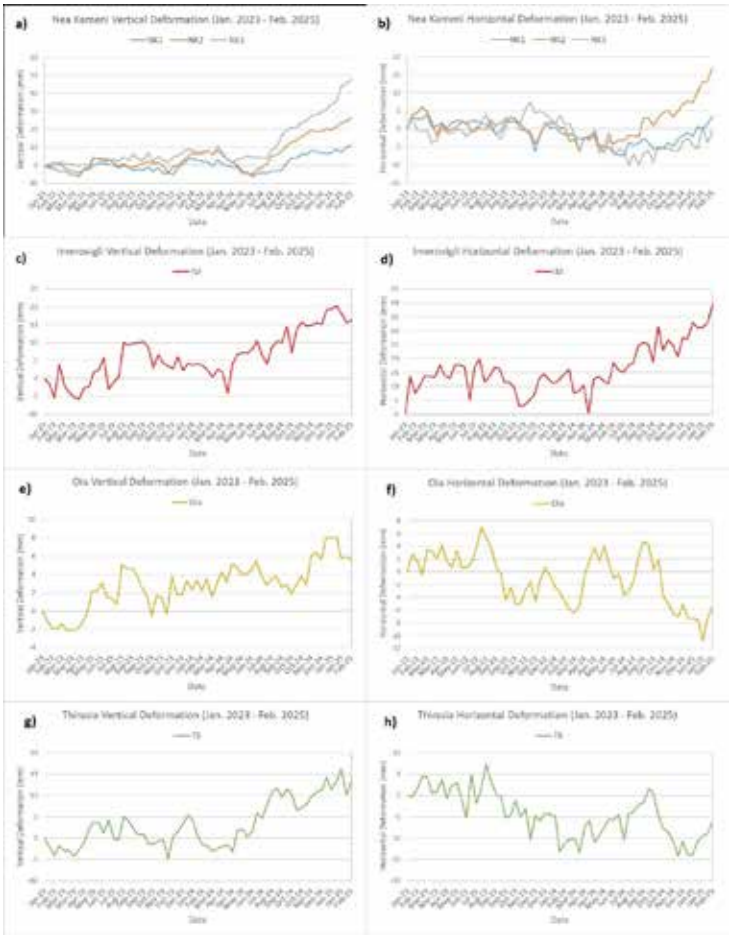

Figure 4. Time-series diagrams showing the vertical (a, c, e, g) and horizontal (b, d, f, h) deformation of Nea Kameni, Imerovigli, Oia & Thirasia respectively.

Conclusions

This research concerned the study of the deformation rate in the caldera of the Santorini volcanic island complex through the MT-InSAR technique SBAS. Using multiple satellite images throughout the studied time period (January 2023 to February 2025) several observations were made concerning the vertical and horizontal deformation velocity. Specifically, the deformation velocity was most significant in the zones closest to the interior of Santorini's Caldera, where Nea Kameni is situated. The area of mainly deformation accumulation lies northwest of Nea Kameni, directly above the submerged caldera and the magmatic reservoir beneath it. The uplifting pattern in that region could suggest swelling within the caldera due to magma accumulation in the magmatic chamber. The notable positive vertical deformation values in northwestern Thira may be the result of increased magmatic processes in the caldera due to the significant and frequent seismicity in the Anydros islet in recent months. This can also be explained by the vertical deformation time-series diagrams, showing a continuous significant increase in deformation velocity past June 2024, suggesting that the notable deformation is related to the beginning of the earthquake swarm event in Anydros. Moreover, the horizontal deformation rate component of the depicted a westward movement trend for both Thirasia, Palaia Kameni and Oia (northwestern Thira), while the remaining Thira area moves eastward, with Nea Kameni being mostly stable with a slight westward trend. These contrasting deformation vectors support the hypothesis of caldera inflation, as the islands of the volcanic complex appear to be moving away from the central caldera, suggesting radial expansion associated with magma intrusion.

Acknowledgements

We acknowledge the contribution of Andreas Karavias (National Technical University of Athens) for his consultation and support during the processing phase of the study. We would also like to acknowledge Dr. Urs Wegmüller, President of Executive Board, director, and Senior project scientist in GAMMA Remote Sensing AG for his ownership of the GAMMA software and his advice during processing. Acknowledgements should be given ESA their ownership of the Sentinel-1 satellite data of the Copernicus program which are provided through open and free sources. Last but not least, we acknowledge the University of Alaska Fairbanks, owners of the ASF DAAC Vertex platform through which the research data were acquired.

References

Alaska Satellite Facility. ASF SAR DAAC Vertex Data Search. Available at: https://search.asf.alaska.edu/ [Accessed 12 Feb. 2025]

Berardino, P., Fornaro, G., Lanari, R., & Sansosti, E., 2002. A new algorithm for surface deformation monitoring based on small baseline differential SAR interferograms. IEEE Transactions on Geoscience and Remote Sensing, 40(11), 2375–2383. https://doi.org/10.1109/TGRS.2002.803792

Castro-Melgar, I., Gatsios, T., Prudencio, J., Ibanez, J. M., Lekkas, E., Parcharidis, I., 2025. Volcano Monitoring: Using SAR Interferometry for the Pre-Unrest of La Palma and the Post-Unrest of Santorini. Remote Sensing for Geophysicists, CRC Press, 440-459. https://doi.org/10.1201/9781003485278.

Chen, X., Tessari, G., Fabris, M., Achilli, V., & Floris, M., 2021. Comparison between PS and SBAS InSAR techniques in monitoring shallow landslides. Understanding and Reducing Landslide Disaster Risk: Volume 3 Monitoring and Early Warning 5th, 155-161. http://dx.doi.org/10.1007/978-3-030-60311-3_17

Chen, Y., Ding, C., Huang, P., Yin, B., Tan, W., Qi, Y., Xu, W. & Du, S., 2024. Research on time series monitoring of surface deformation in Tongliao urban area based on SBAS-PS-DS-InSAR. Sensors, 24(4), 1169. https://doi.org/10.3390/s24041169

Dalla Via, G., Crosetto, M., Crippa, B., 2012. Resolving vertical and east-west horizontal motion from differential interferometric synthetic aperture radar: The L'Aquila earthquake. J. Geophys. Res. Solid Earth 117(B02310). https://doi.org/10.1029/2011JB008689

Farr, T. G., Rosen, P. A., Caro, E., Crippen, R., Duren, R., Hensley, S., Kobrick, M., Paller, M., Rodriguez, E., Roth, L., Seal, D., Shaffer, S., Shimada, J., Umland, J., Werner, M., Oskin, M., Burbank, D. & Alsdorf, D., 2007. The shuttle radar topography mission. Reviews of geophysics, 45(2). https://doi.org/10.1029/2005RG000183

Ferretti, A., 2014. Satellite InSAR data: reservoir monitoring from space. EAGE publications. ISBN: 978-90-73834-

71-2. http://dx.doi.org/10.3997/9789073834712

Foumelis, M., Trasatti, E., Papageorgiou, E., Stramondo, S., Parcharidis, I., 2013. Monitoring Santorini volcano (Greece) breathing from space. Geophysical Journal International 193, 161-170. https://doi.org/10.1093/gji/ggs135.

GAMMA Remote Sensing AG. GAMMA Remote Sensing AG. Available at: https://www.gamma-rs.ch/ [Accessed 12 Feb. 2025]

Gheorghe, M., & Armaş, I., 2016. Comparison of multi-temporal differential interferometry techniques applied to the measurement of Bucharest City Subsidence. Procedia Environmental Sciences, 32, 221-229. http://dx.doi.org/10.1016/j.proenv.2016.03.027

Krassakis, P., 2024. Geospatial intelligence for multi-hazard assessment in coastal areas of the Hellenic volcanic arc. Ph.D. Thesis, Harokopio University, Athens, Greece, 283 p. https://doi.org/10.12681/eadd/56709

Manzo, M., Ricciardi, G.P., Casu, F., Ventura, G., Zeni, G., Borgström, S., Berardino, P., Del Gaudio, C., Lanari, R., 2006. Surface deformation analysis in the Ischia Island (Italy) based on spaceborne radar interferometry. J. Volcanol. Geotherm. Res. 151(4), 399–416. https://doi.org/10.1016/j.jvolgeores.2005.09.010

QGIS Development Team, QGIS. Available at: https://qgis.org/ [Accessed 12 Feb. 2025]

Vougioukalakis, G., Sparks, R. S., Druitt, T., Pyle, D., Papazachos, C., & Fytikas, M., 2016. Volcanic Hazard Assessment at Santorini Volcano: A review and a synthesis in the light of the 2011-2012 Santorini unrest. Bulletin of the Geological Society of Greece, 50(1), 274-283. https://doi.org/10.12681/bgsg.11728

Vougioukalakis, G. E., Satow, C. G., & Druitt, T. H., 2019. Volcanism of the South Aegean volcanic arc. Elements: An International Magazine of Mineralogy, Geochemistry, and Petrology, 15(3), 159-164. https://doi.org/10.2138/gselements.15.3.159

Zhang, Y., Meng, X., Dijkstra, T.A., Jordan, C.J., Chen, G., Zeng, R., & Novellino, A., 2020. Forecasting the magnitude of potential landslides based on InSAR techniques. Remote Sensing of Environment, 241, 111738. ISSN 0034-4257 https://doi.org/10.1016/j.rse.2020.111738

17th INTERNATIONAL CONGRESS of the Geological Society of Greece

BULLETIN OF THE GEOLOGICAL SOCIETY OF GREECE, SP. PUBL.

EXTENDED ABSTRACT 020

Impacts of Climate Change on Medicane Formation: Analyzing SST Changes in the Eastern Mediterranean (1940–2023) using Thematic Maps

Avgerinos E[1]., Kostopoulou E[1]., Tegoulias I[2]., Giannakopoulos C[3].
(1) Department of Geography, University of Aegean, Greece, stratos.avgs@gmail.com (2) Department of Geology, Aristotle University of Thessaloniki, Greece (3) Institute for environmental Research and Sustainable Development, National Observatory of Athens, Greece

Introduction

Rising sea levels, increasing frequency of extreme weather events, and transformations in marine ecosystems present significant challenges for the Eastern Mediterranean region. These changes directly affect maritime routes, port infrastructure, and the broader environment. In this context, understanding the relationship between sea surface temperature (SST) fluctuations and their effects on the environment has become a matter of increasing importance. This paper focuses on an in-depth analysis of SST trends in the Eastern Mediterranean from 1940 to 2023, examining both annual and monthly scales. By analyzing these temperature trends, the study aims to assess their potential environmental impacts, considering both operational and ecological perspectives.

In addition to SST trends, this study includes a detailed examination of extreme weather events, specifically Mediterranean cyclones, also known as Medicanes. A case study of the Mediterranean Cyclone Zorba, which significantly impacted the Eastern Mediterranean in late September and early October 2018, is included. Furthermore, the study references the average monthly SST values for September and October of 2018. Through this integrated approach, the research aims to provide valuable insights into the challenges and risks faced by the region and to offer guidance for future strategies to address these emerging environmental shifts.

Data and Methodology

This study utilized ERA5 Reanalysis data on Sea Surface Temperature (SST) to analyze the Eastern Mediterranean region, from January 1940 to December 2023. The data were examined at multiple temporal resolutions, including annual, monthly, and daily intervals, to capture both long-term trends and short-term variability in SST. The ERA5 dataset, which provides high-resolution, accurate climate data, is publicly available to the scientific community through the Copernicus Climate Change Service, in collaboration with the European Centre for Medium-Range Weather Forecasts (ECMWF). This dataset offers an invaluable resource for researchers and decision-makers involved in climate studies and environmental assessments.

To facilitate the interpretation of SST patterns over time, a series of thematic maps were generated, illustrating spatial and temporal variations of SST across different periods. These maps highlight significant trends, anomalies, and fluctuations in SST within the study area. The maps were created using Python programming, employing data visualization libraries such as Matplotlib and Plotly, in combination with ArcGIS software for spatial analysis and cartographic rendering. This methodological approach allowed for a detailed and comprehensive representation of the SST data, offering insights into both regional and temporal dynamics.

The integration of Python code and ArcGIS software enabled the efficient processing, analysis, and visualization of large datasets, ensuring that the results are both scientifically rigorous and easily interpretable. These visualizations not only serve to illustrate the trends in SST over the decades but also provide a tool for identifying areas of concern, such as regions experiencing rapid warming or significant deviations from historical patterns. The availability of this data to the broader scientific community, alongside the advanced mapping techniques employed in this work, provides a valuable contribution to the ongoing research on climate change and its effects on the Mediterranean region.

Results

The analysis of Sea Surface Temperature (SST) trends in the Eastern Mediterranean region from 1940 to 2023 reveals significant spatiotemporal variations, which are essential for understanding regional climate dynamics and their potential impacts on marine ecosystems and maritime activities.

The average annual SST for the Eastern Mediterranean during the study period is presented in Figure 1, with the red

trend line indicating a clear upward trend from 1940 to 2023. Over this period, SST has increased by approximately 1.5°C, despite notable interannual variability—particularly between 1940 and 2000. Relatively low temperatures are evident between 1975 and 1992, while higher values observed from 2005 to 2023. Post-2000, SSTs rise more consistently and sharply. It is important to note that the rate of increase in sea surface temperature (SST) is directly correlated with the rate of increase in air temperature. However, due to the distinct heat capacity of the ocean as a fluid, compared to atmospheric air, these rates are not equal. Additionally, the acceleration of the warming trend in recent decades is noteworthy, with SST consistently exceeding 20°C from 2010 onwards.

Although fluctuations with unusually cold or warm years are expected, the overall pattern reveals a steady long-term increase.

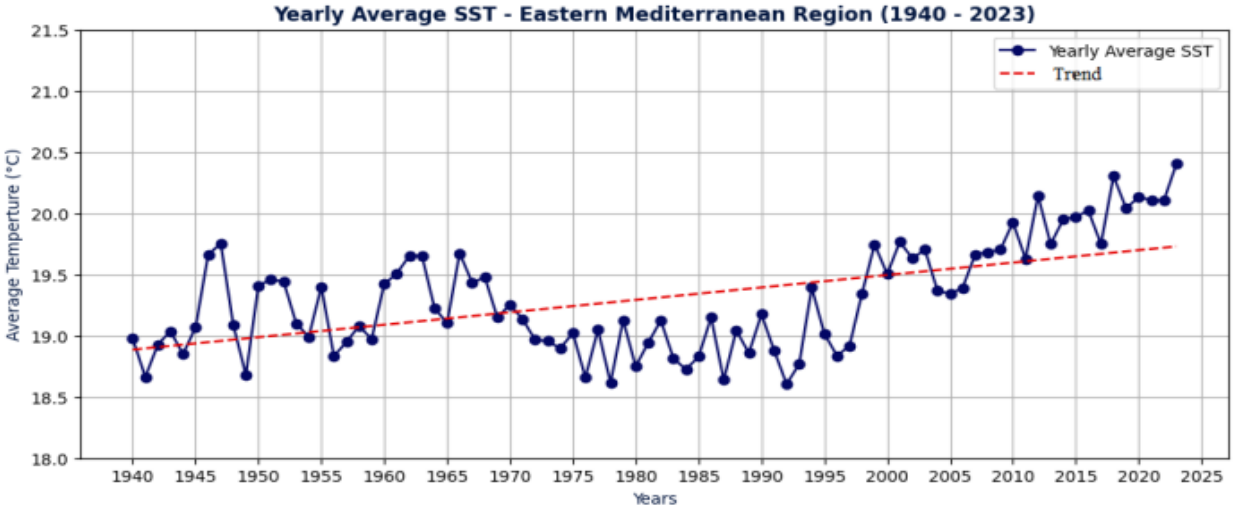

Figure 1. Annual Average Sea Surface Temperature from 1940 to 2023 for the Eastern Mediterranean region, with trend line

The spatial distribution of the average annual SST across the Eastern Mediterranean basin for the period 1940 to 2023 is shown in Figure 2. The spatial analysis of SST reveals several key areas of variability. The warmest waters are in the Gulf of Sirte, south of Crete, around Cyprus, and along the northern coasts of Africa, particularly in the southern and southeastern parts of the basin. In these areas, the average annual SST consistently exceeds 21°C. Previous studies (e.g., Ozer et al., 2022) suggest that the Eastern Mediterranean, due to its relatively small size and limited connection to the Atlantic Ocean, reflects and intensifies global warming trends. Notably, the southeastern part of the basin, bordering Israel, shows the highest temperatures, as water from the Atlantic Ocean has ample time to warm as it moves toward the region.

In contrast, the central and southern Aegean Sea, the Ionian Sea, and the southwestern parts of the Eastern Mediterranean exhibit average annual SSTs ranging from 19°C to 20°C. These regions show a more gradual but consistent warming trend compared to the period prior to 1940 (Bruno, M., 2019 & Lough, J. M., & Coughlan, L. M., 2015).

The coldest SSTs in the Eastern Mediterranean are found in the Adriatic Sea, with average temperatures ranging from 16°C to 18°C, particularly in the northern sections. This area experiences a significant influx of cold, fresh water from rivers in the Italian Alps. Similarly, the northern Aegean Sea is affected by the inflow of water masses from the Black Sea through the Bosporus Strait and the Dardanelles. This water, known as the Black Sea Water (BSW) current, has a lower temperature and salinity, further reducing the average SST in this region (Poulos et al., 1997; Zodiatis, 1996). Moreover, the northern Aegean Sea also receives freshwater contributions from the Evros, Strymon, and Nesto's rivers, as well as from rivers in the Turkish mainland, which further influence the temperature and salinity of the surface waters (Therianos, 1974).

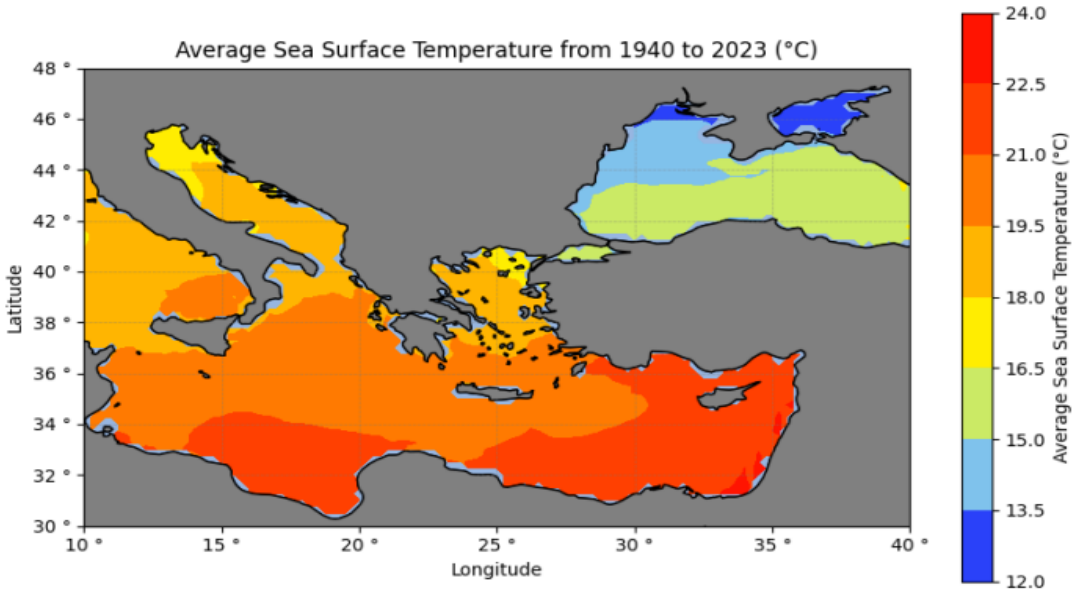

Figure 2. Spatial distribution of the annual average SST in the Eastern Mediterranean from 1940 to 2023

Figure 3 illustrates the average sea surface temperature (SST) in the Eastern Mediterranean for September during the period from 2000 to 2023. The SST range for this period varies from 19°C to 23°C, with the coldest waters located in the Adriatic Sea and the northern Aegean, while the warmest waters are found along the northern African coasts and around Cyprus. This represents a warm period compared to other times, as previously mentioned, with the average SST exceeding 20°C in many locations. The climatic average SST in the Eastern Mediterranean depends on the season, geographical location, and local climatic conditions.

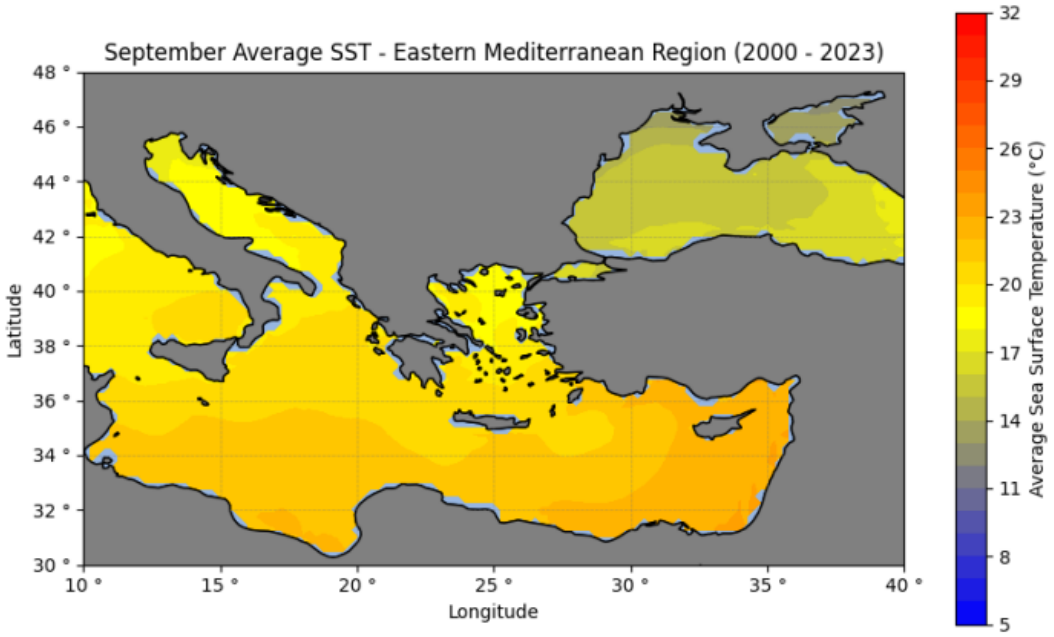

Figure 3. Average SST for September – Period 2000–2023, Eastern Mediterranean

The Mediterranean Cyclone “Zorbas,” which occurred in September 2018, is a significant event that serves as an illustrative case study of the relationship between sea surface temperature (SST) and cyclone formation in the Eastern Mediterranean.

September 2018 was characterized by notably high temperatures, both in terms of air temperature and SST. As depicted in Figure 4, the average SST for several locations across the Eastern Mediterranean basin exceeded 25°C, with temperatures reaching up to 29°C near the Gulf of Sirte and to the east of Cyprus. These elevated sea surface temperatures provided a conducive environment for the development and intensification of a Mediterranean cyclone.

The warm SSTs in the Gulf of Sirte played a crucial role in the cyclogenesis that occurred south of Italy. The energy from the warm waters contributed to the further strengthening of a low-pressure system, transforming it into a Mediterranean Cyclone with tropical characteristics (Tsikoudi, I., et al. 2019). The dynamics of this cyclone underscore the significant influence of SST on the formation and development of such systems in the Mediterranean region.

As the cyclone moved northward toward the Aegean Sea, and with October already underway, the system began to weaken. The decreasing SSTs in the northern regions of the basin no longer provided sufficient energy to sustain the cyclone. Consequently, the system lost strength, and its intensity diminished (Ziv, B., et al., 2018 & Papageorgiou, A., et al., 2020). To illustrate this, Figure 5 presents the average SST for October 2018, highlighting the contrast in sea surface temperatures compared to those in September 2018, as depicted in the preceding figure.

This case study reinforces the critical role that SST plays in the development, intensification, and eventual weakening of Mediterranean cyclones. The warm waters in the southern parts of the Eastern Mediterranean can significantly enhance cyclonic activity, while lower SSTs in the northern regions lead to the dissipation of these systems. Understanding these SST dynamics is essential for improving forecasting and risk assessment of Mediterranean cyclones, which have considerable implications for coastal areas and maritime operations in the region.

The Mediterranean Cyclone Zorbas (Medicane Zorbas) also struck Greece. Specifically, on September 29, 2018, it reached the Peloponnese with maximum winds of 120 km/h and a central pressure of 987 hPa, classifying it as a Category 1 Cyclone. It then moved through the Aegean Sea before weakening in Turkey on October 2. In its path, it caused extensive damage, particularly in the Peloponnese and central Greece. Heavy rainfall, flooding, and strong winds (up to 10-12 Beaufort) affected areas such as Argos, Corinth, and Attica. Rivers overflowed, roads were blocked, and many homes were flooded. In several areas, such as the Municipality of Argos - Mycenae, a state of emergency was declared due to the widespread damage. Zorbas highlighted the increasing risks from such extreme weather events in the Mediterranean, confirming concerns about the impacts of climate change in the region.

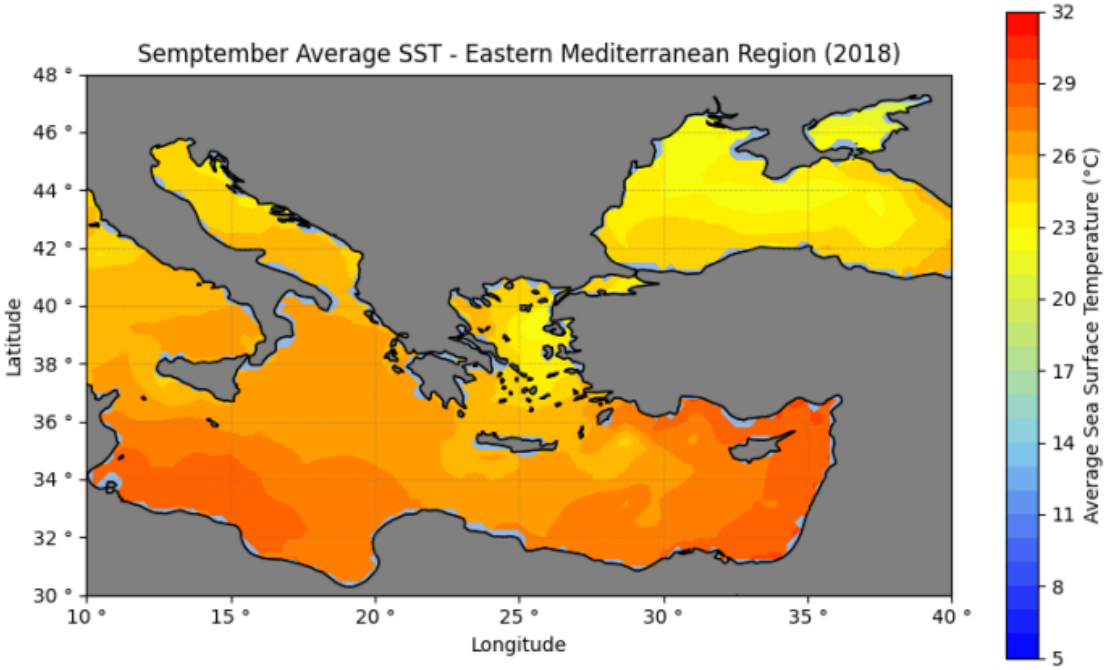

Figure 4. Average SST for September 2018, Eastern Mediterranean

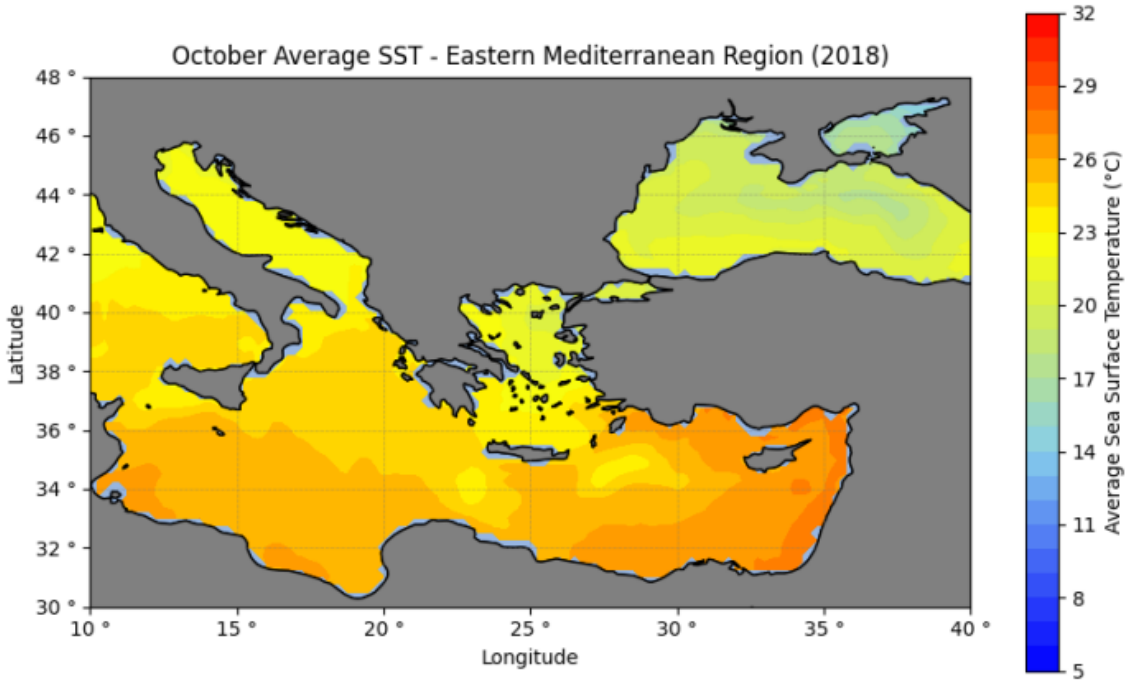

Figure 5. Average SST for October 2018, Eastern Mediterranean

Discussion and Conclusion

The results of this analysis demonstrate a clear warming trend in the Eastern Mediterranean, particularly over the past few decades, with significant regional variability. The southern and southeastern parts of the basin are experiencing the highest SSTs, while the northern Aegean and Adriatic Sea remain cooler due to the influence of freshwater inflows and the BSW current. These findings underscore the importance of continued monitoring of SST in the region.

This study has examined the rising Sea Surface Temperature (SST) in the Eastern Mediterranean from 1940 to 2023, highlighting the significant trends, contributing factors, and implications for the region's environment and maritime industry. The Eastern Mediterranean was selected for this research due to its unique characteristics, such as its semi-closed nature, which results in an accelerated increase in sea temperatures compared to other global seas, as well as its crucial role in linking three continents directly influenced by the weather phenomena that originate here.

Over the past eighty-three years, the SST in the Eastern Mediterranean has consistently risen, with a noticeable acceleration of this warming since the 2010s. The region has experienced an increase of approximately +0.4°C to +0.6°C per decade since the 1980s. During the summer months, SSTs often exceed 26°C, with September being the warmest month. This warming trend, driven by factors such as rising greenhouse gas emissions, alterations in atmospheric circulation, and the reduction of polar ice, has led to a marked increase in the frequency and severity of Mediterranean cyclones (Giorgi, F., et al., 2019 & Gaertner, M. A., et al., 2017). These cyclones, which combine characteristics of both tropical and extratropical systems, have become more prevalent, with notable events including Cyclones "Zorbas" (2018).

The increased SST and the intensification of extreme weather events, such as Medicanes, have profound implications for maritime operations. The impact of Cyclone "Zorbas" on the ports of Peloponnese serves as a clear example of how such events can severely affect the maritime sector.

Considering these findings, it is evident that the rising SST and the increasing frequency of extreme weather events pose substantial challenges to the coastal communities in the Eastern Mediterranean. Therefore, it is crucial to implement strategies to adapt to these changing conditions. Advanced weather forecasting

systems should be developed to improve preparedness, while the resilience of port infrastructure must be strengthened to withstand the impact of these extreme events. Additionally, international cooperation is essential to address the underlying drivers of climate change, such as CO_2 emissions, and to mitigate further environmental impacts.

This research underscores the urgent need for further studies to monitor the ongoing changes in SST and to better understand their long-term effects on marine ecosystems, biodiversity, and global trade routes. Ultimately, proactive measures and informed decision-making will be critical to managing the evolving challenges posed by climate change in the Eastern Mediterranean and beyond.

Acknowledgements

We would like to express our sincere gratitude to the European Centre for Medium-Range Weather Forecasts (ECMWF) and the Copernicus program for providing the essential data used in this study. Their invaluable resources and support have significantly contributed to the success of our research. Without the access to ECMWF's advanced weather and climate data and the Copernicus Earth Observation program's rich datasets, this work would not have been possible. We also appreciate the efforts of all teams involved in data collection, maintenance, and dissemination.

References

Balling Jr, R. C., Vose, R. S., and Weber, G. 1998. "Analysis of Long-Term European Temperature Records: 1751–1995." Climate Research 10: 193–200.

Bruno, M. (2019). *Long-term Sea Surface Temperature Variability in the Mediterranean Sea*. Climate Dynamics, 52(11-12), 7239-7250. https://doi.org/10.1007/s00382-018-4586-9

Carlson, T. N. 1980. "Airflow through Mid-Latitude Cyclones and the Comma Cloud Pattern." Monthly Weather Review 108: 1498–1509.

Cavicchia, L., von Storch, H., & Gualdi, S. (2014). Mediterranean Tropical-Like Cyclones (Medicanes). Atmosphere, 10(4), 206.

Climate Copernicus. 2023. "Climate Indicators – Sea Surface Temperature." April 20. https://climate.copernicus.eu/climate-indicators/sea-surface-temperature.

Copernicus Marine Service. "Ocean Warming." Copernicus Marine Service, https://marine.copernicus.eu/el/explainers/phenomena-threats/ocean-warming.

Copernicus Climate Change Service. "ERA5: Reanalysis Data on Single Levels." Copernicus Climate Data Store (CDS), https://cds.climate.copernicus.eu/datasets/reanalysis-era5-single-levels

Donlon, C. J., Martin, M., Stark, J. D., Roberts-Jones, J., Fiedler, E., and Wimmer, W. 2011. "The Operational Sea Surface Temperature and Sea Ice Analysis (OSTIA)." Remote Sensing of the Environment. https://doi.org/10.1016/j.rse.2010.10.017.

Gaertner, M. A., et al. (2017). "Sea surface temperature and cyclogenesis in the Mediterranean: A comprehensive review." *Atmospheric Research*, 191, 68-83.

Giorgi, F., et al. (2019). "Climate change and Mediterranean cyclones: A new trend." *Environmental Research Letters*, 14(7), 074002.

Leone Cavicchia, Hans von Storch, & Silvio Gualdi (2014). Mediterranean Tropical-Like Cyclones in Present and Future Climate. Journal of Climate. DOI: 10.1175/JCLI-D-14-00339.1

Lionello, P., et al. 2006. "Cyclones in the Mediterranean Region: Climatology and Effects on the Environment."

Noyelle, R., Ulbrich, U., Becker, N., & Meredith, E. P. (2019). Assessing the impact of sea surface temperatures on a simulated Medicane using ensemble simulations. Natural Hazards and Earth System Sciences, 19, 941–955. DOI: 10.5194/nhess-19-941-2019

Lough, J. M., & Coughlan, L. M. (2015). *Warming of the Mediterranean Sea and its Impacts on Marine Ecosystems*. Environmental Research Letters, 10(11), 114003. https://doi.org/10.1088/1748-9326/10/11/114003

Papageorgiou, A., et al. (2020). "The role of sea surface temperature in the intensification of Mediterranean cyclones." *Atmospheric Science Letters*, 21(2), e952.

Tsikoudi, I., et al. 2019, University of Athens. "Dynamic Analysis of a Medicane." https://www.openarchives.gr/aggregator-openarchives/edm/pergamos/000005-_uoa_dl_object_uoadl%3A2878611

Ziv, B., et al. (2018). "The weakening of Mediterranean tropical-like cyclones: A case study of Cyclone Zorba (2018)." *Geophysical Research Letters*, 45(6), 2997-3005.

17th INTERNATIONAL CONGRESS of the Geological Society of Greece

BULLETIN OF THE GEOLOGICAL SOCIETY OF GREECE, SP. PUBL.

EXTENDED ABSTRACT 021

Seasonal Water Column Stratification and Heavy Metal Distribution in the Pinios Dam Reservoir: A Comprehensive Environmental Monitoring Study

Avramidis P.,[1] Ramfos A.[2], Sarris I.[1], Cristodoulopoulos, D.[1], Alexandridis M.[1], Michalopoulou M.[1], Depountis N.[1] Papazisimou S.[3]
(1) Department of Geology, University of Patras, Patra, Greece,
(2) Department of Biology University of Patras, Greece
3) Region of Western Greece, Patras, Greece

Research Highlights: **water stratification and anoxic condition as important environmental parameters for the dam's life cycle**

Introduction

Reservoirs are artificial lakes that play a critical role in water resource management worldwide, providing essential services such as water supply for drinking and irrigation, flood control, and hydroelectric power generation (Directive EU 2020/2184). However, reservoirs, like natural lakes, are susceptible to environmental and anthropogenic influences that can alter their ecological balance. The stratification of water bodies is a key physical process that affects the distribution of temperature, dissolved oxygen, and other physicochemical properties, which in turn impacts water quality and aquatic life. Thermal stratification, particularly in monomictic and dimictic lakes, causes the development of distinct layers in the water column that can become isolated from atmospheric oxygen, leading to hypoxic or anoxic conditions in the deeper layers. These conditions, often exacerbated by nutrient inputs and organic matter decomposition, can significantly affect water chemistry, particularly the solubilization and mobility of heavy metals from sediments. This creates potential environmental hazards, particularly in drinking water reservoirs where water quality is a priority.

The study area is Pinios Dam which is located at northwest Peloponnese which has already recorded as reservoir with high concentrations of Mn and Fe (Michalopoulou et al, 2024). For this study, a detailed bathymetric survey was conducted, four monitoring stations were installed, and seasonal water column profiles were recorded. Additionally, physicochemical parameters, including pH, temperature, conductivity, redox potential, and heavy metal concentrations of Mn and Fe, were measured and analyzed".

Methods

Water samples were collected from the artificial reservoir of the Pinios Dam at four pre-determined stations (SPA1–SPA4), strategically selected to provide comprehensive coverage of the study area. These stations were located along the reservoir's main axis, with depths ranging from 9 m to 35 m. Sampling occurred seasonally, between February 2023 and October 2023, and utilized a multi-depth water sampler equipped with valves suitable for depths up to 100 m. Samples were collected at 4 m intervals from the surface to the bottom, yielding a total of 74 samples.

Physical and chemical parameters, including pH, temperature, dissolved oxygen, and conductivity, were measured using a portable multi-parameter probe (IN-SITU AQUA TROLL 6000). Measurements were taken along the vertical profile of the water column at 10 cm intervals.

Collected samples were analyzed for various chemical parameters, such as chloride (Cl^-), nitrate (NO_3^-), nitrite (NO_2^-), ammonium (NH_4^+), phosphate (PO_4^{3-}), sulfate (SO_4^{2-}), total organic carbon (TOC), total nitrogen (TN), manganese (Mn), and iron (Fe). Analyses were conducted using an ion chromatograph (Dionex ICS-1100) and a spectrophotometer (HACH-LANGE), with quality assurance adhering to ISO 17025 standards.

Results

Seasonal Variations

The study identified notable seasonal variations in the reservoir's physical and chemical parameters.

Temperature stratification was evident during the summer, with surface temperatures peaking at 25°C and bottom temperatures remaining around 15°C. Dissolved oxygen levels decreased with depth, particularly during summer and autumn, indicating thermal stratification and oxygen depletion at deeper layers.

Chemical Composition

Chloride concentrations ranged between 10.12 mg/L and 20.96 mg/L, showing minimal seasonal fluctuation. Nutrient concentrations, particularly nitrates (0.11–1.43 mg/L) and ammonium (0.02–0.36 mg/L), varied with depth and season, reflecting biological activity and nutrient cycling within the reservoir. Phosphate levels were generally below detection limits, except for occasional peaks (up to 0.06 mg/L).

Heavy Metals

Manganese and iron concentrations exhibited significant depth-dependent trends. Mn concentrations ranged from 0.01 mg/L to 0.198 mg/L, while Fe varied from 0.01 mg/L to 0.204 mg/L. Both metals showed elevated concentrations in bottom layers during late summer and autumn, coinciding with reduced oxygen levels.

Conclusions

Thermal stratification played a significant role in shaping the reservoir's chemical profile. The development of distinct temperature layers during summer inhibited vertical mixing, leading to oxygen depletion in deeper layers. This, in turn, facilitated the release of Mn and Fe from sediments into the water column, as indicated by their elevated concentrations at depth.

The distribution of nitrates and ammonium highlighted the complex interplay between biological uptake, decomposition, and nutrient cycling. Elevated nitrate levels near the surface during spring suggest enhanced productivity, while higher ammonium concentrations at depth during late summer point to decomposition processes under low-oxygen conditions.

The observed seasonal and depth-dependent variations in key parameters underline the reservoir's susceptibility to eutrophication and metal mobilization, particularly during stratified periods. These findings are critical for designing management strategies to mitigate potential water quality issues.

Acknowledgements

The authors are grateful for the financial and administrative support of the research by the Region of Western Greece and the Municipality of Ilida.

References

Directive (EU) 2020/2184 of the European Parliament and of the Council of 16 December 2020 on the quality of water intended for human consumption. Available online: https://eur-lex.europa.eu/eli/dir/2020/2184/oj. (accessed on 11 November 2024).

Michalopoulou, M., Depountis, N., Zagana, E., Avramidis, P., 2024. Investigation of the Origin of Elevated Amounts of Iron and Manganese in a Dam Reservoir. Geosciences, 14, 336.

17th INTERNATIONAL CONGRESS of the Geological Society of Greece

BULLETIN OF THE GEOLOGICAL SOCIETY OF GREECE, SP. PUBL.

EXTENDED ABSTRACT 022

A Preliminary Study of Microvertebrate and Invertebrate Fauna from the Early Pleistocene of Koukos region (Kos Island, Dodecanese, Greece)

Authors : Antonios Isidoros Avrithis [1], Efterpi Koskeridou [2], Evangelia Rentoumi [2], Evangelos Vlachos [3], Davit Vasilyan [4, 5]

(1) The Open University, Milton Keynes, United Kingdom, tonyavrithis@gmail.com, (2) Department of Historical Geology and Palaeontology, Faculty of Geology and Geoenvironment, National and Kapodistrian University of Athens, 15774 Athens, Greece, (3) CONICET and Museo Paleontológico Egidio Feruglio, Av. Fontana 140, 9100 Trelew, Chubut, Argentina, (4) JURASSICA Museum, Route de Fontenais 21, 2900 Porrentruy, Switzerland, (5) University Fribourg, Chemin de Musée 6, 1700 Fribourg, Switzerland

Research Highlights

A new locality with amphibians, reptiles, fishes, gastropods, and ostracods is described from the Early Pleistocene of Koukos region in Kos Island. These findings are valuable for palaeoecosystem reconstruction and biogeographical interpretations and represent a rare assemblage of that age in Greece.

Introduction

The island of Kos in the southeastern Aegean Sea was part of the Anatolian peninsula during the Pleistocene and maintained a connection to the mainland till the Last Glacial Maximum (Rohling *et al.* 2014). During the Early Pleistocene, several extinct mammals inhabited the area such as *Anancus* sp., *Homotherium* sp., *Leptobos* sp. (Desio, 1928). During the Late Pleistocene, fossils show a shift towards shallow marine environments (Drinia *et al.* 2010). The area of Koukos has been studied by Charrier and Giglio (1969) who refer to the locality as 'Iliopeia' where some large mammal fossils have been found. The presence of microvertebrates had never been reported before the discovery of the site of Koukos, in Kardamena village of the island. The newly discovered site contains a rich assemblage of amphibians, reptiles and fishes, also described as ectothermic fauna. The co-occurrence of fossil gastropods and ostracods is valuable for palaeoecological interpretations. Further analysis on the biogeographical affinities of these findings will be valuable for deciphering the origins of modern-day distributions of several extant taxa. Finally, this locality is the only site in Greece from the Early Pleistocene which bears both ichthyological and herpetofaunal remains (Argyriou 2022, Delfino & Georgalis 2022, Vlachos, 2022).

Geological Setting

The site is located in the Koukos area of Kardamena village of Kos Island, in Southeastern Mediterranean (fig.1). According to Willmann (1983), the site belongs to the lowermost Tafi formation, which is dated as Lower Pleistocene. Additionally, Magrograssi (1928) has described a gastropod species *Melanopsis pseudopigmea* from the same outcrop.

The section of Koukos consists of claystones, siltstones and sandstones, with the latter dominating. The first layer (fig.2) consists of fossil-free grey claystone, the second layer (fig. 2) is a 25cm green claystone layer with amphibians, reptiles, fishes, ostracods, and gastropods (Table 1). The third layer is yellowish siltstone. The last (fourth) layer, consisting mostly of fossil free sandstones and conglomerates, overlies the previous beds with an erosive base suggesting high energy river deposition (fig. 2).

Materials and methods

Test samples of 2 kg have been obtained from each layer, which have been treated with a solution with 0.1% perhydrol. They have been washed using a series of four sieves of 1 cm, 500 μm, 250 μm and 125 μm mesh sizes. After the discovery of the fossiliferous layer of green clay, another sample of 20 kg was washed.

For the taxonomy of the gastropods, we used Neumayr (1880), Magrograssi (1928), Willmann (1981), Bouchet *et al.* (2005), as well as numerous other studies focusing on the classification of lacustrine

gastropods from the Pleistocene. The ecoregions concept Barbieri et al. (2015) has been applied for the interpretation of fish forms.

Figure 1. Map of Greece, indicating Koukos locality with a yellow star. Maps modified from Wikimedia Commons (https://upload.wikimedia.org/wikipedia/commons/8/87/MapZ.png, https://upload.wikimedia.org/wikipedia/commons/2/24/Kos_location_map.svg)

Figure 2. A. Stratigraphic log of the section, asterisk indicating the sampled fossiliferous bed. B. Field photo of the section with numbers corresponding to the stratigraphic units, red lines indicate the border between strata

Results

The fauna consists of 22 taxa. The vertebrate taxa are 14, of which 6 belong to ray-finned fish, 4 to amphibians, 3 to reptilians and 1 to mammals. The invertebrates are represented by 5 gastropod species and 3 ostracod species.

Class	Family	**Taxon**
Actinopterygii	Cyprinidae	? *Barbus* sp.
		Leuciscus sp.
		Luciobarbus sp.
		Chondrostoma sp.
	Cobitidae	Cobitidae indet.
	Gobiidae	Gobiidae indet.
Amphibia	Salamandridae	Salamandridae indet. (small-sized)
	Ranidae	*Pelophylax* sp.
	Hylidae	*Hyla* sp.
		Bufonidae / Pelobatidae indet.
Reptilia	Geoemydidae	*Mauremys* sp.
	Colubridae	Colubridae indet.
		Colubrinae indet.
Mammalia	Cricetidae	Cricetidae indet.
Gastropoda	Melanopsidae	*Melanopsis pseudopigmea* Magrograssi, 1928
	Valvatidae	*Valvata hellenica* Tournouer, 1877
	Melanopsidae	*Melanopsis gorceixi polyptycha* Tournouer, 1875
	Neritidae	*Theodoxus doricus doricus* (Neumayr, 1880)
	Hydrobiidae	*Iraklimelania coa* Willmann, 1981
Ostracoda	Candonidae	*Fabaeformiscandona* cf. *brevicornis* (Klie, 1925)
		Candona sp.
	Cyprididae	*Ilyocypris gibba* (Ramdohr, 1808)

Table 1. Fauna of Koukos locality

Discussion-Conclusions

The ectothermic vertebrate fauna suggests the presence of running freshwater water body (rivers) with very (*Leuciscus* sp., *Luciobarbus* sp., *Chondrostoma* sp., Cobitidae indet.) slowly flowing or stagnant parts (Gobiidae indet., *Pelophylax* sp., *Mauremys* sp.). The water body was surrounded by hedgerows and meadows with higher vegetation (Salamandridae indet. (small-sized), *Hyla* sp.).

The herpetofauna of the Koukos site contains forms which are broadly present also in present-day Kos and other nearby islands (Valakos et al., 2008). From the perspective of the fossil fauna, Koukos contributes so far to the scarcely studied record of ectothermic vertebrates. *Mauremys rivulata* found previously in Kos but the exact location was missing (Vlachos, 2022) and another freshwater turtle that was discovered in the broader area belonged to the family Trionychidae (Avrithis and Georgalis, 2024). For the amphibians, only 4 sites of that age are found in Greece mainland (Delfino & Georgalis, 2022).

The mollusk fossil assemblage from the Koukos region indicates deposition in a low-energy aquatic system, such as a shallow lacustrine or slow-flowing riverine environment. The investigation of the gastropod species that were found suggest warm, temperate climatic conditions and abundant vegetation with large aquatic plants. Forms like *Melanopsis pseudopigmea*, *Valvata hellenica*, *Iraklimelania coa*, and *Theodoxus doricus doricus* appear to have been adapted to these freshwater habitats. The presence of

Iraklimelania coa in fine-grained lacustrine and riverine deposits suggests the species inhabited low-energy environments, where fine sediments like muds and silts accumulated in areas of reduced flow. These depositional environments are characteristic of slow-moving waters with high sedimentation rates.

Ostracod findings of *Ilyocypris gibba* and *Candona* species are indicative of freshwater bodies like lakes or ponds. Those two genera of freshwater ostracods are often found together in sedimentary deposits. *Ilyocypris gibba* may suggest more stable and warmer freshwater habitats while *Candona* species are adapted to a wider range of temperatures, salinities and dissolved oxygen. Thus, the co-occurrence of these two ostracods may indicate fluctuations between warmer and cooler phases.

The fish fauna contains a remarkable complex, suggesting a link between the Koukos fauna with Asia Minor. This fits with a further fact that the recent freshwater fish fauna of the Island of Kos, being in the ecoregion 7 (the Eastern Aegean), according to Barbieri et al. (2015), which have Asia Minor affinities.

References

Argyriou, T., 2022. The Fossil Record of Ray-Finned Fishes (Actinopterygii) in Greece. In: Vlachos, E. (Eds.) Fossil Vertebrates of Greece 1, Springer Nature, 92-142 https://doi.org/10.1007/978-3-030-68398-6_4

Avrithis, A. I., Georgalis, G. L., 2024. One of the last shelters of soft-shelled turtles (Testudines, Trionychidae) in Europe – first fossil occurrence of a trionychid from the Plio-Pleistocene of Kos Island, Greece. Historical Biology, 1–6. https://doi.org/10.1080/08912963.2024.2302575

Barbieri, R., Zogaris, S., Kalogianni, E., Stoumboudi, M., Chatzinikolaou, Y. Giakoumi S., Kapakos, Y., Kommatas, D., Koutsikos, N., Tachos, V., Vardakas L., Economou, A.N., 2015. Freshwater fishes and lampreys of Greece: An annotated checklist. Monographs on Marine Sciences No. 8. Hellenic Centre for Marine Research: Athens, Greece, 128 p.

Bouchet P., Rocroi J.-P., Frýda J., Hausdorf B., Ponder W., Valdés Á., Warén A. 2005. Classification and nomenclator of gastropod families. Malacologia: International Journal of Malacology, 47, (1–2). Hackenheim, Germany: ConchBooks: 1–397. ISBN 3925919724. ISSN 0076-2997.

Charrier, G., Giglio, A., 1969. Primi risultati di una campagna di rilevamento geologico nell'isola di Coo (Sporadi meridionali – Mare Egeo). Bollettino Associazione Mineraria Subalpina, 6, 482-516.

Delfino, M., Georgalis, G.L., 2022. The Fossil Record of Amphibians (Amphibia: Urodela and Anura) in Greece. In: Vlachos, E. (Eds.) Fossil Vertebrates of Greece 1, Springer Nature, 185-203.

Desio, A., 1924. Appunti geologici sull'isola di Cos (Dodecaneso). Bollettino della Società Geografica Italiana 43, 151-160.

Drinia, H, Koskeridou,E., Antonarakou, A., Tzortzaki, E. 2010. Benthic foraminifera associated with the zooxanthellate coral *Cladocora* in the Pleistocene of the Kos island (Aegean Sea, Greece): Sea level changes and paleoenvironmental conditions. Bulletin of the Geological Society of Greece 43:613–619.

Magrograssi, A., 1928. La fauna levantina di Coo e di Rodi. Atti della Società Italiana di Scienze Naturali e del Museo Civico di Storia Naturale in Milano, 67, 260-264.

Neubauer, T.A., Harzhauser, M., Kroh, A., Georgopoulou, E., Mandic, O., 2014. Freshwater Gastropods of the European Neogene database (FreshGEN). Accessed at http://www.marinespecies.org/freshgen on 2021-01-05. doi:10.14284/363

Neumayr, M., 1880. Über den geologischen Bau der Insel Kos und über die Gliederung der jungtertiären Binnenablagerungen des Archipels. Denkschriften der Kaiserlichen. Akademie der Wissenschaften, Mathematisch Naturwissenschaftliche Classe, 40, 213-314.

Rohling, E., Foster, G., Grant, K., Marino, G., Roberts, A.P., Tamisiea, M.E., Williams, F., 2014. Sea-level and deep-sea-temperature variability over the past 5.3 million years. Nature 508:477-482.

Valakos, E. D., Pafilis, P., Sotiropoulos, K. Lymerakis, P., Maragou, P., Foufopoulos, J., 2008. The Amphibians and Reptiles of Greece. Edition Chimaira, Frankfurt, 463.

Vlachos, E., 2022. The Fossil Record of Turtles and Tortoises (Reptilia: Testudines) in Greece. In: Vlachos, E. (Eds) Fossil Vertebrates of Greece, 1, Springer Nature, 245-282. https://doi.org/10.1007/978-3-030-68398-6_9

Willmann, R. 1983. Neogen und jungtertiäre Entwicklung der Insel Kos (Ägäis,Griechenland). Geologische Rundschau, 72, 815-860 https://doi.org/10.1007/BF01848345

17th INTERNATIONAL CONGRESS of the Geological Society of Greece

BULLETIN OF THE GEOLOGICAL SOCIETY OF GREECE, SP. PUBL.

EXTENDED ABSTRACT 023

Impact of Emission Regulations on the Temporal Trends of Toxicity of Fine Particulate Matter in Los Angeles

Authors: Mohammad Mahdi Badami[1], Yashar Aghaei[1], and Constantinos Sioutas[1]
Affiliation: (1) University of Southern California, Department of Civil and Environmental Engineering, Los Angeles, California, USA

Research Highlights

- Initial reductions in $PM_{2.5}$ mass due to emission controls were followed by increased toxicity from non-tailpipe sources.
- The oxidative potential of $PM_{2.5}$ has risen since 2012, indicating a shift towards more harmful aerosol constituents.

Background

Ambient particulate matter (PM) is a major environmental health challenge worldwide, associated with a variety of serious health issues, including respiratory and cardiovascular diseases, lung cancer, and increased mortality rates. PM is classified based on its size into coarse particles, fine particles ($PM_{2.5}$), and ultrafine particles (UFPs). Among these, $PM_{2.5}$ is particularly hazardous because its small size allows it to penetrate deep into the lungs and enter the bloodstream, leading to systemic inflammation and affecting multiple organs. In densely populated urban areas like Los Angeles, vehicular emissions are the primary source of $PM_{2.5}$, resulting in higher incidences of asthma, heart disease, and other health problems compared to less polluted regions. The frequent air quality alerts in the early 2000s raised significant public health concerns, especially for vulnerable groups such as children and the elderly, prompting urgent regulatory actions aimed at reducing PM emissions from both vehicles and industrial sources.

Over the past few decades, extensive regulatory measures at both federal and state levels have substantially improved air quality in Los Angeles and throughout California. Programs initiated by the U.S. Environmental Protection Agency and the California Air Resources Board have successfully lowered the mass concentrations of primary combustion-related pollutants like organic carbon and elemental carbon. These efforts have led to significant reductions in $PM_{2.5}$ levels and associated health risks. However, despite these successes, the number of ultrafine particles has not decreased proportionally and has even plateaued in recent years. This indicates that current regulations may not fully address all sources of PM, particularly non-tailpipe emissions such as brake and tire wear, as well as the formation of secondary aerosols from volatile organic compounds. Additionally, the chemical composition of $PM_{2.5}$ has become more complex, incorporating a diverse range of toxic substances, including metals and organic compounds, which contribute to its overall oxidative potential and health impacts. These developments highlight the need for regulatory frameworks to evolve, incorporating strategies targeting particulate matter's most harmful components to further enhance air quality and protect public health.

Objectives

The primary aim of this study is to analyze the temporal trends in both the chemical composition and oxidative potential of $PM_{2.5}$ in Los Angeles over the past two decades. Specifically, the research seeks to determine the effectiveness of emission regulations in reducing $PM_{2.5}$ toxicity and to identify emerging sources contributing to any observed changes in oxidative potential. By understanding these dynamics, the study aims to provide insights that can inform more comprehensive and effective air quality management strategies.

Methods

Data on $PM_{2.5}$ oxidative potential were compiled through an extensive review of studies conducted over the past two decades (Badami et al. 2023; Cho et al. 2005; Farahani et al. 2022; Hu et al. 2008; Li et al. 2003; Ntziachristos et al. 2007; Saffari et al. 2014; 2016; Shirmohammadi et al. 2016; 2017; Verma et al. 2009; 2011). The dithiothreitol (DTT) assay data were originally reported in various units (activity per mass or per volume) and were standardized using corresponding PM mass and sampling duration measurements to ensure comparability. Detailed information

on measurement methods, equipment calibration, instrument specifications, and uncertainties can be found in the original publications (Badami et al. 2023; Cho et al. 2005; Farahani et al. 2022; Hu et al. 2008; Li et al. 2003; 2009; Ntziachristos et al. 2007; Saffari et al. 2014; 2016; Shirmohammadi et al. 2016; 2017; Verma et al. 2009; 2011; Zhang et al. 2016). The majority of DTT data were obtained from the Particle Instrumentation Unit (PIU) at the University of Southern California (USC), located in an urban area near downtown Los Angeles, 150 meters from a major freeway (I-110) that is generally situated in the downwind direction of this freeway. Additionally, trends of various chemical species such as metals (e.g., Barium [Ba], Copper [Cu], Manganese [Mn], Zinc [Zn], Chromium [Cr], Nickel [Ni], Cadmium [Cd], Iron [Fe]) and inorganic ions (sulfate [SO_4^{2-}] and nitrate [NO_3^-]) were sourced from the North Main Street monitoring station, operated by the U.S. Environmental Protection Agency (EPA) as part of the Air Quality System (AQS) and Chemical Speciation Network (CSN). These trends correspond to the sampling periods of the reviewed DTT studies, noting that data were only available from 2005 to 2024 due to the absence of CSN data prior to 2005 and the lack of metals data in 2005.

Additional sampling was conducted in January and February 2024 at the PIU of USC to assess contemporary conditions under the latest regulatory environment. $PM_{2.5}$ was collected using pre-baked quartz filters in Sioutas Personal Cascade Impactor Samplers (PCISs, SKC Inc., Eighty-Four, PA, USA) with a flow rate of 9 liters per minute to ensure accurate mass measurements. The oxidative potential of collected $PM_{2.5}$ samples was assessed using the DTT assay, adhering to established protocols.

Results

The long-term analysis of $PM_{2.5}$ oxidative potential in Los Angeles from 2001 to 2024 identified two distinct phases corresponding to different regulatory periods. Between 2001 and 2008, there was a significant decline in DTT activity per volume, decreasing from approximately 0.84 to 0.37 nmol/min/m³. This reduction coincided with stringent tailpipe emission regulations that effectively lowered primary combustion-related pollutants such as organic carbon (OC) and elemental carbon (EC). However, starting in 2012, despite a continued slight decrease in overall $PM_{2.5}$ mass, the oxidative potential began to rise, reaching around 0.97 nmol/min/m³ by 2024. This increase is primarily driven by the stabilization and slight rise in concentrations of metals like Fe and Zn, which are associated with non-tailpipe emissions such as brake and tire wear, as well as the formation of secondary organic aerosols. These changes indicate a shift in the toxicological profile of $PM_{2.5}$, where non-tailpipe sources are increasingly contributing to its oxidative potential consistent with the increase in the vehicle miles traveled (VMT) in this period (Badami, Tohidi, and Sioutas 2024).

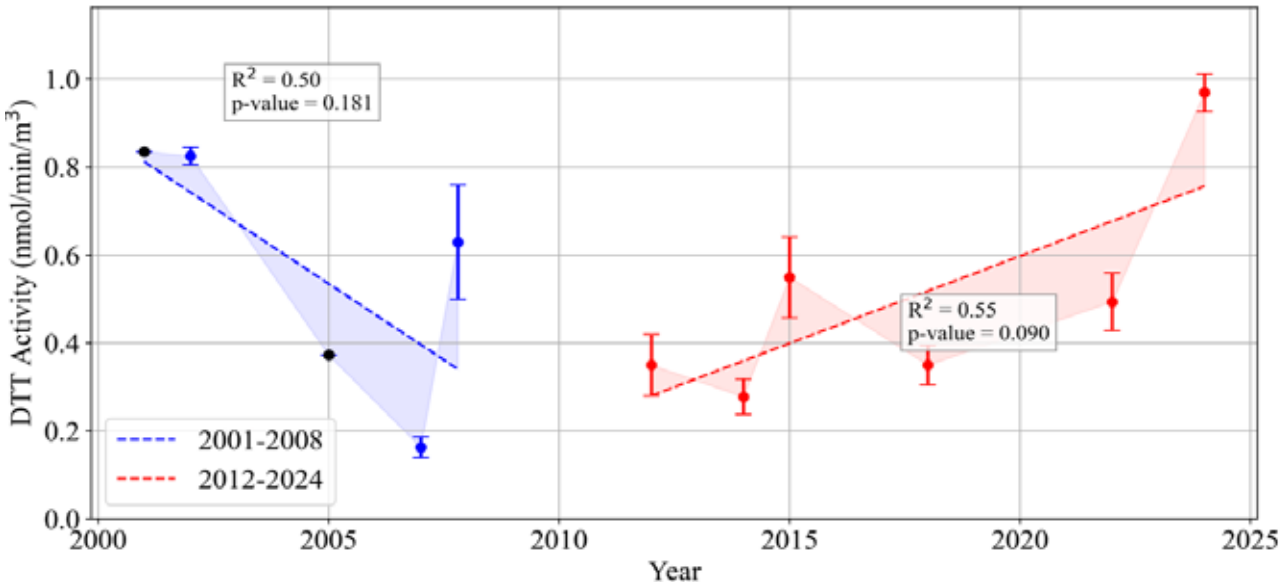

Figure1. $PM_{2.5}$ DTT activity Long-term trends (2001–2024).

Additionally, the correlations between DTT activity and specific $PM_{2.5}$ components have evolved over the study period. Metals including Fe, Zn, Cu, Mn, and Pb demonstrated strengthening correlations with DTT activity, highlighting their growing role in driving the oxidative potential of fine particulate matter. In contrast, the correlation between OC and DTT activity showed a slight decreasing trend, suggesting a reduced influence of tailpipe emissions on oxidative potential over time. EC exhibited a modest increase in its correlation with DTT activity, potentially reflecting its association with non-tailpipe sources rather than its inherent toxicity. These findings underscore the importance of addressing non-tailpipe and secondary emission sources in regulatory frameworks to effectively mitigate the oxidative toxicity of $PM_{2.5}$ and improve public health outcomes.

Conclusions

This study investigated the long-term trends in both the chemical composition and oxidative potential of $PM_{2.5}$ in Los Angeles over the past two decades, utilizing the DTT assay as a measure of particle-induced oxidative stress. The findings reveal that while regulatory measures effectively reduced mass concentrations of primary combustion markers such as OC and EC, notably before 2016, a significant shift has occurred in the composition of $PM_{2.5}$ towards non-tailpipe emission tracers. These unregulated species, including stable or proportionally increasing metals Fe, Cu, and Zn, have contributed to a partial resurgence and stabilization of DTT activity per mass from 2012 to 2024. Additionally, the oxidative potential per volume of fine $PM_{2.5}$ has continued to rise, underscoring the growing impact of non-tailpipe sources and secondary aerosol formation on $PM_{2.5}$ toxicity.

Acknowledgments

This research was supported by the National Institutes of Health (NIH) under grant numbers 5R01ES033660-03, 1RF1NS130681-01, and 5R01AI065617-23. The authors are grateful for the support from the Viterbi School of Engineering at the University of Southern California through the Ph.D. fellowship award.

References

Badami, Mohammad Mahdi, Ramin Tohidi, Mohammad Aldekheel, Vahid Jalali Farahani, Vishal Verma, and Constantinos Sioutas. 2023. “Design, Optimization, and Evaluation of a Wet Electrostatic Precipitator (ESP) for Aerosol Collection.” *Atmospheric Environment* 308 (September):119858. https://doi.org/10.1016/J.ATMOSENV.2023.119858.

Badami, Mohammad Mahdi, Ramin Tohidi, and Constantinos Sioutas. 2024. “Los Angeles Basin’s Air Quality Transformation: A Long-Term Investigation on the Impacts of PM Regulations on the Trends of Ultrafine Particles and Co-Pollutants.” *Journal of Aerosol Science* 176 (February):106316. https://doi.org/10.1016/j.jaerosci.2023.106316.

Cho, A. K., C. Sioutas, A. H. Miguel, Y. Kumagai, and J. R. Froines. 2005. “Redox Activity of Airborne Particulate Matter (PM) at Different Sites in the Los Angeles Basin.” *Environ. Res.* 99:40–47.

Farahani, Vahid Jalali, Abdulmalik Altuwayjiri, Milad Pirhadi, Vishal Verma, Ario Alberto Ruprecht, Evangelia Diapouli, Konstantinos Eleftheriadis, and Constantinos Sioutas. 2022. “The Oxidative Potential of Particulate Matter (PM) in Different Regions around the World and Its Relation to Air Pollution Sources.” *Environmental Science: Atmospheres* 2 (5): 1076–86. https://doi.org/10.1039/d2ea00043a.

Hu, S., A. Polidori, M. Arhami, M. M. Shafer, J. J. Schauer, A. Cho, and C. Sioutas. 2008. “Redox Activity and Chemical Speciation of Size Fractioned PM in the Communities of the Los Angeles-Long Beach Harbor.” *Atmospheric Chemistry and Physics* 8 (21): 6439–51. https://doi.org/10.5194/acp-8-6439-2008.

Li, Ning, Constantinos Sioutas, Arthur Cho, Debra Schmitz, Chandan Misra, Joan Sempf, Meiying Wang, Terry Oberley, John Froines, and Andre Nel. 2003. “Ultrafine Particulate Pollutants Induce Oxidative Stress and Mitochondrial Damage.” *Environmental Health Perspectives* 111 (4): 455–60. https://doi.org/10.1289/ehp.6000.

Li, Ning, Meiying Wang, Lori A. Bramble, Debra A. Schmitz, James J. Schauer, Constantinos Sioutas, Jack R. Harkema, and Andre E. Nel. 2009. “The Adjuvant Effect of Ambient Particulate Matter Is Closely Reflected by the Particulate Oxidant Potential.” *Environmental Health Perspectives* 117 (7): 1116–23. https://doi.org/10.1289/

EHP.0800319.

Ntziachristos, Leonidas, John R. Froines, Arthur K. Cho, and Constantinos Sioutas. 2007. "Relationship between Redox Activity and Chemical Speciation of Size-Fractionated Particulate Matter." *Particle and Fibre Toxicology* 4 (June). https://doi.org/10.1186/1743-8977-4-5.

Saffari, Arian, Nancy Daher, Martin M. Shafer, James J. Schauer, and Constantinos Sioutas. 2014. "Seasonal and Spatial Variation in Dithiothreitol (DTT) Activity of Quasi-Ultrafine Particles in the Los Angeles Basin and Its Association with Chemical Species." *Journal of Environmental Science and Health - Part A Toxic/Hazardous Substances and Environmental Engineering* 49 (4): 441–51. https://doi.org/10.1080/10934529.2014.854677.

Saffari, Arian, Sina Hasheminassab, Martin M. Shafer, James J. Schauer, Talal A. Chatila, and Constantinos Sioutas. 2016. "Nighttime Aqueous-Phase Secondary Organic Aerosols in Los Angeles and Its Implication for Fine Particulate Matter Composition and Oxidative Potential." *Atmospheric Environment* 133 (May):112–22. https://doi.org/10.1016/j.atmosenv.2016.03.022.

Shirmohammadi, Farimah, Sina Hasheminassab, Dongbin Wang, James J. Schauer, Martin M. Shafer, Ralph J. Delfino, and Constantinos Sioutas. 2016. "The Relative Importance of Tailpipe and Non-Tailpipe Emissions on the Oxidative Potential of Ambient Particles in Los Angeles, CA." *Faraday Discussions* 189:361–80. https://doi.org/10.1039/c5fd00166h.

Shirmohammadi, Farimah, Dongbin Wang, Sina Hasheminassab, Vishal Verma, James J. Schauer, Martin M. Shafer, and Constantinos Sioutas. 2017. "Oxidative Potential of On-Road Fine Particulate Matter (PM2.5) Measured on Major Freeways of Los Angeles, CA, and a 10-Year Comparison with Earlier Roadside Studies." *Atmospheric Environment* 148 (January):102–14. https://doi.org/10.1016/j.atmosenv.2016.10.042.

Verma, Vishal, Payam Pakbin, Ka Lam Cheung, Arthur K. Cho, James J. Schauer, Martin M. Shafer, Michael T. Kleinman, and Constantinos Sioutas. 2011. "Physicochemical and Oxidative Characteristics of Semi-Volatile Components of Quasi-Ultrafine Particles in an Urban Atmosphere." *Atmospheric Environment* 45 (4): 1025–33. https://doi.org/10.1016/j.atmosenv.2010.10.044.

Verma, Vishal, Andrea Polidori, James J. Schauer, Martin M. Shafer, Flemming R. Cassee, and Constantinos Sioutas. 2009. "Physicochemical and Toxicological Profiles of Particulate Matter in Los Angeles during the October 2007 Southern California Wildfires." *Environmental Science and Technology* 43 (3): 954–60. https://doi.org/10.1021/es8021667.

Zhang, Xian, Norbert Staimer, Daniel L. Gillen, Tomas Tjoa, James J. Schauer, Martin M. Shafer, Sina Hasheminassab, et al. 2016. "Associations of Oxidative Stress and Inflammatory Biomarkers with Chemically-Characterized Air Pollutant Exposures in an Elderly Cohort." *Environmental Research* 150 (October):306–19. https://doi.org/10.1016/j.envres.2016.06.019.

17th INTERNATIONAL CONGRESS of the Geological Society of Greece

BULLETIN OF THE GEOLOGICAL SOCIETY OF GREECE, SP. PUBL.

EXTENDED ABSTRACT 024

Teachers' experience, attitudes and skills on flood events: The case of Daniel storm 2023, Thessaly, Greece

Bakopoulou A.[1], Dousiaki C.[1], Diakakis M.[1], Andreadakis E.[1], Mavroulis S.[1], Gogou M.[1], Kranis, H., Antonarakou A.[1], Lekkas E.[1]

(1) National and Kapodistrian University of Athens, Department of Geology and Geoenvironment, Athens, Greece, abakopoulou@geol.uoa.gr

Extended Abstract

School environment poses a challenge for the protection against the increasing occurrences of natural disasters (Lekkas & Andreadakis, 2015), and the education of teachers and students alike should be a first-order priority. This pilot study is a first step to reveal teachers' attitudes and skills after the Daniel storm 2023 (Thessaly, Greece) in order to record awareness level in terms of flood risk reduction toward the development of an educated resilient and adaptable school community to decrease flood vulnerability and susceptibility.

Within the scope of this quasi-experimental research, semi-structured interviews were conducted in October and November 2023, focusing on teachers at local primary schools that suffered from the Daniel flood. Questions of the research tool were cross-checked by two educators and responses were qualitatively elaborated by two geoscientists to keep internal validity.

After the qualitative elaboration of interview responses and in terms of teachers' attitude about Daniel flood and their flood background knowledge, it comes out in general that a) there is a diversity in the pre-existing knowledge of teachers regarding floods usually exhibiting low scores of awareness, which is in line with other research (Bakopoulou et al, 2022), and b) the real-life experience of Daniel events has significantly contributed to the raising of awareness within the local school community. The majority of teachers: (i) point out the importance of targeted educational initiatives; (ii) recognize the increased risk in the local flood-affected areas; (iii) highlight the severe interrelation between personal and professional challenges during natural disasters, emphasizing the need for broad and systemic support; (iv) assure that the flood impact on the school environment extends beyond the immediate effects on the classroom, affecting infrastructure and the overall functionality of the school; and (v) acknowledge the importance of preparedness and resilience and the need for further training.

Regarding the emergency management cycle, all teachers are partially aware of it, which means that they either are not aware of the different cycle phases, or are unable to accurately discriminate among each management phase. At the same time, all teachers point out that it was not possible to implement emergency management measures immediately, due to the timing of the storm occurrence. Therefore, they recognize the importance of student and teacher education and skill development on prevention and protection measures, even in cases that students have not been directly affected. Some teachers emphasized the critical role of collaboration and mutual support among school authorities, colleagues, parents and the wider community, while the involvement of school counsellors, psychologists, and social workers is recognized as essential for providing emotional support to students and addressing the psychological impacts of the flood beyond the school environment. External support from other schools and volunteerism are also identified as valuable resources. Donations are claimed to have fostered a positive and inclusive atmosphere within the school community. The use of various communication channels, including social media platforms, has been emphasized as a necessary contribution and seminars and guidelines from educational authorities after the storm provided teachers with valuable insights for addressing the consequences of the floods, highlighting the importance of professional development and guidance.

As far as the flood consequences on school community and school environment are concerned, the storm had a significant impact on students and teachers demolishing their living and learning environment (Lekkas et al 2024). Additionally, the disruption of students' routine, the potential relocation of home or school, and exposure to abundant challenges disturbed their emotional balance and required careful

management and support. Students experienced increased anxiety and fear, with some facing stress and depression. Relocation and adjustment to new environments are recorded as the main factors that contributed to increased emotional stress; while students exhibited violent behaviour after the disaster emphasizing that they should be treated with more compassion, care, patience and tenacity in the post-flood schooling. Additionally, failures in living and learning environment caused concentration disorders to students, which in turn led to low learning abilities in the post-flood period. Besides, teachers expressed emotions of depression, stress and mental and bodily exhaustion; and suffered from severe stress of how to achieve the annual learning goals within such adverse circumstances after the disaster. Despite curriculum rigidity, teachers transformed their teaching goals to emotional ones, addressing the emotional impact and adopting measures, such as engaging in therapeutic activities in classrooms with collaboration with counsellors, psychologists, and parents, where students shared their stories focused on emotional expression and resilience. This goal transition created extra stress on teachers as they had doubts about whether they would succeed in their new goals or not, while the demand to keep in line with educational curriculum goals increased teachers' stress. Another stress factor is the fact that despite their using their own means and resources voluntarily to help especially poor students to overcome difficulties, they often felt inadequate to contribute. Finally, the need for emotional support, relocation and the adaptation of teaching methods emerges as recurring patterns that all teachers faced after the occurrence of the event.

In terms of skill development school programmes, ensuring the safety of students and teachers is an utmost priority, as reflected in the multifaceted approaches adopted by schools; therefore, all teachers claimed that the whole local school community should be trained and educated on flood risk reduction, according to the age of each target-team. Teachers should be trained to effectively support the mitigation of symptoms of post-traumatic stress among student population individually. Berger, Abu-Raiya & Benatov (2016) emphasize the long-term strong benefits and effectiveness in minimizing the symptoms of post-traumatic stress of individual education by trained teachers. However, no teacher had participated in a flood risk reduction programme in the past, even though it is a flood-prone area. Nonetheless, all teachers claimed that skill development school programmes should be engaged and enriched with flood risk reduction, protection and management activities. In addition, teachers insisted that training school community towards making quick, immediate and appropriate decisions in emotionally stressed and adverse during the flood and post-flood periods is of major importance. This could be achieved through skill development school workshops. In this sense, teachers proposed that these skill programmes or workshops should definitely include: (a) concrete simulations, (b) drills organized by local authorities, (c) digital simulations and (d) expert lectures.

Concluding, the implications of the aforementioned data are manifold: the importance of education, training and skill development on flood risk reduction and emergency management before the occurrence of severe weather events and floods constitutes a necessity, while continuous education, adapted to local needs and based on local experiences and local flooded-area history, is crucial for building resilience and preparedness for local schools and local community. Skill development school programmes or workshops can serve as a means to address flood risk reduction and protection education. Addressing these challenges can forward the development of effective support systems, ensuring the mental well-being of school community and fostering an environment that promotes effective post-disaster education. Authorities should consider the aforementioned data so that they establish educational policies aimed at enhancing the preparedness and resilience of school community in the face of flood vulnerability and risk reduction, flood mitigation, resilience and adaptability.

References

Bakopoulou A., Katsetsiadou N.A., Kyriazis E., Alexoudi V., Grambas A., Kotsi E., Stamati E., Antonarakou A., Lekkas E. (2022). Disaster and crisis management awareness level of local authorities in the District of Attica Municipalities before and after training courses. Proc. 16th Int. Congr. Geol. Soc. Greece, 17-19 October 2022, Patras, Greece, Bul. Geol. Soc. Greece, Sp. Pub. 10, Ext. Abs. GSG2022-283. **[Conference Proceedings]**

Berger, R., Abu-Raiya, H., & Benatov, J. (2016). Reducing primary and secondary traumatic stress symptoms

among educators by training them to deliver a resiliency program (ERASE-Stress) following the Christchurch earthquake in New Zealand. *American Journal of Orthopsychiatry*, *86*(2), 236. **[Journal Article]**

Lekkas E. & Andreadakis E., (2015). Introduction to the theory of crisis and disaster management, Department of Geology and Geoenvironment, NKUA, 178p. **[Book]**

Lekkas E, Diakakis M., Mavroulis S., Filis Ch., Bantekas Y., Gogou M., Katsetsiadou K-N., Mavrouli M., Giannopoulos V., Sarantopoulou A., Nastos P., Vassilakis E., Konsolaki A., Kotsi E., Carydis P., Parcharidis I., Tounta S., Falaras T., Skourtsos E., Bakopoulou A., Korkovelos A., Ronzi L., Speis P-D., Lekka Ch., Stamati E., Moraitis S. (2024). The early September 2023 Daniel storm in Thessaly Region (Central Greece). Newsletter of Environmental, Disaster and Crises Management Strategies, NKUA, Issue No 30, January 2024. **[Journal Article]**

17th INTERNATIONAL CONGRESS of the Geological Society of Greece

BULLETIN OF THE GEOLOGICAL SOCIETY OF GREECE, SP. PUBL.

EXTENDED ABSTRACT 025

A (preliminary) comparative gemological-mineralogical study of quartz crystals derived from Greece and Brazil

Bardi E.[1], Lampropoulou P.[1], Sergoulopoulos A.[2], Rogkala A.[1], Giannakopoulou P.P.[1], Margaritis F.[1], Papoulis D.[1], Tsinidis A.[3], Islam I.[4], Petrounias P.[1]

(1) Department of Geology, University of Patras, 265 04 Patras, Greece, eftibardi@gmail.com (2) Department of Geology, University of Patras, 265 04 Patras, Greece (2) Gem Testing Laboratory Athens, Gem-A Athens ATC, 10562 Athens, Greece (3) Field collector, Thessaloniki (4) Department of Geology, Shaheed Benazir Bhutto University Sheringal, Dir Upper, 18030, Pakistan

Introduction

In this study, quartz crystals from Greece and Brazil are studied and characterized regarding their macroscopic and microscopic characteristics, emphasizing on their inclusions. Generally, quartz crystals present a tremendous variety of crystal and fluid inclusions (liquid and gas). So many mineral varieties have been identified in quartz that it would be impossible to mention them all. Specifically, this study focuses on samples originating from Internal Hellenides, namely Serbo-Macedonian and Rhodope Massifs (Greece), and Espinhaço Range (Brazil). Solid and liquid inclusions can provide information about the formation processes, the specific environment and the age that quartz crystals were formed, while they also characterize the quality of these as gemstones (Brace-Thompson, 2023; Deer, Howie, & Zussman, 1992; Roedder, 1984). The results presented in this publication are preliminary as our study is in progress. Different techniques are used in order to investigate the mineral inclusions of the studied samples such as X-ray diffraction (XRD), Scanning Electron Microscope (SEM), Raman spectroscopy (Raman) and the results of their full characterization will be presented in the future.

Geological setting-Geologic Background

Based on recent publications quartz found in Greece is distinguished in two main groups in respect to its formation environment (Maneta & Voudouris, 2010; Voudouris et al., 2004, 2019). The first group involves quartz that is formed in alpine fissures hosted in lithologies such as ortho- and paragneisses (in the Rhodope Massif: Drama, Thassos Island and the Attico-Cycladic Massif: Penteli Mt, Evia, Ios Islands), as well as in amphibolites (Evros, Thassos, Evia and Andros Islands), phyllites (Lesvos Island) and meta-quartzites (Crete Island). The second group, providing gem quality quartz, is related to Tertiary and Mesozoic magmatic-hydrothermal environments and associated rocks (e.g. granitoids, pegmatites, skarns, non-skarn carbonate-replacement deposits, hydrothermal-altered volcanic rocks) found across Greece (Voudouris *et al.*, 2019).

Quartz in Brazil is also found in two main geological settings (Favacho-Silva, 2000). The first includes the hydrothermal vein system of the Serra do Espinhaço, where quartz is of hydrothermal origin and is embedded in rocks of the super-group Espinhaço. Rocks observed are mainly quartzites, followed by phyllites and to a lesser extent meta-conglomerates and carbonate rocks. The second geological setting is the pegmatitic province of Eastern Brazil, where quartz is part of the core of pegmatite veins, associated with granites that have penetrated the synorogenetic turbidities of Salinas formation or its basement (Macauba Group) (Favacho-Silva, 2000).

Materials and Methods

Quartz from Greece was collected from multiple places in the Serbo-Macedonian and Rhodope Massifs, northern Greece. In detail, Greek samples were derived from outcrops found near Lefkopetra in Xanthi, Koinira in Thassos Island, Dassoto, Kato Vrontou, Panorama in Drama and Madem Lakkos in Chalkidiki. The samples from Brazil comprised of colorless and light brown quartz and there is no precise evidence of origin beyond the state where they were sourced from.

Quartz samples from both Greece (19) and Brazil (19) were polished and observed under a Proapex gemological microscope with x10 and x30 magnification. Their selection was based on whether the samples were free of inclusions or presented inclusions for further investigation. This was the reason why seventeen (17) and two (2) samples were

selected from group one and two respectively of the Brazilian quartzes. Most of the samples of the second group were inclusion free. All the studied quartz samples had their refractive indexes and specific gravity calculated. Following, based on previous observations, fifteen samples were chosen and thin sections of these samples were produced. Thin sections were examined under a Leitz Ortholux polarizing petrographic microscope and photographed using a Jenoptik ProgRes C3 digital camera.

Results and discussion

The quartz samples from Greece consist of multiple varieties and derived from the geological environments that are mentioned above. According to their macroscopic characteristics they are classified in four (4) different groups of varieties and they have further been characterized. Representative results of studied samples derived from Greece are presented below.

Amethyst

Five (5) amethyst samples (DAS01A, DAS01B, DAS01C, DAS01E, DAS01F) from the area of Dassoto, Drama were macroscopically and gemologically analyzed and their refractive indices values are 1.543 ± 0.003 and 1.552 ± 0.003 and the specific gravity showed values of 2.62 ± 0.01. These specimens are scepter-shaped and have a light purple color on the crown. In the three crystals where the body of the scepter is preserved, light to dark smoky quartz is observed (Figure 1a).

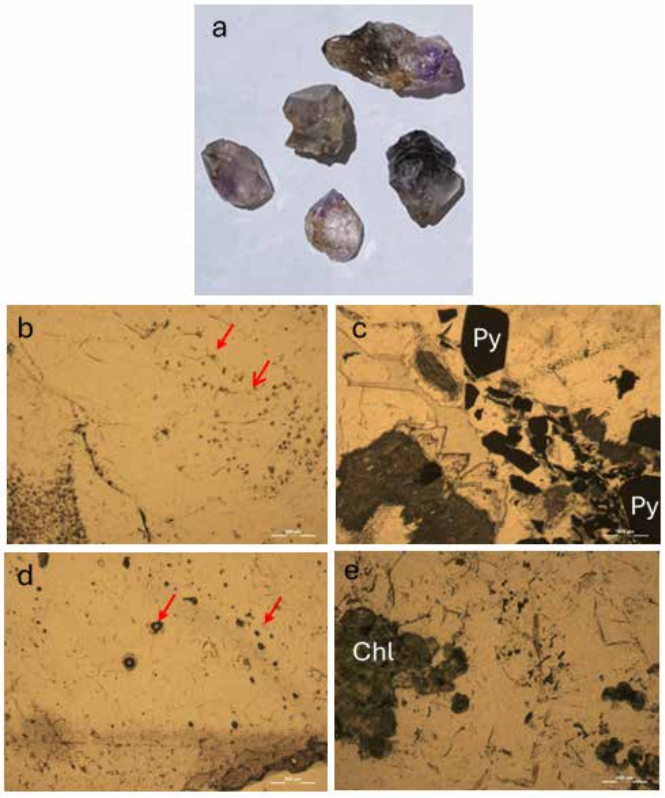

Figure 1. (a) Photo of scepter-shaped amethyst samples from the area of Dassoto, Drama. (b) Photomicrograph of zebra-like inclusions in DAS01B taken in parallel Nicols in transmitted light with magnification x25.(c) Photomicrograph of pyrite included in quartz in MAN01D taken in parallel Nicols in transmitted light with magnification x25. (d)Photomicrograph of two-phase fluid inclusions in KOI01 taken in parallel Nicols in transmitted light with magnification x25. (e) Photomicrograph of chlorite in LEY01A taken in parallel Nicols in transmitted light with magnification x4.

Regarding their microscopic observation, DAS01B sample was selected. Zebra-like inclusions, alternating dark and light parallel color bands related to twinning in the crystal (Gem-A, 2022), iron oxides, negative crystals and feldspars were observed in the DAS01B sample (Figure 1b). In this context, “negative crystals” will refer to hollow, crystal-shaped cavities, particularly exhibiting trigon-like geometry.

Rock crystal

This group includes six (6) samples (DAS01D, PAN01, MAN01A, MAN01B, MAN01C, MAN01D) from the areas of Dassoto, Panorama in Drama and Madem Lakkos in Chalkidiki. Along with amethyst samples from the Dassoto area of Drama, a prismatic crystal of colorless quartz with a few chlorite inclusions was collected and analyzed. This crystal gave values of 1.544 and 1.533 for refractive indices and for specific gravity 2.62. The crystal from Panorama has several inclusions of chlorite, rutile and possibly actinolite. The values of the refractive indices are 1.548 and 1.557 and the specific gravity 2.60. Three of the four samples from the Madem Lakkos deposit in Chalkidiki had their refractive indices measured, while the fourth sample (MAN01D) was excluded due to measurement constraints. Therefore, the refractive index values for Madem Lakkos are1.547±0.002 and 1.556±0.002 and the specific gravity was determined to be 2.65±0.02.

DAS01C and MAN01D samples were analyzed using microscope. Iron oxides in cracks, negative crystals, feldspar, muscovite and chlorite were identified in the DAS01C sample. In the sample MAN01D, pyrite, chlorite, iron oxides in cracks, negative crystals, feldspars and fluid inclusions were identified (Figure 1c).

Table 1. Summary of the refractive indexes of Greece’s quartz.

Samples	**Refractive Indexes**	
Amethyst		
DAS01A	1.540	1549
DAS01B	1.543	1.552
DAS01C	1.545	1.554
DAS01E	1.544	1.553
DAS01F	1.546	1.555
Rock crystal		
DAS01D	1.544	1.553
PAN01	1.548	1.557
MAN01A	1.549	1.558
MAN01B	1.548	1.557
MAN01C	1.545	1.554
MAN01D		
Smoky quartz		
KOI01	1.540	1.549
DAS02A	1.530	1.539
DAS02B	1.548	1.557
DAS03A	1.542	1.551
DAS03B	1.550	1.559
Milky quartz		
LEY01A	1.544	1.553
LEY01B	1.548	1.557
KAT01	1.540	1.549

Smoky quartz

Refractive index measurements were taken from five (5) samples (KOI01, DAS02A, DAS02B, DAS03A, DAS03B), with colors ranging from light to dark, from the areas Koinira in Thassos and Dassoto in Drama. For Koinira, measured values were 1.544 and 1.553. However, they varied significantly between light quartz samples or between light and dark. Specifically, the refractive indices were 1.539 ± 0.009 and 1.548 ± 0.009 for light smoky quartz and 1.546 ± 0.004and 1.555 ± 0.004 for dark smoky quartz from Dassoto. The specific gravity measured for all samples gave values limited to 2.66 ± 0.03.

Samples KOI01, DAS02B, and DAS03C (equivalent to DAS03A and DAS03B) were selected for microscopic observation. Iron oxides in cracks, negative crystals, muscovite and fluid inclusions (one and two-phase) were identified in the KOI01 sample (Figure 1d). In DAS02B iron oxides, fluid inclusions (both one- and two-phase), negative crystals, muscovite and possibly metallic minerals were recognized, while in DAS03C iron oxides in cracks, muscovite and liquid inclusions (both one- and two-phase) occur.

Milky quartz

Three (3) samples were analyzed (LEY01A, LEY01B, KAT01) from Lefkopetra in Xanthi and from Kato Vrontou in Drama. The refractive indices are 1.546 ± 0.002 and 1.535 ± 0.002 for Lefkopetra of Xanthi and for Kato Vrontou 1.540 and 1.459. The specific gravity for all samples is 2.62 ± 0.01.

Samples LEY01A and KAT01 were examined under the microscope. Chlorite and muscovite were the main mineral inclusions found in sample LEY01A (Figure 1f). Iron oxides were detected in cracks, while fluid inclusions and negative crystals are common. In sample KAT01, feldspar, muscovite, clinopyroxene, iron oxides in cracks, fluid inclusions (both one- and two-phase) and chlorite (near the margin) were observed.

Most of the samples from Brazil are consisted of colorless quartz, with two exceptions. They are likely of hydrothermal origin, as the majority predominantly contain two-phase fluid inclusions. The studied samples of Brazil are divided in two varieties and representative results of their characterization presented as follows:

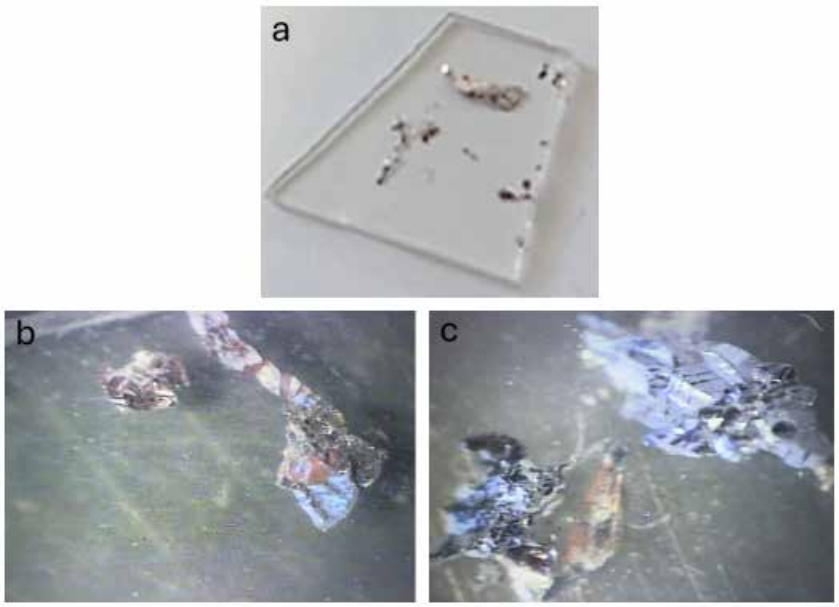

Figure 2. (a) Photo of red and black inclusions showing dendritic form in sample MIN04 from Minas Gerais, Brazil. (b, c) Photomicrographs of red and black inclusions in sample MIN04 as shown in a gemological microscope with magnification x 30.

Rock crystal

In total, seventeen (17) samples were analyzed. Based on macroscopic observation, eleven (MIN03,

MIN05, MIN06, MIN09, MIN10, MIN11, MIN13, MIN14, MIN15, MIN16, MIN17) appear clear and vitreous, containing little to no inclusions. Their refractive indices range from 1.543 to 1.550 and from 1.552 to 1.599with specific gravity of 2.60 ± 0.05. Samples MIN01 and MIN19 exhibit high concentration of liquid inclusions, with measured values1.549+ 0.001 and1.558 + 0.001for refractive indices and 2.63 + 0.01 for specific gravity. In MIN04 and MIN08, red and black inclusions that in localized spots are showing dendritic form were macroscopically visible (Figure 2a), while MIN12 contained orange-colored iron oxides. The refractive indices are limited to 1.543+ 0.007 and 1.552 + 0.007and the specific gravity is 2.59 + 0.05. Finally, although MIN07 appeared mostly transparent, chlorite was observed macroscopically. Its refractive index values are 1.539 and 1.548 and its specific gravity is 2.64.

For their microscopic observation, samples MIN01, MIN03, MIN07, MIN08, MIN12 and MIN15 were selected. Plagioclase, muscovite and fluid inclusions (both one- and two-phase) were observed in MIN01 sample. In MIN03 and MIN07 samples, iron oxides in cracks, fluid inclusions (both one- and two-phase), muscovite, negative crystals and chlorite were distinguished, while in MIN15 negative crystals, iron oxides, muscovite and chlorite were distinguished (Figure 2b). Also, iron oxides, negative crystals, muscovite and hematite were identified in MIN08.

Table 2. Summary of the refractive indexes of Brazil's quartz.

Samples	**Refractive Indexes**	
Rock crystal		
MIN01	1.550	1.559
MIN03	1.550	1.559
MIN04	1.543	1.552
MIN05	1.543	1.552
MIN06	1.550	1.559
MIN07	1.539	1.548
MIN08	1.550	1.559
MIN09	1.549	1.558
MIN10	1.548	1.557
MIN11	1.544	1.553
MIN12	1.550	1.559
MIN13	1.550	1.543
MIN14	1.543	1.552
MIN15	1.543	1.552
MIN16	1.550	1.559
MIN17	1.550	1.559
MIN19	1.549	1.558
Smoky quartz		
MIN02	1.543	1.552
MIN18	1.550	1.559

Smoky quartz

The color of MIN02 and MIN18 samples is presented as light brown color. The refractive indices obtained from the measurement of the two (2) samples are 1.543 + 0.007 and 1.552 + 0.007 and the specific gravity showed values 2.62 + 0.03.

Sample MIN02 was chosen for microscopic observation. Iron oxides in cracks, negative crystals and fluid inclusions (both one- and two-phase) were identified in the sampleMIN02.

Conclusions

Samples from Greece include mineral varieties such as: amethyst, rock crystal, smoky quartz and milky

quartz, while those derived from Brazil mainly include smoky quartz. So far, the following conclusions can be drawn:

- The difference between refractive indices of the same variety or the same country or the two countries is random and no correlation can be concluded.
- As for the specific gravity (SG) in Greek samples, is observed that amethysts, rock crystal from Drama and milky quartz have SG < 2.65 but rock crystal from Chalkidiki and smoky quartz have SG > 2.65. On the other hand, in Brazilian samples, all except two have SG < 2.65. However, they are exceptions in their variety because one is a rock crystal and the other is smoky quartz.
- Even though Brazilian amethyst was not included in this study, it was observed that amethyst from Greece contains zebra-like inclusions. Zebra-like" inclusions are typical of amethyst, but there are not always present in a sample. The observation of this type of inclusion in a Greek sample is worth mentioning.
- Inclusions that were present in every sample were iron oxides in cracks, negative crystals and fluid inclusions. Both muscovite and chlorite were frequently found in both Greek and Brazilian samples.

As this study is still evolving, the evaluation of XRD data of some samples is not completed while their characterization via other analytic techniques (e.g. SEM, FTIR and Raman) is in progress. The results of a fully characterization in macro-micro-nano scale of quartz gem crystals with combined methods will be presented in the future in order to be used as a new data base of gems from Greece and/ or other areas. It is considered that it will be enriched by new research in the future, providing significant geological, gemological information in a more systematic mode.

Acknowledgements

Thanks to the postgraduates student Pahaki M. and graduate student Skontovolou L. for their help, the cutting workshop Michael Hatzimihail that polished the samples and the EAGME laboratories for preparing the thin sections of samples.

References

Brace-Thompson, J. (2023). 9 Types of Inclusions in Quartz. Retrieved from Rockngem.com website: https://www.rockngem.com/9-types-of-inclusions-in-quartz/

Deer, W. A., Howie, R. A., & Zussman, J. (1992). An Introduction to the Rock-forming Minerals (2nd ed., p. 467). Prentice Hall.

Favacho- Silva, M.D. (2000). Variedadesgemológicas de quartzoem Minas Gerais: geologia, mineralogia, causas de cor, técnicas de tratamento e aspectosmercadológicos (Dissertação de Mestrado). Universidade Federal de Minas Gerais.

GIA (2022). Top 5 Most Recognisable Gemstone Inclusions For Gemmologists. Retrieved from The Gemmological Association of Great Britain | Gem-A website: https://gem-a.com/gem-hub/top-5-most-recognisable-gemstone-inclusions-for-gemmologists/

Maneta, V., & Voudouris, P. (2010). QUARTZ MEGACRYSTS IN GREECE: MINERALOGY AND ENVIRONMENT OF FORMATION. Bulletin of the Geological Society of Greece, 43(2), pp.685-696. https://doi.org/10.12681/bgsg.11231

Voudouris P, Katerinopoulos A, Melfos V (2004) Alpine-type fissure minerals in Greece. Documenta Naturae 151, pp.23-45

Voudouris, P., Mavrogonatos, C., Graham, I., Giuliani, G., Tarantola, A., Melfos, V., Karampelas, S., Katerinopoulos, A.,Magganas, A. (2019). Gemstones of Greece: Geology and Crystallizing Environments. Minerals 9(8), p.461, https://doi.org/10.3390/min9080461

Roedder, E. (1984). Fluid inclusions. Reviews in Mineralogy (Vol. 12, p. 644; P. H. Ribbe, Ed.). Mineralogical Society of America.

BULLETIN OF THE GEOLOGICAL SOCIETY OF GREECE, SP. PUBL.

EXTENDED ABSTRACT 026

The UNESCO Global Geopark of Lavreotiki: a pillar for climate change adaptation & the example of sustainable water use, Greece

Barsaki V.[1], Michailidou Ir.2, Peppa F.[2], Kerdela G.[2] & Moraiti E.[1]
(1) Lavreotiki UNESCO Geopark, 1 Koundouriotou Str., 19500 Lavrion, Attica, Greece. e-mail: vasilikibarsaki@gmail.com
(2) Lavrion Environmental Center, L.T.C.P., 19500, Lavrion.

Introduction

UNESCO Global Geoparks are geographically defined areas that combine monuments of significant geological value with elements of ecological, cultural, and aesthetic importance. They are managed with a holistic approach to protection, education, and sustainable development. They are ideal destinations that support local communities and serve the 17 goals of the United Nations' Green Agenda in various ways.

Education in the frame of a UNESCO Global Geopark

One of the main axes of action for geoparks is Education. UNESCO Global Geoparks implement educational programs based on the geodiversity and biodiversity they host. Through collaborative partnerships, they educate and prepare societies for new, modern challenges. Geosites function as experiential laboratories, welcoming students, educators, and visitors to offer them unique experiences.

A good practice of such actions, aimed at preparing societies to tackle the climate crisis and adapt to new conditions, are the workshops for educators organized by the Lavreotiki UGGp in collaboration with the Lavrion Environmental Center (KEPEA) and/or other educational institutions active in the area. These workshops are often organized in the frame of the celebration of an established World Day.

Figure 1. Workshops for teachers and educators within the Lavreotiki UGGp.

The geosites of the Lavreotiki Geopark play a leading role during the workshops, offering stimuli and many opportunities for exploration and interaction with the environment, engaging and inspiring teachers and educators. In the field, the participant does not remain a mere spectator but experiences a rich learning experience. The Lavreotiki Geopark boasts numerous geosites that demonstrate the different environments (terrestrial, lacustrine, marine) that have developed in the territory and record climate changes over geological time, along with the impact on the palaeoenvironment, the societies and the living organisms. Among the notable geosites, are the lacustrine deposits of the "Alogari" hill, the submerged paleo-coasts along the geopark's coastline (such as the submerged port of Thorikos) and the karstic geomorphs of Kaki Thalassa.

Figure 2. Lavreotiki UGGp's geosites: Left: the lacustrine deposits of Alogari hill. Middle: karstic geomorphs of Kaki Thalassa. Right: submerged port of Thorikos.

However, the monuments that make Lavreotiki UNESCO Global Geopark unique in the world, except for its geological heritage and geodiversity, are the sites of mining heritage. The installations of the ancient Greeks for mining and metallurgy represent a perfectly designed infrastructure, harmonized with the climatic conditions of the time.

In antiquity, similar to the present time, Lavreotiki was an arid area with limited water resources but significant water needs. In ancient societies, water covered the biological needs of people, the needs for cultivating the land and raising animals, while large quantities were needed in mining and metallurgy. Given the large industrial zones that had developed in Lavreotiki (for the collection and processing of the ore deposits), the presence of water was of crucial importance. The ancient Greeks had addressed the high demand with innovative methods of water recycling and reuse for the time.

A characteristic example of such a mining heritage monument is the geosite named *"Souriza valley,"* located in the National Park of Sounion. It is the most representative site of ancient mining and metallurgical activity in the geopark, which gave birth to an unparalleled civilization. The entire area (now a declared archaeological site) hosts numerous mining galleries and metallurgical workshops, as well as other facilities for housing miners. Mining and metallurgical work followed a specific practical process, related to the type of extracted product, the depth of the deposits, and the necessary processing and subsequent smelting for the extraction of argentiferous lead. With the development of technology, mining and metallurgical practices improved relatively, and more productive technological installations were invented (Morin, D. *et al*., 2021). As a result, the entire ore-bearing land of Souriza became a vast working area. Today, many of the ore enrichment workshops are very well preserved. The working areas included ore crushing and grinding areas, a washing plant, storage areas for processed ore and concentrate, and one or more water tanks for the operation of the washing plants (Konofagos *et al*., 1970; Papadimitriou, 2017).

Figure 3. Aerial photo of the "Souriza valley" – mining and metallurgy center.

Water management was very well studied. The washing plant installations were developed within the valleys to utilize rainwater runoff from the slopes. Given the lack of atmospheric precipitation, the main concern of the ancient metallurgists was to prevent water loss, which was essential for the operation of the washing plants. For this reason, the internal surfaces of the rainwater tanks, as well as the washing plants and pipelines, were lined with a special hydraulic mortar (Meimaroglou *et al*., 2023).

Case study: World Water Day - sustainable water use

In the context of celebrating World Water Day (on 22nd March each year), the Lavrion Environmental Center, with the participation of the Lavreotiki Geopark, organizes a workshop for all educators, including a 3hours visit to the "Souriza valley" geosite. The main thematic units of the workshop are:

- The importance and use of water in modern societies.
- The importance and use of water in antiquity.
- The journey of water through geological time in the Lavreotiki UNESCO Global Geopark.
- Sustainable management of water, the example of water recycling – the ancient mining center of "Souriza valley".
- Modern challenges in the era of the climate crisis.

The role of the Lavreotiki UGGp

The Lavreotiki geopark hosts geosites that narrate impressive changes related to the distribution of water on the Earth's surface over geological time. From sea-level changes during the Quaternary period to the ancient lakes that existed during the Miocene era and the changes in the hydrological basins of its streams (Pavlopoulos, 1992 & Vasileiou, 2010), the participants of the workshop can understand how significant changes occur on the land we inhabit, cultivate, and exploit. A characteristic example is the ancient Greeks and their efficient water management, as evidenced by the archaeological/mining findings in the Souriza Valley. During the seminar, the aforementioned data are presented, emphasizing the importance of adapting to climate changes and the sustainable management of Earth's resources.

Results

The participation of educators is always high, and they fulfil the program with great interest. Upon completion of the workshop, an evaluation process follows. The table below presents the statistical results of the last workshop (year 2024).

Table 1. Indicative statistical results of the workshop's evaluation form.

No of applications	Hosting capability (No of participants)	No of participants	gender		Evaluation of the workshop		Comments for improvement
			male	female	Satisfied	Not satisfied	
95	20-60	62	19	43	62	-	Longer duration / recurrence

Workshops, such as the latter study case, that offer educators modern scientific knowledge, new perspectives in fundamental issues, such as the sustainable use of water and present free educational tools, enhance school communities and the next generations. Meaningful partnerships, such as the example between the Lavrion Environmental Center and the Lavreotiki UGGp, represent good practices for the adaptation and sustainability of local communities in the era of the climate crisis. They cultivate interdisciplinarity and communicate science and universal values, such as cooperation, respect, inclusion, and quality education, to the general public. These values are included and promoted by the United Nations Sustainable Development Goals (such as SDG 4, SDG 11, SDG 12, SDG 13, and SDG 17).

Figure 1. The SDG's promoted through this educational action of the Lavreotiki UGGp and the Lavrion Environmental Center.

References

Papadimitriou, G., 2017. Ore washeries and water cisterns in the mines of Laurion-Attica. In: Wellbrock, K. (ed.): Schriften der Deutschen Wasserhistorischen Gesell-schaft, Band 27-2, Siegburg, 2017, 395-416.

Konofagos, K., Musshe H., 1970. The helical ore washeries of the ancient Greeks in Lavrion. A lost ancient Greek invention. Transactions of the Academy of Athens, 29.

Meimaroglou, N., Mouzakis, Ch., Kalagri, A. & Kapetanios, A., 2023. Earthen and hydraulic mortars used at Lavrion during classical antiquity (5th-4th century B.C.). A fundamental relationship between earthen building tradition and sophisticated hydraulic binders and concrete. 10.46586/DBM.264.

Morin, D., Herbach, R. & Rosenthal, P. 2021. The Laurion shafts, Greece: ventilation systems and mining technology in antiquity. Historical Metallurgy, 46(1), pp. 9–18.

Pavlopoulos, K., 1992. The geomorphological evolution of South Attica. Athens: PhD Thesis. National and Kapodistrian University of Athens.

Vasileiou, A., 2010. Relief analysis and geotectonic structure of Eastern Attica. Athens: PhD Thesis. Agricultural University of Athens.

17th INTERNATIONAL CONGRESS of the Geological Society of Greece

BULLETIN OF THE GEOLOGICAL SOCIETY OF GREECE, SP. PUBL.

EXTENDED ABSTRACT 027

The world class geodiversity of the Lavreotiki UNESCO Global Geopark's minerals, Lavreotiki Municipality, Greece

Barsaki V.[1], Voudouris P.[2] & Moraiti E.[1]

(1) Lavreotiki UNESCO Geopark, 1 Koundouriotou str., 19500 Lavrion, Attica, Greece. e-mail: vasilikibarsaki@gmail.com

(2) Faculty of Geology and Geoenvironment NKUA, University Campus, Zografou, 15784 Attica, Greece.

Lavreotiki UGGp mineralization

The Lavreotiki Geopark occupies the area where both hypogene and supergene processes created an amazing underground world, decorated with an exquisite variety of minerals of international recognition and value. Its mineralization is unique and of high geodiversity, as the territory contains 748 naturally occurring mineral species, the most of any other district in the world (Rieck, 2024; https://www.mindat.org/loc-1942.html). From about 10 to 7 million years ago, massive tectonic movements along the so-called "Western Cycladic Detachment System", accommodated magma emplacement, and facilitated hydrothermal fluid circulation and ore deposition within permeable lithologies. These processes in combination with subsequent supergene oxidation of the ores, gave birth to one of the most important, historically and economically, polymetallic deposits in the world exploited by the Ancient Greeks and during the modern times (Voudouris *et al.*, 2008; Boshall *et al.*, 2011; Ross *et al.*, 2021).

The mining and metallurgical industry, developed in antiquity -which triggered the cultural and economic development of the city-state of Athens, as well as its hegemonic role in classical times- has gained worldwide scientific interest. Essential questions concerning the mining of ores and their processing remain unresolved (Conophagos, 1980).

Geodiversity

- 5 different types of mineralization are present in the geopark's ore deposits.
- The Lavreotiki UGGp hosts some of the best mineral specimens in the world.
- It hosts the biggest collection of the most impressive pseudomorphs.
- 60 chemical elements of the periodic table are presented in the geopark's ore deposits.
- The extended and ongoing oxidation of the primary ore resulted in the formation of one of the best developed oxidation zones on Earth (up to 270 m thick).
- 25 Type Locality (TL) minerals.
- Slag minerals (150 valid mineral species and 7 Type Locality Minerals).
- The Lavreotiki UGGp is included in the top ten areas, worldwide, with the highest variety in minerals.

Figure 1. Left: Hilarionite FOV: 3mm, right: Agardite-[Nd] FOV: 3mm, (copyright Toth Lazlo).

The TL mineral list of the Lavreotiki UGGp

The geopark hosts ten geosites (ancient and modern mining galleries), where 25 minerals have been identified for the first time worldwide and are included in the International Mineralogical Association's list of Type-locality minerals (IMA list) (Pekov *et al*., 2011; Voudouris *et al.*, 2021; Rieck, 2024). The localities belong to the most impressive and probably the most unique labyrinth mining centers in the world.

Table 1. List of the Type – locality minerals from the Lavreotiki UGGp.

Mineral	Formula	Mining gallery
Agardite – (Nd)	$NdCu(AsO_4)_3(OH)_6 \cdot 3H_2O$	Hilarion 50
Attikaite	$Ca_3Cu_2Al_2(AsO_4)_4(OH)_4 \cdot 2H_2O$	Christiana 132
Drobecite	$CdSO_4 \cdot 4H_2O$	Esperanza
Fabrizite	$Zn_9(SO_4)(OH)_{12}Cl_2 \cdot 6H_2O$	Hilarion
Glaucocerinite	$(Zn_{1-x}Al_x)(OH)_2(SO_4)_{x/2} \cdot nH_2O$	Serpieri
Hilarionite	$Fe^{3+}_2(SO_4)AsO_4)(OH) \cdot 6H_2O$	Hilarion 50
Kamarizaite	$Fe^{3+}_3(AsO_4)_2(OH)_3 \cdot 3H_2O$	Kamariza
Kapellasite	$Cu_3Zn(OH)_6Cl_2$	Sounion 19
Katerinopoulosite	$(NH_4)Zn(SO_4)_2 \cdot 6H_2O$	Esperanza
Katsarosite	$Zn(C_2O_4) \cdot 2H_2O$	Esperanza
Ktenasite	$ZnCu_4(SO_4)_2(OH)_6 \cdot 6H_2O$	Jean Baptiste
Laurionite	$PbCl(OH)$	Kamariza
Lazaridisite	$Cd_3(SO_4)_3 \cdot 8H_2O$	Esperanza
Mereiterite	$K_2Fe(SO_4)_2 \cdot 4H_2O$	Hilarion 50
Natroglaucocerinite	$[Zn_5Al_3(OH)_{16}][(SO_4)_{1.5}Na_{1.5}(SO_4)_{0.75}(H_2O)_9]$	Hilarion
Nickeltsumcorite	$Pb(Ni,Fe^{3+})_2(AsO_4)_2(H_2O,OH)_2$	"km3"
Niedermayrite	$CdCu(SO_4)_2(OH)_6 \cdot 4H_2O$	Esperanza
Pracharite	$CaSb^{5+}_2(As^{3+}_2O_5)_2O_2 \cdot 10H_2O$	Plaka 80
Serpierite	$Ca(Cu,Zn)_4(SO_4)_2(OH)_6 \cdot 3H_2O$	Serpieri
Stergiouite	$CaZn_2(AsO_4)_2 \cdot 4H_2O$	Plaka 80
Voudourisite	$Cd(SO_4) \cdot H_2O$	Esperanza
Tzeferisite	$CaZn_8(SO_4)_2(OH)_{12}Cl_2(H_2O)_9$	Damianos
Zincaluminite	$Zn_6Al_6(SO_4)_2(OH)_{16} \cdot 5H_2O$	Hilarion
Zincolivenite	$CuZn(AsO_4)(OH)$	Kamariza
Zincowoodwardite	$[Zn_{1-x}Al_x(OH_2][(SO_4)_{x/2} \cdot n(H_2O)]$	Christiana

Lavreotiki Geopark's geological heritage contains geosites of international value, most of them representing its amazing underground world. In particular, the geopark hosts ten ancient and modern mining galleries, all branches of the following three mining centers, Plaka, Agios Konstantinos (Kamariza) and Sounion center. The geopark maintains a geodatabase concerning its minerals of international value and the labyrinth mining centers, constantly enriched with the latest scientific discoveries and the corresponding localities.

Acknowledgements

Special thanks to Dr. Karl Heinz Fabritz, Dr Uwe Kolitch and Dr Branko Rieck for their research and offer to the Lavreotiki UGGp.

References

Bonsall, T.A., Spry, P.G., Voudouris, P., Tombros, S., Seymour, K., Melfos, V. 2011. The Geochemistry of Carbonate-Replacement Pb-Zn-Ag Mineralization in the Lavrion District, Attica, Greece: Fluid Inclusion, Stable Isotope, and Rare Earth Element Studies. Economic Geology, 106, 619–651.

Conophagos C. (1980). The Lavrion and the ancient Greek techniques for silver production. Athens, Ekdotiki Athinion, 458 p.

Pekov, I.V., Chukanov, N.V., Zadov, A.E., Voudouris, P., Magganas, A., Katerinopoulos, A., 2011. Agardite-(Nd) NdCu6(AsO4)3(OH)6.3H2O from the Hilarion Mine, Lavrion, Greece: Mineral description and chemical

relations with other members of the agardite-zálesiite solid-solution system. Journal of GEOsciences 57, 249-255.

Rieck B. (2024) Lavrion Mining District, Lavreotiki, East Attica, Attica, Greece, https://www.mindat.org/loc-1942.html

Ross, J., Voudouris, P., Melfos, V., Vaxevanopoulos, M., Soukis, K., Merigot, K. 2021. The Lavrion silver district: Reassessing its ancient mining history. Geoarchaeology, 36(4), 617-642.

Voudouris, P., Melfos, V., Spry, P.G., Bonsall, T.A., Tarkian, M., Solomos, Ch., 2008. Carbonate-replacement Pb-Zn-Ag±Au mineralization in the Kamariza area, Lavrion, Greece: Mineralogy and thermochemical conditions of formation. Mineralogy and Petrology, 94, 85-106.

Voudouris, P., Melfos, M., Mavrogonatos, C., Photiades, A., Moraiti, E., Rieck, B., Kolitsch, U., Tarantola, A., Scheffer, C., Morin, D., Vanderhaeghe, O., Spry, P.G., Ross, J., Soukis, K., Vaxevanopoulos, M., Pekov, I.V., Chukanov, N.V., Magganas, A., Kati, M., Katerinopoulos, A., Zaimis, S., 2021. The Lavrion mines: a unique site of geological and mineralogical heritage, Minerals, 11, 76, https://doi.org/10.3390/min11010076

17th INTERNATIONAL CONGRESS of the Geological Society of Greece

BULLETIN OF THE GEOLOGICAL SOCIETY OF GREECE, SP. PUBL.

EXTENDED ABSTRACT 028

Highlighting the Geological Heritage of the Island of Kythira, Greece

Barsaki V.[1], PhD. Zananiri I.[1]& Moraiti E.[1]
(1) Hellenic Survey of Geology and Mineral Exploration (HSGME), Acharnes, Greece, email: vmparsaki@eagme.gr, vasilikibarsaki@gmail.com

Introduction

The geological heritage of a country consists of sites that reflect its geological history. Geosites are locations where the historical record of the Earth is preserved and testify to its long-term evolution, as well as areas where contemporary planetary processes are recorded. Geological heritage combined with biodiversity constitutes the natural heritage of a territory, describes its unique identity and should be protected for the benefit of present and future generations.

To achieve these goals, in the frame of the "GEOINFRA" project ("Geological Mapping of Greece for the support of innovation and entrepreneurship"), Work package 5 "Documentation of Geosites and Geotrails, Geopark studies" (NSRF 2014-2020/2023), the Hellenic Survey of Geology and Mineral Exploration selected Kythira Island for recording and promoting its geological heritage. Due to its geographical and geotectonic setting, lying in the convergence of two tectonic plates in the southwestern part of the South Aegean Hellenic Arc and between the Ionian and the Aegean Sea, Kythira boasts significant geological, geomorphological and paleontological wealth. Tectonic structures, fossils, gorges, caves, coastal geoforms and rocks await visitors to narrate their own stories and myths.

Geography – geomorphology

Kythira island, located between Peloponnese and Crete along the Hellenic island arc, spans over an area of 280 km^2. The climate is characterized as "Mediterranean", with high relative humidity and strong winds mainly in winter. The dominant relief is semi-mountainous with deep valleys and a maximum altitude of 507 meters (Mermigaris Mount). A smooth plateau exists along the central part of the territory with a few arable zones. The coastline has a length of approximately 52 km and forms many pocket beaches, while the rugged coastal terrain is the combined result of tectonics and lithology along with the significant wave energy, shaping its shores into steep rocky cliffs with deep bays (Gaki *et al*., 2011).

Geology

The geological structure of the island of Kythira constitutes post-Alpine formations, the Pindos Unit overlying the Tripolis Unit and a metamorphic crystalline basement. The latter is highly folded and occupies the northern part of the island. Tripolis Unit and its carbonate rocks form the elongated mountain masses in the eastern and western part of the island; especially in the west limestones reach sea level, creating abrupt cliffs due to offshore faults. Pindos Unit domains are mainly located in the central and southern part of the island. The Neogene sediments extend mainly in the south and are primarily marine with intercalations of fluvial and lacustrine deposits. The latter are composed of sandstones, marls, marly limestones and conglomerates of transgressive (at the top) and regressive (at the bottom) origin. Concerning the tectonics of Kythira, an older pre-Alpine phase of ENE-WSW direction can be distinguished, which folded the metamorphic crystalline basement, followed by an Alpine phase responsible for the folding and faulting of the Tripolis and Pindos Units. Post-Alpine tectonism with NNW-SSE trending faults formed the modern terrain of grabens and horsts. Today, extensional tectonism has resulted in the ongoing uplift of the island and the recording of many catastrophic earthquakes (Lyberis *et al*., 1982).

The geological heritage of Kythira Island

The island of Kythira hosts a geological heritage of national significance. Lying in the convergence of two tectonic plates, next to the orogenic arc of East Mediterranean Sea, the island has been uplifted for millions of years. Kythira rise from the sea and the elements of this movement are reflected in its rocks, relief, and coastlines; ancient Greeks associated these movements with the birth of goddess Aphrodite and her emergence from the sea foam. During the Alpine Orogeny the rocks comprising Kythira's surface, were deformed, folded, and displaced due to the presence of

large-scale fault surfaces (Danamos, 1992 & Marsellos, 2008). Complex processes, accompanied by intense seismic activity, caused significant changes in the paleoenvironment, forming lakes or shallow seas, which are evidenced by the palaeontological findings across the island, e.g. the Mitata settlement (Bartsokas, 1998). The contemporary processes of the Earth sculpt the surface of Kythira and create landscapes of natural beauty and rarity that enrich the nine (9) thematic geotrails designated in the framework of the GEOINFRA project. More than one hundred geosites were recorded and classified in 14 different main categories (fig.1), according to their predominant geological features (Drandaki, 2009 & Moraiti, 2016).

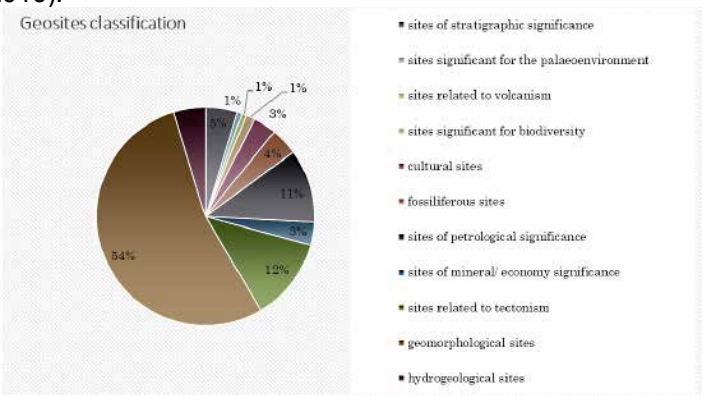

Figure 1. Classification diagram of the geosites recorded at Kythira Island, in the framework of GEOINFRA project.

The marine terraces of Platia Ammos, the oldest rocks of Kythira forming the pre-alpine basement (fig.2), the gorge of Kakia Lagada, Lykodimos beach, the cave of Agia Sophia in Mylopotamos hosting fossils of rudists and fault mirrors forming an impressive steep cliffed coast (fig.3), Kaladi beach, the marine cave on Chytra islet and the thanatocoenosis of lamellibranchia at Mitata (fig.4) are some examples of the most representative sites defining the core of Kythira's geodiversity.

Figure 2. Left: marine terraces at Platia Ammos beach, middle: regressive conglomerates at Platia Ammos beach and right: the oldest rocks of Kythira Island (pre-alpine basement).

Figure 3. Left: Kaki Lagada gorge, middle: Lykodimos beach, a cliffy coast of high aesthetic value depicting, in the left photo, the earth's modern processes and a record of tens of millions of years, while hosting the most impressive isoclinal folded limestones on Kythira Island as shown in the next photoand right: rudist limestones at Agia Sophia cave of Mylopotamos settlement.

Figure 4. Left: Kaladi beach hosting a tombolo/ coastal geoform, middle: marine cave of Chytra islet and right: thanatocoenosis of lamellibranchia at the Mitata suburbs.

Geotourism of Kythira

Geotourism is a mild form of tourism that has been rising during the last decades, especially in Europe (Ólafsdóttir, 2019). In the scope of promoting the geoheritage of Kythira, nine (9) geotrails were designated, connecting attractions of geological, archaeological, historical, cultural, environmental, and religious significance, as well as sites important for biodiversity, aiming to narrate the story of a destination in a holistic way. They were designed either to follow geographical boundaries or to support specific themes and have varying levels of difficulty, while one is a marine route visited solely by boat. During the designation of the trails specific safety specifications for travellers were followed, based on international and national standards

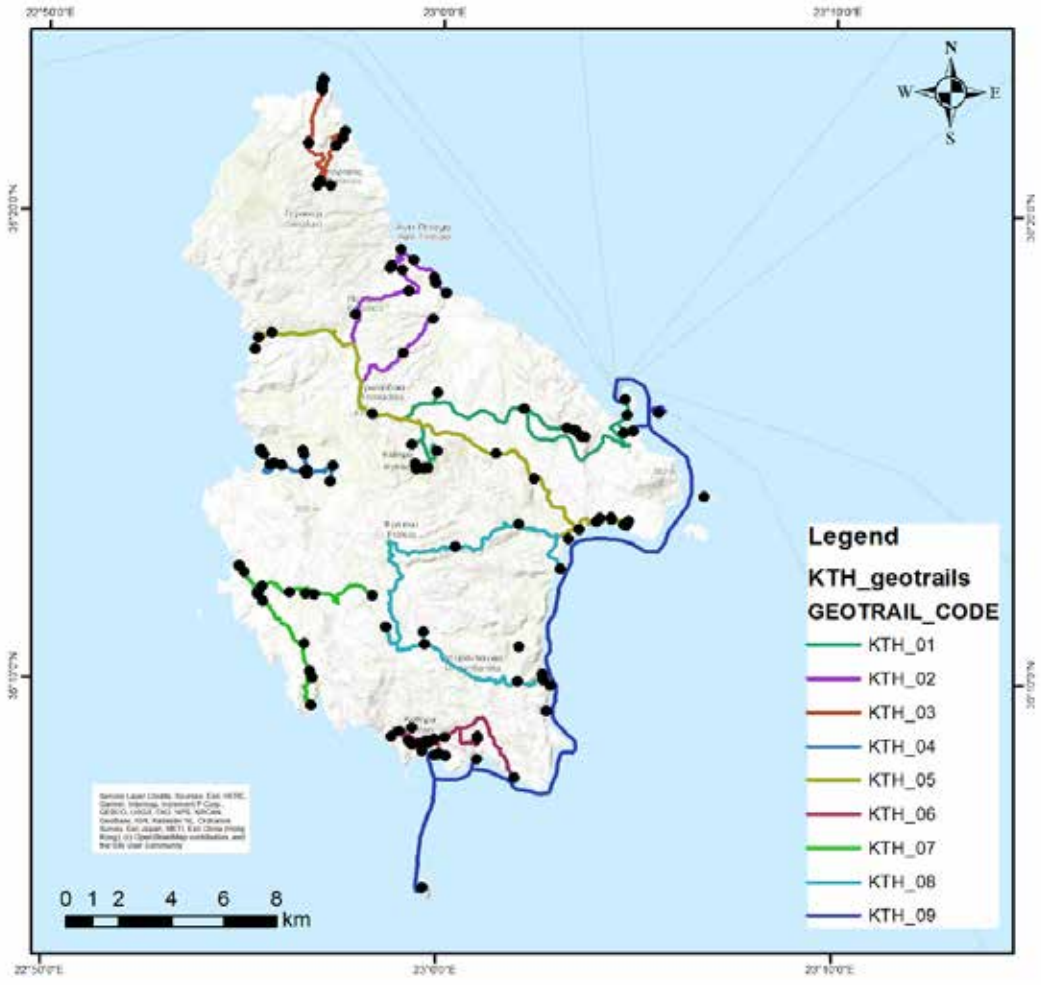

Figure 5. Mapped geotrails of Kythira Island.

Table 1. Presentation of the designed geotrails of Kythira Island.

Code	Name	Descriptive name	Short description	Nr of sites
KTH_01	Diakofti - Mitata	Discovering Kythira	This pleasant and scenic trail starts from the port of Kythira in Diakofti, where visitors first arrive, and ends inland, in the settlement of Mitata. From the first stops, the unique character of Kythira and the main geological features that have contributed to the creation of the island's identity are revealed. At the same time, one observes the dynamic relationship between humans and their natural environment over time and meets the living world of both the modern era and the geological past.	20
KTH_02	Palaiochora - Kaki Lagada	The gorge of the pirates	Linked to the raid of the pirate Barbarossa and the destruction of the Palaiochora Castle, this trail travels us through landscapes of exceptional natural beauty and picturesque settlements of another era, highlighting both modern processes of nature, as well as processes of millions of years that are still active and shape the unique biodiversity and geodiversity of Kythira.	14
KTH_03	Moudari - Karavas - Platia Ammos	Kythira from a different viewpoint	The geotrail starts from Cape Spathi, the northernmost point of Kythira, with its imposing monuments, the geological formations and landforms that compose a familiar landscape for the visitor. Soon the scenery changes and the trail lead us through rocks that do not resemble any other rock of the territory, narrating their own story. These are the most ancient rocks on the island, which today, 350 million years later, lie on the surface.	16
KTH_04	Arei - Mylopotamos - St. Sofia Cave	Unique landscapes	This geotrail of unique natural beauty starts from the traditional settlements of Arei and Mylopotamos, with its picturesque alleys and churches and elaborate bell towers. The valley of the watermills is an important attraction of the island, where nature and man mix in a unique way. The geotrail leads to the castle of Kato Chora and its amazing panoramic view and ends at the cave of Agia Sophia Mylopotamos. The cave hosts impressive speleothems and ecclesiastical elements of high value, while outdoors the scenery is comprised of fossilized limestones, hosting numerous marine organisms, such as rudists (~65 million years old).	16
KTH_05	Avlemonas - Paleopoli - Fratsia - Aroniadika - Lykodimos beach	Contrasts	Starting from the eastern shore of the island and its diverse beaches, the geotrail crosses the Paleopolis basin with its significant archaeological and palaeontological findings and through small, traditional settlements, ends up at the western coastline of the island. Lykodimos beach combines a landscape of wild and rare beauty, hosting steep cliffs, the most impressive isoclinal folds and unique coastal geoforms, remnants of the timeless struggle between the exogenous and endogenous forces of nature.	19
KTH_06	Agia Elessa - Chora (Kythira) - Kalamos - Chalkos beach	Geology and culture	This geotrail highlights the geological and cultural attractions of the capital city of Kythira. Over the centuries, the island has been a crossroad of cultures, mainly due to its geographical location and the many conquerors who controlled the territory during different eras. Visits to the museums of Chora provide reach information on the long history and the identity of the island. Along the geotrail the geology intertwining with man offers beautiful geosites, revealing interesting stories.	16

KTH_07	Keramoti - Kalokerines - Limnaria - Melidoni	Wild nature	This geotrail crosses the western part of Kythira, offering visitors the possibility to wander around rocky landscapes, next to the highest mountain peaks of the territory. The mountainous mass of Agia Elessa, with the homonymous monastery, at an altitude of 476m, owes its formation to a large tectonic structure, perhaps the largest mapped on the island, extending for several kilometres. Heading to Limnaria beach, the type locality of the wildflower *Limonium aphrodita sp.*, the trail crosses "Tyros layers", a geological formation only seen here. The tour ends at Melidoni beach, with an amazing view of the Chytra islet.	15
KTH_08	Kaladi - Agios Ilias - Livadi - Fyri Ammos	Landscapes and colours	The geotrail connects two enchanting destinations on the eastern coasts of the island, Kaladi beach and Fyri Ammos Livadi beach. These are the two most famous beaches of Kythira, where visitors can enjoy the sun and sea in a riot of colours. The geological formations create unique landscapes, with impressive coastal geoforms, alternating with white, red, and yellow rocks, giving the waters turquoise and deep blue hues. Modern earth processes sculpt the relief, and landslide phenomena dominate. Almost the entire trail passes through rocks that formed millions of years ago in a deep ocean, and many Byzantine chapels. Fields with shrub vegetation, and olive groves dominate.	17
KTH_09	Kapsali - Diakofti	...from the sea	This marine geotrail starts from the port of Kapsali. After visiting the islet of Chytra, with the impressive sea cave and its unique biodiversity, hosting the *Sempreviva sp.*, the flower of Paris and beautiful Helen, traverses the coastline of Kythira back to the port. It offers alternative, memorable experiences, allowing visitors either to reach some inaccessible beaches or admire the island's most famous ones by sea. The last attraction is the "Nordland" shipwreck at Diakofti beach, an ideal destination for divers.	20

Geotouristic products designed for Kythira Island in the frame of GEOINFRA project

A total of 150 sites of geological interest were recorded, processed and evaluated, while data concerning the island's biodiversity, cultural heritage and history were collected and enriched the HSGME's geodatabase. The project's outcomes concerning Kythira included:

- 9 mapped geotrails
- 18 interpretation panels for 9 different areas of geological interest, in Greek and English
- 1 mobile application
- 1 geotouristic guide entitled "Kythira"
- 1 ESRI story map entitled "Geotourism in Kythira Island".

Figure 6. Examples of the interpretation panels designed by the HSGME for the promotion of geotourism in Kythira Island.

Acknowledgements

This project was funded by the National Strategic Reference Framework (NSRF), 2014-2020/2023, grant number 5030010 ("Geological Mapping of Greece for the support of innovation and entrepreneurship—GEOINFRA").

References

Bartsokas A., 1998. Palaeontology of Kythira. Kythira Society of Studies Publications.

Danamos G., 1992. Contribution to the geology and hydrogeology of Kythira Island (Greece). Faculty of Geology, School of Science. Ph.D. Thesis, National and Kapodistrian University of Athens, 355p.

Drandaki I., 2009. 3rd C.S.F. Project: Geosites – Geoparks, contribution to sustainable development. IGME Publications (in Greek), pp 40.

Gaki-Papanastassiou K., Maroukian H. & Kourmpanian V., 2011. The morphotectonic evolution of southern half of Kythira Island (Ionian Sea, Greece) during the Quaternary. "Prace Geograficzne", volume 127, p. 49–60.

Lyberis N., Angelier J., and Lallemant S., 1982, Active deformation of a segment of arc: The strait of Kythira, Hellenic arc, Greece, Journal of Structural Geology, 4(3), 299−311.

Marsellos A., 2008. Extension and Exhumation of the Hellenic Forearc Ridge in Kythera. E.S.F. Kidd, The Journal of Geology, volume 116, p. 640–651.

Moraiti E., 2016. A thorough report on the IGME database of geosites – geoparks. IGME Publications (in Greek), pp. 166.

Ólafsdóttir R., 2019. Geotourism. Geosciences, 9(1), 48.

17th INTERNATIONAL CONGRESS of the Geological Society of Greece

BULLETIN OF THE GEOLOGICAL SOCIETY OF GREECE, SP. PUBL.

EXTENDED ABSTRACT 029

Mapping the geo-hazard elements offshore the Ionian Islands (Western Greece)

D. Bartolozzi[1], S. Kothri[2], P. Nomikou[2], M.F. Loreto[3], A. Ganas[4], V. Ferrante[3], O. Kei[5], F. Balsamo[6], D. Lampridou[2], E. Nikoli[2], C. Ranero[7,8]

(1) Università degli Studi di Bologna – Facoltà di Geografia e processi territoriali, Italy
(2) Department of Geography and Climatology - National and Kapodistrian University of Athens (NKUA), Greece
(3) CNR, Istituto di Scienze Marine (ISMAR), Bologna, Italy
(4) Institute of Geodynamics - National Observatory of Athens (NOA), Greece
(5) Università degli Studi di Genova, Dipartimento di scienze della terra, dell'ambiente e della Vita (DISTAV), Italy
(6) University of Parma – Dip. di Scienze Chimiche, della Vita, e della Sostenibilità Ambientale
(7) Institució Catalana de Recerca i Estudis Avançats (ICREA), Barcelona, Spain
(8) Barcelona Center for Subsurface Imaging, ICM, CSIC, Barcelona, Spain

Introduction and objectives

The area offshore the central Ionian Islands (Cephalonia, Lefkada, Zakynthos, and Ithaca), western Greece, is considered as one with the highest seismic activity and tsunamigenic potential among the seismogenic Mediterranean regions. A series of destructive earthquakes, such as the 1953 events (Mw > 6.6; Stiros et al. 1994) that destroyed the island of Cephalonia and Zakynthos, or more recent events such as the 28 October 2018 Mw 6.8 Zakynthos (Ganas et al., 2020) affect the area and most of these have the epicentre located in the offshore. The earthquakes are due to plate convergence across the Ionian Sea, as Africa (Nubia) subducts beneath Peloponnese while a major right-lateral fault (the Cephalonia Transform Fault) transfers horizontal motion towards North where Adria (Apulia) subducts beneath Northwest Greece (Epirus) and Albania (Fig.1). However, a complete mapping and understanding of the all-geological risk elements affecting the offshore of the islands has not yet been produced to date. During recent surveys, carried out in June 2023 on board of the R/V Laura Bassi - the POSEIDON project supported by the Eurofleet+ program and in May 2022 on board of the R/V G. Dallaporta supported by the Italian CNR - IONIANS cruise carried out, a multiscale geophysical dataset has been collected together with sediment samples. The collection of such data was fundamental for our seabed interpretation and for the production of an accurate map of submarine geohazards in this area.

Method

The morphological interpretation is based on TOPAS seismic profiles, EMODNET bathymetry and higher resolution bathymetric data collected in the frame of the POSEIDON 2023 project.

First, we geolocated and uploaded all seismic data on Kingdom software, which we used to view georeferenced seismic profiles and annotate visible morphologies of interest, such as faults, landslide bodies, gas and fluids trapped within sediments (Fig.2).

We then proceeded with the bathymetric interpretation of the seabed in Global Mapper software, which provides tools such as 3D models and 2D bathymetric profiles, through which we were able to locate and recognize several elements of interest (canyons, canyon heads, landslide scars, tectonic deformations etc.).

Finally, merging the seismic interpretation with the bathymetric one, we produced a map of all the morphologies that represent geohazards in the Ionian Island area (Fig. 3). The map was graphically refined using Adobe Illustrator.

The map of geohazards, produced using geophysical data, will be in a second step integrated with geological data obtained by sediments sampled with a gravity corer in a very deep basin (4220 m below sea level) offshore Zakynthos.

Results

The analysis of all available data, following the method above shortly described, allow us to map a series of morphological scarps bounding the western slope of Cephalonia and Lefkada. These scarps correspond with the shallow expression of the Cephalonia Transform Fault, which to the south is organized into a system of horseshoe-shaped faults that to the north merge into a single fault boarding the area off northern Cephalonia and the coast of Lefkada. The entire fault system results more than 120 km-long and, in the southern part, more than 20 km-wide (Fig. 3). We were also able to identify and map in high detail the seafloor displacement and the fault plane north of Lefkada by using Topas data.

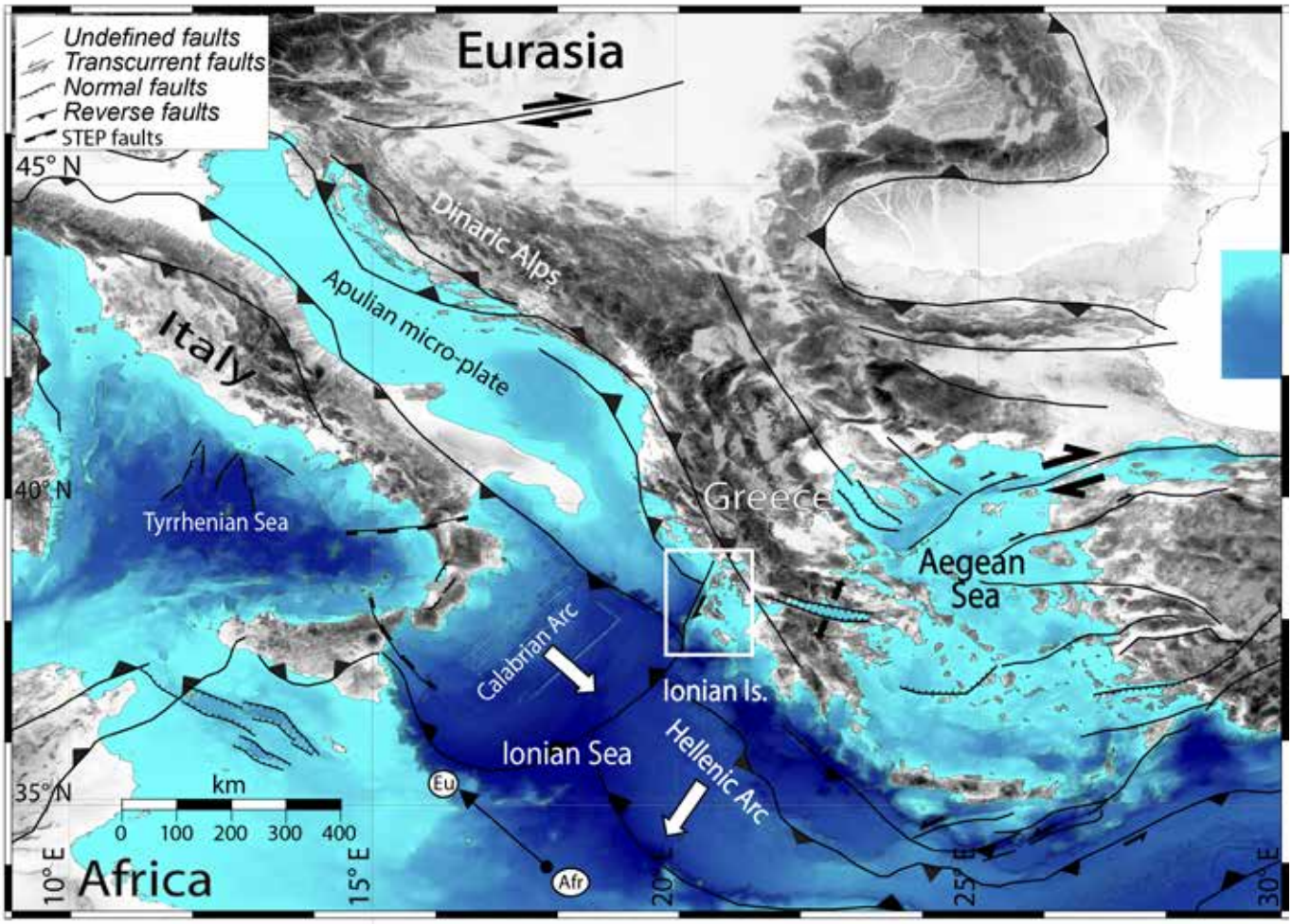

Figure 1. Tectonic map of the central Mediterranean with location of the study area (white box). Bathymetry data download from EMODnet portal https://emodnet.ec.europa.eu/en/bathymetry#bathymetryapproach) and gridded using GMT software (Wessel et al., 2019). Mediterranean structural sketch modified after an online Tectonic Map (Woudloper - Own work, CC BY-SA 1.0) and by Loreto et al., 2020. The Thick white arrows mark the migration of the active accretionary prisms; Black thick arrows mark the main cinematic of faults. Thin black arrow marks the convergence of Africa toward Eurasia. The map is represented in geographic coordinates on Mercator Projection.

A series of submarine channels and canyons have been mapped, most of them located off Lefkada and others along the slope of the elongated N-S ridge south of Cephalonia. Some of these channels

are interrupted or dislocated by the morphological scarp associated with the Cephalonia Fault System. Other canyons, but in smaller quantities, are found along the slope south of Zakynthos and west of the Peloponnese. Here, the numerous landslide scars that have been mapped show a regressive/erosive character. While south of Zakynthos there is a giant landslide with a scar more than 10 km-wide responsible for the intense erosion affecting the slope, which is further shaped by the presence of NE-SW oriented morphological scarps.

The internal basin, bounded by the Ionian Islands and Western Greece (Fig. 3), shows a few small randomly distributed ridges sometimes associated with evaporite upwelling other times associated with tectonic activity. However, the most interesting finding in this basin are the several huge landslides or body collapses buried under recent, Holocene, sediments. These landslide bodies are characterized by great internal chaos and intense gas/fluid release capable of deforming the overlying well-stratified sediments. Several gas/fluid upwellings have also been recorded in the sea strip between Cephalonia and Ithaca (Fig. 2), where they remain trapped under a well-identifiable layer, probably characterized by a lithology with low permeability.

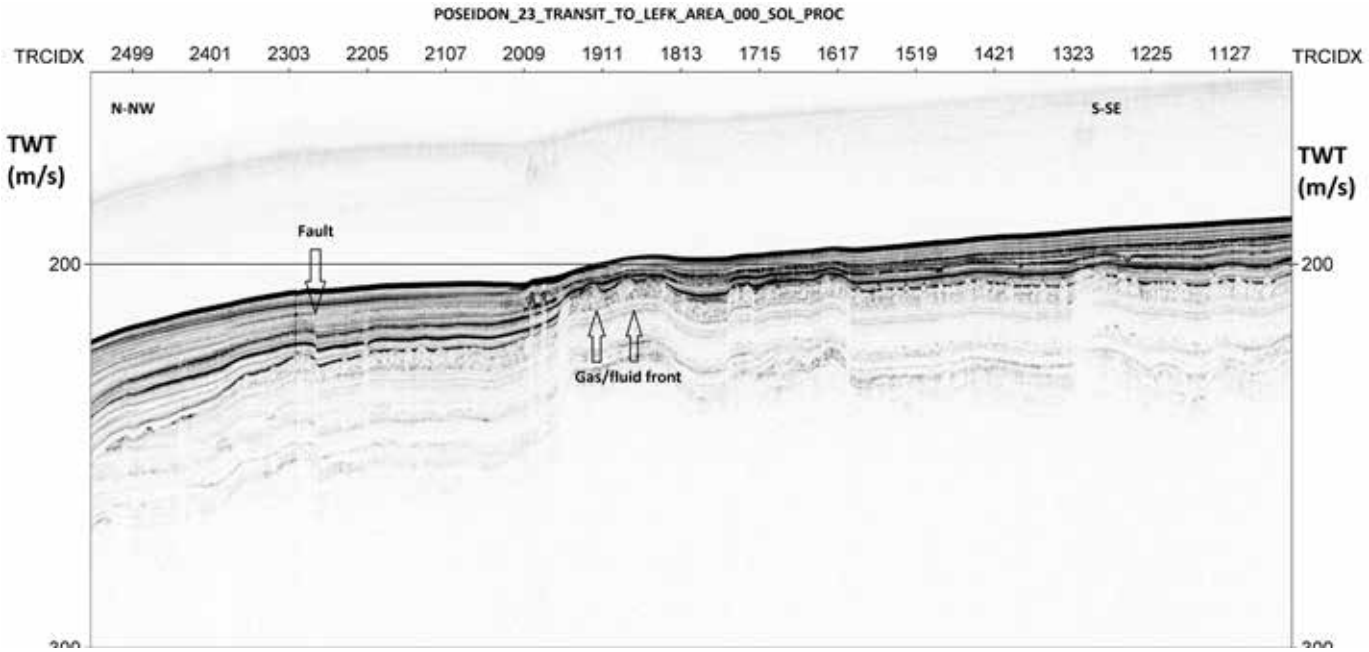

Figure 2. Section of a Chirp profile from data collected during POSEIDON 2023 oceanographic cruise. The fault highlighted on the left is recognizable because of the horizons' offset, while the gas/fluid bubbles can be identified because of whitening effect and of deformation they cause on the host layer.

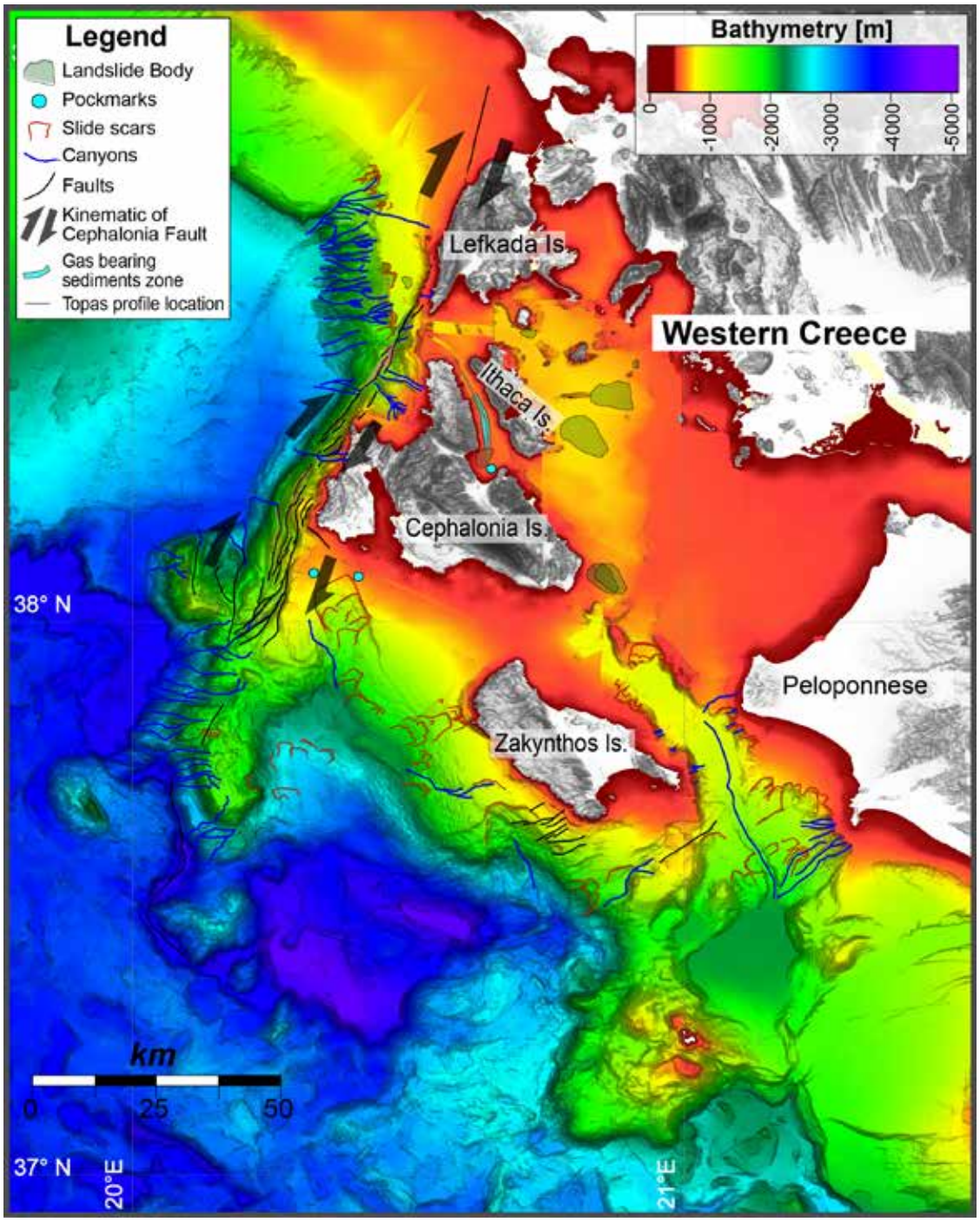

Figure 3. Morpho-bathymetric map of the Ionian Islands (Western Greece) showing the mapped morphological elements that can be associated with the geological hazard of the area. The most relevant hazard elements are represented by the Cephalonia Fault System, which delimits the western side of the islands of Cephalonia and Lefkada, and by the numerous locally large landslides that erode mainly the southern margin of Zakynthos and the Peloponnese. Furthermore, some canyon heads erode sediments very close the coastal line. Some pockmarks have also been mapped, witnessing the abundant gas that fills the shallow sediments. The bathymetry is a combination between EMODnet data (https://emodnet.ec.europa.eu /en/ bathymetry#bathymetry-approach) and the newly collected data during the Poseidon cruise.

Discussion

Based on the method described above, a map of the morphological features associated with geohazards in the offshore area of the Ionian Islands has been produced (Fig. 3). Based on this map, the area can be divided into two main zones: 1) the Kefalonia Transform Fault (CTF) zone and 2) the zone surrounding the island of Zakynthos.

The CTF zone is characterized by a steep slope (with maximum inclination of ca. 44° or 97%) shaped by a series of incisions that delimit small sigmoidal ridges, area south of Cephalonia (Fig. 3). The sigmoidal morphology has been associated with a series of positive flower-like structures bounded by strike-slip faults with a reverse component (Loreto et al., under review). The Cephalonia system becomes very broad to the south and deforms both sediments and rocks (Pre-Apulian unit), resulting in a 25 km-wide deformed area. West of Lefkada, the fault system changes its behavior becoming a single incision associated with a very well-defined morphological scarp (Fig. 3). Furthermore, this area is strongly incised by numerous channels and canyons, some of which are interrupted against the CTF system, others less evident are displaced by the CTF and where it has been possible to do the measurements the dislocation is approximately 500 m. The group of channels and canyons that are located to the north are set along a slope that delimits an anomalously deep plateau. This anomalous tendency of the plateau could be due to the tectonic activity of the Cephalonia fault. At the present stage the analyses carried out are not sufficient to provide the complete correlation between morphologies and tectonics, a step that will be developed in the future.

The surroundings of Zakynthos (zone 2; Fig. 3) are mainly affected by landslides with variable sizes ranging from hundreds of metres to tens of kilometres in scar width. The largest landslide, a giant landslide, located south of Zakynthos (Fig. 3) is in close correlation with the NE-SW oriented morphological steps mapped next to one its flank. These morphological steps have been associated with normal faults displacing sediments towards the southeast. The gravitational control on tectonics has been best explored in Loreto et al. (under review). Since this area is dominated by compressional tectonics, the gravitational instability here must be of enormous magnitude since it has also been recorded on land with earthquakes with normal kinematics (Kassars et al., 2016). Most of the faults inferred from morphological features on the seabed are active. The assessment of the seismogenic potential of these faults will be investigated at a later stage; here we want to drive the attention on the offshore morphological elements that have been mapped in this area for the first time.

Finally, the presence of gas-bearing sediments (Fig. 2) represents a significant risk for the surrounding areas. It has been observed along several margins that when gas accumulates in the sediments the shear strength is greatly reduced predisposing the slope to gravitational instability (Sultan et al., 2004). When the gas accumulated in the sediments is released into the water column it results in the formation of pockmarks (Hovland, 1989) which are frequently related to submarine landslides that can be triggered even in conditions of slope inclination lower than 1° (Kvalstad et al., 2005). Consequently, all the infrastructures installed offshore are exposed to high risk from landslides, sediment subsidence and gas explosion on the seabed (Hovland et al., 2002).

Summary

By combining bathymetric data from Emodnet with the new high-resolution swath bathymetry and comparing this map with the Topas profiles and high-resolution seismic profiles, we have mapped all geohazard elements affecting the area. From the northern part of Lefkada up to the southern part of Cephalonia, the 120 km-long Cephalonia transform fault has been completely mapped. A series of channels, channel heads, landslide scars and multiple slide deposits have been mapped all around the islands, at the continental slope and in the narrow inner basin between the island of Ithaca and the Peloponnese. This new dataset has revealed a seabed extremely shaped by faults, gravitational instabilities, channels and often tectonically-controlled channels, and adds a further step forward in the geological risk assessment of Western Greece.

Acknowledgements

Interpretation of all seismic data combined with morpho-bathymetry has been done using the Kingdom Suite software (S&P Global), freely available under the S&P Global University Grant Program. Geophysical data were collected during the IONIANS cruise supported by internal CNR funding (https://www.ismar.cnr.it/web-content/rapporto-tecnico-n-11/) and aboard of the R/V L. Bassi – INOGS during the POSEIDON cruise supported by the Eurofleet program (http://eurofleet.maris2.nl/cds-report/25). A thanks the the ISMAR-CNR institute of Bologna for hosting my internship.

References

Ganas, A., Briole, P., Bozionelos, G., Barberopoulou, A., Elias, P., Tsironi, V., ... & Mintourakis, I.; 2020: The 25 October 2018 Mw= 6.7 Zakynthos earthquake (Ionian Sea, Greece): A low-angle fault model based on GNSS data, relocated seismicity, small tsunami and implications for the seismic hazard in the west Hellenic Arc. Journal of Geodynamics, 137, 101731.

Hovland, M. (1989). The formation of pockmarks and their potential influence on offshore construction. *Quarterly Journal of Engineering Geology and Hydrogeology*, *22*(2), 131-138.

Hovland, M., Gardner, J. V., & Judd, A. G. (2002). The significance of pockmarks to understanding fluid flow processes and geohazards. *Geofluids*, *2*(2), 127-136.

Kvalstad, T. J., Andresen, L., Forsberg, C. F., Berg, K., Bryn, P., & Wangen, M. (2005). The Storegga slide: evaluation of triggering sources and slide mechanics. In *Ormen Lange–an integrated study for Safe Field development in the Storegga submarine area* (pp. 245-256). Elsevier.

Loreto, M. F., Zitellini, N., Ranero, C. R., Palmiotto, C., & Prada, M. (2021). Extensional tectonics during the Tyrrhenian back□arc basin formation and a new morpho□tectonic map. *Basin Research*, *33*(1), 138-158.

Loreto, M.F., Ferrante, V., Ligi, M., Muccini, F., Palmiotto, C., Petracchini, L., Romano, S., Ganas, A., Argnani, A., Conti, A., Cuffaro, M., Kothri, S., Lampridou, D., Merino, I., Ranero, R.C. and Nomikou, P. Anatomy of the Right-Lateral Strike-Slip Cephalonia Fault to the Western Hellenic Arc Frontal Thrust. *Under review in Tectonics*.

Stiros, S. C., P. A. Pirazzoli, J. Laborel, F. Laborel-Deguen, 1994. The 1953 earthquake in Cephalonia (Western Hellenic Arc): coastal uplift and halotectonic faulting, Geophysical Journal International, Volume 117, Issue 3, Pages 834–849, https://doi.org/10.1111/j.1365-246X.1994.tb02474.x

Wessel, P., Luis, J. F., Uieda, L., Scharroo, R., Wobbe, F., Smith, W. H. F., & Tian, D. (2019), The Generic Mapping Tools Version 6, *Geochemistry, Geophysics, Geosystems*, 20(11), 5556–5564. https://doi.org/10.1029/2019GC008515

17th INTERNATIONAL CONGRESS of the Geological Society of Greece

BULLETIN OF THE GEOLOGICAL SOCIETY OF GREECE, SP. PUBL.

EXTENDED ABSTRACT 030

Assessing earthquake-triggered tsunami hazard in Santorini-Amorgos Tectonic Zone: A deterministic simulation-based approach

Batzakis D.-V.[1], Karymbalis E.[1], Tsanakas K.[1]
(1) Department of Geography, Harokopio University, Athens, Greece, mpatzakis@hua.gr

Introduction

The Aegean region is shaped by the dynamic interactions caused by tectonic plate kinematics. To the north, the Aegean is bounded by the North Anatolian Fault (NAF), the major strike-slip fault that accommodates the westward motion of the Anatolian microplate at a rate of about 2.4 cm/year (Taymaz *et al.*, 2007). The Hellenic subduction zone defines the southern boundary, where the African plate subducts beneath the Aegean microplate at a rate of 0.9 cm/year (Andinisari *et al.*, 2021, and references therein). This process, combined with the westward extrusion of Anatolian microplate, drives the southward retreat of the Aegean microplate at an estimated rate of around 3.5 cm/year (Andinisari *et al.*, 2021, and references therein), resulting in extensive crustal deformation, the development of diverse tectonic and volcanic structures, and various faulting mechanisms in the broader region (Papazachos & Kiratzi, 1996). The south Aegean is characterized by an extensional deformation environment driven by the rollback of the subducting slab (Sachpazi *et al.*, 2016), where crustal stretching leads to the formation of numerous normal faults (Papazachos *et al.*, 1999). This ongoing extensional regime is associated with the presence of active tectonic zones with high seismicity accompanied by the evolution of volcanic centers (Hooft *et al.*, 2017). One of the most distinctive zones is the Santorini-Amorgos Tectonic Zone (SATZ), a geodynamically complex area influenced by subduction processes and extensional tectonics. It is characterized by active faulting, significant seismic activity, and the presence of volcanic centers (Nomikou *et al.*, 2018).

In the early months of 2025, a notable seismic activity was recorded in the area between the islands of Santorini and Amorgos. From January 25 to March 6, more than 4,000 earthquakes were documented, with the largest event reaching a magnitude of 5.3 (IG-NOA, 2025). The high frequency and the magnitude of these earthquakes raised concerns regarding the potential for a stronger earthquake, particularly given the region's complex tectonic setting and its history of significant seismic events. Furthermore, the possibility of a tsunami generated by a major earthquake heightened these concerns, considering the region's experience with such events. This study aims to assess the tsunami hazard in the SATZ by simulating earthquake-triggered tsunami waves. A deterministic approach is adopted, developing worst-case earthquake scenarios based on the dimensions and characteristics of the major active faults within the tectonic zone. Using simulation techniques, the propagation and inundation extent of earthquake-triggered tsunamis are calculated, providing insights into the potential impact of the waves on specific coastal areas of the surrounding islands.

Study Area

The SATZ is located in the South Aegean Sea, bordered by the islands of Santorini, Ios, Amorgos, Astypalaea, and Anafi. It is a seismically active structure that marks the transition from the relatively quiescent western part of South Aegean to the highly active eastern part (Bohnhoff *et al.*, 2006). Recent seismic reflection and bathymetric data revealed that the SATZ is a structural feature composed of tectonic grabens and horsts, formed by the presence of several major and minor faults oriented in a NE-SW direction (Nomikou *et al.*, 2018; Tsampouraki-Kraounaki *et al.*, 2021). Crustal deformation in the zone is mainly dominated by several major faults which control the development of graben-horst structures (Nomikou *et al.*, 2018). These faults exhibit varying dip angles and are characterized by significant fault throws, indicating normal faulting (Nomikou *et al.*, 2016; Nomikou *et al.*, 2018; Preine *et al.*, 2020). However, a right-lateral strike-slip component has been observed, suggesting a trans-tensional stress in the area (Heath *et al.*, 2019; Tsampouraki-Kraounaki *et al.*, 2021, and references therein).

In recent times, the SATZ experienced significant seismic activity, including the M_w ~6 events in 1911 and 1919 (Andinisari *et al.*, 2021). The most prominent event was the 1956 M_w 7.8 earthquake along the Amorgos Fault (AmF), which triggered a tsunami that caused significant run-up along the coasts of the surrounding islands, although the exact source mechanism remains debated (Okal *et al.*, 2009). The major faults within the SATZ include the Ios Fault

Zone (IF) and Amorgos Fault (AmF), which extend across the northern part; the Santorini-Anafi Fault (SAF) and Anydros Fault (AF) located in the central part; and the Anafi-Astypalaea Fault Zone (AnF-AsF), across the southern margin of the SATZ (Figure 1). AmF and SAF exhibit southeastward dipping, IF exhibits southwestward dipping, while AF and AnF-AsF show opposite polarity with northwestward dipping motion (Tsampouraki-Kraounaki *et al.*, 2021). Apart from the AF, these faults are sufficiently long to generate earthquakes of $M_w \geq 7$ (Leclerc *et al.*, 2024).

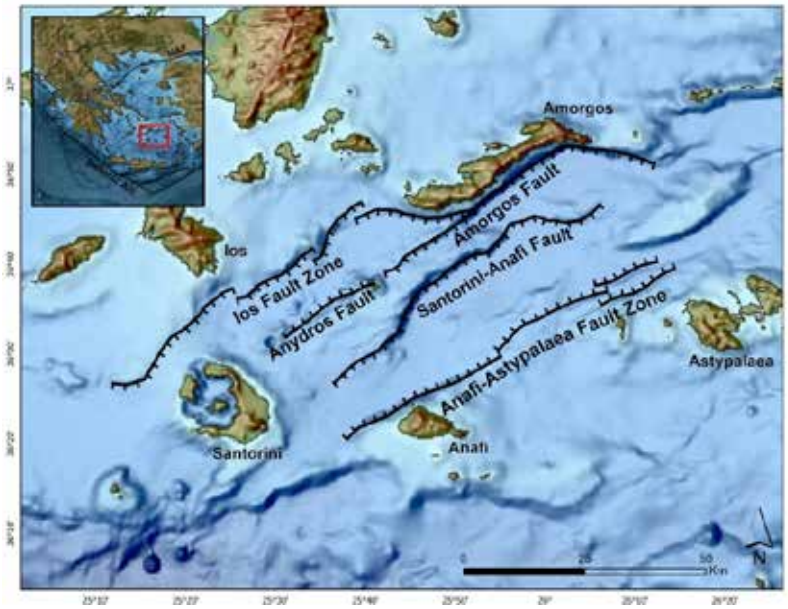

Figure 1. Map of the major active faults in the Santorini-Amorgos Tectonic Zone (modified after Leclerc *et al.*, 2024; Nomikou *et al.*, 2018; Tsampouraki-Kraounaki *et al.*, 2021).

Methodology

Seismic events along the major faults were considered, to analyze the propagation patterns and the potential impact of earthquake-triggered tsunamis within the SATZ. Moreover, five coastal areas hosting settlements—Kamari and Perissa in Santorini, Katapola in Amorgos, Gialos in Ios, and Chora in Astypalaea—were selected for hazard assessment due to their touristic development, extensive human activities, and the presence of critical infrastructure, that make them particularly exposed to tsunami.

The MOST (Method of Splitting Tsunami) numerical model, implemented through ComMIT (Community Model Interface for Tsunamis) modelling framework developed by NOAA, is employed to simulate tsunami generation, propagation, and onshore inundation (Titov *et al.*, 2011). ComMIT utilizes three nested computational topo-bathymetric grids for tsunami simulation. Two coarser grids, which cover broader areas, are used to calculate the initial conditions and the wave propagation in the open sea. A third finer grid, which covers the coastal area, is used to perform the inland penetration calculations. For the coarser grids, topo-bathymetric data from the General Bathymetric Chart of the Oceans (GEBCO-2024), with a resolution of approximately 375 m, were utilized. For the finer grid, a detailed elevation dataset with a resolution of 5 m was used. This dataset was created by combining the 5 m resolution topographic data provided by the Hellenic Cadastre with the bathymetric data from Navionics nautical charts, which have a resolution ranging from 10 m in the nearshore zone to 50 m in deeper offshore areas. The data processing was conducted using GIS software to generate a seamless elevation model for the coastal areas of interest. Adjustments to the coarser grids were performed based on the finer grid to improve their accuracy in the coastal areas under study, where the tsunami impact will be assessed, utilizing the Map Algebra tools in GIS software.

The seismic source mechanism parameters required for the initial phase of tsunami generation were obtained from studies conducted in the SATZ, where bathymetric and seismic data have been presented and analyzed (Nomikou *et al.*, 2016; Nomikou *et al.*, 2018; Tsampouraki-Kraounaki *et al.*, 2021). The fault length and strike used in the simulation were derived from the fault trace as mapped in the study area. The fault width (W) was calculated as W

= H / sinδ, where H is the thickness of the seismogenic layer, assigned a value of 12.5 km according to Andinisari *et al*. (2021), and δ is the average fault dip angle, estimated from the values provided in the aforementioned studies. The magnitude of the potential earthquake was estimated using the regression equation correlating the M_w with the rupture area (S) of the fault, while the mean displacement (u) was calculated using the regression equation that correlates M_w with u, as proposed for dip-slip continental faults by Papazachos *et al.* (2004). Furthermore, it was assumed that the faults would rupture along their entire length, with IF and AnF-AsF considered as a single fault. These estimations were obtained by applying Equations (1) and (2), respectively.

Log(S)=0.78Mw-2.56 (1)

Log(u)=0.72Mw-2.28 (2)

A depth of 10 km was assigned to the potential earthquake for all the faults, based on observations of recent seismicity in the SATZ (IG-NOA, 2025). The epicenter of the earthquake was defined as the midpoint of the fault length, and the distance (d) from the fault trace was calculated as d = D / tanδ, where D is the earthquake depth. A rake value of -135° was used, consistent with the NOA fault catalog for the AmF (Ganas *et al.*, 2013), adopting a normal right-lateral oblique slip for the faults. All the parameters used in the simulations are listed in Table 1 and the fault planes are represented in Figure 2. The results were overlaid on a satellite imagery basemap using GIS to visualize the extent of inundation and calculate the run-up.

Table 1. Seismic source parameters used for tsunami simulation calculations.

Seismic source	Earthquake epicenter (°)		Length (km)	Width (km)	Rupture area (km²)	M_w	Depth (km)	Mean displacement (m)	Strike (°)	Dip (°)	Rake (°)
	Latitude	Longitude									
Ios Fault Zone	36.54925	25.50823	55	17.7	973	7.11	10	2.00	48	45	-135
Amorgos Fault	36.77155	25.93779	40	16.3	652	6.89	10	1.38	48	50	-135
Anydros Fault	36.64383	25.51760	20	17.7	354	6.55	10	0.79	235	45	-135
Santorini-Anafi Fault	36.64002	25.90768	60	15.2	912	7.08	10	1.89	45	55	-135
Anafi-Astypalaea Fault Zone	36.57636	25.90581	65	15.2	988	7.12	10	2.03	237	55	-135

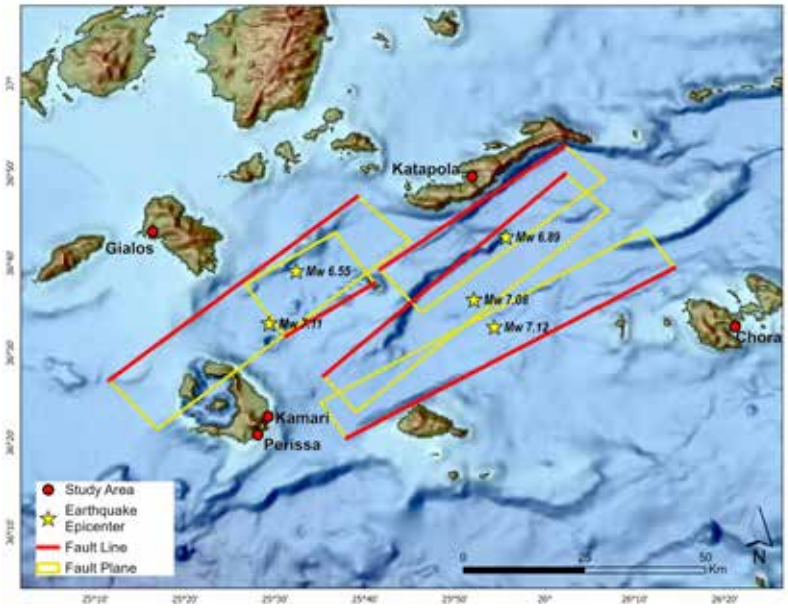

Figure 2. Map of the selected tsunamigenic earthquake sources and study areas. The rectangles represent the surface projection of the fault planes used in this study for tsunami simulations.

Results

The numerical simulations illustrated the generation and propagation of tsunami waves triggered by the five selected earthquake scenarios (Figure 3). The computed initial wave amplitude fields revealed the sea surface displacement, which corresponds to the uplift and subsidence associated with each seismic event. The main wave direction and the maximum observed amplitudes were aligned with the fault strike, primarily propagating toward the northwest and southeast. The wavefront time frames also captured the interactions with underwater features which create bathymetric variations, influencing tsunami propagation. Notably, the Anydros horst, which hosts Anydros Islet in the central-western part of the SATZ, plays a significant role in wave diffraction. These bathymetric variations, along with coastal morphology, impact the wave refraction and amplification, especially in the nearshore zone. The highest wave heights, reaching up to 2.5–3 m, were observed near the southern coasts of Ios and the western coasts of Astypalaea, generated by the largest earthquake scenarios of IF, SAF and AnF-AsF.

Table 2 summarizes the estimated tsunami arrival times at the study areas for each tsunamigenic source, measured in minutes after the earthquake. The arrival times range from several minutes to tens of minutes, with variations due to the proximity of each study area to the respective fault. Among the study areas, Perissa and Chora experienced the fastest tsunami arrival following an earthquake along the AnF-AsF, and Kamari after an earthquake along the AF, with waves reaching the coast in just 10 minutes. In contrast, the longest arrival time of 40 minutes was observed in Chora following an earthquake along the IF.

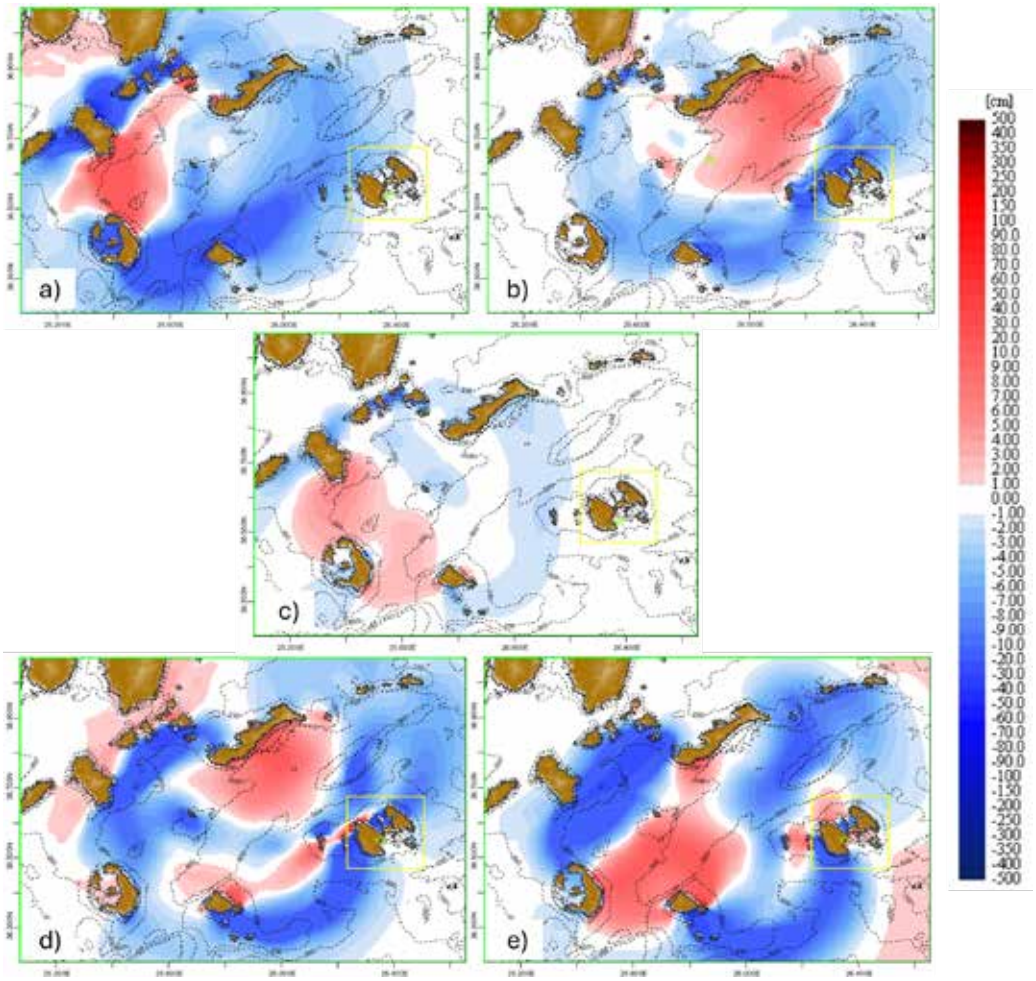

Figure 3. Wave propagation and amplitude distribution for the seismic sources along: a) IF, b) AmF, c) AF, d) SAF, and e) AnF-AsF, shown as snapshots approximately 10 minutes after the seismic events.

Table 2. Tsunami arrival times for each seismic source at the study areas, measured in minutes following the seismic events.

Seismic source	Calculated arrival times (in minutes after the seismic event)				
	Gialos	Katapola	Kamari	Perissa	Chora
Ios Fault Zone	15	25	20	25	40
Amorgos Fault	30	15	20	25	30
Anydros Fault	25	25	10	15	35
Santorini-Anafi Fault	30	35	20	25	30
Anafi-Astypalaea Fault Zone	30	35	15	10	10

The tsunami simulations also provided insights into the extent of coastal inundation and the run-up in the studied coastal areas. The run-up values varied across the five coastal areas, reflecting both the magnitude of the seismic events and the coastal morphology (Table 3). The IF, SAF and AnF-AsF scenarios consistently produced higher run-up values in most study areas. Specifically, IF resulted in the highest run-up value in Gialos, while AnF-AsF produced the highest run-up in Ghora, with both areas experiencing a maximum run-up of 2.8 m. The SAF and AnF-AsF also exhibited high run-up values along the eastern coast of Santorini, with maximum run-ups of 2.4 m observed in Kamari and 2.2 m in Perissa. High run-up values of 2.3 m were observed in Gialos, resulting from the AnF-AsF scenario, and 2.1 m in Gialos and Chora from the SAF. The highest run-up from the AmF was recorded in Perissa, with a value of 1.8 m, followed by 1.5 m in Gialos. The AF appeared to generate the smallest run-up, with values of 0.4–0.6 m observed in Kamari, Perissa, and Gialos. This suggests that the fault may not produce large tsunamis due to its smaller size. Figure 4 illustrates the maximum inundation extent and corresponding flow depth values in the study areas for the various seismic scenarios.

Overall, the observed tsunami inundation extent and run-up values in the selected study areas are not substantial enough to cause a major disaster. However, in Gialos (Ios), Katapola (Amorgos), and Chora (Astypalaea), the inundation flows extend into the coastal zone, affecting the residential zone. Notably, these coastal settlements also host the main ports of the islands, meaning that a potential tsunami could exacerbate a seismic crisis by disrupting critical infrastructure used for emergency response efforts. In Kamari and Perissa, Santorini, the inundation does not appear to extend beyond the coastal front, possibly resulting in large waves along the shoreline without extensive inland penetration.

Table 3. Observed run-up values (in meters) in the study areas for the various seismic sources. N/A indicates no observed run-up.

Seismic source	Observed run-up values (in meters)				
	Gialos	Katapola	Kamari	Perissa	Chora
Ios Fault Zone	2.8	2.3	1.6	1.4	0.8
Amorgos Fault	1.5	1.3	1.4	1.8	0.6
Anydros Fault	0.4	N/A	0.6	0.5	N/A
Santorini-Anafi Fault	2.1	1.9	2.4	2.2	2.1
Anafi-Astypalaea Fault Zone	2.3	1.4	2.4	2.2	2.8

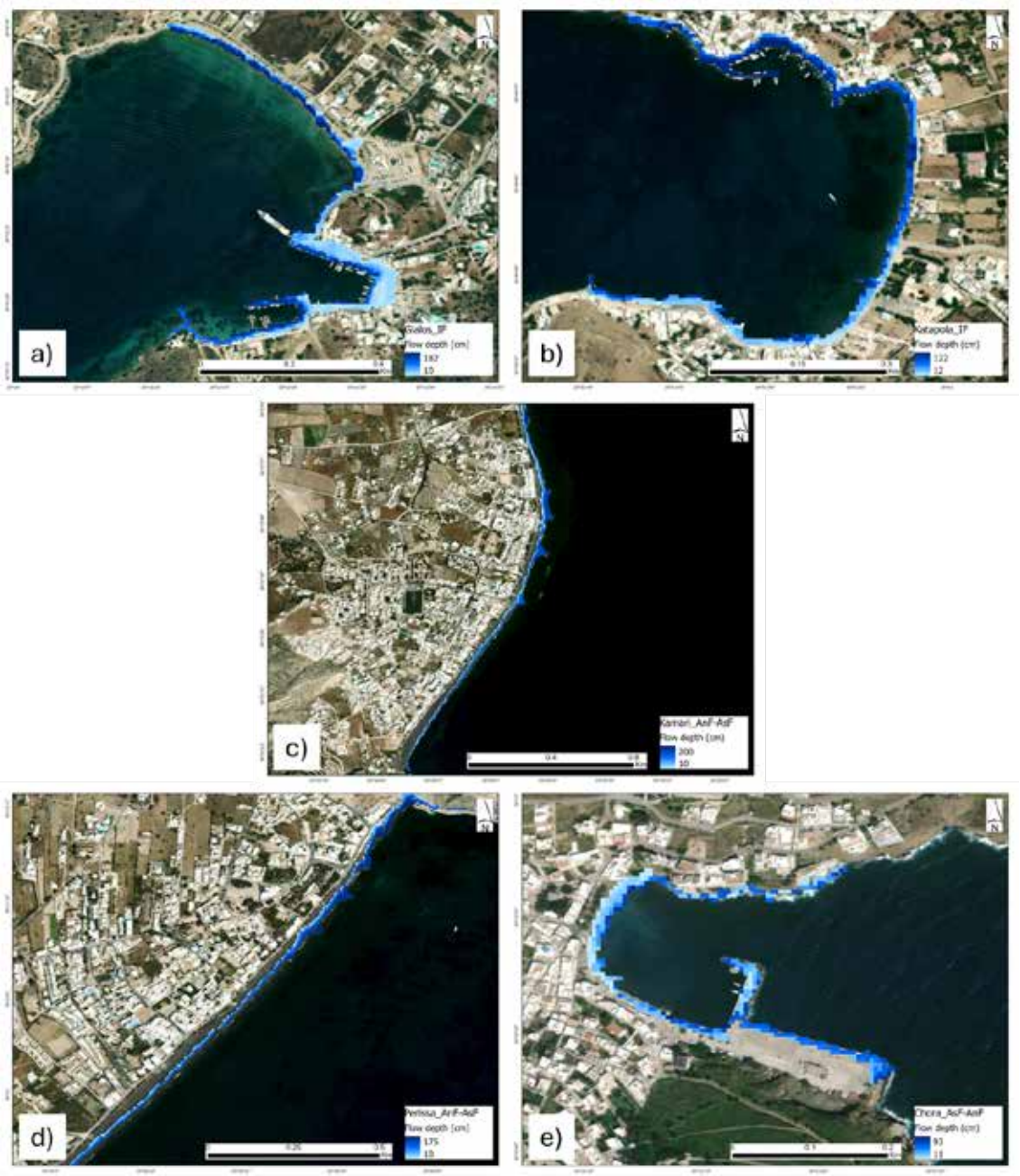

Figure 4. Maximum observed inundation extent in the study areas for the various seismic sources considered in the simulation scenarios: a) Gialos, Ios b) Katapola, Amorgos c) Kamari and d) Perissa, Santorini and e) Chora, Astypalaea. The associated fault is indicated in the map legends.

Concluding Remarks

The study assessed the earthquake-triggered tsunami hazard within the Santorini-Amorgos Tectonic Zone by examining worst-case scenarios. Through simulations of tsunami wave generation, propagation, and inundation from various well-documented seismic sources, the results demonstrated significant variations in tsunami arrival times across the study areas, ranging from just a few minutes to over 40 minutes, depending on proximity to the seismic sources. The observed inundation extent and run-up values indicated localized impact, with a maximum run-up of 2.8 m recorded at Gialos (Ios) and Chora (Astypalaea), and 2.3 m at

Katapola (Amorgos) potentially affecting residential zones and the main ports of these islands. In contrast, Kamari and Perissa (Santorini) experienced a maximum observed run-up of 2.4 and 2.2 m, respectively, with the inundation extending only slightly beyond the coastline. Although earthquake-triggered tsunamis pose a potential hazard, the results suggested that these events are unlikely to lead to a disaster in the study areas.

References

Andinisari, R., Konstantinou, K. I., Ranjan, P., 2021. Seismicity along the Santorini-Amorgos zone and its relationship with active tectonics and fluid distribution. Physics of the Earth and Planetary Interiors, 312, 106660.

Bohnhoff, M., Rische, M., Meier, T., Becker, D., Stavrakakis, G., Harjes, H. P., 2006. Microseismic activity in the Hellenic Volcanic Arc, Greece, with emphasis on the seismotectonic setting of the Santorini-Amorgos zone. Tectonophysics, 423(1–4), 17–33.

Ganas, A., Oikonomou, I. A., Tsimi, C., 2013. Noafaults: a digital database for active faults in Greece. Bulletin of Geological Society of Greece, 47(2), Chania, Greece, p. 518.

General bathymetric Chart of the Oceans (GEBCO), Gridded Bathymetry Data-2024, available at: https:// https://download.gebco.net/

Heath, B. A., Hooft, E. E. E., Toomey, D. R., Papazachos, C. B., Nomikou, P., Paulatto, M., Morgan, J. V., Warner, M. R., 2019. Tectonism and Its Relation to Magmatism Around Santorini Volcano From Upper Crustal P Wave Velocity. Journal of Geophysical Research: Solid Earth, 124(10), 10610–10629.

Hooft, E. E., Nomikou, P., Toomey, D. R., Lampridou, D., Getz, C., Christopoulou, M. E., O'Hara, D., Arnoux, G. M., Bodmer, M., Gray, M., Heath, B. A., VanderBeek, B. P., 2017. Backarc tectonism, volcanism, and mass wasting shape seafloor morphology in the Santorini-Christiana-Amorgos region of the Hellenic Volcanic Arc. Tectonophysics, 712, 396–414.

Institute of Geodynamics-National Observatory of Athens, 2025. Observations and preliminary results on the seismic sequence between Santorini and Amorgos, available at: https://www.emsc.eu/Special_reports/?id=351

Leclerc, F., Palagonia, S., Feuillet, N., Nomikou, P., Lampridou, D., Barrière, P., Dano, A., Ochoa, E., Gracias, N., Escartin, J., 2024. Large seafloor rupture caused by the 1956 Amorgos tsunamigenic earthquake, Greece. Communications Earth and Environment, 5(1), 663.

Nomikou, P., Hübscher, C., Papanikolaou, D., Farangitakis, G. P., Ruhnau, M., Lampridou, D., 2018. Expanding extension, subsidence and lateral segmentation within the Santorini-Amorgos basins during Quaternary: Implications for the 1956 Amorgos events, central - south Aegean Sea, Greece. Tectonophysics, 722, 138–153.

Nomikou, P., Hübscher, C., Ruhnau, M., Bejelou, K., 2016. Tectono-stratigraphic evolution through successive extensional events of the Anydros Basin, hosting Kolumbo volcanic field at the Aegean Sea, Greece. Tectonophysics, 671, 202–217.

Okal, E. A., Synolakis, C. E., Uslu, B., Kalligeris, N., Voukouvalas, E., 2009. The 1956 earthquake and tsunami in Amorgos, Greece. Geophysical Journal International, 178(3), 1533–1554.

Papazachos, B. C., Papaioannou, C. A., Papazachos, C. B., Savvaidis, A. S., 1999. Rupture zones in the Aegean region. Tectonophysics 308(1-2), 205–221.

Papazachos, B. C., Scordilis, E. M., Panagiotopoulos, D. G., Papazachos, C. B., Karakaisis, G. F., 2004. Global relations between seismic fault parameters and moment magnitude of earthquakes. Bulletin of the geological society of Greece, 36(3), Thessaloniki, Greece, p. 1482.

Papazachos, C. B., Kiratzi, A. A., 1996. A detailed study of the active crustal deformation in the Aegean and surrounding area. Tectonophysics 253(1-2), 129–153.

Preine, J., Schwarz, B., Bauer, A., Hübscher, C., 2020. When There Is No Offset: A Demonstration of Seismic Diffraction Imaging and Depth-Velocity Model Building in the Southern Aegean Sea. Journal of Geophysical Research: Solid Earth, 125(9), 1–19.

Sachpazi, M., Laigle, M., Charalampakis, M., Diaz, J., Kissling, E., Gesret, A., Becel, A., Flueh, E., Miles, P., Hirn, A., 2016. Segmented Hellenic slab rollback driving Aegean deformation and seismicity. Geophysical Research Letters, 43(2), 651–658.

Taymaz, T., Yilmaz, Y., Dilek, Y., 2007. The geodynamics of the Aegean and Anatolia: Introduction. In Taymaz, T., Yilmaz, Y., Dilek, Y. (Eds), The Geodynamics of the Aegean and Anatolia. Geological Society Special Publication 291, 1–16.

Titov, V. V., Moore, C. W., Greenslade, D. J. M., Pattiaratchi, C., Badal, R., Synolakis, C. E., Kânoğlu, U., 2011. A New Tool for Inundation Modeling: Community Modeling Interface for Tsunamis (ComMIT). Pure and Applied Geophysics, 168(11), 2121–2131.

Tsampouraki-Kraounaki, K., Sakellariou, D., Rousakis, G., Morfis, I., Panagiotopoulos, I., Livanos, I., Manta, K., Paraschos, F., Papatheodorou, G., 2021. The Santorini-Amorgos shear zone: Evidence for dextral transtension in the south Aegean back-arc region, Greece. Geosciences, 11, 126, 1–36.

17th INTERNATIONAL CONGRESS
of the Geological Society of Greece

BULLETIN OF THE GEOLOGICAL SOCIETY OF GREECE, SP. PUBL.

EXTENDED ABSTRACT 031

Oceanographic survey M192 off Milos reveals tectonic controls on hydrothermal vent distribution in a complex volcanic-tectonic system of the South Aegean

Bejelou K.[1], Nomikou P.[1], Bühring S.[2], Papanikolaou D.[1], Kilias S.[1], Koschinsky A.[3], Bach W.[2], Haase K.[4], Ferreira C.[2], Bazhenova E.[2], Bach A.[2], Azakura Y[2], Lampridou D.[1], Belka A.[1], Anagnostou E.[3], Varotsou E.[1], Kothri S.[1]

(1) National and Kapodistrian University of Athens, Athens, Greece (2) MARUM – Center for Marine Environmental Sciences, University of Bremen (3) Constructor University, Bremen, Germany (4) Friedrich-Alexander-Universität Erlangen-Nürnberg

Introduction

Milos is located at the southwestern edge of the Cyclades islands in the Aegean Sea, Greece, and is part of the South Aegean Volcanic Arc (Pe-Piper, et al., 2005). The island's geological history includes volcanic activity from the Late Pliocene to the Early Pleistocene, with the last subaerial eruption occurring around 80,000 years ago (Sonder, 1924; Fytikas, 1977; Fytikas, et al., 1986). Its tectonic background is characterized by alternating phases of extension and compression related to volcanic activity during the Pliocene-Pleistocene (Angelier, et al., 1977). The neotectonic and active faults of Milos have produced a block structure, characterized by the occurrence of specific stratigraphic formations in each block (Papanikolaou, et al., 1990). These faults have served as conduits for geothermal fluids, resulting in hydrothermal alteration of the adjacent volcano-sedimentary formations and giving birth to several exploitable ore deposits (Fytikas, 1989). The most active onshore vent fields are located in the Aghia Kiriaki area, along the eastern edge of the Fyriplaka Volcano, near the intersection of the NW-SE and ENE-WSW active faults. As for the offshore domain, extensive hydrothermal venting has been documented in Paleochori, Adamas Bay and Voudia Bay (Dando, et al., 1995; Dando, et al., 2000). Specifically, in Paleochori area, from shore up to depths of almost 500 m, hydrothermal venting is manifested through emissions of gases and high-temperature fluids, often associated with bacterial mats and/or hydrothermal mineral precipitates (Puzenat, et al., 2021).

Highly dominant tectonic features are two major fault zones bounding the central block of the Milos – Fyriplaka tectonic graben, which hosts the Fyriplaka volcanic crater and numerous vent fields both onshore and offshore (Papanikolaou, et al., 1990). Seismic activity, such as the earthquake of 5.2 ML on March 20, 1992, in the southeastern part of the graben, caused extended impacts, including structural damage on buildings, seismic fractures, variations in intensity and temperature of gas emissions, landslides, rockfalls and liquefaction phenomena (Papanikolaou et al., 1993). A recent study has confirmed ongoing seismic and ground deformation along a NW-SE, east-dipping fault on Milos Island, through microseismicity recordings, and InSAR data, showing a significant ground motion of up to 1 cm/yr across the fault (Ganas et al., 2022).

This study combines geodynamic constraints with high-resolution geophysical data to determine the influence of tectonic processes over the distribution of hydrothermal vent fields on the continental shelf around Milos as well as their evolution in relation to sea-level changes particularly since Middle Pleistocene, with the most recent lowstand averaging around 130 m in depth (Seibold & Berger, 1993), thus documenting the interconnection of hydrothermal activity associated with volcanism, tectonics and climatic fluctuations both onshore and offshore.

Data collection and Methodology

The cruise M192, conducted in August 2023 on board the RV Meteor investigated the area offshore Milos in terms of the geomorphology, geology, geochemistry and microbiology of marine hydrothermal systems in a transect from the shallow continental shelf, photic zone off Milos to the deep, offshore, aphotic zone (Bühring et al, 2024, Nomikou et al., 2025 under review). The mission was separated into 2 legs. The major aim of Leg 1 was the systematic mapping using the multibeam echosounder system of RV Meteor, the parasound system and the AUV (Autonomous Underwater Vehicle) MARUM-SEAL in expansive areas around Milos was performed during cruise M192 of R/V Meteor, 08 August – 05 September 2023. On the second leg (M192_2) the hydrothermal vent areas targeted during the first leg were systematically sampled by multicorer and identified with the ROV MARUM-SQUID.

Results and Discussion

Processing of the acquired bathymetric data revealed that the coastal zone around Milos features a distinct shelf and slope area separated by a shelf break, which varies in depth around the island (130-220m), being deeper and disrupted on the eastern side (Fig. 1). The shelf break depth varies due to tectonic deformation, from 130-150 m on the western block (consistent with pre-Holocene sea levels) to 170-220 m in the southeastern tectonic graben, reflecting active faulting. This survey also provided us with the first documentation of Hydrothermal Vent Fields (HVFs), related to volcanism in the modern Milos geothermal system, up to depths of about 220 m and confined within the continental shelf. The distribution of the discovered vent fields around Milos Island is highly selective at the SE and NW coastal zone covering a small percentage of the Milos offshore domain. The present study reveals that these vent fields illustrate a strong correlation between hydrothermal vent fields and active faults, highlighting the interplay between tectonics and geothermal activity. Some of the discovered vent fields are associated with the NW-SE Milos Gulf–Fyriplaka tectonic graben, which hosted the last volcanic eruption 80,000 years ago. Others align with E-W and WNW-ESE faults in southeastern Milos.

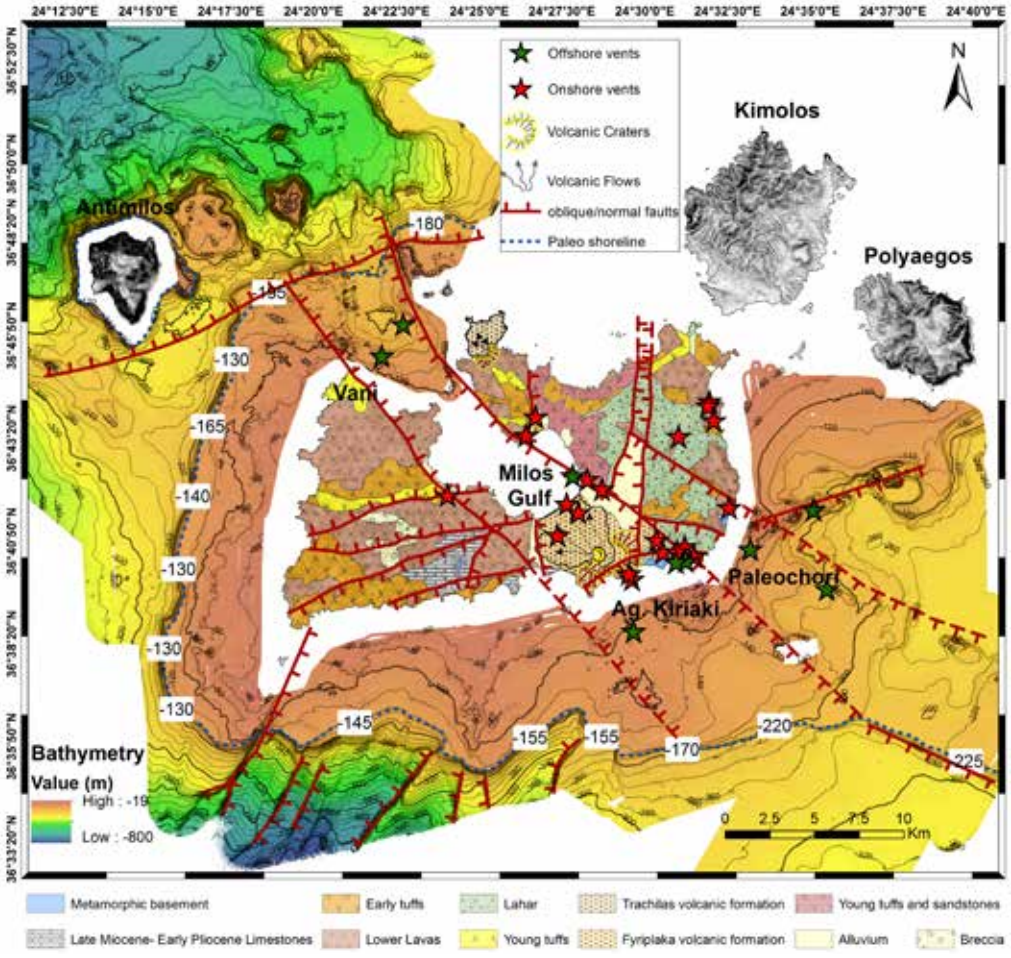

Figure 1. Synthetic tectonic map based on the swath data, the parasound seismic profiles acquired during the M192 expedition and the produced morphologic slope map. Onshore geologic map modified after Papanikolaou et al., 1990.

Two key tectonic features, the NW-SE Milos Gulf–Fyriplaka graben and the ENE-WSW fault system near Fyriplaka Volcano, separate the island's geothermal activity. The most active offshore vent fields occur at Paleochori (Puzenat, et al., 2021) along the southern coast, while Aghia Kiriaki (Fig. 1) hosts the primary onshore vent field at the intersection of active faults.

Depths of detected hydrothermal activity reveal distinct distributions varying in depth from 130 to 220 m. Despite this variation, the prevailing depth is around 110 m, with fewer hydrothermal manifestations beyond

150 m. The shelf break subsidence due to tectonic processes thus seem to strongly influence the location, depth, and activity of geothermal vent fields, with faults acting as conduits for hydrothermal fluids while leaving other regions inactive.

Notably, the E-W neotectonic faults of SW Milos and NE-SW trending faults on the SE slope do not extend onto the shelf and lack associated hydrothermal activity creating geothermal activity gaps.

Conclusions

The oceanographic research M192 around Milos, a young volcanic island in the South Aegean, revealed the offshore prolongation of the Milos major tectonic zones and their interconnection to high-temperature hydrothermal vents and continental shelf volcanism.

Hydrothermal activity has persisted beneath the Milos shelf since the Late Pleistocene, independent of active faulting, and continues today. This evolution reflects a combination of tectonic processes and climatic shifts, alternating between subaerial erosion during sea-level lowstands and submarine venting during highstands. These findings may apply to similar volcanic and geothermal systems in island arcs at convergent plate boundaries.

Acknowledgements

We are thankful to the METEOR-Berichte, Cruise M192, Pireus – Limassol, 08 August – 05 September 2023, the technical staff of the R/V METEOR, and all of the shipboard personnel for a great expedition. We also thank the member organizations of this cruise University of Bremen and MARUM for the financial aid and the supply of all the necessary equipment for preparing and completing the expedition. We would also like to acknowledge the contribution of the program IKYDA 2024: Bridging the Gap between hydrothermal biogeochemistry and Volcano-Tectonics: Exploring Synergies Along the Hellenic Arc off Milos (BITECHELL), for the promotion of the exchange and scientific cooperation between Greece and Germany.

References

Angelier, J, Cantagrel, J-M and Vilminot, J-C. 1977. Neotectonique cassante et volcanisme plio-quaternaire dans l'arc egeen interne; l'ile de Milos (Grece). *Bulletin de la Société Géologique de France.* 1977, Vols. S7-XIX, 1, pp. 119-124.

Bühring, S., Koschinsky, A., Bach, W., Elvert, M., Kleint, C., Kumawat, P., Maak, J., Meckel, E.-M., Nomikou, P., Röttgen, C., and Schefuß, E.: Discovery of a unique submarine hydrothermal system between shallow photic and deep dark sites around the Greek island of Milos (Aegean Sea, Greece), EGU General Assembly 2024, Vienna, Austria, 14–19 Apr 2024, EGU24-17022, https://doi.org/10.5194/egusphere-egu24-17022, 2024.

Dando, P.R., et al. 1995. Gas venting rates from submarine hydrothermal areas around the island of Milos, Hellenic Volcanic Arc. *Continental Shelf Research.* 1995, Vol. 15, 8.

Dando, P.R., et al. 2000. Hydrothermal studies in the Aegean Sea. *Physics and Chemistry of the Earth, Part B: Hydrology, Oceans and Atmosphere.* 2000, Vol. 25, 1, pp. 1-8.

Fytikas, Michael. 1977. Geological and Geothermal Study of Milos Island. 1977, Vol. XVIII, 1, p. 228.

Fytikas, Michael. 1989. Updating of the geological and geothermal research on Milos island. *Geothermics.* 1989, Vol. 18, 4, pp. 485-496.

Fytikas, Michael, et al. 1986. Volcanology and petrology of volcanic products from the island of Milos and neighbouring islets. *Volcanology and Geothermal Research.* 1986, Vol. 28, 3-4, pp. 297-317.

Ganas, Athanassios, Karakonstantis, Andreas, Kapetanidis, Vasilis, Tsironi, Varvara, Karamitros, Ioannis, Efstathiou, Eirini, Karasante, Ilektra and Kassaras, Ioannis. 2022. Ground deformation and microseismicity patterns onshore Milos, Cyclades, Greece. *Bull. Geol. Soc. Greece.* 2022, Sp. Publ. 10, pp. 663-664, ISBN: 978-960-98709-8-6.

Nomikou, P., Bejelou, K., Koschinsky, A, Ferreira, C., Papanikolaou, D., Lampridou, D., Kilias, S., Anagnostou, E., Elvert, Röttgen, Maak, Bach, A., Bach, Belka, A., Bazhenova, E., Haase, K., Kleint, Kothri, S., Kurahashi, Liao, Meckel, Pedre, Schäfer, Schefuss, Seidel, Varotsou, E., & Bühring S. 2025. Bimodal distribution of hydrothermal vent fields on the shelf platform reveals tectonic and sea-level controls. *Nature Geoscience.* Under review.

Papanikolaou, Dimitrios, Lekkas, Efthymis and Syskakis, D. 1990. Tectonic analysis of Milos geothermal field. *Bull. Geol. Soc. Greece.* 1990, Vol. 24, pp. 27-46.

Papanikolaou, D., Lekkas, E., Syskakis, D., & Adamopoulou, E. (1993). Correlation of neotectonic structures with the geodynamic activity in Milos during the earthquakes of March 1992. Bull. Geol. Soc. Greece, XXVIII/3, pp. 413-428.

Pe-Piper, Georgia and Piper, David. 2005. *The South Aegean active volcanic arc: Relationships between magmatism and tectonics.* [ed.] Michael Fytikas and Georges E. Vougioukalakis. s.l. : Elsevier Science, 2005. pp. 113-133. Vol. Developments in Volcanology. ISSN 1871-644X.

Puzenat, V., Escartín, J., Martelat, J., Barreyre , T., Le Moine Bauer, S., Nomikou, P., Gracias, N., Allemand, P., Antoniou, V., Coskun, O., Garcia, R., Grandjean, P., Polymenakou, P., Schouw, A., Vallicrosa, G., Vlasopoulos, O. 2021. Shallow-water hydrothermalism at Milos (Greece): Nature, distribution, heat fluxes and impact on ecosystems. *Marine Geology.* 2021, Vol. 438, p. 106521.

Seibold, E., & Berger, W. H. (1993). Sea Level Processes and Effects of Sea Level Changes. In The Sea Floor: An Introduction to Marine Geology (2nd edition ed., pp. 127--155). Berlin, Heidelberg: Springer Berlin Heidelberg. doi:10.1007/978-3-662-22519-6_6

Sonder, Richard August. 1924. Zur Geologie und Petrographie der Inselgruppe von Milos. *Zeitschrift für Vulkanologie.* 1924, 8, pp. 181-237. 29.

17th INTERNATIONAL CONGRESS of the Geological Society of Greece

BULLETIN OF THE GEOLOGICAL SOCIETY OF GREECE, SP. PUBL.

EXTENDED ABSTRACT 032

Storm Daniel flooding of Larissa City: embankments failure the aftermath

Belesis A.[1], Tsentzos I.[1] , Belesis M.[1], Koukouvelas I.K.[2]
1.Ermogenous 6, 41447 Larissa, Greece; abelesis1960@gmail.com
2 Department of Geology, University of Patras, 26504 Patras, Greece

Introduction

Storm Daniel was a catastrophic cyclone that became the costliest cyclone outside the North Atlantic Basin. The storm caused extensive flooding in Greece, Bulgaria, Turkey, and Libya. It was initiated on September 3rd, 2023, and on September 5th, the village of Zagora received 759 millimeters of rain (Kolios and Papavasileiou 2024). The storm flooded many villages in the low-lying area of Karditsa, in the Thessaly Plain, and towns and villages were blocked by water (Dimitriou *et al.* 2024; Kalafatis *et al.* 2024; Mavroulis *et al.* 2024).

In Larissa, after rains ended on 8th of September 2023, the water continued to rise as the Pineios River overflowed to reach 9.5 m, more than twice the typical level of 4 m. The Pineios River Basin in Thessaly occupies an area of about 11,000 km2 (Kalafatis *et al.* 2024). Its hydrologic basin is drained by the Pineios River, the third longest river in Greece at 213 km. Major tributaries of the river are the Malakassiotiko, Mourgkanis, Portaikos, Lithaios, Pamissos, Enipeas, and Titarisios, which all drain extensive meteorologically and geologically heterogeneous areas (Bathrellos *et al.* 2018).

Historical data shows that the Pineios River flooding at Larissa happens approximately every 25 years, primarily during winter (i.e. Bathrellos 2005; Bathrellos *et al.* 2018). These data indicate building damage and casualties in Larissa over the last centuries. Two of the most severe flooding events devastated the city in 1883 and 1901. Thus, to prevent the town from flooding in the 1930s, the BOOT company was entrusted to construct a riverbed for water diversion outside the city. Finally, this riverbed was finished by the Ministry of Public Works sometime after 1935. After WWII, in the 1950s, part of the Pineios water was returned to the old riverbed, with a controlled flow from a dam located west of Larissa City. The reactivation of the old riverbed was related to the city's craft economy during this period. The old riverbed remains active for aesthetic reasons and as a recreational area. In previous years, the Larissa area was included in the epicentral area of the Damasi 2021 earthquake. Two strong earthquakes of magnitudes 6.3 and 6.1, on March 3rd and 4th, respectively, happened during this earthquake while a long aftershock activity was also noticed (Koukouvelas *et al.* 2021; 2023 Sarchosis *et al.* 2022). During this seismic activity, the peak ground acceleration in Larissa was 0.16 g (Sarchosis *et al.* 2022). The study area is about 20-30 km SE of the two epicenters, respectively.

This work describes the embankments during the three days of flooding in Larissa City. For this reason, we provide field examples and descriptions to understand the embankments' problems and propose some improvements to their network along the Pineios River in Larissa's territory.

Material and methods

Immediately after the Daniel storm, on the 8th of September 2023, a sector of Larissa City came under the pressure of flooding due to the river overflow reaching 9.5 m. A series of embankments along the river came under pressure. We executed repeated fieldwork in an area characterized by meanders and two riverbeds, the old one flowing through the city and the post-1935 riverbed flowing a few hundred meters north of the old one (Figure 1). During the fieldwork, we mapped overtopping, piping, seepage, and foundation defects. Furthermore, we used Google Earth scenes after the flooding to define the results of embankment failure and to measure the dimensions of the embankments approximately.

Figure 1. Google Earth scene showing the study area, showing localities of embankment problems in close proximity with the Larissa City. Inset shows the location of the study area in Greece.

Data

Five embankment sites were analyzed in detail because these localities caused severe flooding (Figure 1). Embankments, or levees or dykes, are constructed mainly from earth materials and are used to confine stream flow preventing flooding events. Five major embankment sites failed during the storm Daniel from west to east called hereinafter DEYAL, Kioski, Alkazar Stadium I and II, and Alsos (Fig. 1 and Table 1).

Table 1. Embankment dimensions and configurations

	DEYAL	Kioski	Alsos	Alkazar Stadium I and II
Embankment crest width (m)	7,00	7,00	7,00	20,00
Embankment height (m)	5,00-6,00	4,00-5,00	5,00	5,00
Embankment slope (inner and outer)	2:3	1:1,20	2:3	2:3

In the first site, the embankment problems start as seepage. However, this seepage stopped due to the immediate reaction by local authorities during the flooding accumulating earth material and the final repair of the site just after the flood (Fig. 2).

Figure 2. (a) Google Earth scene showing two failed low-height embankments. (b) Field photo of the two failed embankments. (c) The embankment at the DEYAL site was repaired immediately after the flooding. All the localities are at the west entrance of Larissa City, near DEYAL facilities.

The second site at Kioski locality is related to a severe embankment destruction that caused the flooding of large cultivated area and a block of buildings. After the flooding, a 100 m long by 50 m wide and 7 m deep erosional basin was created. This basin is probably the result of extensive water pipping before the embankment collapsed due to overtopping (Fig. 3). At present the embankment is fully restored (Fig. 3). In the same site, we also noticed the existence of small-scale slides across the embankment suggesting that the flooding caused significant problems across the Kioski embankment and the whole area needs analytic inspection. Of particular importance in the Kioski failure is a basin developed on both sites of the embankment that is interpreted as the result of flow along the structural interface of the embankment and the diffused flow through granular media below its foundation.

Figure 3. Google Earth scene showing the Kioski failure on October 2023 note on the satellite view the produced basin due to the embankment failure and the deposited material over cultivated lands. The lower left photo shows the restored embankment a few days after the flooding the photograph was taken looking west. The photograph to the right shows the basin at the south of the embankment.

The Alkazar Stadium sites I and II are two cases where initial piping was stopped by the immediate response by the authorities with the use of earth materials to stop seepage successfully (Fig. 4).

Figure 4. Google Earth scene (left) and field photo (right) of piping failure at locality Stadium just after the Pineios River flooding. The white rectangle in satellite scene show the area of field photo.

Flooding results at the Alsos embankment (Fig. 5) show its destruction for a length of 55 m. In this particular area, at the junction of old and new riverbeds, the flow of the river rise attained a maximum level. As a result, the embankment failed, and the water moved in the river's floodplain over cultivated lands to the northeast. The failure of the embankment in this area was the result of water overtopping. Overtopping phenomena were noticed for 100 m in total beyond the point of the embankment collapse. Concomitantly, the embankment destruction caused the deposition of significant thickness mud over cultivated lands (Fig. 5 blue arrow). The failure at Kioski and Alsos caused the flooding of a large area to the north.

Figure 5. Google Earth scene of the repaired embankment at Alsos locality. The blue arrow shows the flow direction and mud deposition on the cultivated lands. This embankment failure caused by extensive overtopping of the Pineios River.

In addition, second-order failures on the embankments during flooding are noticed in several places ruptures on top of the embankments (Fig. 6a). We interpret these cracks as the result of lateral spreading processes. Except for the along-strike cracks, they are mapped at several places circular to elliptical holes resulting from piping (Fig. 6b). The circular ruptures are interpreted as small-scale landslides commonly developed at the embankments.

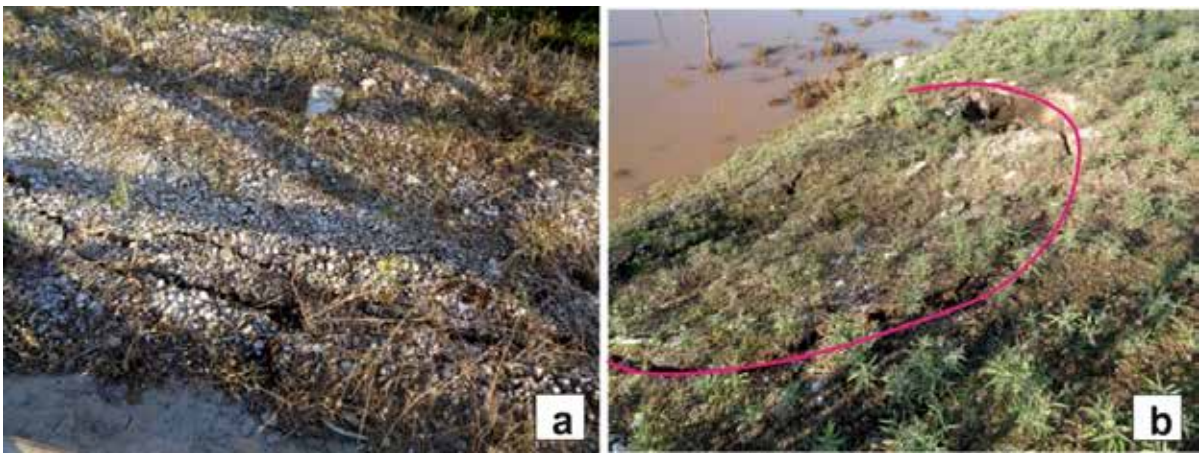

Figure 6 Second order failures of embankments.

In summary, the embankments in the study area are constructed with fine-grained materials were failed for two main reasons: the piping and overtopping. These embankments are categorized as hydrologically or seismically deficient. Notably, in 2021, the area of flooding was rocked by a strong seismic sequence that caused significant ground acceleration in the area of Larissa and their surroundings.

Overtopping manifests when the level of water is higher than the embankment crest elevation, as was the case of Kioski and Alsos. Piping failure of the embankment is caused in DEYAL, probably by the removal of soil particles through the intergranular flow within the soil mass of the embankment.

Discussion

In Greece, Daniel's severe rainfall led to flooding that caused more than two billion euros in damage, making it the costliest recorded storm for the country. Typical embankments in the study area are 80 m at their base and a height of up to 10 m. However, it has to be noticed that these dimensions vary along the entire length of the embankments. Their construction age is from 1930-1970, and their age of construction is ranging from 55-100 years old. The risk of failure of embankments that channelize a river is produced due to seepage induced by temporary and occasional impoundments taking place on the upstream side as a consequence of exceptional rainfalls is frequently underestimated. Commonly the failure of embankments results from the following factors: the flooding event, the hydraulic weakness and the embankment's geotechnical weakness or any combination of these three factors. However, the failure of embankments due to seepage and other water-related issues is often underestimated. In addition, considering climate change will have impacts on flood magnitudes and frequency in the same area we propose that the protection of the villages and cities has to be revised. In particular, for the case of Larissa and its flood hazard, the embankments need inspection after the 2021 earthquake and the 2023 flooding. However, as the area where these embankments are constructed is the Pineios floodplain it is also important to consider the processes related to the stratigraphy of the floodplain.

Conclusions

In five cases, close to Larissa City we mapped almost catastrophic types of failure by sudden, rapid, and uncontrolled release of impounded water. In three cases the emergency action of the local authorities prevents the failure.

Based on the severity of the flooding we considered the failures of the embankments in the territory of Larissa as of low hazard potential. However, given that the area was inflicted by a strong earthquake in 2021 and the flooding in 2023 we consider that a program of careful embankment inspection has to be considered as urgent.

References

Bathrellos G. 2005. Geological, Geomorphological and Geographic Study of Urban Areas in Trikala Prefecture—Western Thessaly. Ph.D. Thesis, National & Kapodistrian University of Athens, Athens, 561 p.

Bathrellos G.D., Skilodimou, H.D., Soukis K., Koskeridou E. 2018. Temporal and Spatial Analysis of Flood Occurrences in the Drainage Basin of Pinios River (Thessaly, Central Greece). Land 7, 106; doi:10.3390/land7030106. **[Journal Article]**

Dimitriou, E.; Efstratiadis, A.; Zotou, I.; Papadopoulos, A.; Iliopoulou, T.; Sakki, G.-K.; Mazi, K.; Rozos, E.; Koukouvinos, A.; Koussis, A.D.; et al. 2024. Post-Analysis of Daniel Extreme Flood Event in Thessaly, Central Greece: Practical Lessons and the Value of State-of-the-Art Water-Monitoring Networks. Water, 16, 980. https://doi.org/10.3390/w16070980. **[Journal Article]**

Kalafatis, A., Kyriou A., Nikolakopoulos K. 2024. Mapping of large-scale flooding in Thessaly region using Sentinel data. Earth Resources and Environmental Remote Sensing/GIS Applications XV, edited by Karsten Schulz, Ulrich Michel, Konstantinos G. Nikolakopoulos, Proc. of SPIE Vol. 13197, 131970F.

Kolios, S.; Papavasileiou, N. 2024. Daily Rainfall Patterns During Storm "Daniel" Based on Different Satellite Data. Atmosphere, 15, 1277. https://doi.org/10.3390/ atmos15111277 **[Journal Article]**

Koukouvelas, IK, Nikolakopoulos, KG, Kyriou, A, Caputo, R, Belesis, A, Zygouri, V, Verroios, S, Apostolopoulos,

D, Tsentzos, I, 2021. The March 2021 Damasi Earthquake Sequence, Central Greece: Reactivation Evidence across the Westward Propagating Tyrnavos Graben. Geosciences, 11, 328. doi.org/10.3390/geosciences11080328. **[Journal Article]**

Koukouvelas, I.K., Caputo, R., Nikolakopoulos, K.G., Kyriou, A., Famiglietti, N.A. 2023. Is the Mesochori Fault a Key Structure for Understanding the Earthquake Activity during the 2021 Damasi Earthquakes in Northern Thessaly, Greece? Geosciences, 13, 331. https://doi.org/10.3390/geosciences13110331 **[Journal Article]**

Mavroulis, S.; Mavrouli, M.; Lekkas, E.; Tsakris, A. 2024. Impact of the September 2023 Storm Daniel and Subsequent Flooding in Thessaly (Greece) on the Natural and Built Environment and on Infectious Disease Emergence. Environments, 11, 163. https://doi.org/ 10.3390/environments11080163 **[Journal Article]**

Sarhosis V., Giarlelis C. Karakostas·C., Smyrou E., Bal I.E., Valkaniotis S., Ganas A. 2022. Observations from the March 2021 Thessaly Earthquakes: an earthquake engineering perspective for masonry structures. Bulletin of Earthquake Engineering, 20, 5483–5515. **[Journal Article]**

17th INTERNATIONAL CONGRESS
of the Geological Society of Greece

BULLETIN OF THE GEOLOGICAL SOCIETY OF GREECE, SP. PUBL.

EXTENDED ABSTRACT 033

Morphotectonic analysis of Antimilos volcanic Group

Belka A.[1], Nomikou P.[1], Bühring S.I.[2], Bejelou K.[1], Lampridou D.[1], Kothri S.[1], Varotsou E.[1], Bach A.[3], Papanikolaou D.[1]

(1) Department of Geology and Geoenvironment, National and Kapodistrian University of Athens, Athens, Greece, aretibelka@gmail.com (2) MARUM- Center for Marine Environmental Sciences, University of Bremen, Bremen, Germany (3) Faculty of Geosciences, University of Bremen, Bremen, Germany

Introduction

The Aegean Volcanic Arc, a crucial part of the Hellenic Arc and Trench System, is situated along the convergent boundary of the northward-subducting African Plate beneath the European Plate and since the Late Miocene beneath the Aegean Plate This volcanic arc has demonstrated continuous activity for at least the last 45 million years, as evidenced by various geological studies (McKenzie, 1972; Le Pichon et al., 1979; Papanikolaou, 1993; Royden & Papanikolaou, 2011). The current geodynamic structure includes the Hellenic Trench, a 1500-km-long arcuate trough extending from the Ionian Sea to the Libyan Sea, with the South Aegean volcanic arc developed parallel to it.

The Milos volcanic center comprises a cluster of islands located at the junction between the Myrtoon Basin, Cretan Basin, and southwestern border of the Cycladic plateau. This region includes Milos, Kimolos, Antimilos, Poliaigos, and smaller islets such as Akrathi and Arkadi. Antimilos is positioned 8.9 km northwest of Milos Island and is entirely composed of volcanic rocks with its highest elevation reaching 686 m (Sonder, 1924; Marinos, 1961). The volcanic deposits on Antimilos have been dated to approximately 0.32 million years ago (Fytikas et al., 1986), though this only represents a portion of its volcanic history.

Antimilos Onshore Geology

The island of Antimilos serves as the subaerial manifestation of the only composite volcano within the Milos Volcanic Field, as established by Fytikas et al. (1986) and Vougioukalakis et al. (2019). This roughly triangular island features two prominent topographic elevations: the rounded northern peak reaching approximately 686 meters, and a smaller southern peak at 435 meters. The simplified stratigraphy of Antimilos, as shown in the modified by Marinos (1961) geological map (Fig. 1a, 1b), consists of several distinct layers. Multiple dacitic domes overlying lower pyroclastic formations, with one major dome forming northern peak Sterna and other minor domes comprising Agiokastro peak and Alonia crater. Distinct eruptions have followed with new dacitic products emerging at Agiokastro peak alongside two neighboring craters and new andesitic products at Sterna peak, where thin volcanic flows extend toward eastern and western slopes from previous dacitic domes in a relatively smooth relief compared to earlier steep slopes.

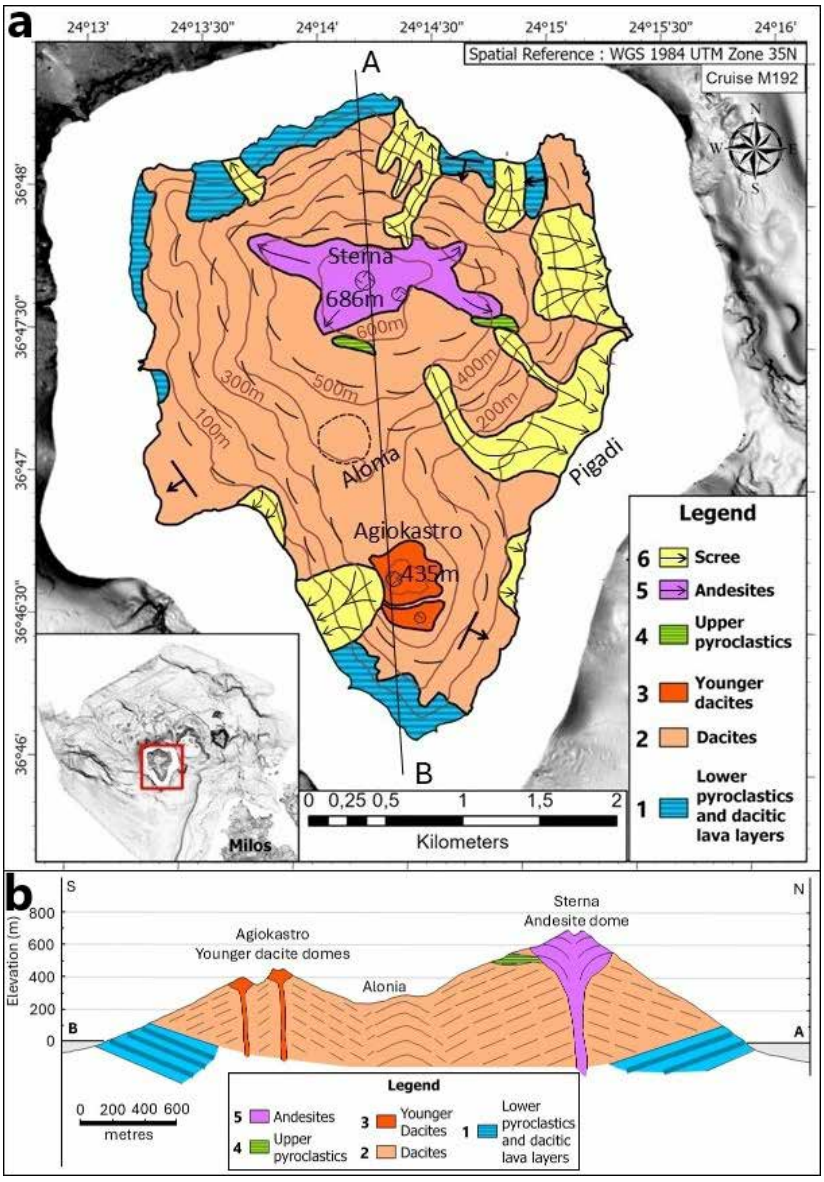

Figure. 1. (a) Geological map of Antimilos Island, modified after the geological sketch of Marinos (1961). (b) N-S Geological Profile across the Antimilos volcano.

Materials and Methods

The survey aboard R/V METEOR during cruise M192 (August 8 – September 5, 2023) utilized the EM710 multibeam echosounder for high-resolution seabed mapping. The system, operating effectively at depths of 3–2000 meters with a swath width up to 5.5 times water depth, covered areas from northern Milos southeastward. Data acquisition, managed via SIS software, integrated sound speed profiles and collected bathymetric (.all) and water column data (.wci), excluding AUV deployment/recovery phases.

Bathymetric data were processed in Qimera QPS, with manual corrections using Slice Editor and 3D Editor, resulting in a 5-meter resolution CUBE surface. Seismic profiles from the ATLAS PARASOUND P70 system provided morphological and sub-bottom data via high- and low-frequency parametric sonar.

Results

The constructed bathymetric map of the seafloor morphology around Antimilos Island reveals intricate features and distinct geological formations (Fig. 2). The analysis indicates that the seafloor morphology

transitions from the shelf zone, which extends up to approximately 140 meters in depth, down to the deeper regions of the southern Myrtoon Basin at around 1000 meters. Notably, in the transect from NW Milos to Antimilos, the Milos shelf exhibits a width of about 5 km, while that of Antimilos is significantly narrower, measuring less than 1 km. Between these two regions lies a small basin with depths ranging from 300 to 320 meters.

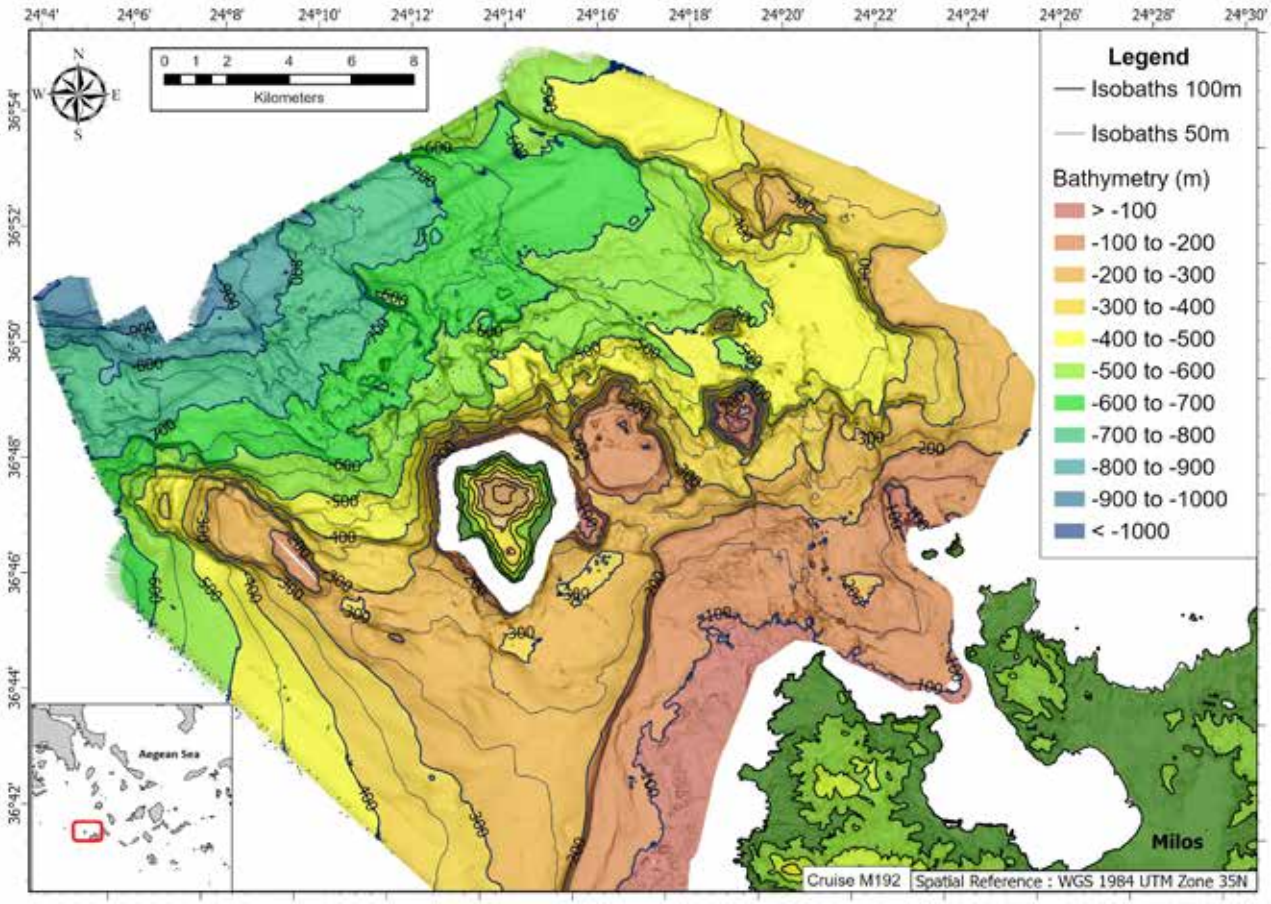

Fig. 2. Detailed swath bathymetry map of the Milos-Antimilos volcanic field (resolution 5 meters). The onshore DEM is obtained from SRTM and has a pixel size of about 30 meters resolution. The location of Antimilos is given in the inset map.

Three prominent submarine volcanic domes are identified to the east of Antimilos (Fig. 3) : Bangos cone, Shallow cone, and Deep cone. The largest of these is Bangos cone, followed by the medium-sized Shallow cone and the smaller Deep cone located further north. The NW slope hosting Antimilos and these three sea mounts is bordered by two significant NW-SE trending cliffs: one from the northeast at depths between 300 and 600 meters, marking the boundary with the Cycladic plateau, and another from the southwest at similar depths forming what is referred to as the Western Ridge. Bangos Dome stands at 349 meters tall and the summit has a flat top with a mean water depth of 140–145 meters. This flat area likely resulted from wave erosion during periods of low sea level. Shallow Cone reaches a total height of 417 meters with its summit at a depth of 58 meters. Although wave activity during the Last Glacial Maximum eroded its summit, it remains the shallowest cone among the three. A shelf has developed at depths between 130-140 meters. Deep Cone has with a total height of 226 meters and a conical shape that narrows significantly towards the summit with its peak at 293 meters below sea level. Due to its depth, it has remained unaffected by low sea level fluctuations that have impacted the other two domes.

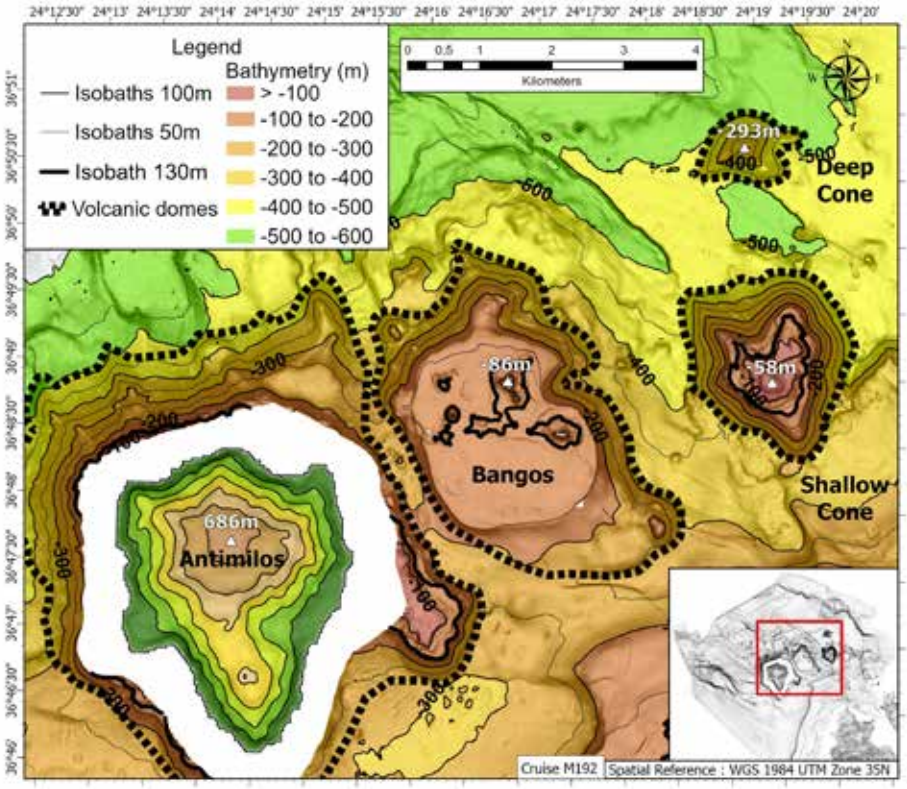

Figure. 3. Bathymetric map showing the boundaries of the volcanic domes NE of Antimilos island.

The hummocky area (Fig. 4) located offshore northwestern Antimilos is characterized by a rough, blocky terrain and has been identified as a significant Volcanic Debris Avalanche (VDA) deposit, which plays an essential role in understanding the geological processes that have shaped the area. The VDA covers approximately 72 km² and consists of numerous blocks that vary widely in size, shape, and orientation (Fig. 4). A detailed morphometric analysis was conducted on them, focusing on several key parameters such as height, area, distance from the coastline, and volume. The vertical drop-to-run-out ratio (H/L) was calculated to assess the mobility of the displaced material. The analysis revealed a total of 88 individual blocks distributed along the foot slope, extending up to 8.3 km from the coastline. Their orientation generally aligns with the slope's direction but also displays a discernible trend along a SE-NW axis.

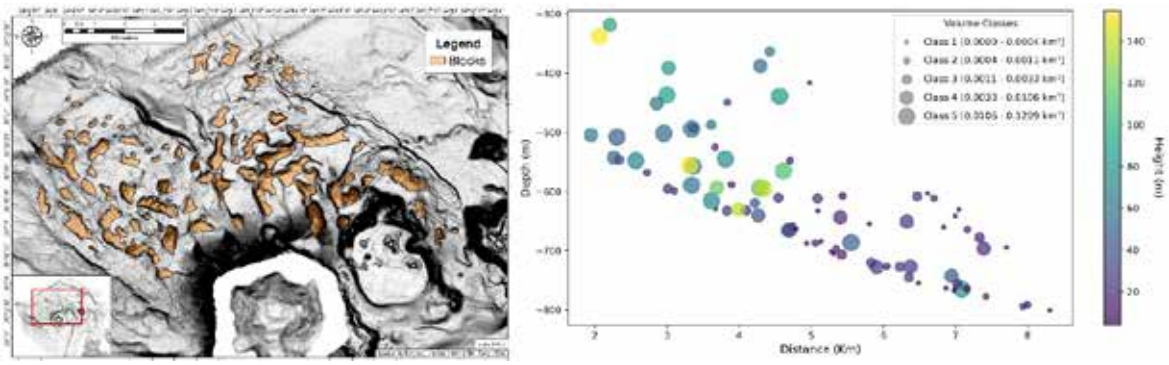

Figure. 4. VDA Blocks. (a) Gray-shaded map showing the identified blocks. (b) Scatter plot depth vs distance from the coastline of the block. The color scale indicates the height of each block.

Conclusions

The morphotectonic analysis of the Antimilos volcanic field, northwest of Milos Island, reveals four volcanic structures: the subaerial Antimilos volcano and three submarine volcanoes. The volcanic relief is 1180 m for Antimilos, 350 m for Bangos, 420 m for the Shallow and 200 m for the Deep Cone. Except for the Deep Cone the other three domes are highly affected by the climatic fluctuations, which have peneplained the Bangos dome at 140 m depth and have created a broad shelf zone at 100-140 m depth in Antimilos Island and the Shallow Cone. The available Middle Pleistocene age of 0.32 Ma indicates a pre-Holocene volcanic activity including the development of the shelf at least during the last three low stands. On the contrary, all three submarine volcanic cones are rather geometric, indicating one major volcanic phase, probably also of Middle Pleistocene age, judging from the development of the shelf in the two shallow cones.

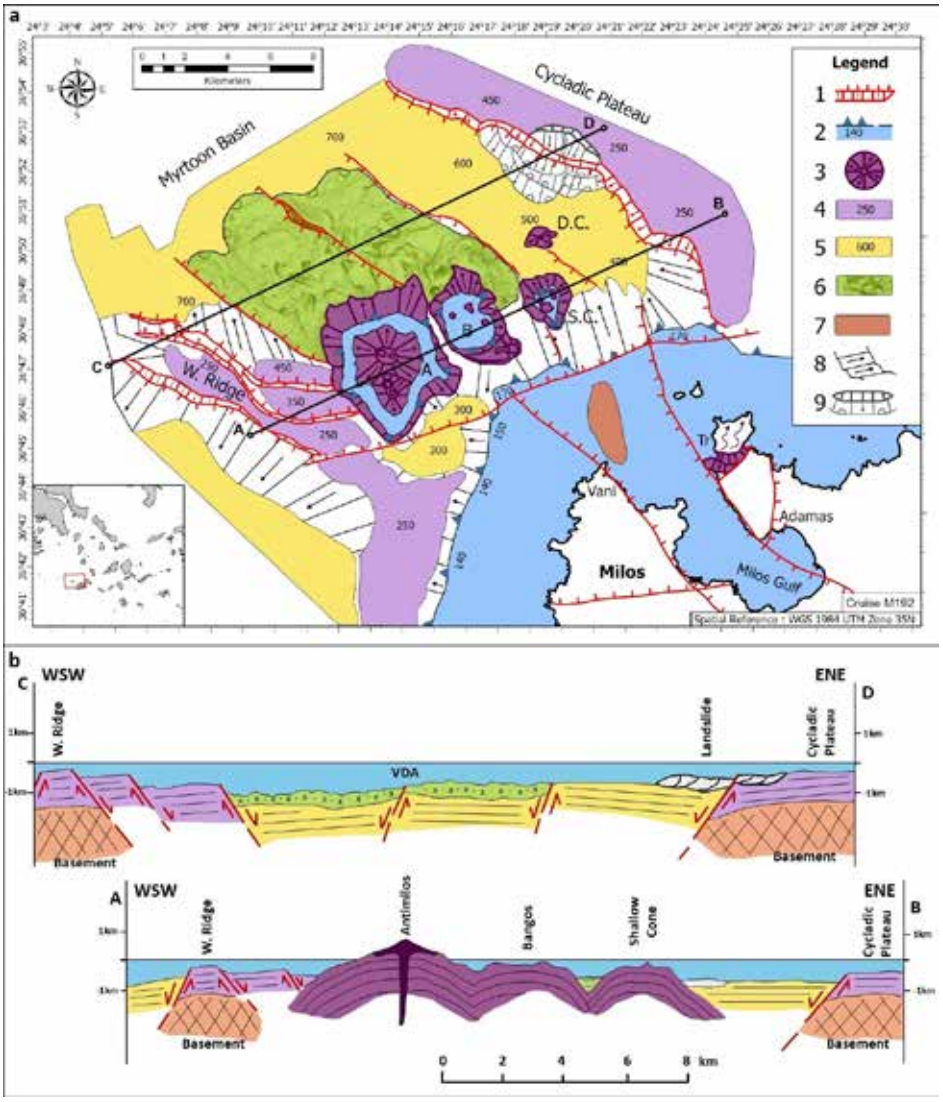

Figure 5. Morphotectonic map of the Milos-Antimilos volcanic field. Tr : Trachilas volcano, A : Antimilos Island, B : Bangos Cone, S.C. : Shallow cone, D.C. : Deep cone, 1 : Normal fault, 2 : Shelf and shelf break, 3 : Volcanic dome, 4 : Submarine Plateau, 5 : Basin, 6 : VDA – Flow direction, 7 : Distribution of flairs, 8 : Moderate morphological slope, 9 : Landslide and related fans. b) Subparallel tectonic profiles through the shallow (A-B profile at 300-500 m depth) and the deep (C-D profile at 500-800 m depth) parts of the Antimilos tectonic graben. The main elements are the three volcanic domes along the shallow profile and the VDA deposits along the deep profile.

The Antimilos group lies at the 7 km wide shallow zone extending between 250 m and 500 m depth within the 17 km long depression/tectonic graben formed to the NW of Milos, bounded by two prominent NW-SE normal faults one towards the NE from the Cycladic plateau and another from the SW from the Western Ridge (Fig. 5). Three additional NW-SE faults traverse the graben's central zone at depths of 600–900 m, confining extensive VDA deposits originating from the Antimilos and Bangos domes. This hummocky area contains volcanic blocks transported several kilometers northwest from their sources. The volcanic domes of Antimilos are located at depths of 500–250 m within the graben's shallow zone, while deeper profiles feature VDA deposits bordered by intra-basin faults. An intermediate zone (200–300 m depth) separates Antimilos from the NW Milos shelf, delineated by an ENE-WSW fault zone over 20 km long. This fault disrupts the NW Milos shelf, causing displacements of up to 30 m and delimiting the Vani hydrothermal vent field. Despite the shared NW-SE fault trend in both areas, there is no structural continuity across the ENE-WSW fault zone. The fault's 20 m Holocene displacement over 14 ka corresponds to a slip rate of 1.43 mm/year. The volcanic domes' development reflects climatic fluctuations, with low-stand periods (~100 ka) causing subaerial erosion and high-stand periods (10–20 ka) promoting marine deposition. Antimilos exhibits dacite and andesite domes with minor pyroclastic deposits, while Bangos, Shallow, and Deep Cones consist solely of volcanic domes, the Bangos Cone accompanied by two minor domes.

A vast hummocky area of VDA deposits with sliding blocks of volcanics occurs to the NW of Antimilos and Bangos domes, reaching 5-7 km distance down to 700-800 m depth, bounded by NW-SE normal faults at the central zone of the Antimilos tectonic graben. Their distribution aligns with the SE-NW trend of debris flows (Alexandri et al., 2001; Nomikou et al., 2013, 2014). The Antimilos VDA deposits shows several similarities to the VDA deposits reported from Santorini and Nisyros along the eastern part of the Aegean volcanic arc.

Acknowledgements

We are thankful to the the Dept. of Geology & Geoenvironment of the University of Athens (NKUA-GREECE), the University of Hamburg, and the collaborative project from the DFG Emmy Noether Group Hydrothermal Geomicrobiology, led by chief scientist S.I. Bühring, titled "Bridging Hydrothermal Sites Along the Hellenic Arc off Milos from Shallow to Deep". We also thank the Programme for the promotion of the exchange and scientific cooperation between Greece and Germany IKYDA 2024 "Bridging the Gap between hydrothermal biogeochemistry and Volcano-Tectonics: Exploring Synergies Along the Hellenic Arc off Milos (BITECHELL)", and all the shipboard personnel for a great expedition.

References

Alexandri, M, Papanikolaou, D., Nomikou, P. and Ballas, D. (2001) 'Geological Structure of the Myrtoon Basin (Aegean Sea) Based on Swath Bathymetry', Rapport Commission International Pour lexplorationscientifique de La MerMediterranee, 36 (3).

Fytikas, M. et al. (1986) 'Volcanology and petrology of volcanic products from the island of Milos and neighbouring islets', Journal of Volcanology and Geothermal Research, 28(3–4), pp. 297–317.

Le Pichon, X.L. and Angelier, J. (1979) 'The hellenic arc and trench system: A key to the neotectonic evolution of the eastern mediterranean area', Tectonophysics, 60(1–2), pp. 1–42.

Marinos, G. (1961) 'The Antimilos volcano in Aegean Sea', Bull Geol Soc Greece IV (1), pp. 38–50.

McKenzie, D. (1972) 'Active tectonics of the Mediterranean region', Geophysical Journal International, 30(2), pp. 109–185.

Nomikou, P., Papanikolaou, D., Tibaldi, A., Carey, S., Livanos, I., Bell, K.L.C., Pasquarè, F.A., Rousakis, G. (2014) 'The Detection of Volcanic Debris Avalanches (VDAs) Along the Hellenic Volcanic Arc, Through Marine Geophysical Techniques.', In Submarine Mass Movements and Their Consequences: 6th International Symposium, edited by Sebastian Krastel, Jan-Hinrich Behrmann, David Völker, Michael Stipp, Christian Berndt, Roger Urgeles, Jason Chaytor, Katrin Huhn, Michael Strasser, and Carl Bonnevie Harbitz, 339–49. Cham: Springer International Publishing.

Nomikou, P., Papanikolaou, D., Alexandri, M., Sakellariou, D. and Rousakis, G. (2013) 'Submarine Volcanoes along the Aegean Volcanic Arc', Tectonophysics, 597–598:123–46.

Papanikolaou, D. (1993) 'Geotectonic evolution of the Aegean', Bull. Geol. Soc. Greece, 28(1), 33-48.
Royden, L.H. and Papanikolaou, D.J. (2011) 'Slab segmentation and late Cenozoic disruption of the Hellenic arc', Geochemistry, Geophysics, Geosystems, 12(3), p. 2010GC003280.
Sonder, R. (1924) 'Zur Geologie and Petrographie der Inselgruppe yon Milos', Zeitschr. Volc, 8, pp. 11–231.
Vougioukalakis, G. E., Satow, C. G., & Druitt, T. H. (2019) 'Volcanism of the South Aegean Volcanic Arc. Elements', 15(3), 159–164.

17th INTERNATIONAL CONGRESS of the Geological Society of Greece

BULLETIN OF THE GEOLOGICAL SOCIETY OF GREECE, SP. PUBL.

EXTENDED ABSTRACT 034

The Geoheritage as a tool to engage children with the Sustainable Development Goals in UNESCO Global Geoparks: Best practices of educational activities from Lesvos Island UNESCO Global Geopark

Konstantina Bentana[1,2], Nikolaos Zouros[1,2]
(1) UNESCO Chair on Geoparks and Sustainable Development of Insular and Coastal Areas, Department of Geography, University of the Aegean, Greece, k.bentana@aegean.gr, (2) Natural History Museum of the Lesvos Petrified Forest

Introduction

Geoheritage constitutes an excellent tool for UNESCO Global Geoparks for the teaching of many cognitive subjects as well as the education of school students of all educational levels in a series of fundamental local or global problems that our society faces (Bentana and Zouros, 2020).

At the same time, UNESCO and other international organizations have been urging educators to seek out and utilize new learning environments outside the classroom, as well as pedagogical tools such as geological heritage in UNESCO Global Geoparks, in order to engage students with issues of sustainability and environmental protection (UNESCO, 2019).

UNESCO Global Geoparks utilize all aspects of their geological heritage in combination with natural and cultural heritage to enhance the education of children and their understanding of contemporary local or global problems (UNESCO, 2016).

However, for the next generation to be able to address contemporary problems, they must know what these problems are. A good way to ensure this is by engaging children to the subjects of the Sustainable Development Goals (SDGs). At the same time, the Sustainable Development Goals help children to understand our impact on the planet, to see the bigger picture and what role we can all play in taking responsibility.

By integrating geological heritage and processes with broader environmental, cultural, and social narratives, UNESCO Global Geoparks offer immersive, hands-on learning experiences among young learners. These natural learning environments not only highlight Earth's dynamic history but also provide a unique platform to illustrate the interconnectedness of geological and natural systems with human activities. In this context, geological heritage becomes a compelling pedagogical tool for introducing children to the Sustainable Development Goals.

This paper aims to explore how geological heritage, when combined with educational infrastructure and active engagement, can effectively involve school students in learning about the UN Sustainable Development Goals. Drawing on best practices from educational activities successfully implemented by the Natural History Museum of the Lesvos Petrified Forest, management body of the Lesvos Island UNESCO Global Geopark, this paper highlights how such initiatives provide meaningful learning experiences beyond the traditional classroom setting. By using local examples and fostering international collaborations, these programs offer students a rich context for understanding global challenges and contribute to the development of informed and active citizens.

Methods

The methodology used for this paper involved a qualitative case study, focusing on the educational activities implemented by the Natural History Museum of the Lesvos Petrified Forest within the Lesvos Island UNESCO Global Geopark. This methodology included an analysis of the educational programmes, focusing on their content, target school student groups, and connections to the Sustainable Development Goals. In addition, the study included the documentation of these educational activities to demonstrate how geoheritage education is applied in alignment with the Sustainable Development Goals in practice. In this paper, we analyzed three educational programmes based on the age of the children: 5-8, 9-12 and 13-17 years old.

Results

Lesvos Island UNESCO Global Geopark offers a wealth of geosites such as the Petrified Forest, which has

been designated a Protected Natural Monument, volcanoes, hot springs, important fossiliferous sites, faults, waterfalls, coastal landforms, which constitute significant evidence of the geological history of the Aegean area and contributed to the island's recognition as UNESCO Global Geopark (Zouros *et al.*, 2015).

Geosites and the rich geoheritage of the island are the main tools that are used for educational purposes by the Natural History Museum of the Lesvos Petrified Forest, the management body of the Lesvos UNESCO Global Geopark. The Museum actively utilizes the island's unique geoheritage in its educational programmes to engage children with the subjects of the Sustainable Development Goals. The educational activities analysed demonstrate a strong connection between geological heritage and the Sustainable Development Goals, and cultivate active citizens.

The first educational programme analysed is entitled "The Deinotherium and the Animals of the Petrified Forest" and is dedicated to school students 7-9 years old.

The programme aims to help children acquire values for the protection of biodiversity and geological heritage. The educational programme focuses on the paleoenvironment of the Petrified Forest, allowing students to identify different fossilized plant species and learn about the animals that coexisted 20 million years ago. Children get to know the animals through the replica of the Lesvos Deinotherium and the Liota crocodile. A theatrical play has been designed for younger children, and the pupils embody roles from the dramatized story of the Petrified Forest (Figure 1).

Geoheritage link: The diverse fossilized flora and fauna within the Petrified Forest showcase the rich biodiversity of the past ecosystems of Lesvos. This provides a baseline for understanding current biodiversity and the impact of habitat loss and environmental change.

Connecting Geoheritage to SDG: 15 "Life on Land"

Preparing active citizens: Students participate in discussions about the need for protecting present-day biodiversity, engaging in activities like creating their school and home gardens, and returning to the Museum petrified tree trunks that they identify by accident.

Figure 1. Children embody roles from the dramatized story of the Petrified Forest.

The second educational programme analysed is entitled "Climate change: learning about the impacts by observing the Lesvos Petrified Forest" and is dedicated to school students 9-12 years old.

The aim of the educational programme is students to understand the consequences of climate change on biodiversity. At the Petrified Forest Park and at the exhibition room of the Natural History Museum of the Lesvos Petrified Forest, children analyze fossilized leaves and tree rings to understand the past climate of Lesvos (Figure 2). Children continue their research at the botanical garden of the museum and are asked to look for evidence about the climate in the modern ecosystem of the Lesvos Petrified Forest area. By observing the vegetation at the time the Petrified Forest lived and the current vegetation, they record the data they collected, process it, and draw their conclusions about the consequences of climate change in the biodiversity of the region over the last 18Ma. Children then compare their results about past climate with the current climate crisis,

discussing the accelerated rate of change and the human impact.

Geoheritage link: The Petrified Forest itself is a direct record of past climate and environmental change during the early Miocene. Fossilized plants provide evidence of a subtropical forest ecosystem and the subsequent environmental shifts caused by volcanic activity and changing climate conditions.

Connecting geoheritage to SDG: 13 “Climate Action”

The Petrified Forest of Lesvos provides invaluable records of past climate change, aiding in the scientific understanding of current and future climate trends.

Preparing active citizens: International collaborations between schools from Lesvos and schools from other UNESCO Global Geoparks around the globe are implemented, encouraging children to participate in common activities. One such activity was implemented in collaboration with Maiella UNESCO Global Geopark (Italy). School students were encouraged to join the educational action “I LOWER THE LIGHTS, LIGHT UP THE FUTURE!” where school students were encouraged to turn off the lights in their school on a specific day and to discover what they can do themselves to save energy in their everyday life at school and at home and how they can become active citizens (Figure 3).

Figure 2. Children participate in research activities at Lesvos Petrified Forest for past climate records.

Figure 3. Children from Vatousa Elementary school joined the educational action “I LOWER THE LIGHTS, LIGHT UP THE FUTURE!” and turned off the lights in their school.

The third educational programme analysed is entitled “Natural Processes on our planet. All about the earthquakes” and is dedicated to school students 13-17 years old.

The main part of the educational programme is the experiential activity of earthquake simulation on the museum's seismic simulator. The seismic simulator has been shaped like a school classroom, and children experience devastating earthquakes from Greece and around the globe. On the seismic simulator the children are trained on how to respond to earthquakes and learn about preparedness measures (Figure 4).

Geoheritage link: Lesvos is located in a seismically active region. Understanding the geological processes that lead to earthquakes is crucial for building resilient communities.

Connecting geoheritage to SDGs: 11 "Sustainable cities and communities"

Knowledge of geological hazards, such as earthquakes, is critical for developing resilient and sustainable urban and rural communities.

Preparing Active Citizens: Students become more informed about earthquake hazards and are empowered to take proactive steps for their safety and contribute to community resilience efforts.

Figure 4. Children participate in the experiential activity of earthquake simulation on the museum's seismic table and are implementing the preparedness measures in case of an earthquake.

Conclusions

Geoheritage serves as an exceptionally powerful and effective pedagogical tool for engaging children with the Sustainable Development Goals. The comprehensive educational activities developed and implemented by the Natural History Museum of the Lesvos Petrified Forest in the Lesvos Island UNESCO Global Geopark provide a robust model for how to leverage geological heritage to foster environmental awareness, promote sustainable practices, and empower young generations. By offering hands-on activities, interdisciplinary approaches and age-appropriate learning experiences, these programs aim to foster a deeper understanding of sustainability challenges and empower students to become informed, responsible, and active citizens committed to a sustainable future. The best practices and valuable lessons learned from the Lesvos Island UNESCO Global Geopark are highly adaptable and can be effectively applied in other UNESCO Global Geoparks and diverse educational settings worldwide, contributing significantly to global sustainability efforts.

References

Bentana, K., Zouros, N., 2020. Educational activities to enhance geomorphological heritage sites in Lesvos UNESCO Global Geopark.

UNESCO, 2016. UNESCO Global Geoparks contributing to the Sustainable Development Goals. Celebrating Earth heritage, Sustaining local Communities.

UNESCO, 2019. Framework for the implementation of Education for Sustainable Development (ESD) beyond 2019, 40 C/23.

Zouros, N., Bentana, K., Valiakos, I., Vasilieadou, K., Thomaidou, E., 2015. Guide of the Lesvos Geopark.

17th INTERNATIONAL CONGRESS of the Geological Society of Greece

BULLETIN OF THE GEOLOGICAL SOCIETY OF GREECE, SP. PUBL.

EXTENDED ABSTRACT 035

Environmental controls on *Globorotalia menardii* size variability preceding the Tortonian/Messinian boundary

Besiou E.[1], Kontakiotis G.[1], Vasiliev I.[2], Antonarakou A.[1]

(1) Department of Historical Geology-Paleontology, Faculty of Geology and Geoenvironment, School of Earth Sciences, National and Kapodistrian University of Athens, Panepistimiopolis, Zografou, 15784 Athens, Greece (2) Senckenberg Biodiversity and Climate Research Centre, Senckenberganlage 25, D-60325 Frankfurt am Main, Germany

Research Highlights

Analyzing the potential drivers of *Globorotalia menardii* size variability in the eastern Mediterranean, we compare the *G. menardii* maximum diameter with the most significant regional environmental parameters during the Late Miocene. Among the examined abiotic factors, the strongest correlations were found to be with oxygen isotopic composition ($\delta^{18}O$) and sea surface salinity (SSS), while the correlations with sea surface temperature (SST) and carbon isotopic composition ($\delta^{13}C$) of planktonic foraminifera were relatively weak, suggesting that salinity had a greater impact on *G. menardii* size than sea surface temperature or primary productivity.

Introduction

Morphological changes in marine microorganisms have been of increasing interest to more and more researchers over the last decades. The size variability of species, a significant morphological parameter, can be altered by paleoceanographic changes reflecting global environmental events and/or local hydrographic changes (Schmidt *et al.*, 2004; Metcalfe *et al.*, 2015). Particularly, planktonic foraminifera are commonly preferred for morphological investigations, as they capture the abiotic environmental parameters in water masses, such as temperature, salinity, stratification and productivity (Adebayo *et al.*, 2023), but also for their abundance and global distribution (Schmidt *et al.*, 2004). Moreover, it has been observed that planktonic foraminifera can reach their maximum size under favorable conditions in the water column, while away from these areas occurred the opposite (Hecht, 1976), indicating their adaptive responses to the modified water mass structure (Friesenhagen, 2022; Besiou *et al.*, 2023). For the documentation of test size alterations, several studies have been carried out on illustration of the morphological variability of both Neogene and modern planktonic foraminifera. Particularly for the studies dealing with *G. menardii*, most of them have been performed in the Pacific, Atlantic, and Indian Oceans (Bhonsale and Saraswat, 2012; Knappertsbusch, 2016, 2022; Friesenhagen, 2022), showing that its size varies significantly over the different oceanic basins. Nevertheless, there is a gap in the morphometric study applied to the sedimentary archive of Mediterranean basin, without any evidence of size distribution patterns of *G. menardii* from this marginal subtropical setting.

Objectives

In our effort to examine how the environmental factors interplay with the observed morphological variability, we mainly attempt to investigate which environmental factor had the greatest influence on the size alterations of *G. menardii* specimens picked up from Potamida section (Crete Island, eastern Mediterranean; Fig. 1).

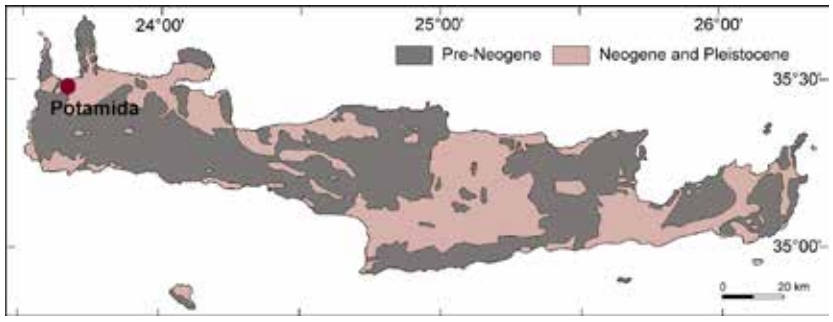

Figure 1. Geological sketch map of Crete Island, showing the Potamida section position (red circle).

On this context, the size variations of the analyzed species correlated to TEX_{86}-derived SST and SSS reconstructed values (Besiou *et al.*, 2024). Additional indices such the coiling direction and the species abundance were also evaluated as biotic measures of the foraminiferal ecological optimum conditions.

Material and Methods

The studied samples were collected from Potamida section in western Crete during the Thalys Project in 2017. Potamida section consists of blue-grey marls in the Tortonian and white-beige pelagic marls to clay limestones towards the Messinian (Agiadi *et al.*, 2017; Moissette *et al.*, 2018). The chronostratigraphic framework of the study section resulted from the combination of planktonic foraminiferal biostratigraphy, magnetostratigraphy and cyclostratigraphy published in Besiou *et al.* (2024) (Fig. 2). For size analysis, 10 specimens of *G. menardii* form 5 were handpicked from the >250 μm size fraction split per sample for the 7.36–7.24 Ma time interval. Then, the foraminiferal shells were positioned to capture the maximum diameter of each individual in the umbilical side and were photographed by a LEICA MZ16 stereo-zoom microscope supplemented by a digital camera connected to a computer. For testing the potential relationship to environmental perturbations, $\delta^{18}O$ and $\delta^{13}C$ isotopes measured on the shallow-dweller *Globigerinoides obliquus*. Moreover, SST estimates were calculated based on TEX_{86} biomarker proxy and SSS through the combined stable isotope and biomarker-based SST data.

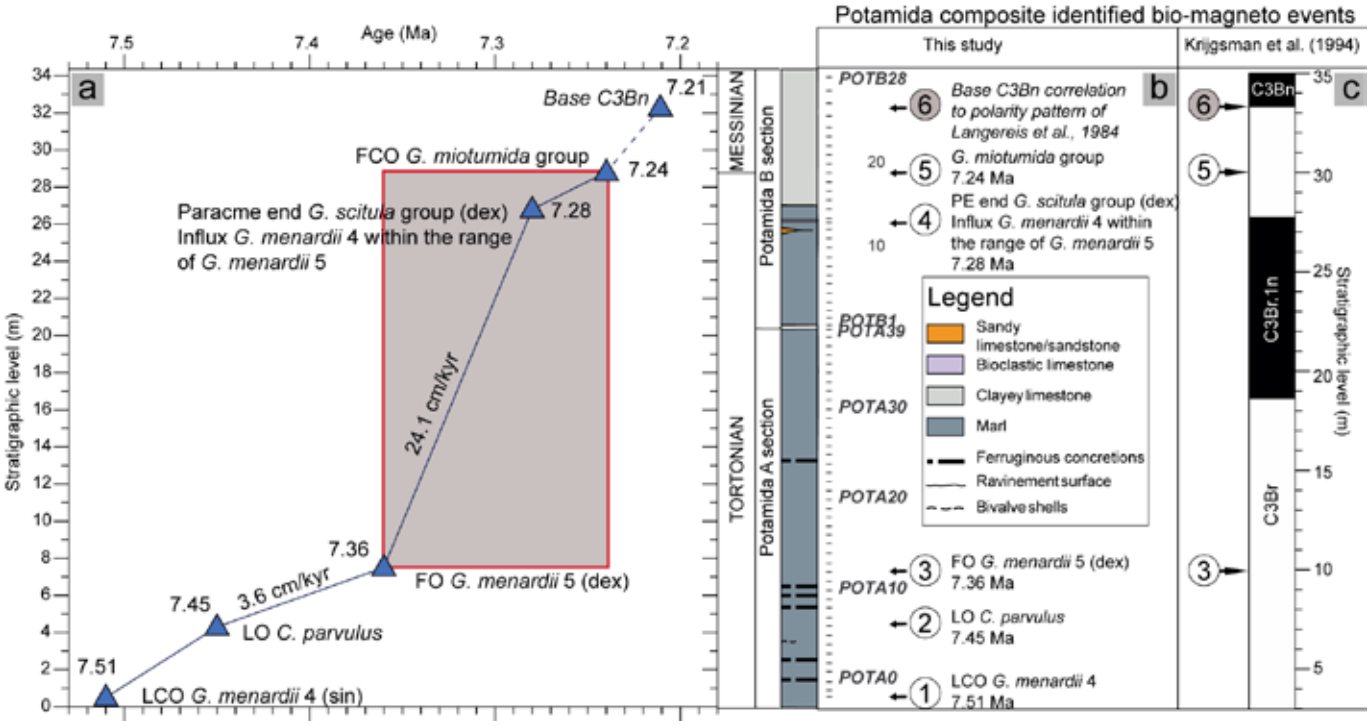

Figure 2. a) Age model of the composite Potamida section (modified by Besiou et al. 2024) with marked the studied time interval (represented by the red frame). b) The lithostratigraphy of the section along with five astronomically calibrated planktonic foraminiferal bio-events (labelled from 1 to 5) and the base of C3Bn magnetic polarity zone labeled in grey circle as event 6. c) The composite magnetostratigraphy based on Krijgsman et al. (1994).

Results

The evaluation of the existing dataset of Late Miocene Potamida section showed that optimum conditions in *G. menardii* are better inferred from its preferred environmental conditions rather than its relative abundance.

Therefore, the relative abundance may not the best descriptor of optimum growth conditions in planktonic foraminifera as the observed pattern is possibly attributed to adaptation strategies of the targeted species as a response to regional environmental forcings (Besiou *et al.*, 2023). Moreover, the coiling direction of this species within the study time interval remained constant (dextral) and not environmentally controlled. Size analysis further highlighted a quite large range of sizes between 330-450 μm (Fig. 3), consisting of small, intermediate and large specimens. These three groups of test sizes clearly reflect a biological adaptation to the significant environmental changes that took place in the Mediterranean Sea during the latest Tortonian. The distribution pattern of the average size of *G. menardii* varies significantly over the 7.36-7.24 Ma time interval. Size fluctuations are better correlated with the oxygen isotopic signal and more explicitly with the SSS reconstructions, indicating that the morphological characteristics are mostly influenced by the vertical changes of upper water column stratification in terms of salinity variations within the thermocline. This relationship is inversely proportional, with higher salinity conditions leading to smaller sizes in *G. menardii*.

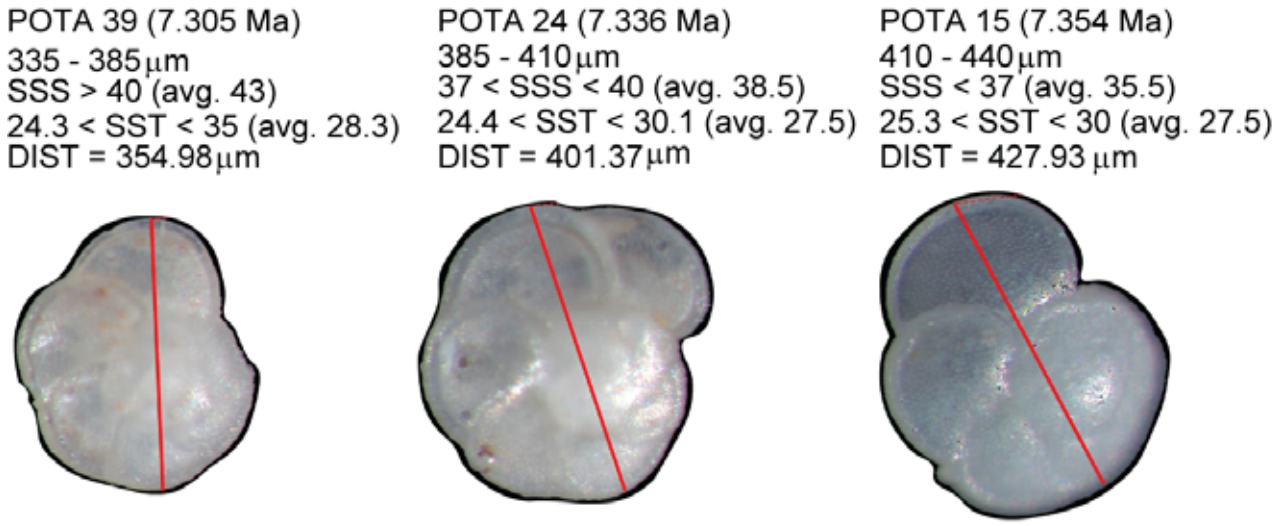

Figure 3. Images of *G. menardii* specimens separated in three maximum size groups (from the left to the right small, intermediate and large specimens).

Conclusions

The linear correlation analyses among the environmental parameters indicated that the dependence of test size on the temperature is not primary as initially thought to be, but secondary. Within such a highly evaporative stressed environment, salinity exerts a stronger influence on the size of *G. menardii* compared to sea surface temperature. Moreover, primary productivity seems to have only a minimized effect in such an ultra-oligotrophic setting as the Late Miocene eastern Mediterranean. The large size variability observed in Potamida samples corresponds to both small and large specimens of *G. menardii* (including intermediates) that were produced during colder/saltier and warmer/fresher sea water events in the lower and upper thermocline, respectively. Overall, our findings highlight the importance of analyzing species-specific paleoceanographic records around the globe by evaluating the shell size response to different environmental drivers in a regional context.

Acknowledgements

The authors would like to acknowledge the Goethe Universität–Senckenberg BiK-F and the Department of Historical Geology–Paleontology of the National and Kapodistrian University of Athens (NKUA) for providing laboratory facilities.

References

Adebayo, M.B., Bolton, C.T., Marchant, R., Bassinot, F., Conrod, S., de Garidel-Thoron, T., 2023. Environmental Controls of Size Distribution of Modern Planktonic Foraminifera in the Tropical Indian Ocean. Geochemistry 24, e2022GC010586. **[Journal Article]**

Agiadi, K., Antonarakou, A., Kontakiotis, G., Kafousia, N., Moissette, P., Cornée, J.J., Manoutsoglou, E., Karakitsios, V., 2017. Connectivity controls on the late Miocene eastern Mediterranean fish fauna. International Journal of Earth Sciences 106, 1147–1159. **[Journal Article]**

Besiou, E., Kontakiotis, G., Vasiliev, I., Moissette, P., Cornée, J.-J., Antonarakou, A., 2023. Evolutionary Palaeoecological and Morphological Response of *Globorotalia menardii* to Environmental Stress Conditions Preceding the Tortonian-Messinian Boundary in the Mediterranean Basin, Journal of Marine Science and Engineering 11(6), 1228. **[Journal Article]**

Besiou, E., Vasiliev, I., Kontakiotis, G., Agiadi, K., Methner, K., Mulch, A., Krijgsman, W., Antonarakou, A., 2024. Large and rapid salinity fluctuations affected the eastern Mediterranean at the Tortonian–Messinian transition. Palaeogeography, Palaeoclimatology, Palaeoecology 656, 112568. **[Journal Article]**

Bhonsale, S., Saraswat, R., 2012. Abundance and size variation of *Globorotalia menardii* in the Northeastern Indian Ocean during the late quaternary. Journal of the Geological Society of India 80, 771-782. **[Journal Article]**

Friesenhagen, T., 2022. Test-size evolution of the planktonic foraminifer *Globorotalia menardii* in the eastern tropical Atlantic since the Late Miocene. Biogeosciences 19, 777-805. **[Journal Article]**

Hecht, A.D., 1976. An ecologic model for test size variation in Recent planktonic foraminifera; applications to the fossil record. Journal of Foraminiferal Research 6, 295-311. **[Journal Article]**

Knappertsbusch, M., 2016. Evolutionary prospection in the Neogene planktic foraminifer *Globorotalia menardii* and related forms from ODP Hole 925B (Ceara Rise, western tropical Atlantic): evidence for gradual evolution superimposed by long distance dispersal? Swiss Journal of Palaeontology 135, 205-248. **[Journal Article]**

Knappertsbusch, M., 2022. Morphological evolution of menardiform globorotalids at Western Pacific Warm Pool ODP Hole 806C (Ontong-Java Plateau) Evolution morphologique du groupe de *Globorotalia menardii* au Site ODP 806C (Ontong-Java Plateau, Pacifique tropical occidental). Revue de Micropaléontologie 74, 100608. **[Journal Article]**

Krijgsman, W., Hilgen, F., Langereis, C.G., Zachariasse, W.J., 1994. The age of the Tortonian/Messinian boundary. Earth and Planetary Science Letters 121, 533–547. **[Journal Article]**

Metcalfe, B., Feldmeijer, W., de Vringer-Picon, M., Brummer, G.J.A., Peeters, F.J.C., Ganssen, G.M., 2015. Late Pleistocene glacial–interglacial shell-size–isotope variability in planktonic foraminifera as a function of local hydrography. Biogeosciences 12, 4781-4807. **[Journal Article]**

Moissette, P., Cornée, J.J., Antonarakou, A., Kontakiotis, G., Drinia, H., Koskeridou, E., Tsourou, T., Agiadi, K., Karakitsios, V., 2018. Palaeoenvironmental changes at the Tortonian/Messinian boundary: A deep-sea sedimentary record of the eastern Mediterranean Sea. Palaeogeography, Palaeoclimatology, Palaeoecology 505, 217–233. **[Journal Article]**

Schmidt, D.N., Renaud, S., Bollmann, J., Schiebel, R., Thierstein, H.R., 2004. Size distribution of Holocene planktic foraminifer assemblages: biogeography, ecology and adaptation. Marine Micropaleontology 50, 319-338. **[Journal Article]**

17th INTERNATIONAL CONGRESS of the Geological Society of Greece

BULLETIN OF THE GEOLOGICAL SOCIETY OF GREECE, SP. PUBL.

EXTENDED ABSTRACT 036

Cultivating FAIR principles for multi-hazard assessment

Bonatis P.[1], Anagnostou V.[1], Karakostas V.[1], Kouroukla C.[1], Papadimitriou E.[1], Adamaki A.[2], Andriopoulou-Mounteanou S-A.[3], Bathrellos G.D.[3], Bitharis S.[1], Foumelis M.[1], Karolos I-A.[1], Kaviris G.[4], Papageorgiou E.[1], Pikridas C.[1], Sakkas V.[1], Skilodimou H.D.[3], Spingos I.[4], Zymvragakis A.[4]

(1) Aristotle University of Thessaloniki, Thessaloniki, Greece, mponatis@geo.auth.gr (2) Lund University, Lund, Sweden (3) University of Patras, Rio, Greece (4) National and Kapodistrian University of Athens, Athens, Greece

Research Highlights

- HOMEROS stands for “Harmonising Observations from Multi-hazard Environments in Research for Open Science”.
- The project aims to deliver FAIR-compliant tools and datasets to enhance disaster preparedness and resilience in high-risk regions through transparent and collaborative research.

Introduction

In today’s interconnected world, communities face a diverse range of hazards, including natural disasters like earthquakes, floods, and landslides, as well as human-induced events. To address these challenges, the HOMEROS project aims to strengthen multi-hazard assessment methodologies in seismology, geodesy, and geology (Figure 1). Leveraging technical solutions suited to the big data era, HOMEROS represents a significant advancement in standardizing research processes, promoting collaboration, and enhancing understanding and prediction capabilities for natural hazards through Open Science practices. By adhering to FAIR principles (Findable, Accessible, Interoperable, Reusable), HOMEROS ensures that its research outputs are transparent, reproducible, and universally accessible, maximizing their value for the scientific community and stakeholders. Focusing on high-risk areas in Greece with significant seismic activity, strong earthquakes, floods, and landslides, HOMEROS will compile earthquake catalogues and assess ground deformation products to provide a comprehensive evaluation of seismic hazards. Additionally, it will enhance the understanding of flood and landslide risks, vital for effective mitigation strategies.

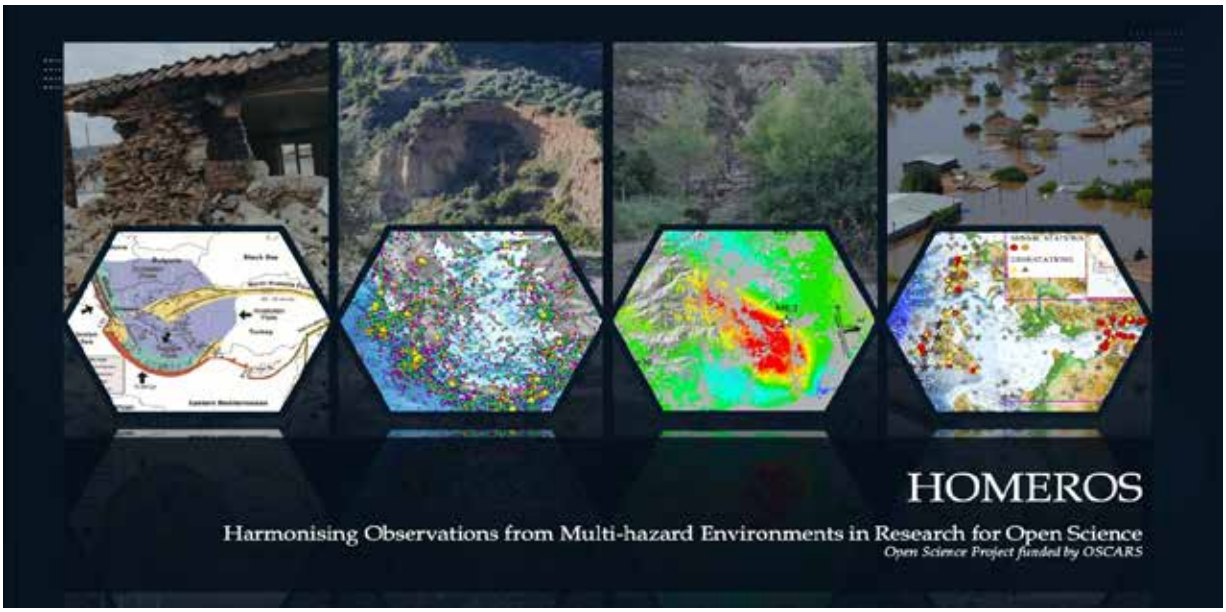

Figure 1. Official logo of the HOMEROS project, highlighting its multi-hazard focus

Objectives

The HOMEROS project addresses the critical need for robust and standardized multi-hazard assessment methodologies in a rapidly evolving risk landscape. By leveraging the power of Open Science and interdisciplinary collaboration, the project aims to advance scientific knowledge, foster data-driven decision-making, and enhance community resilience. Its objectives focus on three key pillars:

- Integration with Open Science environments: HOMEROS aims to utilize platforms such as the European Open Science Cloud (EOSC) and the Environmental Research Infrastructure (ENVRI) Hub (Adamaki & Vermeulen, 2023) to create accessible ecosystems for data sharing. This builds on prior integration efforts in ENVRI projects and promotes FAIR principles to ensure the usability and reproducibility of research outputs.
- Enhancing multi-hazard assessment: The project seeks to develop methodologies for integrating diverse datasets, including seismic, geodetic, and geological data. It will advance the understanding of earthquakes, floods, and landslides through the creation of detailed models, maps, and inventories.
- Fostering collaboration and communication: HOMEROS aspires to strengthen partnerships among research institutions, infrastructures, and projects. Results will be shared through Open Access publications, workshops, and training resources.

Multi-hazard environments - Pilot areas

The HOMEROS project focuses on two high-risk pilot areas in Greece, the central Ionian Islands and the western Gulf of Corinth (Figure 2), which represent diverse and complex multi-hazard environments. These regions have been selected due to their significant seismic activity and susceptibility to other natural hazards, such as floods and landslides. By studying these areas, HOMEROS aims to develop and demonstrate innovative methodologies for multi-hazard assessment.

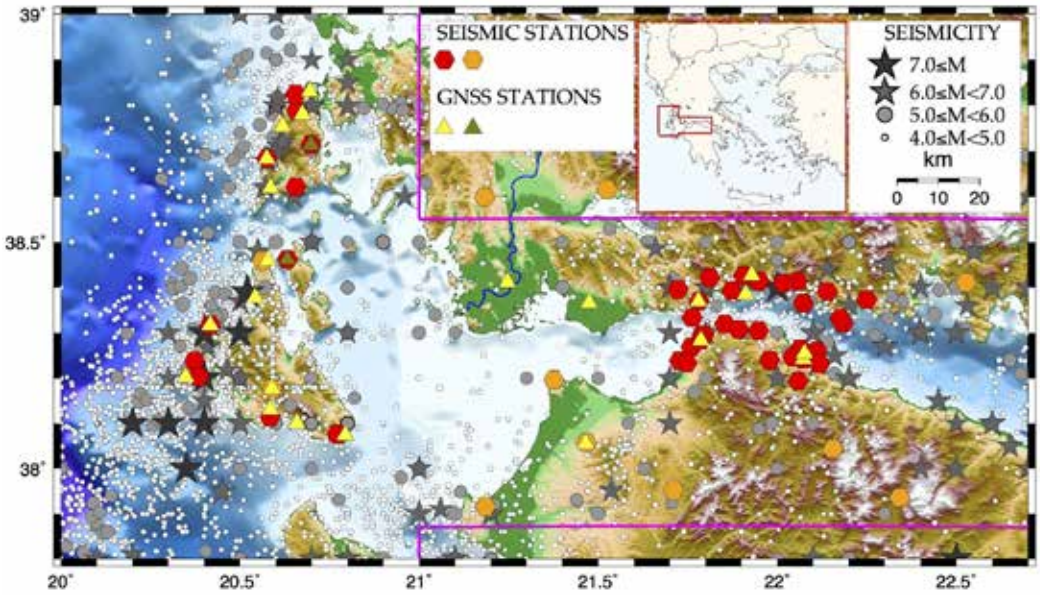

Figure 2. Map of the pilot areas encompassing the central Ionian Islands and western Corinth gulf. Different symbols denote the epicenters of all known earthquakes in the study area with magnitudes M>4.0 as shown in the upper right inset. The central inset shows the territory of Greece with the study area enclosed in the red polygon. Hexagons illustrate the positions of the seismological stations providing online access to their recordings. Yellow triangles depict the installation sites of GNSS stations in operation, whereas the olive triangles the positions where additional GNSS stations are planned to be installed in the framework of the project, collocated with already existing and operated seismological stations.

The central Ionian Islands, along with the western Gulf of Corinth, accommodate the highest seismicity in the eastern Mediterranean, exhibiting high deformation rates (Pikridas et al., 2016; Bitharis et al., 2024) and frequent occurrences of strong earthquakes (e.g., Karakostas et al., 2015; Sakkas et al., 2022). The compilation of earthquake catalogues (e.g. from the Euro-Mediterranean Seismological Centre - EMSC, the European Plate Observing System - EPOS providers as the ORFEUS infrastructure, the database of the Aristotle University of Thessaloniki - AUTh seismological center, and others), comprising historical, instrumental, and recent events, along with focal mechanism and stress field data, represent a significant contribution to the understanding of seismic hazard. Earthquakes are among the most impactful geohazards in Greece given that more than 50% of seismic energy in Europe is released in the country. A reliable seismic hazard model can contribute to seismic risk mitigation. To that end, Peak Ground Acceleration (PGA) and Peak Ground Velocity (PGV) together with a site-specific analysis (Uniform Hazard Spectra - UHS and hazard curves) in the most populated towns can provide a holistic evaluation of seismic hazard (e.g., Kaviris et al., 2022; 2024). Besides strong earthquakes, the aforementioned areas along with parts of the northern Peloponnese have experienced severe floods and landslides that resulted in loss of life and substantial loss of property, along with extensive damage to the natural and built environment and key infrastructure (Bathrellos et al., 2017; Skilodimou et al., 2018). Maps displaying the spatial distribution of flood and landslide hazards are invaluable at identifying areas at risk (Skilodimou et al., 2019; Bathrellos et al., 2024). The project will enhance the understanding of the spatial distribution of historical and recently recorded floods, along with the identification of flood – prone areas, which constitute critical input information on effective flood-risk mitigation. Regarding landslides, they are mostly observed in the mountainous part of the Gulf of Corinth, the Ionian Islands, and parts of western Peloponnese, where serious damage has been repeatedly caused to sections of urban areas and the road network. Landslide hazard assessment maps are important tools for prediction and mitigation of natural disasters. In this context, the project will work on an inventory map that includes recorded landslide events, crucial for understanding the landslide hazard.

Data and Methods

Comprehensive multi-hazard assessment requires diverse data sources and advanced methodologies to address the complexity of natural hazards. HOMEROS will integrate high-quality datasets from seismology, geodesy, and geological monitoring to provide robust and reproducible insights. Seismic data from regional networks form the basis for compiling earthquake catalogues, analyzing focal mechanisms, and studying ground deformation, all of which are critical inputs for seismic hazard assessment. Geodetic observations, including GNSS and InSAR, enhance the understanding of tectonic deformation (Bonatis et al., 2024) and enable the integration of precise ground deformation monitoring with broader hazard assessments. Flood and landslide hazards can be assessed using historical records and remote sensing data. Spatial analyses and advanced techniques, such as InSAR, help to identify flood and landslide prone areas (Aslan et al., 2020). These methods are complemented by the development of inventories that catalog historical events. A key component of the project is the harmonization of data and the application of Open Science principles to ensure all research outputs are transparent, reproducible, and widely accessible. Collaborative platforms and tools will be utilized to integrate datasets from diverse sources, fostering interdisciplinary research and promoting knowledge sharing. Reproducible workflows will enable the seamless combination of datasets and methodologies to deliver actionable insights into natural hazards.

Exploitable results

The HOMEROS project aims to deliver a range of results that will significantly advance multi-hazard assessment and enhance disaster resilience (Table 1). A primary output will be open-access datasets, including earthquake catalogues, ground deformation products, flood hazard maps, and landslide inventories. These datasets will adhere to FAIR principles and will be shared through platforms such as EPOS ERIC, ENVRI repositories, and other open repositories (e.g., GitHub, Zenodo). These data products will provide valuable resources for advancing research and fostering interdisciplinary collaboration.

Another key outcome is the development of transparent and reproducible research workflows documented through tools like Jupyter Notebooks. These workflows will demonstrate the integration of diverse datasets and methodologies, enabling researchers to replicate and adapt the processes for similar studies. This documentation will serve as a best-practice guide for future multi-disciplinary research projects.

Table 1. Summary of the key outcomes of HOMEROS

Output	Description	Impact
Open-access datasets	Comprehensive datasets including earthquake catalogues, ground deformation products (GNSS and InSAR), flood hazard maps, and landslide inventories.	Enabling improved hazard modeling, interdisciplinary research, and data-driven policy-making.
Scientific publications	Peer-reviewed articles published in Open Access journals, showcasing HOMEROS methodologies and findings.	Advancing scientific knowledge.
Training modules	Educational resources designed to teach Open Science principles, data sharing practices, and the utilization of research tools like Jupyter Notebooks and ENVRI/EOSC services.	Capacity building among researchers, students, and professionals, fostering widespread adoption of Open Science practices.
Integration demonstrators	Showcase of pathways to integrate data pipelines from diverse sources, including ENVRI and EOSC infrastructures, to highlight interoperability and scalability.	Improved data interoperability.
Policy recommendations support tools	Practical outputs such as hazard maps and risk models suited for policymakers and disaster management stakeholders.	Enhancing disaster preparedness and resilience.

Conclusions

HOMEROS represents a vital step forward in addressing the growing complexity of multi-hazard environments. By harmonizing data from diverse scientific domains and adhering to Open Science principles, the project tackles key challenges in making hazard assessment both comprehensive and accessible. It lays the foundation for more integrated and scalable approaches to understand natural hazards, from earthquakes to floods and landslides, in high-risk regions. The emphasis on FAIR principles ensures that HOMEROS outputs not only benefit current research but also provide a robust framework for future innovations in hazard modeling. The project's focus on high-risk areas, such as the Ionian Islands and the Gulf of Corinth, will demonstrate its applicability, while offering scalable solutions that can be adapted to other geohazardous regions worldwide. Lastly, the outputs including open-access data, scientific publications, and training modules, will serve as valuable resources for academia, policy-making, and disaster management, fostering a safer and more resilient society.

Acknowledgements

The authors acknowledge the OSCARS project, which has received funding from the European Commission's Horizon Europe Research and Innovation programme under grant agreement No. 10112975.

References

Adamaki, A., Vermeulen, A., 2023. ENVRI-FAIR D5.7: ENVRI-Hub design study, Zenodo. https://doi.org/10.5281/zenodo.8119522.

Aslan, G., Foumelis, M., Raucoules, D., De Michele, M., Bernardie, S., Cakir, Z., 2020. Landslide Inventory Mapping and Monitoring Using Persistent Scatterer Interferometry (PSI) Technique in the French Alps. Remote Sensing 12(8), 1305.

Bathrellos, G. D., Skilodimou, H. D., Chousianitis, K., Youssef, A. M., Pradhan, B., 2017. Suitability estimation for urban development using multi-hazard assessment map. Science of the Total Environment 575, 119-134.

Bathrellos, G.D., Koukouvelas, I.K., Skilodimou, H.D., Nikolakopoulos, K.G., Vgenopoulos, A.L., 2024. Landslide causative factors evaluation using GIS in the tectonically active Glafkos River area, northwestern Peloponnese, Greece. Geomorphology 461, 109285.

Bitharis, S., Pikridas, C., Fotiou, A., Rossikopoulos D., 2024. GPS data analysis and geodetic velocity field

investigation in Greece, 2001–2016. GPS Solutions 28, 16.

Bonatis, P., Karakostas, V., Kaplon, J., Papadimitriou, E., Kaviris, G., Ilieva, M., Foumelis, M., Pikridas, C., 2024. Co-seismic and post-seismic slip associated with the 2021 M_w5.9 Arkalochori, Central Crete (Greece) earthquake constrained by geodetic data and aftershocks. Tectonophysics 889, 230481.

Karakostas, V., Papadimitriou, E., Mesimeri, M., Gkarlaouni, Ch., Paradisopoulou, P., 2015. The 2014 Kefalonia doublet (Mw6.1 and Mw6.0) central Ionian Islands, Greece: Seismotectonic implications along the Kefalonia Transform Fault Zone. Acta Geophysica 63, 1-16.

Kaviris, G., Zymvragakis, A., Bonatis, P., Kapetanidis, V., Voulgaris, N., 2022. Probabilistic and Scenario-Based Seismic Hazard Assessment on the Western Gulf of Corinth (Central Greece). Applied Sciences 12(21), 11152.

Kaviris, G., Zymvragakis, A., Kapetanidis, V., Kouskouna, V., Spingos, I., Sakellariou, N., Voulgaris, N., 2024. A Logic-Tree Based Probabilistic Seismic Hazard Assessment for the Central Ionian Islands of Cephalonia and Ithaca (Western Greece). Journal of Seismology 28, 1087-1103.

Pikridas C., Bitharis S., Fotiou A., Rossikopoulos D., Katsougiannopoulos S., Spanakaki K, Karolos I., 2016. Monitoring seismic displacements using GNSS data with PPP method. Bulletin of the Geological Society of Greece 50 (3), 1563-1569.

Sakkas, V., Kapetanidis, V., Kaviris, G., Spingos, I., Mavroulis, S., Diakakis, M., Alexopoulos, J., Kazantzidou-Firtinidou, D., Kassaras, I., Dilalos, S., Vassilakis, E., Kotsi, E., Tselentis, G.-A., Lekkas, E., Voulgaris, N., 2022. Seismological and Ground Deformation Study of the Ionian Islands (W. Greece) During 2014-2018, a Period of Intense Seismic Activity. Applied Sciences 12, 2331.

Skilodimou, H. D., Bathrellos, G. D., Koskeridou, E., Soukis, K., Rozos, D., 2018. Physical and anthropogenic factors related to landslide activity in the Northern Peloponnese, Greece. Land 7(3), 85.

Skilodimou, H.D., Bathrellos, G.D., Chousianitis, K., Youssef, A.M., Pradhan, B., 2019. Multi-hazard assessment modeling via multi-criteria analysis and GIS: a case study. Environmental Earth Sciences 78, 47.

17th INTERNATIONAL CONGRESS of the Geological Society of Greece

BULLETIN OF THE GEOLOGICAL SOCIETY OF GREECE, SP. PUBL.

EXTENDED ABSTRACT 037

Development of an index-based methodology for assessing coastal vulnerability at a national scale and preliminary results

Boumpoulis V.[1], Michalopoulou M.[1], Kazolias A.[3], Geraga M.[2], Depountis N.,[1] Papatheodorou G.[2]

(1) University of Patras, Department of Geology, Laboratory of Engineering Geology, Greece, vasileios_boumpoulis@ac.upatras.gr

(2) University of Patras, Department of Geology, Laboratory of Marine Geology and Physical Oceanography, Greece

(3) University of Peloponnese, Department of Digital Systems, Sparti, Greece.

Research Highlights: **Development of an index-based equation and methodology for assessing coastal vulnerability in Greece at a national scale**

Introduction

Coastal areas are one of the most vulnerable environments and due to their continuously growing population, their protection is of great importance for society and economy. Moreover, climate change can increase the intensity of climate related coastal hazards, especially coastal erosion and sea level rise, whose adverse impacts on coastal zones are expected to be significant even under the most optimistic emission scenario (IPCC 2022). Against these rising threats, different risk and vulnerability assessment methodologies have been developed to understand the processes underpinning coastal hazards. More specifically, the assessment and calculation of coastal vulnerability, focusing on coastal erosion processes, is accomplished with the following methods: (a) methods based on a specific vulnerability index, (b) methods based on a sequence of indicators, (c) methods based on geographical information system (GIS)-based decision-making systems and (d) methods based on dynamic computational model (Ramieri et al. 2011).

In the present study, the use of a method based on a specific vulnerability index, and more specifically the Coastal Vulnerability Index (CVI) approach was chosen to assess vulnerability along the Hellenic coastlines and for this reason it was named HCVI. The CVI is a very productive, low-cost and effective tool for mapping and managing coastal risks. In this way, it provides an initial identification of coastal vulnerability to facilitate local and regional authorities in preparing coastal management and protection plans, coastal zone regulation and adaptation strategies against erosion.

However, despite the effective application of the CVI index, there are limited publications in the literature addressing its use at the national scale. Furlan et al. (2021), developed a modified CVI index (MDim-CVI) for Italy, incorporating four different sub-indices: a) Coastal Forcing, b) Environmental, c) Social and d) Economic. In addition, López Royo et al. (2016), estimated coastal vulnerability for the entire coastal zone of Spain again using a modified CVI index, which was calculated for 4 different future climate models (RCPs) of sea level rise, based on IPCC future projections.

The aim of this project is the creation, implementation and presentation of the Hellenic Coastal Vulnerability Index (HCVI) for the assessment of vulnerability along the Hellenic coastlines and the creation of a national scale vulnerability map.

Methodology

For the calculation of coastal vulnerability at a national scale, the classic vulnerability index CVI (Coastal Vulnerability Index) was chosen, with the following variables: 1) Geological resilience, 2) Coastal Slope, 3) Historical shoreline change, 4) Significant wave height, 5) Sea level rise and 6) Tidal range.

The calculation of CVI for the Hellenic coastlines was carried out using the equation proposed by (Gornitz (1991) according to which the result is equal to the square root of the product of the variables divided by the number of variables. For the calculation of the CVI, the coastline of Greece was divided into coastal segments of 100 meters, precisely at the same locations where transects were created for calculating

the historical shoreline change using the DSAS software (Digital Shoreline Analysis System version 6) (Himmelstoss et al., 2024).

The equation for calculating HCVI is presented below:

$$HCVI = \sqrt{\frac{a * b * c * d * e * f}{6}}$$

where a: Geological resilience, b: Significant average wave height, c: Coastal slope, d: Historical shoreline change, e: Average tidal range, f: Sea level rise (SLR).

The initial step before calculating the Coastal Vulnerability Index is to determine the range values of each variable to classify them with a specific vulnerability value, for example, from very low to very high vulnerability. The five (5) ranges of vulnerability classification values used in this project are presented in Table 1.

Table 1. Vulnerability classification ranges for each of the variables used in the HCVI calculations.

Variables	Very Low (1)	Low (2)	Moderate (3)	High (4)	Very High (5)
Geological resilience	Limestones, plutonic and metamorphic rocks	Flysch, evaporites, igneous and semi-metamorphic rocks	Neogene deposits (hard soils- soft rocks)	Quaternary loose materials with a higher percentage of coarse-grained materials (sand, gravel and pebbles)	Quaternary loose materials with a higher percentage of fine or mixed phase deposits (silts and sands)
Significant Wave Height (m)	<0.3	0.3–0.6	0.6–0.9	0.9–1.2	>1.2
Coastal Slope (%)	>12	12- 9	9 – 6	6 – 3	<3
Historical Shoreline Change (m/y)	>(+1.5)	(+1.5)–(+0.5)	(+0.5)–(-0.5)	(-0.5)–(-1.5)	<(-1.5)
Average Tidal Range (m)	<0.2	0.2–0.4	0.4–0.6	0.6–0.8	<0,8
Sea Level Rise (mm/y)	<1.8	1.8 - 2.5	2.5 – 3.0	3.0 – 3.4	>3.4

Geological resilience is one of the most important variables in the equation of HCVI as it assesses the resistance of any geological formation to erosion. The more resistant the formation is to erosion, the lower the vulnerability class corresponds to. Based on this principle, the data of the geotechnical map of Greece, published by EAGE, which includes 28 engineering-geological units at a scale of 1:500,000, were used. Subsequently, the units were grouped into five vulnerability classes, according to the guidelines for the European coastal zone of the EUROSION programme (EC 2004), as presented in Table 1.

Wave height is the main hydrodynamic force, which causes sediment transport leading to erosion. Therefore, vulnerability is higher as wave height increases, while it decreases with lower wave height. Therefore, in CVI applications, wave height is included as an indicator of wave energy, influencing the coastal sediment balance. For the calculation of the significant wave height, data produced through ERA5 reanalysis from 2001 to 2017 (Copernicus database) were used (https://cds.climate.copernicus.eu/datasets/sis-ocean-wave-indicators?tab=overview).

A coast characterized by a gentle slope is considered more vulnerable to erosion than a coast with a steeper slope during an inundation event (Boumboulis et al. 2021). As a result, the coastline is classified as low vulnerability on steep coasts and as high vulnerability in gentle coasts. The coastal slope variable for Greece was determined by processing the Digital Elevation Model (DEM) (5X5 m) of Greece for a range of 8 km from coast to land. More specifically, after the creation of the DEM, it was processed to calculate the coastal slope, expressed as a percentage,

based on the distance between the 10m elevation contour and the coastline of Greece.

For the calculation of the historical shoreline change, multi-spectral satellite images of Greece from 1984 to 2024 as derived from the satellite system of Landsat and processed with ArcGIS Pro were used in order to extract the shoreline in various time periods. The evolution or rate of change of the shoreline is an important variable that indicates the deposition/erosion regime in an area. In this work, the extracted shorelines of 1984 and 2024 were used for the calculation of the rate of change from 1984 to 2024, while the DSAS software was used for the statistical visualization and estimation of the rate of change of the shoreline by calculating the end point rates (EPR). The EPR is calculated by dividing the distance of coastlines (between the oldest and more recent coastlines) by the number of years between their captured dates.

According to Gornitz (1991), macro-tidal environments (high tidal range) are vulnerable to erosion, because they can create stronger currents and cause larger sediment transportation in comparison with the micro-tidal environments. The Greek coastline has low vulnerability to erosion due to the prevailing micro-tidal regime so in the present study, this hypothesis was adopted. The data used for the calculation of tidal range was retrieved from Copernicus and confirmed Greece's low tidal range (https://cds.climate.copernicus.eu/datasets/sis-water-level-change-indicators-cmip6?tab=overview).

SLR is the annual mean increase or decrease of water elevation measured at tide gauges, and is the sum of eustatic, hydro-isostatic and tectonic factors. In this specific research, sea level rise data derived by the Copernicus platform are used, which are attributed to time series based on historical records of sea level changes (https://cds.climate.copernicus.eu/datasets/sis-water-level-change-timeseries-cmip6?tab=overview).

Results

The spatial distribution of the HCVI along the Hellenic coastlines, calculated using the equation proposed in the methodology, is illustrated in the map in Figure 1, highlighting two specific areas identified as having high and very high vulnerability. In particular, the Northwestern Peloponnese and a significant part of Northern Greece were identified under the regime of high and very high vulnerability.

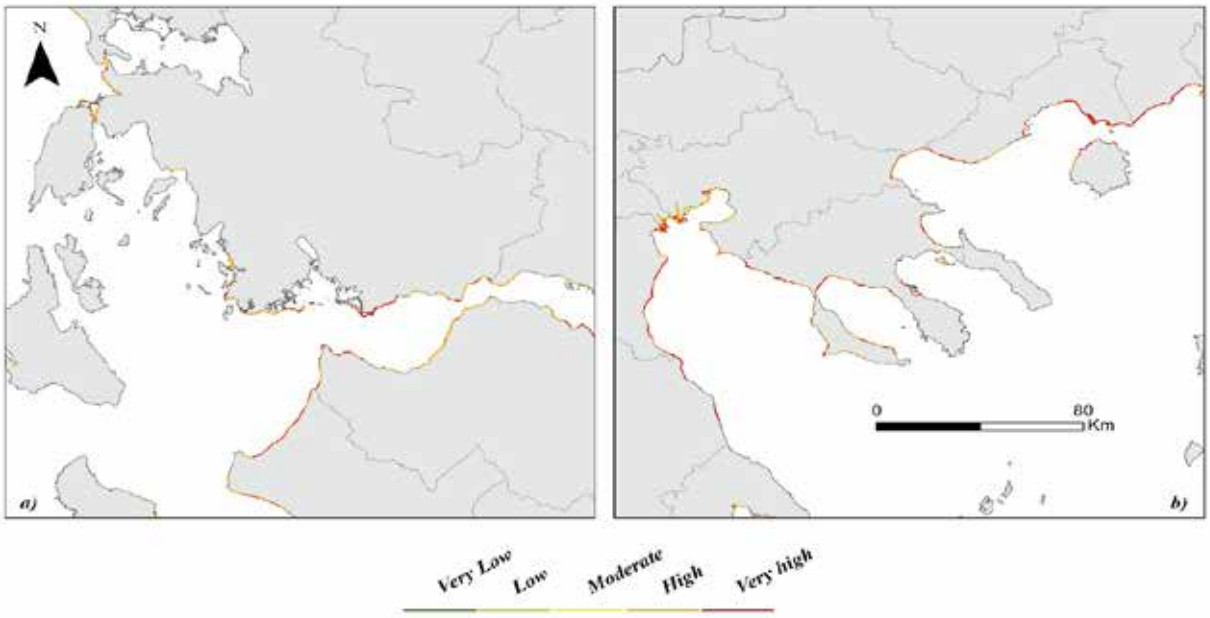

Figure 1. Spatial distribution of high and very high vulnerability classes in a) Northwestern Peloponbese and b) Northern Greece.

More specifically, a large part of the northern Peloponnese (northern and southern part of the Gulf of Patras, southern part of the Gulf of Corinth) is under a high and very high vulnerability regime. Similarly, under the regime of high to very high vulnerability is also the western part of the Peloponnese (Gulf of Kyparissia

and the shoreline from Kalogria to Kyllini) (Figure 1a). The rest of the Peloponnese is characterized by low and moderate vulnerability, with only small areas exhibiting high to very high vulnerability, notably in the Messenian and Laconian Gulfs.

A significant part of the coastline extending from the Regional Unit of Larissa to the Kassandra Peninsula is characterized by high to very high vulnerability due to the presence of gentle slopes and geological formations of low resistance to erosion (Figure 1b). Similarly, a significant part of the coastline of the Regional Unit of Kavala, as well as the entire coastline of the Regional Units of Xanthi and Evros, are characterized by high to very high vulnerability.

Most of the country's islands are in a very low to low vulnerability regime, as they are composed of rocky geological formations and steep slopes. Exceptions are the islands of Rhodes, Limnos, Lesvos, Corfu and Crete, where a large part of their coasts are in a high and very high vulnerability regime.

Conclusion

Among a variety of other indexes and methodologies, the Coastal Vulnerability Index (CVI) was chosen as a method for the estimation and calculation of vulnerability as low-cost and effective tool for mapping and managing coastal risks at a national scale. It is important to note that the coastal vulnerability assessment methodology used in this study was implemented for the first time on a national scale in Greece. Therefore, the application and the produced results can inform national strategic decisions regarding the impacts of climate related hazards on coastal zones.

However, the HCVI results presented in this study are preliminary and are expected to be further improved by incorporating additional variables into the final model, drawing on indicators identified in existing methodologies from literature. This could lead to adjustments of the index and improvements of the findings on the vulnerability of the Greek coasts.

Despite the presence of high percentage of High and Very High vulnerability classes in the study area potential future climate projection was not included in the model, which means that the vulnerability regime could be increased in the future with severe impacts for the entire coastline of Greece.

Acknowledgements

The current research was funded by the Onasis Foundation in the framework of the project "Vulnerabilty of Greek coasts due to climate change" ("Initiative 1821-2021" - Protovoulia 21).

References

Boumboulis, V., Apostolopoulos, D., Depountis N., Nikolakopoulos, K., 2021. The Importance of Geotechnical Evaluation and Shoreline Evolution in Coastal Vulnerability Index Calculations. J Mar Sci Eng 9:423. https://doi.org/10.3390/jmse9040423

EC [European Commission] 2004. Living with Coastal Erosion in Europe – Sediment and Space for Sustainability. OPOCE, Luxembourg. http://www.eurosion.org/project/eurosion_en.pdf.

Furlan, E., Pozza, PD., Michetti, M., et al., 2021. Development of a Multi-Dimensional Coastal Vulnerability Index: Assessing vulnerability to inundation scenarios in the Italian coast. Sci Total Environ 772:144650. https://doi.org/10.1016/j.scitotenv.2020.144650

Gornitz, V., 1991. Global coastal hazards from future sea level rise. Palaeogeogr Palaeoclimatol Palaeoecol 89:379–398. https://doi.org/10.1016/0031-0182(91)90173-O

Himmelstoss, E.A., Henderson, R.E., Farris, A.S., Kratzmann, M.G., Bartlett, M.K., Ergul, A., McAndrews, J., Cibaj, R., Zichichi, J.L., and Thieler, E.R., 2024. Digital Shoreline Analysis System version 6.0: U.S. Geological Survey software release, https://doi.org/10.5066/P13WIZ8M.

IPCC 2022. Impacts of 1.5°C Global Warming on Natural and Human Systems

López Royo, M., Ranasinghe R., Jiménez J.A., 2016. A Rapid, Low-Cost Approach to Coastal Vulnerability Assessment at a National Level. J Coast Res 32:932–945. https://doi.org/10.2112/JCOASTRES-D-14-00217.1

Ramieri, E., Hartley, A.J., Barbanti, A., et al., 2011. Methods for assessing coastal vulnerability to climate change. Eur Environ Agency, Eur Top Cent Clim Chang impacts, vulnerability Adapt 1–93

17th INTERNATIONAL CONGRESS of the Geological Society of Greece

BULLETIN OF THE GEOLOGICAL SOCIETY OF GREECE, SP. PUBL.

EXTENDED ABSTRACT 038

Development of a Geographic Information System for the Near-Real-Time Management of the seismic risk. Case study: The city of Mytilene, Lesvos (Greece)

E. Bouranta[1], J.N. Hatzopoulos[1]
[1]University of Aegean, Department of the Environment, University Hill, 81100 Mytilene, Greece.

[*]Corresponding author:
E-mail: bourant_e@yahoo.gr , bouranta@webmail.aegean.gr tel:6973855260

ABSTRACT

Mytilene is the capital of Lesvos, the largest island in the North Aegean. The region of North Aegean is a geotectonically complex area because its geodynamic status is directly affected by the North Anatolian Fault Zone. The seismic activity negatively impacts the material and technical infrastructure and, by extension, social and economic life. This fact makes mitigation of negative impacts of seismic events imperative. This paper describes the development of a web-based GIS for disaster response in Mytilene, Lesvos (Greece), urban area through the ArcGIS Online application (https://www.esri.com). WebGIS technologies provide a wide range of solutions for fault mapping, data analysis, and publication of results. The completion of this project contributes to the improvement of methodologies and applied technologies and the proposal and development of new ones, indicating the direction for the implementation of similar research projects and the introduction of new geographic information technologies in seismic risk management.

Keywords: Earthquakes, emergency management, GIS, Web-based

1. Introduction

An earthquake is a highly challenging natural phenomenon to forecast, making each occurrence essential for advancing research (Darzi et al., 2022). Geographic Information System (GIS) can support disaster management as a powerful tool for collecting, storing, analyzing, modeling, and displaying large amounts of data. Online GIS combines the advantages of both GIS and the Internet. The WebGIS is addressed to a broad target of end users and supports the implementation of seismic risk mitigation strategies. Web GIS is one of the most widely used technologies for the propagation of open data for multiple purposes. WebGIS technologies have also been widespread for natural risk assessment and communication (*Daud et al., 2024; Vinueza-Martinez et al., 2024*). Web GIS and geodatabase technologies have been used to advance interactive tools for defining seismic hazard scenarios and risk analysis (Pessina & Meroni, 2009; *Aye et al., 2015*). The ArcGIS Online application (https://www.esri.com) helps create interactive maps.

An Earthquake Information Management System (EIMS) is a system that records, collects, keeps, retrieves, and analyzes inputs, produces reports and required information for earthquakes, and informs the responsible stakeholders. The information does not comprise an end but contributes to better decisions in policy design, disaster planning, management, monitoring, and evaluation of disaster plans and damage reduction (*Ajami & Fattahi, 2009; Kirschenbaum et al., 2017).*

Earthquake Information Management Systems (EIMS) use ArcGIS (Geographic Information System) to map and visualize ground vibration, the pattern of damaged buildings, and demographic information about a community (*Cao et al., 2023)*. Once the location and magnitude of an earthquake have been determined, the EIMS will assess the distribution of ground vibrations, building failures, casualties, transmission system failures, power, and water outages, population displacement, and the cost of repairing potential faults (Ajami et al., 2008; Cao et al., 2023). In this study, we developed a Web GIS for earthquake management and monitoring in the urban area of Mytilene, Lesvos (Greece). Decision-makers and the general public can use our Web-based GIS model.

2. Materials and methods

2.1. General description of the analyzed area

Lesvos is the third largest island of the Greek Islands, with 1.632 square kilometers in extent. It is located in the northeastern Aegean Sea. Mytilene is the capital of the island of Lesvos and the Prefecture of Lesvos. The geology can be summarized as a basement composed of Alpidic and pre-Alpidic metamorphic rocks, which were covered later by post-Alpine formations, mainly Miocene volcanic rocks and Neogene marine and lacustrine deposits (Soulakellis et al., 2006). The island was characterized by high seismicity hazards and had been affected many times by powerful, devastating earthquakes. Mytilene is the capital of Lesvos and is located in the eastern part of the island. The altitude fluctuates from 0 to 100 m, and it is a smooth relief.

2.2. Methodology

The steps of the methodology include:

1. Microtremor measurements and processing

Microtremor measurements have been conducted to study the site effect and the site ground response in case of an earthquake in the urban area of Mytilene. The Horizontal-to-Vertical Spectral Ratio (HVSR) technique has been applied to ambient noise measurements (Nakamura's technique). The Nakamura technique is helpful for subsurface soil structure and site response studies (*Araque-Pérez, 2024*). The microtremor HVSR method has been widely used in seismic micro-zonation and site effect studies.

Ambient noise measurements have been performed in Mytilene from May 2012 to February 2013. One hundred measurements of ambient noise have been conducted throughout the city. The measurements were carried out from Monday to Friday from 23:00-02:30. A global Positioning System (GPS) module localizes the spatial position of each measurement point (Hatzopoulos & Hatzopoulos, 2024). The sampling rate was 200Hz, and the recording duration was 30 minutes. These data are acquired according to guidelines proposed by Duval et al. (2004). The sites of microtremor recordings were selected to cover all the different geological formations of the area. Figure 1 shows the locations of measured points in the urban town of Mytilene.

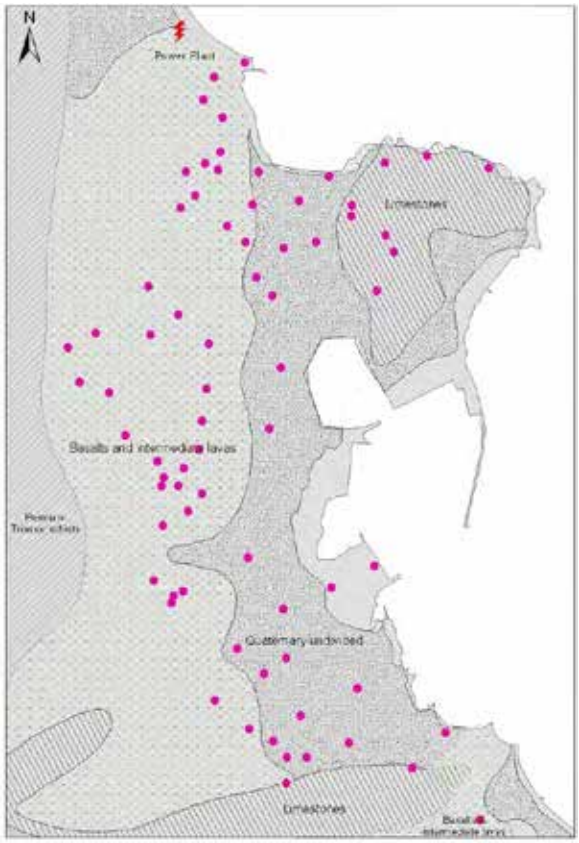

Figure 1. Position map of microtremor measurements in the urban area of Mytilene

2. Deployment of temporary strong motion network

A strong motion sensor network was deployed in the three different geological formations to provide valuable information for the region (Fig. 2). A total of 198 seismic events were recorded from December 15, 2014, to July 20, 2015, for the study area.

Figure 2. One of the three stations. The accelerograph is on the left, and the GPS is on the right.

The spatial distribution of the strong motion parameters, such as the Peak Ground Acceleration (PGA), Peak Ground Velocity (PGV), and Peak Ground Displacement (PGD) observed at the urban area of Mytilene are presented with the use of a Geographic Information System (GIS) environment (Figures 3, 4, 5). The results provide valuable information on earthquake hazards before and after detrimental seismic events to supply systems supporting civil protection decisions for prevention and emergency response.

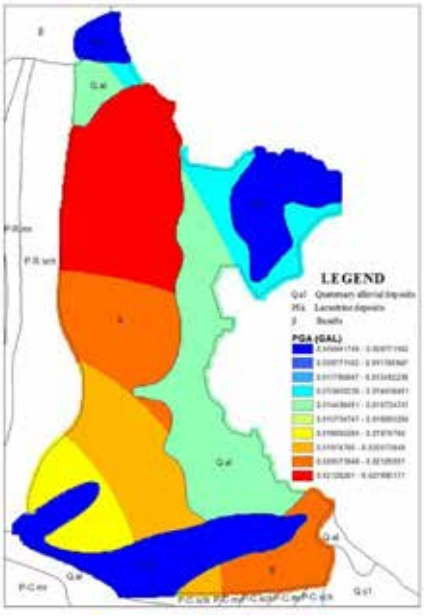

Figure 3. Spatial Distribution of PGA

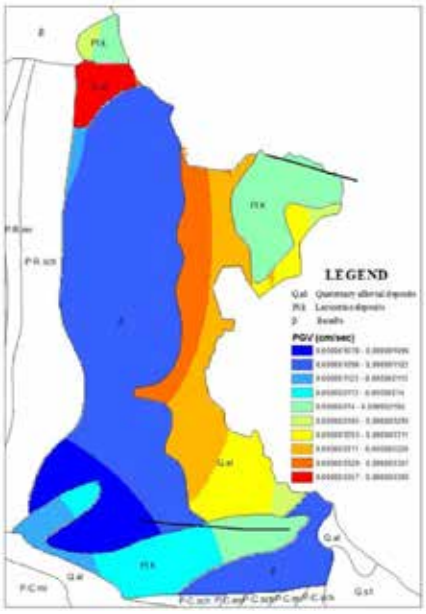

Figure 4. Spatial Distribution of PGV

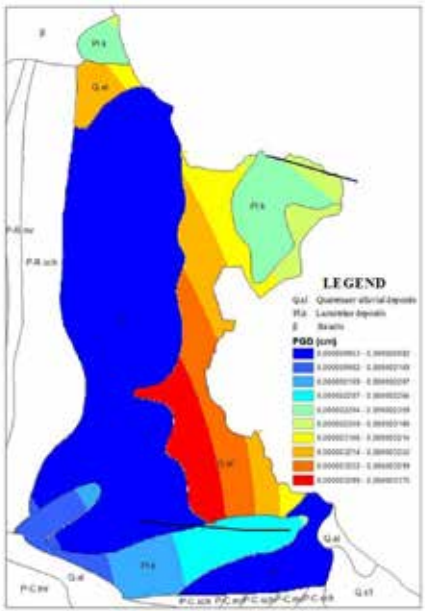

Figure 5. Spatial Distribution of PGD

3.

3. Development of a Web-based interface for earthquake management and monitoring

Finally, dynamic seismic hazard maps were created for the urban complex of Mytilene. Dynamic maps enable the user to manage geoinformation via the Internet. Creating a dynamic map requires the use of a network GIS. (web GIS). This is a GSP that can work and be used on the Internet. Using the ArcGIS Online application (https://www.arcgis.com/home/), the corresponding dynamic maps of maximum ground acceleration (PGA), maximum ground speed (PGV), and maximum ground shift (PGD) were created. The application allows the creation of custom cartographic compositions with user data and the ability to select a background.

3. Results and Discussion

The pilot strong-motion network comprises three stations, which were, however, strategically positioned to represent distinct geological formations. The objective was not to achieve full spatial coverage, but rather to evaluate the potential for site-specific, geology-dependent ground response. This approach serves as a foundation for the future expansion of the network. The correlation of recorded motion data with subsurface characteristics provides valuable insights into the spatial variability of seismic site effects.

WebGIS is constantly gaining ground in decision-making and spatial planning applications, as it enables researchers and stakeholders to benefit from the visualization, exchange, and evaluation of geospatial data with minimal effort and cost. Both scientific staff and stakeholders having access to the correct data at the right time can make the right decisions to mitigate the effects and address the risks of an impending earthquake. Thus, an online GIS can be a powerful tool in all phases of a disaster management cycle. The proposed platform distinguishes itself through its focused application at the local scale, effectively integrating in-situ microtremor measurements with real-time strong-motion data. A key innovation lies in its capacity to generate dynamic seismic hazard maps and offer interactive tools designed to serve both technical experts and the broader public, thereby enhancing accessibility and practical utility in risk communication.

The generated maps of maximum ground acceleration (PGA), maximum ground velocity (PGV), and maximum ground displacement (PGD) can give an idea of the magnitude of the damage that an earthquake can cause depending on the existing local soil conditions. Assessing the effects of an earthquake enables preparedness and immediate response to the crisis in the event of an earthquake. The dynamic maps that are created can be shared via a link. Following the link below gives the user direct access to dynamic maps: http://arcg.is/1QIlj1X (Fig.6).

Figure 6 is a screenshot of the application and illustrates the interface of the WebGIS application, showing the PGA map, where users can interactively explore areas of maximum ground acceleration based on different parameters. The map highlights the spatial variation of PGA across the region, helping stakeholders prioritize high-risk zones.

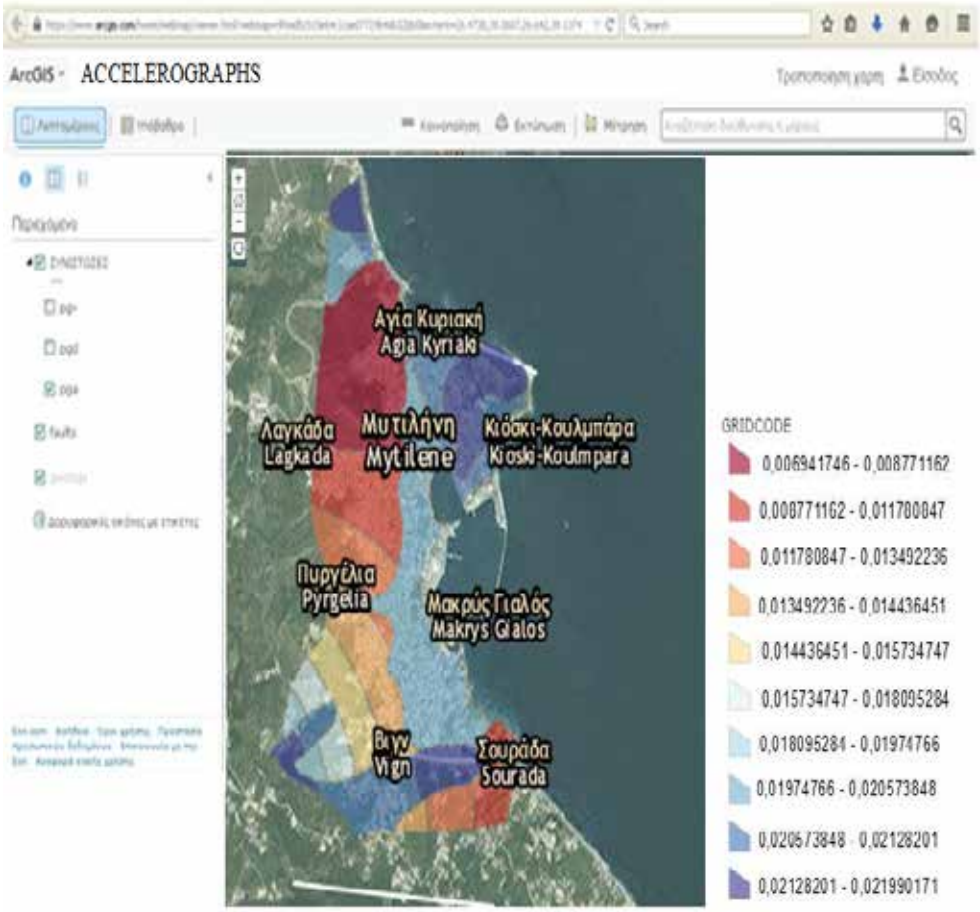

Figure 6. Screenshot of application

The analysis conducted in this study highlights the criticality of using WebGIS tools for earthquake preparedness and disaster management. For the city of Mytilene, the generated maps indicate specific areas that are more vulnerable to seismic activities due to local soil conditions. In particular, zones with high PGA and PGV values should be given priority in terms of preventive measures and resource allocation. These high-risk areas can guide city planners and emergency response teams to implement targeted interventions that mitigate potential damages.

Moreover, the findings suggest that immediate attention should be focused on zones with critical infrastructure and dense populations in an earthquake. Prioritizing these areas ensures residents' safety and essential services' functionality. The application of WebGIS in identifying and visualizing such zones proves invaluable for proactive planning and efficient disaster response. By integrating real-time data and dynamic maps, stakeholders can make informed decisions that enhance the resilience of Mytilene to seismic hazards.

The obtained results can be a valuable tool for the rational management of seismic risk as they can be applied at any stage of disaster management (mitigation, preparedness, response, rehabilitation). In the future, as far as the online GIS is concerned, this will mainly be addressed to experts and the general public. For this reason, a mechanism could be created to offer solutions to non-skilled people, such as making a discussion forum. Developing an application using open-source or free software could also be addressed to any user, enabling the general public to participate in decision-making processes.

The developed WebGIS system demonstrates strong potential for future scalability and functional

expansion. One of its most promising directions lies in the integration of additional datasets, such as detailed building inventory information—including structural typology, construction year, and height—as well as socio-economic indicators like population density, age distribution, and social vulnerability indices. Incorporating such multidimensional data would enable the generation of more sophisticated and realistic seismic risk scenarios, tailored to both the physical and human dimensions of urban environments. Furthermore, the integration of Building Information Modeling (BIM) technologies with the WebGIS framework could pave the way for a unified risk management platform, combining geospatial intelligence with structural-level detail. This holistic approach would significantly enhance the capacity for pre-event planning, impact assessment, and post-event response in earthquake-prone areas. Finally, registering building stock data in an electronic database would make it possible to create seismic risk scenarios, which would be a helpful guide for the relevant services.

Acknowledgement.

Bouranta Evangelia was supported by the Greek State Scholarships Foundation (IKY). The authors would like to express sincere thanks and appreciation to **Professor Filippos Vallianatos** for his invaluable guidance, insightful feedback, and continuous support throughout the development of this work.

References

Ajami, S., & Fatahi, M. (2008). Reduce destroys and rule of Earthquake Information Systems: The comparative study in Turkey, Afghanistan and Iran. In *Proceedings of the International Disaster and Risk Conference (IDRC)* (August 25–29). Davos, Switzerland.

Ajami, S., & Fattahi, M. (2009). The role of earthquake information management systems (EIMSs) in reducing destruction: A comparative study of Japan, Turkey, and Iran. *Disaster Prevention and Management, 18,* 150–161.

Araque-Pérez, C. (2024). Reevaluating soil amplification using multi-spectral HVSR technique in La Chana neighborhood, Granada, Spain. *Journal of Seismology.*

Aye, Z. C., Jaboyedoff, M., Derron, M., Westen, C. J., Hussin, H., Ciurean, R. L., Frigerio, S., & Pasuto, A. (2015). An interactive web-GIS tool for risk analysis: A case study in the Fella River basin, Italy. *Natural Hazards and Earth System Sciences, 16,* 85–101.

Cao, Y., Xu, C., Aziz, N.M., & Kamaruzzaman, S.N. (2023). BIM-GIS Integrated Utilization in Urban Disaster Management: The Contributions, Challenges, and Future Directions. Remote. Sens., 15, 1331.

*Darzi, A., Bessason, B., Halldorsson, B., Molina, S., Kharazian, A., & Moosapoor, M. (2022). High spatial-resolution loss estimation using dense array strong-motion near-fault records. Case study for Hveragerði and the Mw 6.3 Ölfus earthquake, South Iceland. International Journal of Disaster Risk Reduction, 73***, 102894.**

Daud, M., Ugliotti, F. M., & Osello, A. (2024). Comprehensive analysis of the use of Web-GIS for natural hazard management: A systematic review. *Sustainability.*

Hatzopoulos, J., D. J. Hatzopoulos (2024). *Topographic Mapping.* Second Edition. Boca Raton, FL: Universal Publishers.

Kirschenbaum, A.A., Rapaport, C., & Canetti, D. (2017). The impact of information sources on earthquake preparedness. International journal of disaster risk reduction, 21, 99-109.

Pessina, V., & Meroni, F. (2009). A WebGIS tool for seismic hazard scenarios and risk analysis. *Soil Dynamics and Earthquake Engineering, 29,* 1274–1281. https://doi.org/10.1016/j.soildyn.2009.03.001

Soulakellis, N., Novak, I., Zouros, N., Lowman, P., & Yates, J. (2006). Fusing Landsat-5/TM imagery and shaded relief maps in tectonic and geomorphic mapping: Lesvos Island, Greece. *Photogrammetric Engineering & Remote Sensing, 72*(6), 693–700.

Vinueza-Martinez, J., Correa-Peralta, M., Ramírez-Anormaliza, R., Franco Arias, O., & Vera Paredes, D. (2024). Geographic information systems (GISs) based on WebGIS architecture: Bibliometric analysis of the current status and research trends. *Sustainability.*

17th INTERNATIONAL CONGRESS of the Geological Society of Greece

BULLETIN OF THE GEOLOGICAL SOCIETY OF GREECE, SP. PUBL.

EXTENDED ABSTRACT 039

Facies and depositional architecture of Upper Miocene tidal flat sedimentation in Kefalonia and Corfu Islands, West Greece

Bourli N.[1], Botziolis Ch.[1], Papadopoulou P.[2], Zelilidis P.[2], Zoumpouli E.[1], Iliopoulos G.[2], Maravelis A.G.[3], Tripsanas E.[4], Oikonomopoulos I.[4], Pagoulatos A.[4], Zelilidis A.[1]

1 University of Patras, Department of Geology, Laboratory of Sedimentology, 26504, Patras, Greece, n_bourli@ac.upatras.gr

2 University of Patras, Department of Geology, Laboratory of Paleontology and Stratigraphy 26504, Patras, Greece.

3 Department of Geology, Aristotle University of Thessaloniki 54124 Thessaloniki, Greece

4. HELPE Upstream S.A., Hellenic Energy Holdings S.A., 8ª Chimaras str., 15125 Marousi Athens, Greece.

This research involves the integrated sedimentological and paleontological analysis of the Neogene tidal deposits in the eastern parts of the Hellenic Fold and Thrust Belt, in South Kefalonia (Paliolinos - Avithos coast) and in NW Corfu (Arillas coast) islands. The study of tidal is supported by illustrative outcrop photographs, with a particular emphasis on two synthetic outcrops. Sedimentary logs were generated to document detailed bed-by-bed measurements, descriptions, and identification of sedimentary structures. Additionally, over 75 samples were chosen for age determination and paleoenvironmental analysis. Micropaleontological analysis encompassed 52 samples from South Kefalonia and 23 samples from NW Corfu and the results point to an Upper Miocene time interval. The sedimentological examination revealed sixteen distinct sedimentary structures within the studied deposits. The study results indicate for NW Corfu that the deposition displays fluctuations between low and high energy episodes, predominantly representing a tidally-influenced continental shelf (Figure 1a); whereas in the South Kefalonia deposition took place in a back-barrier restricted basin and highly active margins (Figure 1b). The different tidal environments, in the two studied regions, were related with the different tectonic conditions. When the tidal environment in a basin mostly controlled either by transfer or strike-slip faults, open shelf tidal environment could be formed; whereas when the major influence is the normal or the thrust faults then a tidal back-barrier environment could be formed.

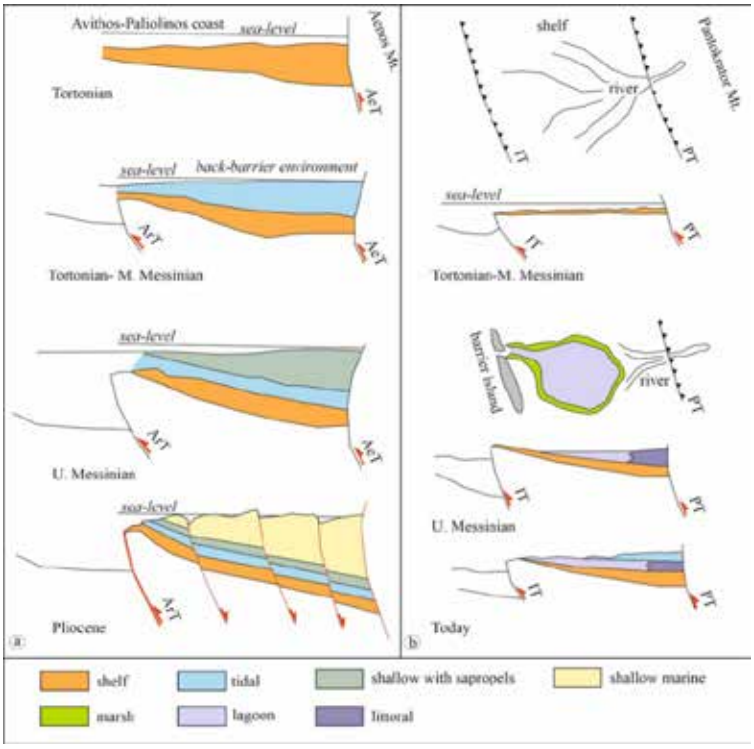

Figure 1. Evolutionary models for two studied areas.

Key words: Kefalonia Island, Corfu Island, shallow-marine tidal deposits, open coast tidal flats, Greece.

17th INTERNATIONAL CONGRESS of the Geological Society of Greece

BULLETIN OF THE GEOLOGICAL SOCIETY OF GREECE, SP. PUBL.

EXTENDED ABSTRACT 040

Tsunami modelling for a potential earthquake between Santorini and Amorgos (Greece)

Bufféral S.[1], Briole P.[1], Dupont A.[2], Escartin J.[1], Heinrich P.[2]
(1) Laboratoire de Géologie, ENS-CNRS, UMR3538, PSL University, Paris, France - simon.bufferal@ens.fr
(2) CEA, DAM, DIF, F-91297 Arpajon, France

Highlights

The seismic swarm that struck northeast of Santorini Island (Greece) in February 2025 highlights the critical need to assess tsunami hazards in this historically vulnerable region. Using Okada's model for seafloor displacement and subsequent tsunami simulations, we discuss hypothetical tsunami scenarios from shallow normal faults identified around the recent swarm. Our simulations suggest that a potential tsunami could impact the eastern coast of Santorini in as little as 6 minutes and reach the surrounding islands within 25 minutes. For a magnitude Mω = 6.3–6.5 earthquake, heights along nearby coastlines could range from 0.1 to 0.6 meters, with localized amplification possible in closed bays. Based on these scenarios, we propose a strategic placing of tide gauges at Agios Nikolaos Port (Anafi) and Agios Andreas (Astypalaia) to enhance tsunami detection and improve regional early warning capabilities.

Context

A volcano-tectonic unrest has been active since late 2024 in the surrounding area of the Santorini volcano, in the Aegean Sea (Greece), peaking with a significant seismic swarm during the first half of February 2025, along a fault zone that ranges between Santorini and Amorgos islands. This region is characterized by both significant volcanic and seismic hazards, as it lies along the volcanic arc associated with the Hellenic subduction zone and an active rift likely related to the Anatolian extrusion. Historically, the area has experienced destructive tsunamis, notably a volcanic-induced event after the Minoan eruption at Santorini around 1600 BC (McCoy and Heiken, 2000; Friedrich *et al.*, 2006; Manning *et al.*, 2006; Goodman-Tchernov *et al.*, 2009) and an earthquake-triggered tsunami after the 9 July 1956 earthquake along the eastern coast of Amorgos (Galanopoulos, 1957; Ambraseys, 1960; Okal *et al.*, 2009; Leclerc *et al.*, 2024). The 2025 seismic crisis has been occurring in the southwestern continuity of the 1956 earthquake zone, underlining the need for a reevaluation of the seismic and tsunamigenic hazards in the area.

Potential for seismic rupture

The seismic crisis began in September 2024 within the Santorini caldera, then migrated northeast of the island starting on 27 January 2025. During February 2025, approximately 200 earthquakes with magnitudes Mω ≥ 4.0 and 8 events with Mω ≥ 5.0 were recorded[1]. At the time of writing (March 2025), seismic activity has been slowing down, although earthquakes exceeding Mω ≥ 4.0 continue to occur intermittently. With geodetic modelling indicating a total slip in the middle to lower crust of an equivalent seismic moment of $2 \cdot 10^{19}$ N·m, i.e., over an order of magnitude greater than the cumulative moment released seismically, the possibility of a stronger earthquake triggered by elastic loading of the upper crust cannot be ruled out. Independent studies have found that the observed surface deformation is consistent with a slow-slip event occurring on a low-angle, southeast-dipping plane initiating below 7 km depth (Briole *et al.*, *in review*). Assuming a listric geometry, this segment would intersect the surface at the mapped location of the West Ios Fault, according to the NOAfaults database (Ganas, 2024; see Table 1 and Figure 1). The present study explores the possibility of rupture on the shallow, locked portion of that fault, and the tsunami that would follow. We model such a scenario by simulating a shallow earthquake producing 0.8 m of slip on a fault measuring 22 km in length and 11 km in width, with an average dip of 50°, consistent with a moment magnitude of Mω = 6.5. This scenario is compared with two additional candidate faults from the NOAfaults database (see Table 1), each approximately 14 km long and 9 km wide, with a dip of 60°. A slip of 0.8 m on such a fault would correspond to a moment magnitude of Mω = 6.3. The focal mechanism for a hypothetical rupture on the Ios West Fault (GR2691) is presented in Figure 1.

1 https://bbnet.gein.noa.gr/HL/databases/database

Table 1. Characteristics of the two candidate faults considered.

Fault Code	Name	Length	Width	Centroid (°E, °N, Depth)	Azimuth	Dip	Slip Type
GR2691	Ios West fault	22.0 km	11 km	25.51, 36.72, 5 km	N054°	50° SE	Pure normal
GR3219	Anhydros Fault	14.6 km	9 km	25.71, 36.52, 7 km	N045°	60° NW	Pure normal
GR3222	SAF-SW Branch	13.5 km	9 km	25.55, 36.58, 7 km	N222°	60° SE	Pure normal

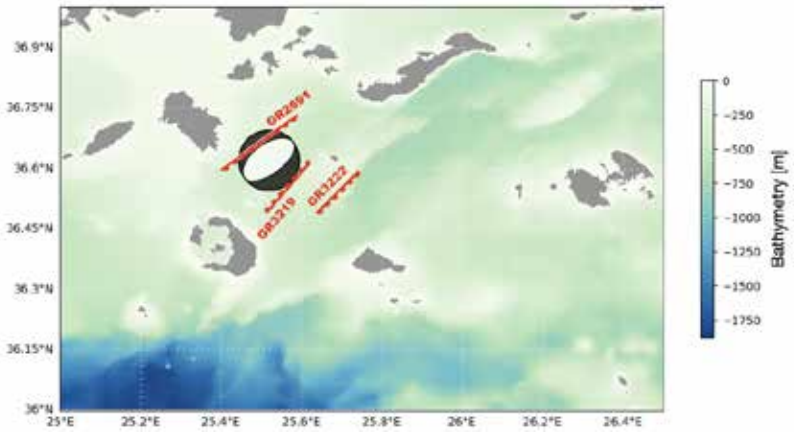

Figure 1. Focal mechanism of a hypothetical rupture on Ios West Fault (GR2691): N054°, 50°SE, pure normal slip.
Simplified surface traces of faults GR3219 and GR3222 are also represented.

Tsunami simulations

We use Okada's equations (Okada, 1985) to calculate the seafloor displacement induced by potential ruptures on the main faults surrounding the 2025 seismic zone (see Table 1 and Figure 1). The Glimsdal transfer equation (Glimsdal *et al.*, 2013) is then applied to evaluate the initial water surface deformation (Figure 2). Finally, tsunami propagation is modelled using the Taitoko code, developed by the Commissariat à l'Énergie Atomique (CEA, France), based on shallow-water wave equations (Heinrich *et al.*, 2021; Heinrich *et al.*, 2024). These calculations use bathymetric data from the European Marine Observation and Data Network (EMODnet[2]), with a grid resolution of 110 meters.

Figure 2 illustrates the initial water surface displacement for an instantaneous and homogeneous normal slip of 80 cm on fault GR2691, with its upper edge located at 1 km depth.

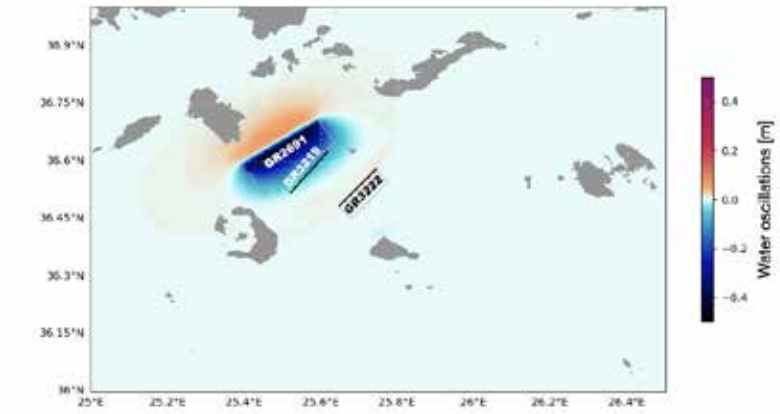

Figure 2. Initial water displacement for 80 cm homogenous normal slip stopping at 1 km depth on Ios West Fault (GR2691). Surface projection of the rupture patch is represented with a rectangle. Potential rupture areas on faults GR3222 and GR3219 are also drawn.

2 https://emodnet.ec.europa.eu/en

Figure 3 shows the wave position after 10 minutes of propagation for the same model. One of the key results of our simulations is that, if an earthquake were to occur in the zone of unrest, the first wave would reach:

- the eastern coast of Santorini in 6 to 15 minutes, depending on the fault location and dip direction;
- Agios Nikolaos Port (Anafi Island) in 11 to 16 minutes;
- Katapola Port (Amorgos Island) in 20 to 25 minutes;
- Chora Port (Ios Island) in 20 to 27 minutes.

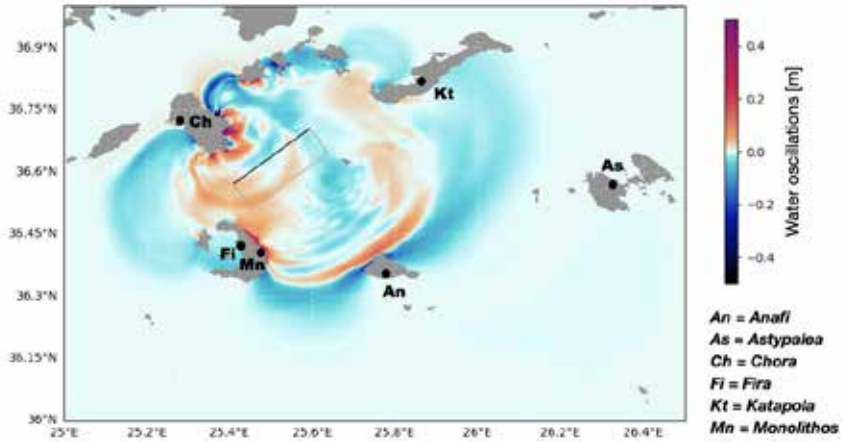

Figure 3. Location of the wave after 10 minutes of propagation for the scenario of a rupture with an 80 cm normal slip stopping at 1 km depth on fault GR2691. The locations of the main harbors are indicated.

Figure 4 presents these arrival times for key ports and coastal areas for a rupture on fault GR3222. These short arrival times emphasize the critical need for early anticipation to ensure an effective response for at-risk populations.

According to our simulations, a tsunami generated by such ruptures would produce wave heights between 0.2 and 0.5 m along the coastlines of nearby islands (Figure 5). The precise wave height depends on the depth and location of the rupture. While these heights may seem moderate, they represent a significant volume of displaced water and high wave energy upon coastal impact, as observed in Samos in 2020 (Kalligeris *et al.*, 2022), with potential risks to people and infrastructure. Due to their geomorphological configuration, bays and inlets are particularly vulnerable to wave amplification, making coastal flooding highly likely in the most pessimistic scenarios.

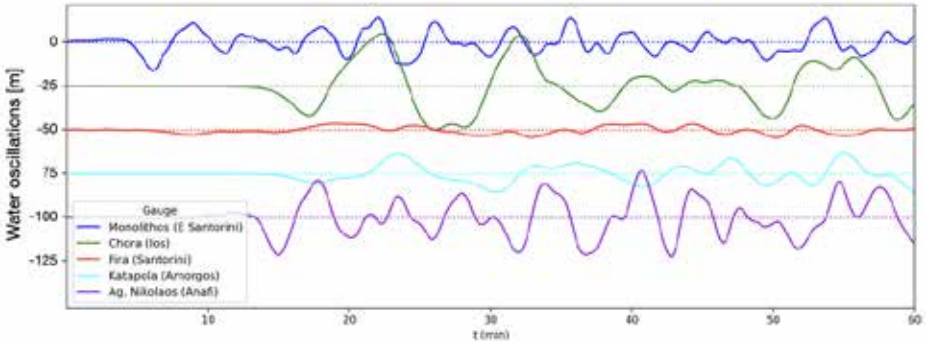

Figure 4. Arrival times at nearby harbors relative to the earthquake origin time for 80 cm normal slip stopping at 3 km depth on fault GR3222.

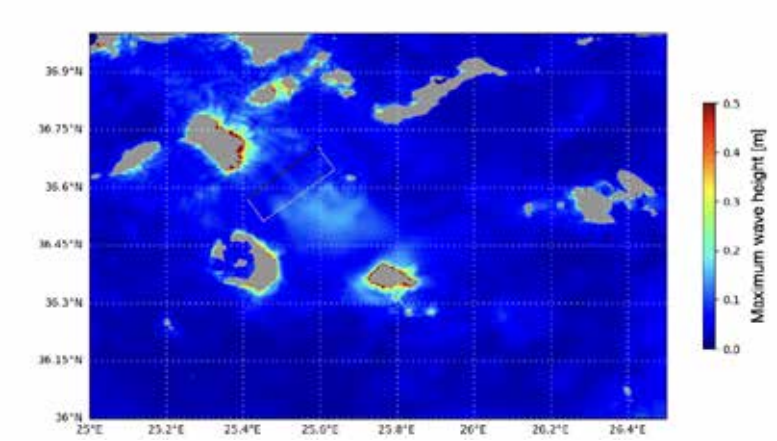

Figure 5. Maximum wave height for 80 cm normal slip stopping at 1 km depth on fault GR2691. These large-scale results do not take into account further local wave amplification phenomena in bays and inlets.

Figure 6 shows the water movement in Chora Bay (Ios Island) for two fault locations:

- GR3219: northwest dip, southwest of Anhydros Island.
- GR3222: southeast dip, south of Anhydros Island.

The upper edge of the rupture is tested at 1 km, 3 km, and 5 km depth.

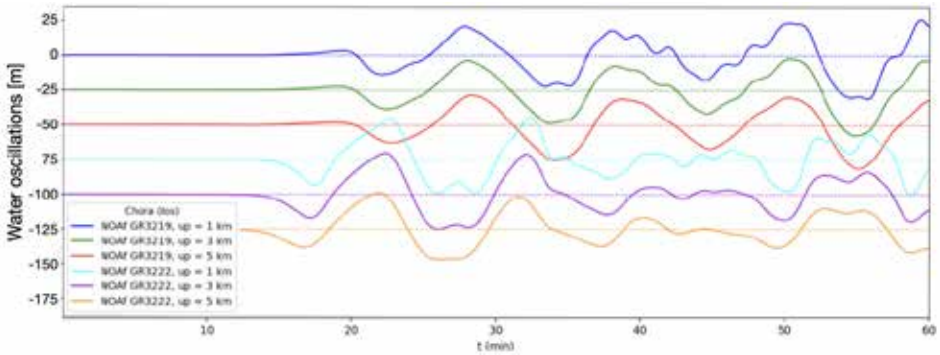

Figure 6: 1-hour water oscillations in Chora Bay (Ios) for two faults and three upper rupture depths.

Our simulations indicate that, in this configuration with several closely spaced islands, the rupture location is the primary factor influencing both wave arrival times and wave attenuation or amplification, depending on interactions with headlands, islands, or underwater obstacles. For instance, shifting the hypocenter 15 km north significantly reduces the wave amplitude reaching Chora Bay (Figure 6). Unlike lower-magnitude earthquakes, whose effects are quickly dampened by upper-crustal layers, the depth of the upper fault edge appears to play a secondary role, provided it remains within realistic values for the region. As shown in Figure 6, variations in depth have a negligible impact on tsunami amplitude, with a maximum discrepancy of only a few centimeters. The azimuth and dip angle of the fault also have limited influence on tsunami morphology, as any normal fault generates an initial water surface depression with a relatively consistent shape. This is confirmed by tests made using the same fault location but opposite fault dips.

Comparison with the 1956 Amorgos Tsunami

On 9 July 1956, a magnitude Mω = 7.1–7.8 earthquake struck south of Amorgos Island, just a few dozen

kilometers north of the current seismic swarm. This event generated an exceptionally large tsunami, with waves reaching up to 20 meters in height in Astypalaia, causing three direct fatalities on Kalimnos Island and several injuries and severe coastal damage in the nearby islands (Ambraseys, 1960).
For a long time, the unusual size of this tsunami was attributed to a submarine landslide (Galanopoulos, 1957; Okal *et al.*, 2009), which was believed to have displaced a large volume of water, producing a wave of exceptional intensity. However, recent studies have failed to find clear evidence of such a landslide, shifting the focus to the hypothesis of a co-seismic displacement of approximately 10 meters as the primary cause (Leclerc *et al.*, 2024).
Given the steep submarine slopes in the region, which show evidence of past landslides, a similar scenario cannot be ruled out for the ongoing seismic crisis, potentially leading to a much stronger tsunami. This study does not specifically address this less likely hypothesis.

Implications for a useful monitoring of future tsunamis

In response to recent tsunami events, studies that used local high-resolution bathymetric data digitized from nautical charts demonstrated that incorporating finer (e.g., ~10 m pixel resolution) bathymetric grids into models significantly modifies tsunami waveforms, potentially doubling wave amplitudes at the coastline (Zahradník *et al*., 2022; Alfonsi *et al*., 2024). It is therefore highly problematic that, despite the existence of numerous high-resolution bathymetric datasets in the Aegean Sea, none are freely accessible. This situation introduces significant reliability issues for tsunami modelling and poses a critical risk to civil safety, as emergency preparedness scenarios may be underestimated, leading to inadequate hazard assessment.
It should also be noted that environmental factors, such as tidal conditions and atmospheric pressure, can intensify the impact of tsunamis. These key parameters call for continuous monitoring of sea level heights and coastal subsidence in the region. In this framework, as part of the ongoing GNSS deployment aimed at monitoring, among others, the Santorini magma chamber inflation, a priority should be given to co-located GNSS and tide gauge stations.
Based on our simulations, closed bays such as the Santorini Caldera, where sub-meter amplitude waves either do not arrive or arrive with a significant delay, should be avoided. Instead, we recommend the maintenance and continuity of instruments on the east coast of Santorini (e.g., NOA-99[3]), where waves arrive quickly with minimal interference or attenuation.
Our results highlight the need for more tide gauges in the region, to monitor water movements in the event of a tsunami, to better constrain climate-change-induced sea level rise, and, ideally, to provide early warning if the gauges are positioned at strategic locations along possible wave paths. High-frequency sampling (~1 Hz) is advised to ensure a rapid and accurate tsunami alert. In the framework of the current instrumentation of the Santorini region, we suggest two more locations for additional tide gauge installation:
● Port of Agios Nikolaos, on the island of Anafi. This harbor appears to be a strategic location for early warning. Simulations show that waves always reach it quickly due to the deep waters offshore. It is not located in an enclosed bay, and the coastline is relatively smooth, minimizing the effects of wave interference. From a broader regional perspective, southern Anafi is an optimal monitoring site as it would be among the first coasts to be hit by a tsunami arriving from the south, particularly likely given the seismic hazard in Crete, which hosts both the Hellenic subduction zone and active normal faults.
● Port of Agios Andreas, on the north coast of the island of Astypalaia. Given the high amplitude of the waves that reached this coast after the 1956 earthquake (Ambraseys, 1960), the harbor of Agios Andreas, on the north coast of Astypalaia, appears as a suitable location for studying large-scale wave propagation in the region.

Conclusions

● The possibility of a tsunami triggered by volcanic or seismic events in the highly active southern Aegean

3 http://antares.gein.noa.gr/TAD_Server/SensorData.aspx?id=53

Sea is significant and must be taken into account. Local populations and tourists should be adequately prepared, particularly by being informed about potential wave propagation scenarios resulting from such events. Civil protection authorities should also be ready to issue tsunami alerts rapidly.

● Accurate knowledge of wave trajectories and arrival times is crucial for enhancing preparedness and improving tsunami early warning protocols. Tsunami wave modelling allows for identifying the most suitable observation sites, whether for post-event analysis to understand tsunami processes or for real-time monitoring to support early warning systems. It also helps distinguish less strategic locations, such as enclosed harbors, where waves tend to be delayed and are less representative of regional tsunami impacts.

● Additional tide gauges are needed to better constrain tsunami models and support the development of early warning capabilities. Moreover, sea-level sensors serve as valuable tools for monitoring broader phenomena, such as climate change-induced sea-level rise, underscoring the need for long-term installations capable of producing reliable time series with minimal influence from local effects like coastal subsidence.

● The critical lack of publicly available coastal bathymetric data introduces significant uncertainties into tsunami modelling, putting people's lives at risk. Addressing this urgent issue by ensuring the existence of comprehensive and accessible coastal bathymetric datasets is, therefore, of paramount importance.

References

Alfonsi, L., Cesaroni, C., Hernandez-Pajares, M., Astafyeva, E., Bufféral, S., Elias, P., Belehaki, A., Tsagouri, I., Yang, H., & Guerran M., 2024. Ionospheric response to the 2020 Samos earthquake and tsunami. Earth Planets Space 76, 13. https://doi.org/10.1186/s40623-023-01940-2

Ambraseys, N., 1960. The seismic sea wave of July 1956 in the Greek Archipelago: J. Geophys. Res., v. 65, p. 1257–1265.

Briole, P., Ganas, A., Serpetsidaki, A., Beauducel, F., Sakkas, V., Tsironi, V., & Elias, P., Volcano-tectonic interaction at Santorini. The crisis of February 2025. Constraints from geodesy. Geophysical Journal International.

Friedrich, W.L., Kromer, B., Friedrich, M., Heinemeier, J., Pfeiffer, T., & Talamo, S., 2006. Santorini eruption radiocarbon dated to 1627–1600 B.C. Science, 312, 548, doi: 10.1126/science.1125087.

Galanopoulos, A.G., 1957. The seismic sea wave of 9 July 1956. Prakt. Akad. Athens, 32, 90–101 (in Greek).

Ganas, A., 2024. NOAFAULTS KMZ layer Version 6.0 (version 6.0) [Data set]. Zenodo. https://doi.org/10.5281/zenodo.13168947

Glimsdal, S., Pedersen, G.K., Harbitz, C.B., & Løvholt, F., 2013. Dispersion of tsunamis: does it really matter? Natural Hazards and Earth System Sciences, 13(6), 1507–1526.

Goodman-Tchernov, B.N., Dey, H.W., Reinhardt, E.G., McCoy, F., & Mart, Y., 2009. Tsunami waves generated by the Santorini eruption reached Eastern Mediterranean shores. Geology, 37(10), 943–946.

Heinrich, P., Dupont, A., Menager, M., Trilla, A., Gailler, A., Delouis, B., & Hébert, H., 2024. Simulation of the Mediterranean tsunami generated by the Mw 6.0 event offshore Bejaia (Algeria) on 18 March 2021. Geophysical Journal International, 237(3), 1400–1413.

Heinrich, P., Jamelot, A., Cauquis, A., & Gailler, A., 2021. Taitoko, an advanced code for tsunami propagation, developed at the French Tsunami Warning Centers. European Journal of Mechanics-B/Fluids, 88, 72–88.

Kalligeris, N., Skanavis, V., Charalampakis, M. et al., Field survey of the 30 October 2020 Samos (Aegean Sea) tsunami in the Greek islands, 2022. Bull Earthquake Eng 20, 7873–7905. https://doi.org/10.1007/s10518-021-01250-6

Leclerc, F., Palagonia, S., Feuillet, N., et al., 2024. Large seafloor rupture caused by the 1956 Amorgos tsunamigenic earthquake, Greece. Commun Earth Environ, 5, 663, doi: 10.1038/s43247-024-01839-0.

Manning, S.W., Ramsey, C.B., Kutschera, W., Higham, T., Kromer, B., Steier, P., & Wild, E.M., 2006. Chronology for the Aegean Late Bronze Age 1700–1400 B.C. Science, 312, 565–569, doi: 10.1126/science.1125682.

McCoy, F., & Heiken, G., 2000. Tsunami generated by the Late Bronze Age eruption of Thera (Santorini), Greece. Pure and Applied Geophysics, 157, 1227–1256, doi: 10.1007/s000240050024.

Okada, Y., 1985. Surface deformation due to shear and tensile faults in a half-space. Bulletin of the Seismological Society of America, 75(4), 1135–1154.

Okal, E.A., Synolakis, C.E., Uslu, B., Kalligeris, N., & Voukouvalas, E., 2009. The 1956 earthquake and tsunami in Amorgos, Greece: Geophys. J. Int., 178, 1533–1554.

Zahradník, J., Aissaoui, E. M., Bernard, P., Briole, P., Bufféral, S., De Barros, L., et al., 2022. An atypical shallow Mw 5.3, 2021 earthquake in the western Corinth rift (Greece). Journal of Geophysical Research: Solid Earth, 127, e2022JB024221. https://doi.org/10.1029/2022JB024221